Investigating the biomechanics and biochemistry underlying MRI measures of neuronal function

Frida Hauge Torkelsen

PhD

University of York
Chemistry
September 2022

Abstract

This thesis investigates the biophysical mechanisms underlying functional magnetic resonance imaging (fMRI) measures of brain activity. Diffusion-weighted fMRI (DWfMRI) has been suggested as an alternative to the established Blood Oxygenation Level Dependent (BOLD) method. It is speculated to be sensitive to transient microstructural changes within active brain tissue, which could provide a more direct measure of neuronal activity than techniques relying on attendant haemodynamic changes. DWfMRI has yet to become widely accepted however, as the mechanism driving the observed signal is not well understood. Here, experimental and theoretical investigations of the fMRI signal are presented.

As part of this work, a functional MRI study was undertaken to compare BOLD and DWfMRI responses to stimulated brain activity in human volunteers. The effect of different experimental protocols were explored, with an emphasis on stimulus design. Analysis methods and their potential impact on interpretation of the response are explored.

Neuronal activation is accompanied by heamodynamic changes detectable with Optical Imaging Spectroscopy. Additionally, there is a growing base of evidence showing microstructural changes in excited neuronal tissue. This tortuosity change might be observable through the use of Spatial Frequency Domain Imaging (SFDI). These properties can be observed in the animal model and compared with fMRI to aid interpretation. The following work presents the development of in-vivo optical imaging techniques for the measurement of tissue optical property changes during brain activity. This includes theoretical explorations of the analysis pipeline, and of the potential limitations of these techniques and their sensitivity.

A Monte Carlo simulation of light transport through tissue was written to provide calibration data for the optical imaging methods. The simulation was used to explore the impact of tissue parameters on the optical results and inform interpretation. The simulation was extended to explore tissue absorption in the context of biophotomodulation.

Acknowledgements

I would like to thank everyone who has provided advice and guidance throughout the completion of this thesis. Firstly I would like to thank my supervisor, Dr Aneurin Kennerley for devising the project and providing guidance throughout. This work would not have been possible without the practical training and continued support in trouble shooting which is required for experiments of this nature.

My sincerest thanks to Professor Alex Wade from the Department of Psychology for insightful discussions, and for providing additional perspectives and always inspiring advice over the years.

I would like to give special thanks to Dr. André Gouws from the York Neuroimaging Centre for incredible patience and problem-solving attitude in helping me with running the MR system. Thanks should also go to the YNiC staff for providing support and training for the MR experiments completed at the centre.

I'm also very grateful to Dr. Christopher Reardon and Professor Thomas Krauss from the Department of Physics, for their advice on the design of the optical system. Their willingness to share their expertise was greatly appreciated.

Many thanks to Dr Heidi Baseler of the Department of Psychology, for great interdisciplinary collaboration during my participation in the photobiomodulation work, and for helpful discussions throughout.

Special thanks to Victoria Annis, technician at the Centre for Hyperpolarisation in Magnetic resonance, for all the help with practical matters great and small.

Thank you to Annabel Smith and the rest of the group of Professor Miles Whittington for allowing me to borrow materials for use in method development.

Thank you also to the team at the Biological Services Facility for their support of the lab experiments. I would also like to thank everyone at the Chemistry workshop for creating some of the components needed for the imaging setup.

Lastly, I would like to express my sincerest gratitude to everyone who volunteered to take part in my functional MRI study. This work would not have been possible without their contribution.

Author's declaration

I declare that this thesis is a presentation of original work and I am the sole author. This work has not previously been presented for an award at this, or any other, University. All sources are acknowledged as References.

Contents

List of Tables

List of Figures

1 Introduction

Brain activity can be mapped using a range of techniques, and a well accepted method is magnetic resonance imaging. It is commonly used in both clinical applications,[1] such as in planning of brain tumor resection,[2] mapping of cortical functions for epilepsy interventions,[3] Alzheimer's identification[4] and monitoring, or evaluation of traumatic brain injury,[5] and in research, where it is used to study for example memory,[6] language[7,8] and ageing.[9,10] The standard functional MRI method, Blood Oxygenation Level Dependent (BOLD) fMRI, was first introduced in 1990 by Ogawa *et al.*[11] The measured BOLD signal is complex, and relies on physiological changes in cerebral blood oxygenation, flow, volume and oxygen extraction fraction, as well as on physical parameters, including magnetic susceptibility, volume fraction, vessel orientation and more. Since active regions of neurons require the influx of fresh oxygenated blood to replenish the cells with energy, BOLD maps have been thought of as activation maps, with an increase in blood flow being interpreted as a direct effect of oxygen consumption or energy usage of the brain tissue.[12,13] It is however important to note that the BOLD signal is an *indirect* measure of activation. Since the signal is a composite effect of haemodynamic rather than neuronal changes, the response is driven by changes in nearby vessels. It can include contributions from vessels remote from the activation site due to the anisotropic density of vessels and draining patterns in the brain,[14] and the signal is weighted towards the surface, where vessel diameters are larger. Neurovascular coupling, the mechanisms which links neuronal activity to blood flow increase, is also not fully understood,[15] and this behaviour can change with brain region,[16–18] age[19] and pathology.[20–22] The interpretation of the BOLD signal is therefore not straight forward.

LeBihan et.al. (2001) proposed an alternative measure of neuronal activity with MRI.[23] They suggested that brain cellular volume changes could be measured as an alternative, more direct indicator of neuronal activity. There is growing evidence of cell volume changes in activated brain tissue from *ex-vivo* work, this has been measured in model systems such as brain slices and cell cultures from rat, using optical birefringence,[24] piezoelectric tranducers,,[25] microscopy[26] and intrinsic optical imaging.[27,28] The method proposed for the detection of this process is called Diffusion Weighted func-

tional MRI (DW-fMRI). MRI can be made sensitive to the microscopic diffusion of water molecules through tissue. As the molecules move within a spatially varied magnetic field, the phase shifts become distributed, and this loss of coherence can be detected as a signal attenuation.[29] This means that water molecules can in turn be used to probe the tissue microstructure, as diffusion of the molecules will be affected by the cellular structures and cell sizes and orientations.[29] Diffusion of water has been shown to decrease with neuronal activation,[23,30] and it has been suggested that this is caused by the swelling of cortical cells[31] and by a shrinking of the extracellular space which increases its tortuosity,[32] in turn restricting local diffusion.

Importantly, the DW-fMRI response to activation occurs several seconds before the BOLD response,[30] as shown in Figure 1.1. The rapid onset could indicate that the DW-fMRI response is linked very directly to neuronal activity or linked to a fast coupling mechanism,[33] and could therefore measure a more immediate effect of this activity than the haemodynamic response. It has been stipulated that if the signal is largely caused by cell swelling, the location of the response could be closer to the site of the activation compared to BOLD, and that the response would be more closely aligned with the temporal onset of activity.[29] If haemodynamic contributions could be reduced, the signal could also be less affected by the many physiological confounds of concern in BOLD mentioned previously. DW-fMRI has however not become widely used, perhaps due to the fact that the biophysical origin of the signal is still not fully understood.[34] It is still debated whether the signal is caused by cell swelling,[33] haemodynamic effects,[35] or a combination of the two.[36] It has been shown that the diffusion response persists under neurovascular coupling inhibitors, which quench the BOLD response while maintaining the neuronal response as demonstrated by local field potential (LFP) recordings.[33] This would suggest the DW-fMRI signal contains a component which is not vascular in origin. It has also been observed in ganglia[37] and brain slices[17] without blood, with the use of neurotransmitters. Another group concluded the DfMRI signal is vascular in origin after a hypercapnia study, where the short rise time could not be observed for high b-values.[36] Yet another group used calcium imaging combined with diffusion MR measurements, which indicated a direct correlation between the depolarisation of the neuronal cell membrane and water diffusion changes during hyperexcitability in cell cultures, but they could not find correlation

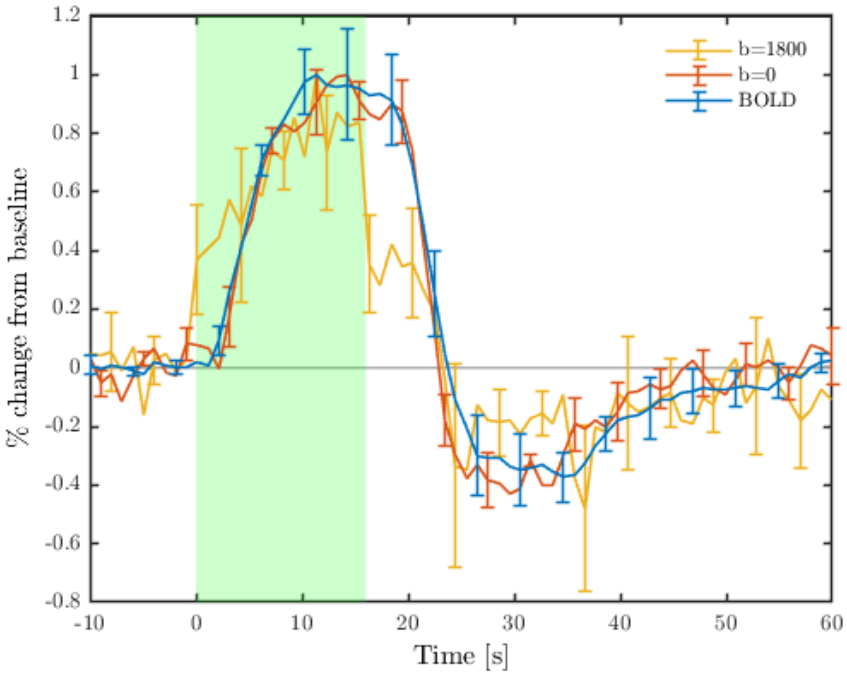

Figure 1.1: Time courses of the response to a 16 second visual stimulus (highlighted in green) as measured with BOLD (blue) and with DW-fMRI with a b-value of 0 (red), and with DW-fMRI with a b-value of 1800 (yellow), averaged across participants. The response measured with a high diffusion weighting shows a more rapid onset after stimulus start, in agreement with the results in the study by Le Bihan et. al.

to normal neuronal activity, suggesting the DW-fMRI signal is not sensitive enough to detect it.[34]

This thesis aims to verify the signal source of the DW-fMRI by using concurrent high resolution optical measurements of the tissue microstructure. The technique developed detects, for the first time, cellular swelling alongside the DW-fMRI signal using Spatial Frequency Domain Imaging (SFDI). This optical imaging method measures remitted light from tissue to provide information on the absorption and scattering properties of the tissue.[38,39] Scattering measurements can be used to indicate changes in cell size.[24] As cells expand, the membrane refractive index changes, changing the measured scattering parameters. If cellular swelling drives the DWfMRI signal, the time course of scattering changes should be in agreement with the rapid onset of its response. Absorption can be related back to the concentrations of chromophores in the tissue. The highest absorbing of these are oxy-

genated and deoxygenated haemoglobin, while other major chromophores are cytochrome, lipids and water. As oxy- and deoxyhaemoglobin have distinct absorption spectra, the remitted light can be used to monitor their concentrations. The optical measurements therefore allows deconvolution of the haemodynamic contributions from the DW-fMRI signal. By employing these two techniques together, information about diffusion, absorption and scattering can be recorded for the same neuronal event, providing information on the link between cellular swelling and measured diffusion.

Providing a proof for the signal source of the DWfMRI response could provide confidence in the technique, bringing it to further use and development. If the method could offer improvements in how neuronal activity is measured, this would have benefits both in clinical and research applications which currently rely on BOLD fMRI. Further, the concurrent investigation of neuronal activity and the simultaneous haemodynamic changes, could help improve understanding of the tight interconnectivity between the two, known as neurovascular coupling. As well as being the target of academic interest, with rapidly increasing number of citations in recent years,[40] neurovascular coupling has been shown to be impaired in a range of pathological conditions, and holds potential as an indicator in health and disease. In particular, there is growing evidence for impairment of neurovascular coupling in Alzheimer's Disease (AD).[21] AD and vascular dementia is a leading cause of death, and while it remains a complex disease it is thought to have a significant neurovascular component.[21]

1.1 Neurovascular coupling

The brain requires large amounts of energy, which it derives primarily from oxygen and glucose. The brain does not have the means of storing energy reserves, it therefore requires rapid and sufficient supply of nutrients to be transported to the activated areas via the blood stream.[40] This is regulated by a process known as neurovascular coupling, which describes the interplay between neuronal activity and the associated changes in blood flow.

The definition of the neurovascular unit (NVC, Section 1.1.2) in 2001, identified key vascular and neuronal components involved in the regulation of cerebral blood flow.[41] Interest in the topic is still increasing in recent years due to the interest in neurodegenerative diseases previously assumed to be unrelated to the vascular system.[40] By emphasising the relationship between cerebral blood supply and brain cells, this definition challenged the classification of for example Alzheimer's disease as a neurodegenerative and stroke as a cerebrovascular diseases. Technological advances have also enabled researchers to investigate this connection further.[40]

Neurovascular coupling has gained much interest within neuroscience and psychology.[18,20,40,42] Understanding of the cells' control of blood flow is central to understanding brain function, as well as to and to develop treatments for defects to cerebral blood flow control which can be associated with neurological disorders such as stroke, hypertension and Alzheimer's disease.[16] Neurovascular coupling is also key to interpreting functional imaging data[43] The complex interplay between neuronal activity and heamodynamic changes drives the observed signal changes, and has therefore been an important topic in neuroimaging since the early uses of fMRI in the 1990s.[11,44,45] Angelo Mosso invented the first neuroimaging technique in 1881,[46] and in 1890, Roy and Sherrington first discovered the ability of an active region of neurons to increase local cerebral blood flow.[47] In 1945, Craigie[48] showed that the density of vasculature changed throughout the brain, and that increases in neuronal activity was associated with a change in blood flow. This close coupling was established with the development of the blood-oxygenation level dependent (BOLD) imaging technique in 1990 by Ogawa *et al.*[11]

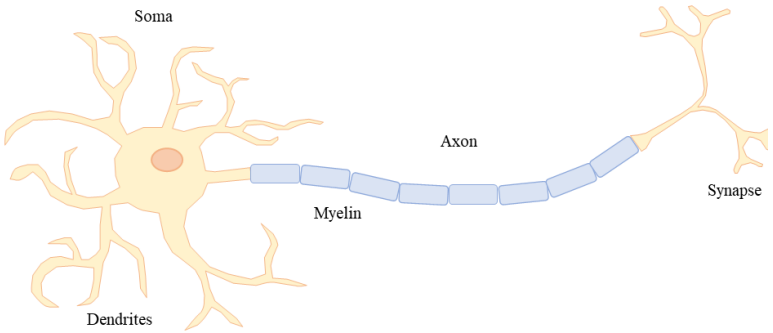

Figure 1.2: The structure of a neuron. The soma is the cell body, which contains the nucleus of the cell. The axon extends away from the cell body, and can reach over a meter in length in humans. It is covered in a myelin sheet, which accelerates propagation of electrical signals along the axon.

1.1.1 Neuronal activity and metabolism

Neurons are specialised cells which transmit information between each other and to muscle or gland cells. A schematic of the neuron structure is shown in Figure 1.2. It consists of the cell body or soma containing the nucleus and cytoplasm, an axon which extends to form branched nerve terminals, and dendrites which receive information from other neurons. Groups of interconnected neurons, known as neural circuits, communicate using chemicals transmitted via synapses, which form the contact points between their dendrites and axons.

Neurons exchange information in the form of electrical and chemical signals. They are able to generate electrical potentials by maintaining voltage gradients across their cell membranes. These gradients are caused by the difference in intra- and extracellular concentrations of charge-carrying ions like Na^+, K^+, Cl^- and Ca^{2+}. When it is not activated, this is referred to as the resting membrane potential, and ranges between -40mV and -90 mV.[49] The gradients are controlled via the voltage-gated ion channels within the cell membrane on the axon and soma. A stimulus causes specific ion-channels in the cell membrane to open, which allows ions to flow through, changing the membrane potential. With a large enough voltage charge, it creates an all-or-none electrochemical pulse known as an action potential. When the neuron 'fires', this cross-membrane potential travels along the axon of the cell, activating the synapse connecting it with other cells. Non-neuronal cells in the brain and spinal cord known as glia do not generate electrical

impulses, but they form myelin, a substance consisting of lipids and protein. Myelin can form a layer covering the axons of neurons, and cause the electrical signalling via the axon to accelerate.

If a neuron responds at all, it responds completely. Greater intensity stimulation does not give a stronger signal, but the firing frequency can get higher.[50] This depends on the type of receptor. Tonic receptors are slowly adapting. These respond to steady stimulus with a steady firing rate, and an increased intensity of stimulus usually increases the firing frequency. Phasic receptors are quickly adapting. These types respond to steady stimulus by decreasing or stopping firing. One example of this is skin touching an object; at first the neurons fire, but on continued contact they stop. Neuronal activity can also undergo habituation,[51] where the response to a stimulus dampens on repetition. This can be observed with fMRI, for example with visual and auditory stimulus.[52,53]

After a firing event, the synapses need to be reset. The maintenance of Na^+/K^+ ion gradients across the cell membrane relies on the energetic compound ATP[54] Neurons are responsible for $70-80\%$ of the energy consumed by brain cells, the rest is used by glial cells such as astrocytes, oligodendrocytes, and microglia.[55] On firing, the synapse releases neurotransmitters like glutamate. Astrocytes surround the neuronal synapses, taking up glutamate and converting it to glutamine, which is returned to the neurons. This resets the synapse for the next event. Glutamate requires three Na^+ ions to be taken up alongside it to remain electrochemically neutral, which activates the Na^+/K^+ ion pumps to reset the osmotic gradient. This is a metabolic process, and the energy required is released by converting ATP to ADP. The astrocyte requires conversion of two ATP molecules per glutamate metabolised.[56]

The ATP required by neurons and glial cells is regenerated from ADP through the metabolism of glucose in the mitochondria, Figure 1.3. First, glucose enters the cell and is phosphorylated to G6P. This is a rapid process, therefore a steep glucose gradient is maintained over their membranes.[54] In neurons, G6P proceeds to the glycolytic pathway and the pentose phosphate pathway (PPP). This generates building blocks for DNA and RNA while reducing $NADP^+$ to NADPH, a species which is important for mitigating against oxidative stress.[57] Glycolysis (Figure 1.4) is an anaerobic

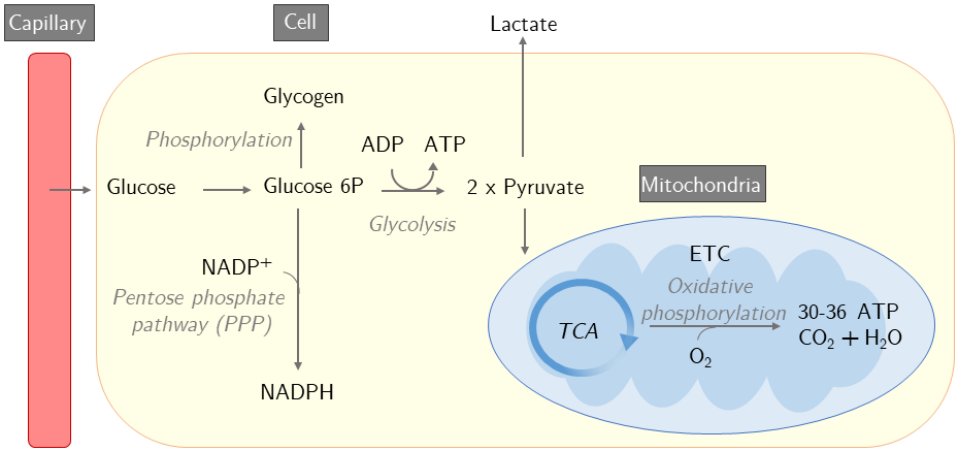

Figure 1.3: The metabolism of glucose, which regenerates ATP from ADP.

process which converts glucose into to pyruvate molecules, meanwhile producing ATP from 2 ADP. Pyruvate can be actively transported into the mitochondria. There, it is further converted to Acetyl coenzyme A (acetyl-CoA) which is metabolised through the tricarboxylic acid (TCA) cycle, as shown in Figure 1.5.[57] The TCA cycle generates energetic compounds in the form of three NADH, one $FADH_2$ and one GTP. NADH and $FADH_2$ are electron carriers, which go on to take part in the electron transport chain (ETC). Most of the ATP produced by aerobic metabolism of glucose is generated in the ETC, which consists of five main protein complexes located in the inner membrane of the mitochondria, Figure 1.3. NADH and $FADH_2$ donate their electrons to Complexes I and II respectively, and these pass the electrons on through the complex chain, allowing a series of redox reactions occur. Energy is generated through this process, and it causes hydrogen ions to build up in the matrix space outside the inner membrane, forming an electrical and chemical concentration gradient across it. In response, the H^+ ions diffuse back across the membrane mainly by passing through ATP synthase, driving it to oxidatively phosphorylate ADP to ATP. Overall this process consumes O_2, with each glucose molecule generating 30-36 molecules of ATP, as well as water and CO_2, which is released back to the plasma.[58]

Astrocytes' G6P can also be used in the PPP, however it is primarily metabolised via glycolysis to produce lactate from generated pyruvate, with very little mitochondrial oxidation.[59] Unlike neurons, astrocytes are also able to store glucose is as glycogen, which is the largest form of energy

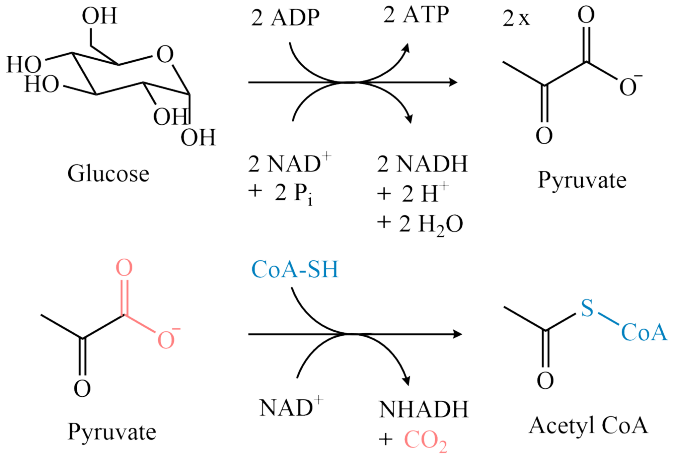

Figure 1.4: A glucose molecule can be converted into two pyruvate molecules. Pyruvate is converted into acetyl CoA, which takes part in the TCA cycle.

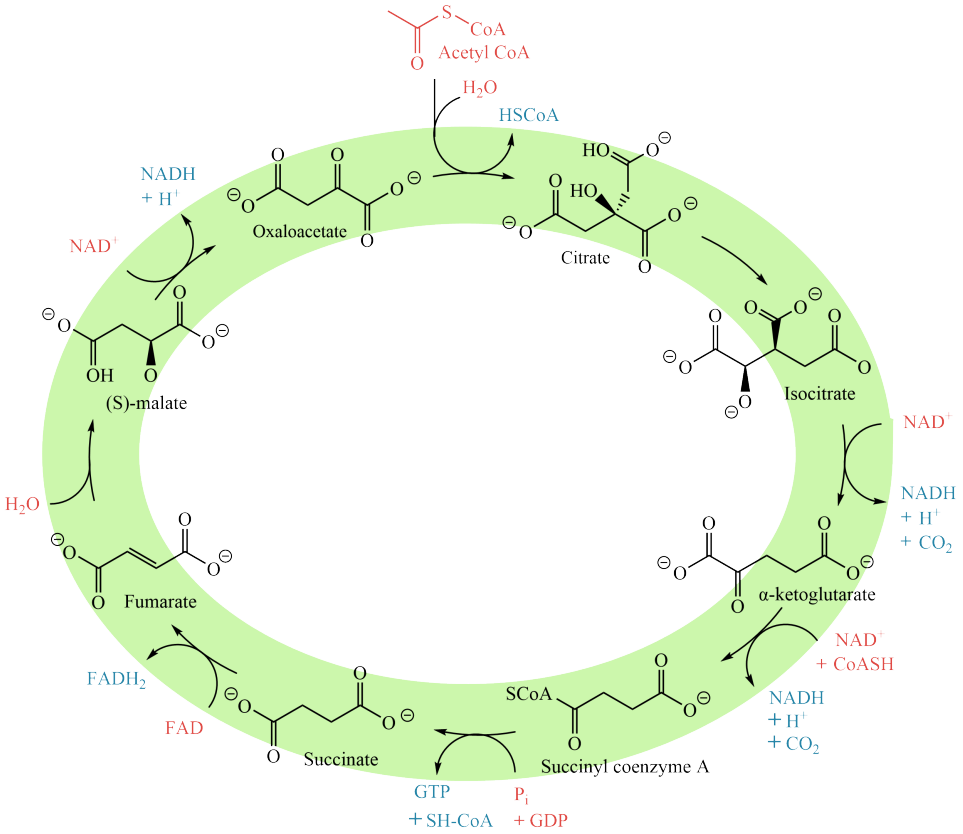

Figure 1.5: The TCA cycle. Inputs and outputs are marked in red and blue respectively. Acetyl CoA is produced from pyruvate and provides an acetyl group to the cycle. Overall the process generates three NADH, one $FADH_2$ and one GTP.

reserve in the brain.[58]

Neurons are predominantly oxidative, processing glucose to form NADPH through the PPP, while astrocytes are mostly glycolytic,[59] generating lactate and pyruvate.[57] The oxygen is delivered by the blood stream, where it is carried by the red blood cells through binding to haemoglobin (Section 1.3.1). Since neurons operate via aerobic mitochondrial metabolism they are very sensitive to hypoxia, surviving only 3 to 5 minutes in an anoxic environment[60] Astrocytes on the other hand are primarily anaerobic. Although they can generate ATP via the TCA cycle, they mainly rely on anaerobic glycolysis, and can in fact be cultured for up to 24 hours from human brain tissue.[61] Although astrocytes require much less energy to function than neurons, they have direct access to the vasculature, as capillaries are to a large extent covered by their endfeet.[62] This has led to the suggestion that astrocytes act as mediators, transferring additional energetic species to neurons.[63]

The brain requires large amounts of energy, accounting for around 20 percent of the body's energy use.[64] Although the brain's energy is primarily transferred through the metabolism of glucose, other energy sources can be used if glucose is not available. Examples of this is during fasting, when ketones are metabolised, and during intense physical activity, when the use of lactate is increased.[58] There are limited options for energy storage, so the brain relies almost entirely on the blood stream for supplying the metabolites required in ATP production.[64] The regulation of blood supply to active neurons is therefore crucial to their function and health, with a reduction in the brains' metabolism of glucose and oxygen playing a role in neurodegenerative disorders as well as in ageing.[58]

1.1.2 The neurovascular unit

The neurovascular unit (NVU) refers to the network of components that control the blood flow to the brain. It comprises neurons, astrocytes, pericytes, the blood-brain barrier, endothelial cells, myocytes and extracellular matrix components,[41] as well as the blood vessels themselves.[65] The interplay between these components controls the vasodilation and vasoconstriction in regions of the brain in order to moderate the local levels of oxygen, nutrients and by-products. The NVU is functionally heterogeneous throughout the brain,[65] and the density of the NVU components varies along the angioar-

chitecture. An overview is shown in Figure 1.6.

The brain blood supply comes from two pairs of arteries; the carotid arteries at the front of the neck and the vertebral arteries along the back of the neck. These come together at the base of the brain to form the circle of Willis, which is connected to the anterior, middle and posterior cerebral arteries supplying all areas of the brain. They divide into progressively smaller arteries and arterioles along the brain surface before entering into the brain tissue.[66] They reach the capillary beds, which form a densely connected network. The majority of the supply of oxygen and nutrients to the cells takes place via the capillaries. Capillaries are thin, 5 to 10μm. Red blood cells can therefore barely fit through it, yet their velocity through the cerebral capillaries is quite high, ranging between 0.3 and 3.2 mm per second. This speed varies by region, as some regions of brain tissue have higher metabolic demands, requiring more rapid supply.[66]

The blood-brain barrier provides a boundary between the brain and the blood stream, allowing for the entry of nutrients from the blood to the brain and the exit of by-products back to the blood stream. This ensures that metabolites such as glucose, amino acids and ketones can transfer efficiently through selective transport, while also protecting the brain by limiting the diffusion from the blood to the brain of solutes that could damage the neurons. The blood-brain barrier consists of capillary endothelial cells with tight junctions that inhibit water-soluble molecules from entering, allowing only small nonpolar lipids and gases like O_2 or CO_2 to passively diffuse across according to their concentration gradients.[65] Any other nutrients require passive or active mediated transporters. Proteins for example must cross by interaction with receptors and transporters. Carbohydrates, amino acids, fatty acids and organic cations and anions are transferred transferred in by solute carrier proteins.[58] Glucose is carried by various transporters, and of these the levels are highest for GLUT1 and GLUT3. Glucose crosses the blood-brain barrier by the help of GLUT1. The barrier cells have unidirectional transporters which, during glucose or oxygen deprevation, couple the sodium electrochemical gradient to admit glucose against its concentration gradient. GLUT3 ensures it is taken up by the neurons, this transporter has a higher affinity and transport capacity for glucose than the others, and can therefore ensure the neurons are supplied with glucose even if concentrations are low.[58]

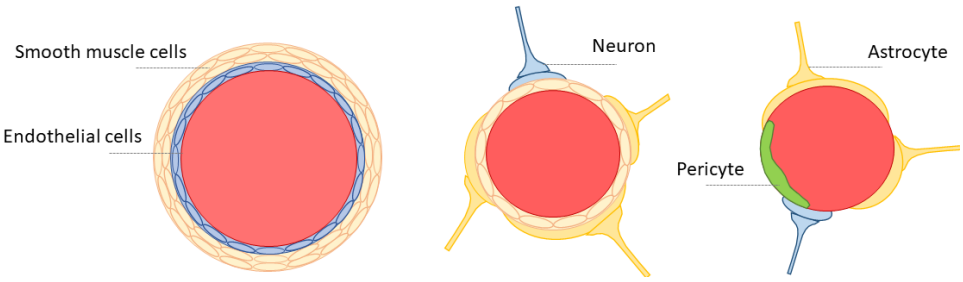

Figure 1.6: Penetrating arterioles enter the brain tissue, As arterioles move deeper into the brain and become thinner, the environment around them change. Pial artieries (left) run along the cortical surface, within the subarachnoid space. They enter the brain and become penetrating arterioles (middle), reaching down to the capillary beds. Here, neurons and astrocytes start appearing. By the capillaries (right) the smooth muscle cells have been replaced by pericytes.

The environment directly surrounding arterioles vary by region, as shown in Figure 1.6. Arteries entering the brain from the subarachnoid space are covered by a layer of smooth muscle cells (SMC) and pia mater, which becomes thinner as the arterioles reach deeper into the brain.[40] The arterioles are met by the endfeet of astrocytes. On the capillaries the SMC layer is replaced by pericytes, which emerge between the endothelial cells and the astrocyte endfeet.[65] Pericytes are contractile cells which regulate and stabilise the microvascular cerebral blood flow.[67] Pericytes at different locations along the capillary function differently; those near the arteriole are likely more involved in the blood flow regulation, those in the middle are thought to be important for maintaining the blood-brain barrier, and those at near the venule may regulate the flow of immune cells.[67]

Brain tissue is itself heterogeneous, with noticeable structural differences depending on depth. This has given rise to the classification of brain layers, as shown in Figure 1.7. Cajal describes the nerve cells as arranged into four layers, from the molecular layer closest to the surface, down through the layer of small pyramidal cells, then the layer of large pyramidal cells, and finally the layer of polymorphous cells.[68] Perpendicular to the surface, neurons responsible for similar tasks are grouped together as they need to communicate. These 'columns' of neurons have similar response behaviours.[69]

1.1.3 Neurovascular coupling mechanism

The proposed mechanisms by which blood flow is increased during brain activity are sometimes described as either 'feedback' or 'feedforward'. Work

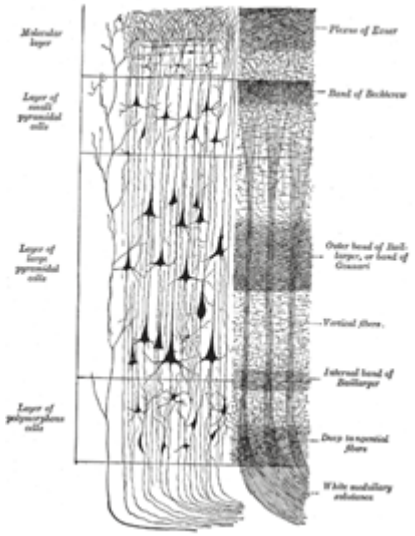

Figure 1.7: The structure of nerve cells for the different brain layers, as described by Cajal.

as early as 1890 proposed feedback mechanisms, which suppose that the metabolic demands of the neurons drive the blood flow response.[47] Blood flow not only delivers oxygen and glucose, but brings away by-products of brain metabolism such as lactate and CO_2, as well as Aβ and τ, which are building blocks for plaques and tangles that are present in Alzheimer's Disease.[70] Some of the by-products, including adenosine, CO_2, H^+ and lactate, are vasodilators. It has therefore been suggested that the build up of these products causes the expansion of vessels, which facilitates the increase in blood flow associated with activation.[71] Blocking of adenosine receptors has indeed been shown to reduce the blood flow response to activation.[71] The feedback model is in agreement with studies showing that oxygen and glucose is reduced in the active region prior to the blood flow response.[72] This initial reduction in O_2 is also shown to increase deformability of red blood cells, which leads to increased blood flow in capillaries.[73] Feedforward mechanisms propose that increase in cerebral blood flow is independent of metabolism, and instead is driven by neurovascular signalling pathways. This model is supported in the work of Fox and Raichie,[74] which showed that during activity, the blood flow increases much more than the oxygen metabolic rate ($CMRO_2$). cerebral blood flow increase is therefore greater than that required to supply the tissue with oxygen, and in fact occurs even when oxygen and glucose is present in excess. Their work challenged the

idea of CBF changes being metabolically driven. This is also key to the production of a BOLD signal; although the consumption of O_2 has increased, activity causes the oxygenation of the venous blood to *increase*, as the increased blood flow more than compensates for this.[75] The mechanism for this signalling is still unclear,[16] there may be multiple pathways. The models are not mutually exclusive. Recent work suggests neurovascular coupling is caused by a combination of the two; it is largely caused by a feed-forward triggering of blood flow through signalling, with a feed-back mechanism adjusting the blood flow based on the regional metabolism.[16] The influence of the two models is also likely to vary by region. Different brain regions have widely different base oxygen levels[76] and vascular structure, and in some areas this could cause local hypoxia on activation, driving vasodilation and resulting in CBF increase.[40]

Already in 1897 it was suggested astrocytes could regulate cerebral blood flow.[68] They are in contact with neurons, and their endfeet envelop cerebral blood vessels, giving them a good location for mediating neurovascular coupling. This appears to be controlled via Ca^{2+} transients, as the concentration of Ca^{2+} within astrocytes is raised during neuronal activity,[77] and Ca^{2+} has been shown to cause both dilations and constrictions in nearby arterioles.[78] This ability was investigated in brain slices under different levels of pO_2.[79] Uncaging Ca^{2+} in 95% O_2 solutions caused arteriole constriction, but in 20% O_2, which is closer to physiological levels, the process reversed, giving arteriole dilation. The role of astrocytes in neurovascular coupling was challenged by an *in vivo* two-photon study which indicated calcium increase occurred after the onset of arteriolar dilation, and that vasodilation was preserved in mice lacking the primary pathway for astrocytic Ca^{2+} increase.[80,81]

Pericytes may contribute to regulation of microvascular blood flow, this was suggested as early as 1923, due to their suitable location on capillaries.[82] Pericytes express contractile proteins and are located on the capillaries where there are no smooth muscle cells.[83] Pericytes' ability to constrict and dilate have been shown *in situ*, for example in retinal capillaries, where they respond to neurotransmitters due to changes in Ca^{2+} concentration. This has also been shown in brain slices, where pericytes constrict capillaries under noradrenaline and dilate them under glutamate.[16] A study by Hall *et al*[84] used this behaviour to conclude that capillaries are dilated by the pericytes

being actively relaxed. They used *in vivo* two-photon imaging to monitor pericyte dilation in the somatosensory cortex of mice during whisker pad stimulation. Results indicated that the pericytes are the first to dilate after a stimulus, therefore playing a major role in the regulation of blood flow in the brain. They observed far greater dilations of the capillaries where pericytes were present. Pericytes also have the ability to propagate between each other.[16] In response to electrical stimulus in retina and cerebellar slices, it has been shown that pericytes have the ability to propagate these signals to distant pericytes.[85] This ability combined with the relative proximity of neurons to pericytes compared to arterioles, has lead to the suggestion that vascular signals could be initiated by pericytes and propagated to upstream arterioles.[16]

Neurovascular coupling is impaired in certain diseases and pathological conditions. Examples of this include hypertension, Alzheimer disease, and ischemic stroke.[20] The alterations can come in various forms, such as reduced global cerebral perfusion which can follow cardiac arrest or hypotension, or microvascular changes in white matter, which can be linked to for example hypertension or diabetes.[86] If the blood flow response to activation is reduced, it could reduce the oxygen and glucose supply to neurons, reducing neuronal activity and cerebral function.[21] Cerebral blood flow plays an important role in vascular dementia, with damage to the vascular supply or reduced blood flow together with neurodegeneration being the leading cause of cognitive impairment.[86] In Alzheimer's disease (AD), blood flow changes can become less responsive to neuronal activity, known as neurovascular decoupling.[21] This has been linked to a breakdown of the neurovascular unit through pericyte deficiency.[87] Altered neurovascular coupling and a delayed vessel dilatory response, has been measured by optical imaging of retinal vessels and investigated as a potential biomarker of AD.[88] A stroke can cause local structural damage which alters the coupling, or cause changes to the vasoreactivity, reducing the CBF increase caused by activation.[20] Instances of this are also found in fMRI studies of multiple sclerosis (MS) patients, who have been shown to have reduced BOLD and CBF responses to visual stimuli.[21] One study also reported altered neurovascular coupling in patients with chronic stress.[22] Breakdown of the neurovascular unit and therefore neurovascular coupling has also been found in normal ageing,[89] which is the biggest risk factor for Alzheimer's disease and vascular dementia.[21]

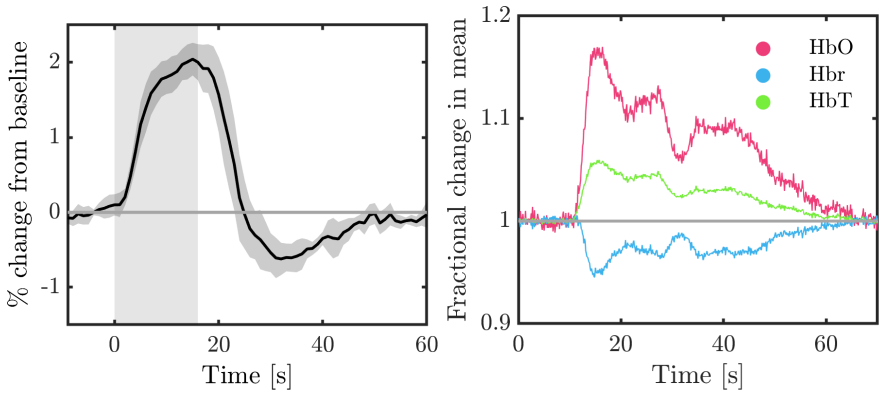

Figure 1.8: Left: The time course of a BOLD response to a 16 second stimulus, averaged across ten participants. Right: An example hemodynamic response for a 16 second whisker stimulus in the rat, from old data acquired previously in the group.

1.1.4 Implications for fMRI

The mechanisms of neurovascular coupling is key to the interpretation of fMRI data.[16] During neuronal activity, the energy demands of the cells increases the cerebral metabolic rate of oxygen ($CMRO_2$), which describes the rate at which oxygen is transferred to the cells. To supply enough oxygenated haemoglobin (HbO) and nutrients, there is an increase in cerebral blood flow (CBF), with arterial blood flowing towards the active site, causing an increase in the regional blood volume (CBV). This process also washes out the deoxygenated haemoglobin (Hbr).

A typical haemodynamic response to activation is shown in Figure 1.8 The BOLD fMRI signal is a composite measurement, indicating changes in cerebral blood volume, flow and $CMRO_2$. Paramagnetic deoxyhaemoglobin distorts the local magnetic field to a much greater extent than diamagnetic oxygenated haemoglobin. This has the effect of changing the frequency and phase of nearby spins. In order to detect this process, BOLD measures the T2* relaxation (Section 1.3.1), which largely depends on the local concentrations of deoxyhaemoglobin.[11] The blood flow supplies a surplus of oxygen (with CBF increasing by 2:1 over $CMRO_2$),[74] The relative concentration of deoxyhaemoglobin is reduced during activity. As the Hbr concentration decreases, the BOLD signal increases, and is therefore indicative of over-oxygenation in the activated region.

There is still some debate about which parts of the vascular system drive the hemodynamic changes. Arteries and arterioles have been viewed as driv-

ing the blood flow response to activation because these are the site of most vascular resistance[20,90] and are rich in SMCs which are absent on capillaries.[91] Much of the activity related CBF increase is however believed to be caused by the capillaries.[67] Capillaries are closer to neurons than arteries, and because they have large surface areas, even small changes in diameter could produce large changes in flow.[16] The early idea of capillary recruitment suggested that closed or slowly perfused capillaries are opened during brain activity.[92] *In vivo* imaging has however showed that almost all capillaries are already fully perfused under physiological conditions.[93] Capillary dilation occurs before dilation of penetrating arterioles (by 1.38 ± 0.38 s),[84] and is therefore not a passive effect of increased flow in the larger vessels. Capillary diameter is believed to be controlled to a significant extent by the active relaxation of pericytes. One study[94] observed these actions of pericytes *in vivo* using two-photon microscopy, but also found increase in flow of red blood cells through capillaries without pericyte induced capillary dilations. They therefore concluded precapillary and penetrating arterioles are responsible for regulating blood flow, rather than capillaries. Another study have argued that the contractile cells on capillaries are actually SMCs, and that true pericytes do not have this ability, with blood flow being regulated instead by arteriole SMCs.[91] These contradictions could however be due to difficulties of distinguishing pericytes and SMCs, as pericytes are morphologically heterogeneous and there is a lack of specific markers for them.[40]

BOLD is however not indicative of capillary CBF changes, but of a combination of contributions. Activity in specific neural regions can elicit a BOLD response from a wider area of interconnected vessels. Although arteries can dilate quite significantly, giving between 5 and 25% increase in diameter[95] it is veins that contribute most significantly to the BOLD signal. Arteries are smaller in volume and have high oxygenation ($> 95\%$) and therefore give relatively little contribution to the signal. Meanwhile venous blood has an oxygen saturation of 0.45,[96] and the signal is large due to the large increases in deoxygenated haemoglobin. The heterogeneity of the angio-architecture of the brain will influence the location of the signal. The layout of larger veins entering the brain with branching at depths, means that the heavily venous signal is both delayed and shifted closer to the surface relative to the activated capillaries.[14] The density of brain

capillaries also varies significantly within the brain depending on location and energy needs, with higher capillary density in gray vs. white matter.[66] In addition, volume exchange effects can impact the signal independently of blood oxygenation changes, for example through arterial changes in CBV that displace extravascular tissue.[97]

In early research it was assumed that the behaviour of neurovascular coupling represented a linear dependence of haemodynamic response to neuronal activity,[98,99] however more recent studies suggest it varies between brain regions,[16–18] across age groups[19] and between the contexts of health and disease.[21,22] Regional differences have been detected for example by using BOLD fMRI and electrophysiological measurements during whisker-stimulus in the rat,[18] and by BOLD and local field potentials in the monkey visual cortex.[100] The depth dependent fMRI signal changes show a fast onset in deep layers, with the initial dip pronounced in layer I, and concurrent measurements of arteriole and capillary diameters with two-photon microscopy have indicated a propagation of vasodilation upstream toward the cortical surface and downstream to the capillary beds.[95] BOLD models are therefore becoming increasingly complex[101] and are starting to account for layer-dependence.[102]

Neurovascular coupling is additionally important to DW-fMRI, as the signal could depend on activity related neuronal or glial cell swelling.[23] It is unclear which cells swell in response to activation. Pericytes' active dilation to regulate capillary flow is one example, but swelling has also been observed in neurons[103] and astrocytes.[104] Cellular volume is regulated by anion channels, which are important for decreasing the cell volume after osmotic swelling.[103,104] When separating the soma from the dendrites and axon of mouse cortical neurons, Cl^- currents are reduced by a half, indicating the volume sensitive channels are present in both the soma and dendrites.[103] Astrocytes can dilate due to aquaporins in their membranes. These are proteins that act as channels, allowing water to flow through. The process is controlled by osmotic gradients, in turn caused by clearance of excessive K^+ due to high neuronal activity. Both neurons and astrocytes swelling is triggered by osmotic gradient.[104]

1.2 The basics of MRI

1.2.1 Background

MRI relies on the nuclear property of spin, which represents a nucleu's quantum mechanical angular momentum. Protons spin at a given rate whether in a magnetic field or not. A spinning charge generates a magnetic dipole moment, and the spin property causes the nuclei to be magnetic, along its spin axis. The nuclear magnetic moment is given by

$$\mu_N = \frac{e\hbar}{2m_p} \tag{1.1}$$

where e is the charge of the particle, $\hbar$ is the reduced Planck constant and m_p the mass of the proton. For a proton the charge is $+1e$. The spin can be thought of as a vector, with components along the x, y and z-axes. It has a quantised magnitude, and depends on the particle type, and is denoted by the spin quantum number, S. According to quantum mechanics, the spin component along the z-axis, S_z can take $2 \cdot S$ values. For hydrogen, which has $S = 1/2$, there are therefore two possible values, $S_z = +1/2$ and $S_z = -1/2$.

In water the nuclei undergo diffusion, where random motion which causes them to interact and change each others local environments. At room temperature thermal collisions have energies that are much higher than needed to reorient a nucleus in a magnetic field, however it is well shielded and only interact weakly with the environment. Since the nuclei experience random and weak interactions, the precession will over time be very similar to that of non-interacting particles; the orientations of the magnetic dipoles are random, and the magnetization faces in different directions to form a nearly spherical distribution.

In the absence of an outside influence the magnetisation of a group of spins will form a nearly spherical distribution. If the nuclei are affected by a static external magnetic field, they will however have a tendency to point in the direction of the external field. The net magnetization vector, representing the average magnetisation at any given time, will therefore be pointing in this direction.

In a magnetic field, the two nuclear spin states of the proton become separated by an energy gap, ΔE. This is referred to as the Zeeman effect.

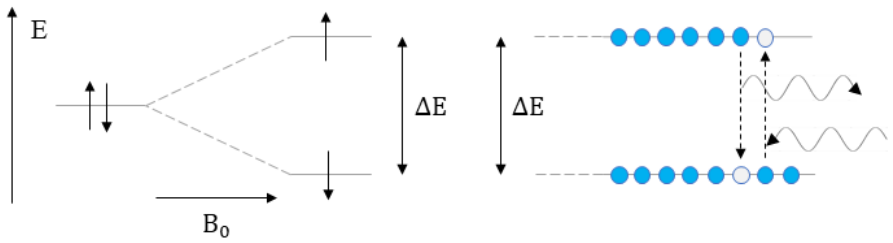

Figure 1.9: (Left) The Zeeman effect. The introduction of a nucleus, here with spin quantum number 1/2, into the external magnetic field causes the energy levels to split, with an energy gap ΔE given by the Zeeman Equation. (Right) The populations of spins for each energy state at thermal equilibrium is determined by the Boltzmann distribution. Transitions between states requires absorption or emission of energy.

This separates the spin states into a low energy and a high energy state. The Zeeman equation describes how this energy gap scales with the magnetic field strength, B_0.

$$\Delta E = \gamma h B_0 \tag{1.2}$$

Here γ is the gyromagnetic ratio of the nucleus, which represents the ratio of the particles' magnetic moment to its spin angular momentum.

The introduction of the external magnetic field causes the distribution of spins to rotate around the field direction, referred to as precession. The precession frequency is proportional to the field, and is given by the resonance Equation 1.5. For a proton, $\gamma = 2.675 \times 10^8$ rad $\mathrm{s}^{-1}\mathrm{T}^{-1}$. The gyromagnetic ratio is also the ratio between the observed angular frequency of Larmor precession (in rad s^{-1}) and the strength of the magnetic field in proton NMR applications, such as in MRI imaging. For this reason, the value of γ is often given in units of MHz/T.

Although the lower energy state would be favoured by the spins in order to minimise the system's energy, the presence of thermal motion causes a group of spins to be distributed between these states in accordance with the Boltzmann relationship, which is given in Equation 1.3. N_1 and N_0 are the populations of the upper and lower levels, ΔE is the energy difference between the two states, k is Boltzmanns constant and T is the temperature in Kelvin. There will be a slight excess of spins in the lower energy state, however the population difference is very small (around one in one million at 1 T).

$$\frac{N_1}{N_0} = e^{\frac{-\Delta E}{kT}} \tag{1.3}$$

MRI measures the relaxation of nuclear spin from an excited state back to equilibrium. The spins can transition between the states by either absorbing or emitting a photon with energy equal to the difference between the two states. The Planck relation (Equation 1.4) relates a photon's energy to its frequency, ν.

$$E = h\nu \tag{1.4}$$

Here h represents Planck's constant, which is $6.626 \cdot 10^{-34}$ Js. The significance of this constant is that energy can only be absorbed or released in discrete quantities. The frequency a photon must have in order to cause a transition between the two states can be found by combining Equations 1.2 and 1.4 to give Equation 1.5. This is the Larmor or resonance equation and the resonance frequency ν is therefore called the Larmor frequency.

$$\nu = \gamma B_0 \tag{1.5}$$

The system is excited using a radio frequency (RF) pulse. This causes the distribution of spins to rotate, in such a way that the net magnetisation vector is at an angle relative to the Z-direction and it will start to precess around the Z-axis at the Larmor frequency. Spins in the higher energy state can transition by spontaneously emitting energy in the form of RF at the reference frequency. Over time the spins will relax back to their equilibrium state, where the net magnetisation vector lies along the direction of the external magnetic field.

After excitation the spins undergo relaxation via two mechanisms each describing the orthogonal vector evolution of the magnetisation vector. Figure 1.10 shows this in terms of the respective time constants. T_1 or spin-lattice relaxation describes longitudinal relaxation of the net magnetisation vector. The M_Z vector, which describes the Z-component of the magnetisation, returns to its original position via an exponential recovery, with the time constant T_1.

$$M_Z = M_0(1 - e^{-\frac{t}{T1}}) \tag{1.6}$$

T_2 or spin-spin relaxation describes the transverse relaxation of the net magnetisation vector. The excited protons go out of phase with each other. Figure 1.10 shows exponential decay of the signal as the transverse compo-

nents of magnetisation, M_{XY}, start to dephase.

$$M_{XY} = M_{XY0}(e^{-\frac{t}{T2}}) \tag{1.7}$$

T1 relaxation is the process by which the longitudinal magnetization (M_z) approaches equilibrium. This represents a loss of energy, as the spins return from the excited state to their thermal equilibrium. The energy is transferred to the surrounding nuclei, atoms, and molecules through inelastic interactions. Collisions, rotations, or electromagnetic interaction from the nearby nuclei cause fluctuating magnetic fields, and if their RF fields are very close to the resonance condition, energy will be transferred in the form of very small amounts of heat. T1 relaxation is therefore sometimes referred to as spin-lattice or thermal relaxation. The amount of energy is very small compared to the molecular kinetic energies, it is therefore dispersed quickly and is typically small compared with body temperatures. From the Equation 1.6, the T1 time will be the time after excitation when the z-component of the net magnetisation has returned to $(1 - \frac{1}{e})$, or around 63%, of its maximum value. Different biological materials have T1 values ranging from a few tenths of a second to several seconds.

T2 relaxation causes the transversal magnetization perpendicular to the magnetic field (Mxy) to decrease exponentially, as shown in Figure 1.10. This represents a dephasing of spins, so that coherence between the transverse components of the net magnetisation decays until the spins become randomly distributed in the transverse plane. T2 relaxation accompanies all T1 relaxation processes, as a change in energy would affect both transverse and longitudinal spin components. It can also occur separately, therefore T2 is always shorter than T1. This secular T2 relaxation is caused by tissue factors affecting the local magnetic field, such as presence of nearby molecules containing iron or electronegative oxygen. Unlike the T1 processes, it progresses via elastic interactions, where energy is preserved. Here spins are affected by their neighbouring spins magnetic field, without loss of energy to the environment, it is therefore sometimes referred to as spin-spin relaxation. The T2 process is fast compared to T1, therefore T1 relaxation times are longer than or equal to T2.

T_2 assumes decay due to the random interactions between spins, however the signal actually decays faster than what what T_2 would predict. T2*

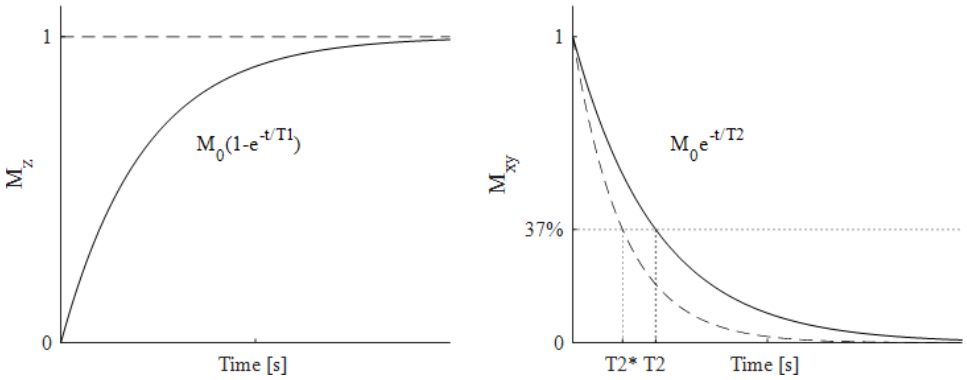

Figure 1.10: T1 recovery (left) and T2 decay (right). T_2* relaxation causes the transversal magnetisation to decay faster than what would be expected for T2 alone.

relaxation includes static magnetic field effects, additional to the tissue-characteristic effects causing T2 relaxation. These are fixed factors like small inhomogeneities in the applied magnetic field B_0, differences in the magnetic susceptibility of different types of tissue which distorts the field further, especially at the boundaries between tissue and air, and any type of metal that might be present in or on the patient. T2* relaxation is given by Equation 1.8.

$$\sqrt{\frac{1}{T_2*} = \frac{1}{T_2(random)} + \frac{1}{T_2(fixed)}} \tag{1.8}$$

Tissues have inherent relaxation times, and can therefore be distinguished in T1 and T2-weighted MR images. Spin-lattice and spin-spin relaxation is most efficient when the motion of the nuclei, in the form of rotation and translations causing variation of the local magnetic field, is close to the Larmor frequency. Since the Larmor frequency is proportional to the field strength, this optimal tumbling rate changes at higher field (Figure 1.11). Free water has a range of tumbling rates and is mostly inefficient at T1 and T2 relaxation. It therefore has long relaxation times and shows up as dark or low-signal areas in T1-weighted images, and bright in T2-weighted images. The field strength has little effect on the rates because the fraction of water with a given frequency of motion does not change much. Water molecules are small and magnetically de-shielded, as the dipole exposes H nuclei to the external field by pulling electron density away from them. Fat on the other hand has large molecules where the protons are magnetically

shielded. This leads to a lower resonance frequency and short relaxation times, which causes it to give high signal in T1-weighted images, appearing bright, and to appear dark in T2-weighted images. As an example CSF (T1≈4.1 seconds and T2=1.8 seconds at 3T)[105] contains much more water than white matter (T1≈900 ms and T2≈70 ms at 3T)[106] and relaxation times are longer. T2 is shorter in tissues than for example CSF, because the motion of protons in water and in macromolecules is slowed down by the interaction between them, more closely resembling the Larmor frequency. For less mobile protons, a higher field strength means a smaller fraction of them will have tumbling rates on the scale of the Larmor frequency, therefore T1 will increase, and typically be proportional to $B0^{(1/3)}$ for most biological tissues. Proteins, large macromolecules and more solid tissues such as tendons have short T2 relaxation times. These have slow motion below the Larmor frequency, and re-orient slowly, causing nearly static local magnetic fields. T2 relaxation accompanying T1 can be lengthened by increasing the field, as T1 is lengthened, but the relaxation due to static fields is not much affected. T2 can however be reduced at high field in the case of molecular diffusion which appears to be accentuated at high fields, and for chemical exchange which is more efficient at high field, this can for example occur in brain imaging at 7T due to structures containing iron. Bone will appear dark primarily because the water density is low, and the water there would be mostly bound to collagen and have short T2. The water protons resonate slightly faster than those in fat, the difference in resonance frequency is known as the water-fat chemical shift. Several methods have been developed to take advantage of these differences to suppress or separate the signal from the water and fat.

1.2.2 Detection and localisation of the signal

The MRI signal is detected using coils which are orthogonal to each other and to the static field. Transverse magnetisation that rotates around the direction of the main magnetic field will induce an AC current in an orthogonal coil. This current oscillates at the Larmor frequency. When excited spins undergo relaxation this signal, reflecting the magnitude of M_{XY}, takes the form of a free induction decay (FID), as shown in Figure 1.12. Because of the dephasing of the spins, the envelope of the signal forms an exponential decay, with the time constant T2*. This signal obtained is largest if

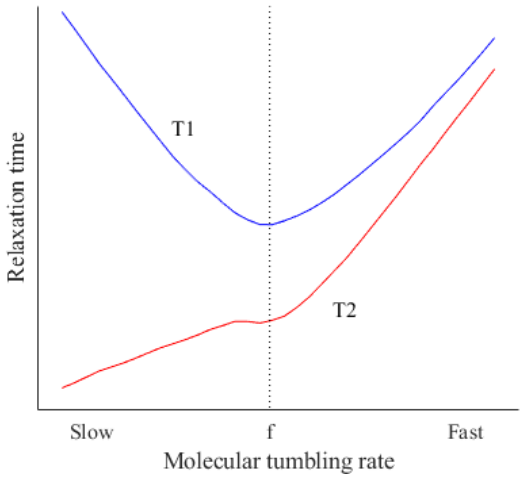

Figure 1.11: The motion of molecules, or tumbling rate, affects both T1 and T2 relaxation times. The T1 relaxation is most efficient when the molecular motion approaches the Larmor frequency, this can be seen as a minimum on the curve. T2 depends additionally on local magnetic fields present at motions below the Larmor frequency.

the spins are flipped by 90° so that the net magnetisation vector lies in the XY-plane. The time-domain FID signal can be Fourier transformed to give a representation in the frequency-domain, forming the basis of the NMR spectrum. The receiver coils orthogonal arrangement allows them to pick up signals as sine waves from two axes simultaneously, one records the part of the signal that is in phase with the reference signal (the real channel) and one that is 90° out of phase (the imaginary channel).

The time between excitation and when the signal is measured is called the echo time (TE), and the time between measurements is the repetition time, TR. The length of TE and TR determines the T1 or T2 contributions to the signal in MRI images. A long TR will give the longditudinal magnetization M_z time to re-align with M_0, but with a shorter TR the differences between the T1 relaxation of different tissues will be more apparent. A short TE means little T2 relaxation has occurred, so two tissues with different T2 values are not well differentiated. T2 weighting therefore requires long TR to minimise T1 contribution and long TE, but too long TE would give very little signal, so the sensitivity to T2 is best when TE close to equal to T2. A short TR and short TE maximises T1 contrast while minimising T2, giving a T1 weighted image. TE and TR can also be set to minimize contributions of both T1 and T2, with a long TR and a short TE. This gives a proton

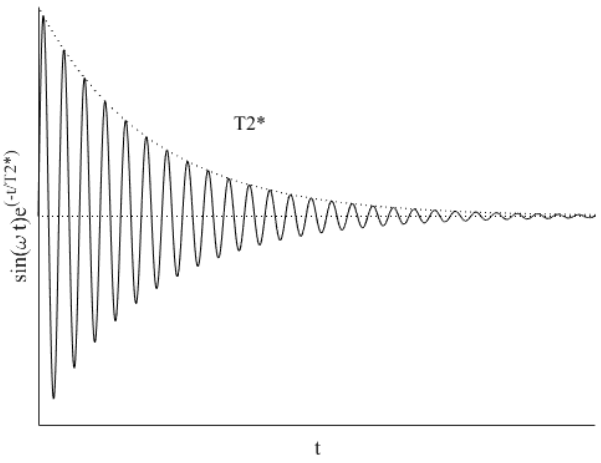

Figure 1.12: Free-induction decay (FID)

density weighted image.

In order to determine the origin of the signals, MRI uses magnetic field gradients. A magnetic field gradient is a linear change in magnetic eld strength along a given direction through the magnet. This is generated by gradient coil pairs positioned along the three main axes around the bore of the magnet, by passing equal current through the coil pairs in opposite directions. The field gradient passes through the centre of the magnet, where the eld is always constant. By varying the current in each coil, a gradient can be created as a linear combination of the components along the x, y and z directions. Across the gradient, the nuclei will have different resonant frequencies in accordance with the Larmor equation (1.5). The signal amplitude at a location along the gradient will therefore be proportional to the number of spins, or concentration at the given point.

Slice encoding involves applying an RF pulse along with a gradient to selectively excite spins in a 'slice' of the sample. The slice selection gradient creates a linear variation in the resonance frequencies across the sample in an axis perpendicular to the slice, and the accompanying RF pulse excites the spins among them which have the corresponding frequency. In order to achieve a uniform excitation of spins at a specific frequency, the RF pulse should be a sinc pulse, which is the Fourier transform of a square wave in frequency space. Since the full shape of a sinc pulse would have infinite side lobes, the generated pulse is truncated to a finite range. The

RF will therefore actually excite a small range of frequencies depending on its bandwidth, and with a stronger gradient these frequencies will occur in a thinner section of the sample. The limit for how thin a slice can be imaged is dependent on the maximal steepness of the gradient, which is determined by the maximal current. Gradients are also characterised by their slew rate; this is a measure of how fast the system can reach the peak amplitude, and sets the limits for the minimum achievable TE and TR. A fast slew rate requires a high voltage.

State of the art scanners use Fourier transform imaging techniques for spatial encoding. After excitation of a slice, phase and frequency encoding gradients are applied. The phase encoding gradient is turned on for a short time, and causes dephasing; the spins phase will depends on their position along the gradient. After the gradient is turned off, the spins will return to have the same frequency, however the phase difference persists after the gradient is turned off. The frequency encoding gradient is applied during readout of the signal, perpendicular to the direction of the phase encoding. The frequency encoding gradient causes a linear change in local resonance frequencies along the gradient direction. The effect of these gradients is that spins will have a frequency and phase which depends on their position along the X and Y directions in the slice along the Z direction.

The raw data collected is referred to as k-space, Figure 1.13. There will be a line in k-space corresponding to each phase encoding step, and each line will consist of a point for each step in the frequency encoding. Filling in k-space requires application of several phase encoding gradients. The duration of the acquisition sequence will therefore be a product of repetition time, the number of phase encoding steps, and the number of frequency encoding steps. K-space is the Fourier transform of a magnetic resonance image, with each point in k-space containing data from all locations within the image.

1.2.3 Methods in MRI

MRI sequences are commonly based on either a spin-echo (SE) or a gradient-echo (GRE) sequence. A spin-echo sequence is shown in Figure 1.15. It involves applying a 90° pulse followed by a 180° rephasing pulse. The first pulse flips the spins into the transverse plane, as shown in Figure 1.14. Spins will precess at slightly different speeds due to slight variations in the local microscopic field. Due to T2 relaxation, the spins will start to dephase. The

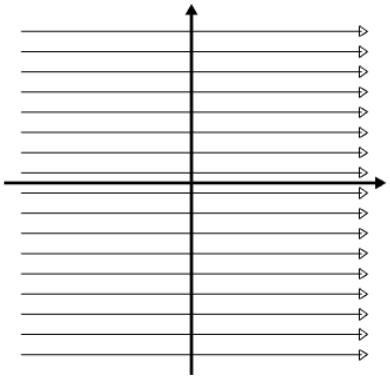

Figure 1.13: K-space contains a line for each phase encoding step (vertical), and each line contains a point per frequency encoding step (horizontal).

next pulse is applied after half the echo time. This inverses the transverse magnetisation so that it becomes flipped in the transverse plane. This has the effect of rephasing the spins; as they continue they will eventually realign at the echo time TE $= 2t$. This is when the center of the spin echo occurs and the signal is read. The sequence can be repeated, and the time used for each is called the repetition time TR. The 180° pulse can be applied several times for each repetition to give Multi-Echo SE. The echo becomes progressively smaller due to T2 relaxation, and this can be used for T2 mapping. It can also be used for phase-encoding: the 180° pulse can be repeated with a different phase encoding for each. This allows recording of multiple echoes for each TR, which fills multiple lines of k-space per 90° pulse, and drastically reduces imaging time. SE can be used to obtain T2-weighted rather than T2*-weighted images. The T2* relaxation which occurs due to static field inhomogeneities is reversed by the 180° refocusing pulse. SE is therefore less affected by susceptibility artefacts than GE sequences. T2 weighting in SE does however require long TR and therefore long acquisition times.

A gradient echo (GE) sequence consists of two gradients which are of equal strength and opposite polarity. The first is a dephasing gradient, which accelerates the dephasing of the spins, Figure 1.15. This reduces the FID by a known amount. The second gradient is a rephasing gradient which reverses the phase. It will only refocus spins that were affected by the dephasing gradient, returning the FID as a gradient echo. Effectively, spins are refocused fast by reversing their directions rather than by inverting them as in SE. T2 and T2* processes are unaffected, and the FID continues

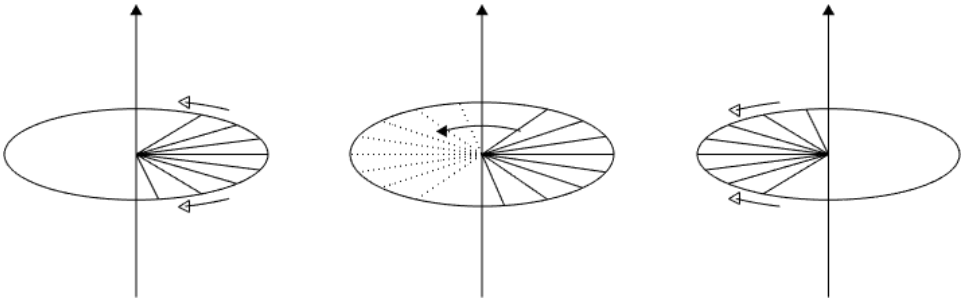

Figure 1.14: The spin echo sequence rotates the net magnetisation vector by 90°, and the spins start to dephase (left). The second pulse then flips the transverse magnetisation (middle). As the spins continue to move in the same direction as before (right), they will eventually realign. Slower precessing spins have not moved far, while the faster spins now have a longer way to travel. This causes them to rephase, which is when the spin echo occurs.

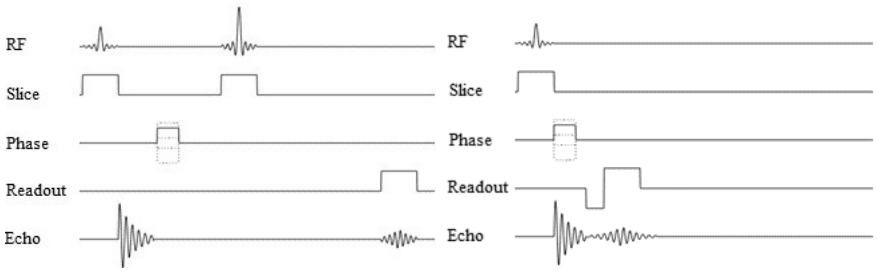

Figure 1.15: A spin-echo sequence (left) and a gradient-echo sequence (right).

to decay with time constant T2*. The peak echo occurs when the area under the rephrase gradient is equal to that under the diphase gradient. The rephasing gradient can be left on for twice the time of the dephasing gradient, to frequency-encode the signal. In GE the flip angles are less than 90°, usually $10-80°$, so the longditudinal magnetization is recovered faster. This allows for shorter TR and TE and therefore shorter acquisition times. GE forms the echo without the need for the 180° pulse, the TE is therefore shorter than for SE. The lack of refocusing pulse also means there is a T2* contribution, making GE more prone to magnetic susceptibility artefacts than SE. This can give a T2* weighted image. The magnetic field can be distorted by species such as iron, providing for instance a method to image iron deposition, as well as forming the basis for BOLD fMRI. If the TR is reduced, the transverse magnetisation will not be fully decayed before the next repetition. This will be affected by the flip angle too. Depending on how this is dealt with the sequence can be either a GE with spoiled residual

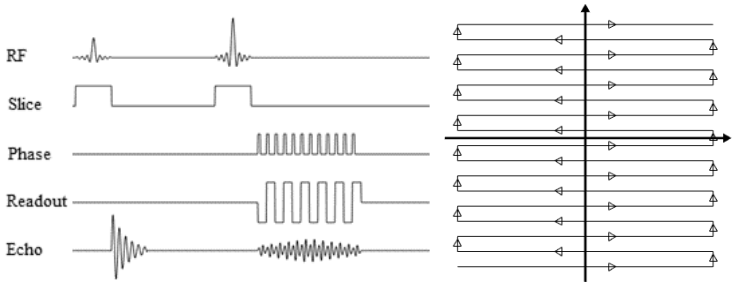

Figure 1.16: The EPI sequence (left). (Right) K-space is traversed along the frequency (horizontal) and phase (vertical) encoding axes.

transverse magnetisation or a steady state GE where the residual transverse magnetisation is conserved and participates in the signal.

Standard imaging techniques require several repeats to fill the phase adjusted lines of k-space. This causes long scan times, especially for larger matrix sizes, which is impractical for functional imaging. Echo-planar imaging, or EPI, is a very fast acquisition technique able to obtain 15 to 30 images in a second. This is useful to image fast processes in the body such as in fMRI. As an example, EPI is capable for example of imaging the heart without the motion artefacts which would blur the image in other forms of MRI.[107,108] It can also be used in diffusion and perfusion imaging, for example to evaluate stroke.[109] The fast imaging time is accomplished by acquiring all the lines in k-space in a single repetition time TR. EPI uses a single RF excitation to record multiple lines of data, either traversing k-space in one excitation, called single-shot EPI, or in a small number of excitations, called multi-shot EPI. Figure 1.16 shows the sequence diagram used in SE-EPI. After the SE Rf-pulses, strong frequency encoding gradients are applied repeatedly with an alternating polarity, with a low-magnitude phase encoding gradient between each. This has the effect of traversing k-space as shown in Figure 1.16. The initial gradients are used to move the signal from the middle of the k-space to the left bottom corner. Each oscillation of the readout gradient corresponds to a line in k-space. Positive frequency lobes sweep k-space left-to-right, negative lobes right-to-left, while each step in phase encoding gives a step increase along the y-axis.

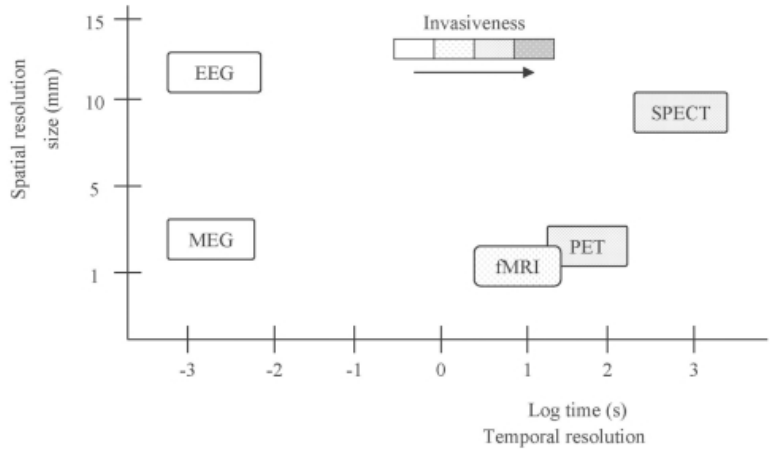

Figure 1.17: fMRI can provide good spatial resolution while maintaining good temporal resolution.

1.3 Functional MRI

Functional magnetic resonance imaging (fMRI) is a prevalent method for imaging brain activity. Compared to other imaging modalities it provides high spatial resolution of around 1 mm and good temporal resolution.[110] Although gadolinium or iron based contrast agents are sometimes used, fMRI techniques such as BOLD and ASL can also be non-invasive, and do not require any injections or radiation. It has a higher temporal resolution than PET, which requires radiation and is less readily available in clinical settings. Electroencephalography (EEG) and magnetoencephalography (MEG) are a more direct measure of neuronal activity than fMRI and have very high temporal resolution. MEG and EEG however have lower sensitivity than fMRI and localisation is more difficult.[111] Determining the sources of the EEG or MEG signal requires assumptions which can depend on mathematical, biophysical or neurophysiological models.[112] Since its invention in the 1990s, fMRI and has therefore been widely used in cognitive neuroscience.[113–116]

1.3.1 BOLD fMRI

Blood Oxygen Level-Dependent (BOLD) imaging is the predominant fMRI technique, as it is relatively easy to implement, and has good functional contrast.[117] It detects a composite signal caused by regional changes in blood saturation, blood flow and blood volume. The measurement relies on the change in magnetic susceptibility observed with the oxygenation state

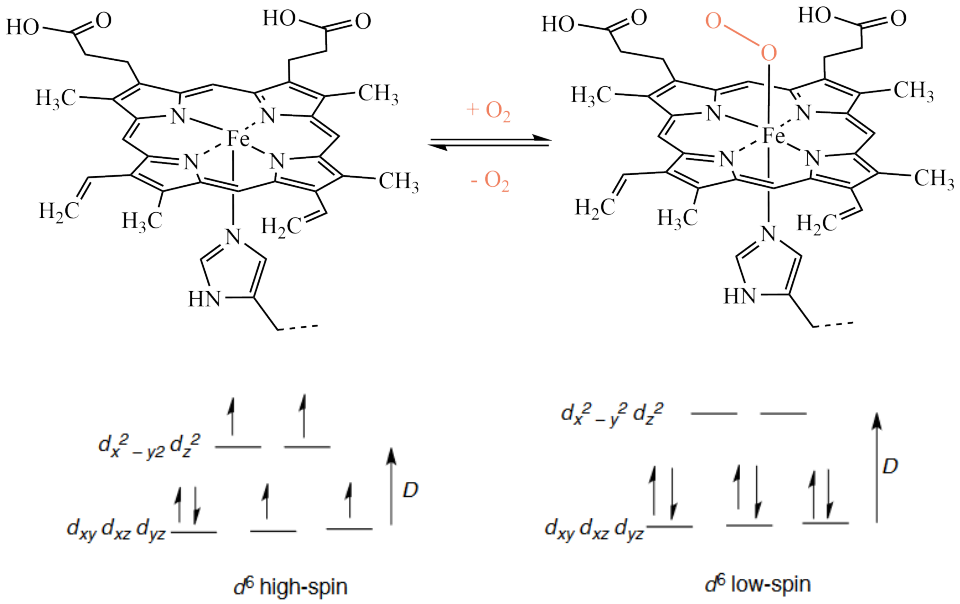

Figure 1.18: The structure of the heme B group. Different hemes exist, with the major ones being A, B, C and O. These are based on the same central heterocyclic ring structure, called a porphyrin, but have different functional groups on the pyrrole sub-units. Oxygen binds to heme via the sixth position of the central iron ion. Deoxyhaemoglobin (left) is paramagnetic (0.273 ppm relative to water), while oxyhaemoglobin (right) is diamagnetic (-0.008 ppm relative to water). The Fe^{2+} ion in deoxyhaemoglobin has a high-spin $3d^6$ electron configuration, leaving four unpaired electrons. On binding of the oxygen, the ion changes to a low-spin d^6 state.

of haemoglobin, which is diamagnetic in the oxygenated state and paramagnetic in the deoxygenated state. Haemoglobin contains heme groups, shown in Figure 1.18, which is capable of binding oxygen. The centrally held iron ion coordinates with the four nitrogen atoms in the plane of the heme group, as well as being covalently bound to the protein via nitrogen positioned below the ring. The sixth position can be reversibly bound to O_2; one oxygen atom binds to the iron and the other extends outward in an "end-on-bent" geometry. When there is no oxygen bound to the iron centre, a very weakly bonded water molecule can take its place. In deoxyhaemoglobin, the iron centre is ferrous, with an Fe^{2+} oxidation state. When oxygen binds to the haemoglobin, it temporarily oxidises Fe^{2+} to Fe^{3+}, while turning into the form O_2^-.

Deoxyhaemoglobin is paramagnetic. Paramagnetism is caused by unpaired electrons, and in HBr the heme iron is in a high spin state, with four unpaired electrons (S=2). Oxyhaemoglobin exists in the low spin state, with

no unpaired electrons (S=0), it is therefore weakly diamagnetic. When the oxygen dissociates from haemoglobin, the iron in the heme group transitions from a low spin state to a high spin state.[118] As shown in Figure 1.18, this takes the central ion from a configuration with no unpaired electrons, which is diamagnetic, to a configuration with four unpaired electrons, which is paramagnetic. Deoxyhaemoglobin has a magnetic susceptibility of $\Delta_{\chi_{deoxy}} = (0.273 \pm 0.006)$ ppm relative to water,[118] while oxyhaemoglobin has $\Delta_{\chi_{oxy}} = (-0.008 \pm 0.003)$ ppm. Fully oxygenated blood is therefore slightly more diamagnetic than water.

Paramagnetic materials are weakly attracted by an external magnetic field, while diamagnetic materials are repelled. The presence of both these species distort the local magnetic field, but due to their relative magnetic susceptibility difference, the paramagnetic deoxyhaemoglobin has a much greater effect on the local field than oxygenated haemoglobin. This distortion has the effect of changing the frequency and phase of nearby spins. Changes in the regional concentrations of oxy- and deoxyhaemoglobin therefore creates time-dependent changes in T_2* relaxation times.

Attempts have been made at creating models of the BOLD response, however these complex interactions are not fully understood. A BOLD response is shown in Figure 1.19. The response typically begins within around 500 ms and peaks after 3-5 s after stimulus onset.[119] At the peak it reaches a few percent change relative to baseline. An initial increase in deoxyhaemoglobin is often seen at the onset of stimulus, and the origin of this behaviour has been controversial for years.[120] This was detected as a an 'initial dip' in the BOLD signal[45] after first being observed by intrinsic optical imaging.[121] After the sharp onset, the signal slowly returns to baseline over several seconds. For an ongoing stimulus, the peak is instead followed by a drop to a plateau, which occurs 6-12 seconds after stimulus onset.[122] There is also a post-stimulus undershoot which is often observed[44,123] as a significant lowering of the baseline after a stimulus, and the origin of this is still under debate.[124] This undershoot is transient, but highlights the importance of stimulus design, as leaving long enough gaps between stimulus repeats will allow the system to return to baseline.

The early balloon model[125] from 1998 considered volume and deoxyhaemoglobin content, providing the signal as a non-linear function of these. Here, an increase in flow is thought to inflate the venous 'balloon' and dilute

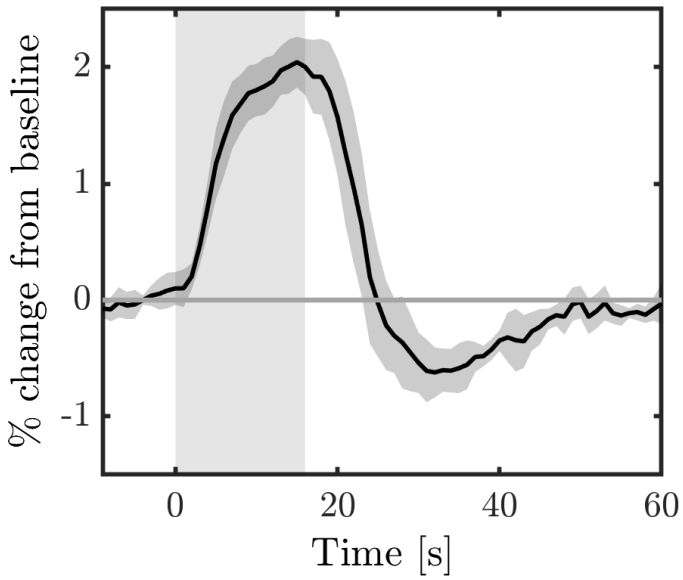

Figure 1.19: A typical BOLD response. The data was averaged from ten volunteers during a visual stimulus (16 seconds flickering checkerboard with 54 second interval, 15 repeats).

the deoxygenated blood and pushing it out at an increased rate, increasing the BOLD signal. This allows for an initial dip in signal, because prior to inflation the increased blood flow is not yet large enough to counteract the increase in $CMRO_2$. It also provides a post-stimulus undershoot as the balloon relaxes after the flow reaches a peak, causing a reduction in the dispelling of deoxygenated blood. Experiments have since suggested the physiological response is more complex, and that blood flow and oxygen metabolism could be parallel and perhaps driven by different mechanisms of neuronal activity.[124] A negative BOLD signal can often sometimes be measured, this occurs most frequently in cortical regions near areas of positive signal, but its origins are still unclear.[126,127]

It was initially thought that the BOLD signal was linearly related to activity, with all increase in neuronal activity resulting in a proportional increase in the regional blood flow. Attempts were therefore made to represent the signal by a haemodynamic response function (HRF) convolved with a function describing neuronal activity.[128] Later work showed the response has non-linear scaling with respect to the frequency, amplitude and duration of the stimulus. The typical response peaking after 3-5 s is seen for a short (< 1 s) to medium length stimulus,[119] with more complex non-linear dynamics for a prolonged stimulus (> 8 s).[129] Responses to longer

stimuli will have the same time to peak as for shorter stimuli, and show a plateau effect.[126] Blood flow response to stimulus also varies by age and pathology.[111]

1.3.2 Other fMRI methods

Unlike the composite signal of BOLD, other fMRI techniques are able to measure individual parts of the haemodynamic response. Cerebral blood flow can be measured with arterial spin labeling (ASL) fMRI. This is a non-invasive technique which relies on the arterial water. Rather than measuring percentage change like BOLD, it gives an absolute value which is more physiological, and it has a higher spatial and temporal resolution. There are however challenges to ASL, the main one being a poor signal-to-noise ratio.[130] Measurements are confounded by partial volume effects, where the spatial limitations caused by fast imaging causes grey matter, white matter and CSF to contribute to the signal in a voxel, and the difference in flow measured is affected by the difference in voxel heterogeneity. Another issue is the transit times required for the labeled blood to reach the region of interest, the imaged region could contain voxels with labeled blood headed for another voxel or voxels which the labeled blood has not reached yet. This requires a compromise between the delay between labeling and measurement, and the loss of signal due to relaxation.[131]

Another technique is vascular space occupancy (VASO) fMRI, which measures changes in cerebral blood volume. This is achieved through the non-invasive measurements of changes in extravascular water signal. It measures changes in CBV rather than in blood oxygenation which is done with BOLD. Blood and tissue have different T1 properties, and VASO uses an inversion recovery pulse to null out the signal from blood. It can therefore measure signal from the tissue, and the intensity will be proportional to (1-CBV).[132] VASO provides improved localisation compared with BOLD, giving signal peaks in the middle cortical layers where the neuronal activity response to stimulus is greatest.[132] However, VASO fMRI has lower sensitivity than BOLD, with about 1/3 the contrast-to-noise ratio (CNR). There is also a need to account for CSF. The original model assumes a voxel contains tissue and blood, so the increase in blood volume would indicate an equal decrease in tissue volume. CSF has a long T1 time which means it is likely to have negative magnetisation at the nulling time, and could

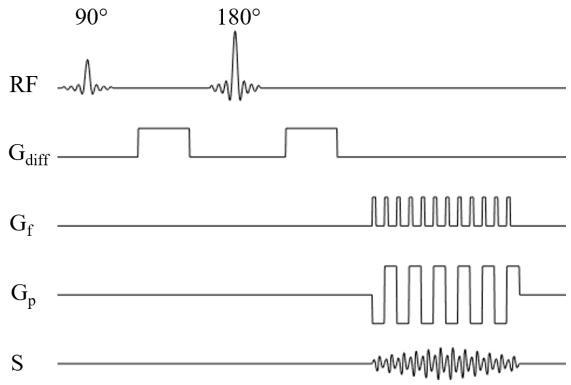

Figure 1.20: A diffusion weighted MRI sequence. The diffusion gradients (G_{diff}) are applied on either side of the 180° refocusing pulse. Readout is typically done using EPI, to reduce the effect of motion.

therefore complicate interpretation.[132]

1.3.3 Diffusion Weighted fMRI

Diffusion Weighted functional MRI (DW-fMRI) has been suggested as an alternative, more direct indicator of neuronal activity than BOLD.[30] It relies on measuring brain cellular volume changes by detecting changes in water diffusion through activated areas of the brain. DW-fMRI is based on expanding the method of Diffusion Weighted Imaging (DWI) which is used to map diffusion in tissue. In pure water, the molecules follow brownian motion, diffusing freely. In tissue the water molecules are restricted, as they interact with cell membranes and macromolecules which changes their motion. Cell membranes create barriers which limit the available extracellular and intracellular space. The more cells are present, the more restricted the motions become. With few cells, the extra-cellular space is large and water molecules can diffuse more freely, and move through damaged cell membranes. In highly cellular areas with many intact cell membranes, like tumor tissue, the extra-cellular space is reduced and motions restricted. Water in extra- and intra-cellular space and intravascular space all contribute to the MR signal observed.[133]

The DWI measurement is based on a T_2-weighted spin-echo sequence, adding symmetric bipolar gradients, applied either side of the 180° refocusing pulse, as shown in Figure 3.3. The diffusion gradients are described by the b-value, which is used to denote the degree of diffusion weighting. The

b-value is a function of the gyromagnetic ratio, the gradients' magnitude G and width δ and the spacing between them Δ according to Equation 1.9. Static molecules will receive phase information from the first gradient and be rephased by the second, leaving the signal intensity preserved. Moving molecules are not completely rephased by the second gradient, so signal intensity is lost. DWI measures the degree of signal attenuation, which is proportional to the degree of water motion.[133] This is described by Equation 1.10, where S is the signal intensity, S_0 is the signal at $b = 0$, b is the b-value and D the apparent diffusion coefficient. This technique can be used to distinguish tissues based on their cellularity and is used for example for imaging tumors.

$$b = \gamma^2 G^2 \delta^2 (\Delta - \frac{\delta}{3}) \tag{1.9}$$

$$S = S_0 \cdot exp(-b \cdot D) \tag{1.10}$$

DW-fMRI measures this effect over time, with observable decreases in diffusion of water during neuronal activation.[30,33] The Le Bihan group showed the implementation of DW-fMRI, acquiring its responses to visual stimuli and comparing these with BOLD measurements (Figure 3.1).[30] By increasing the b-value, they were able to detect a more rapidly onsetting response, which they interpreted as a reduction in the haemodynamic component of the signal. If this method measures changes in cell volume, DW-fMRI has the potential to provide better spatial specificity, and a response with better temporal agreement with stimulus onset than BOLD.[29] The cellular response is a more immediate effect of the activity than the haemodynamic response, and their location is closer to the site of the activation. In line with this, the DW-fMRI response to activation occurs several seconds before the BOLD response.[30] This could suggest that the diffusion response is linked either directly to neuronal activity or to it through a fast coupling mechanism.[33] If the DW-fMRI signal is largely driven by cellular changes rather than heamodynamics, it is less likely to be affected by the many physiological confounds of concern in BOLD.

Diffusion Weighted fMRI has not become as widely used as BOLD, likely because the relationship between the DW-fMRI signal and cellular swelling is still contested.[17,31,34] Early DW-fMRI studies attributed the signal changes directly to neuronal activity,[30,33] however this has been challenged, with one prominent concern being the possibility of haemodynamic contributions

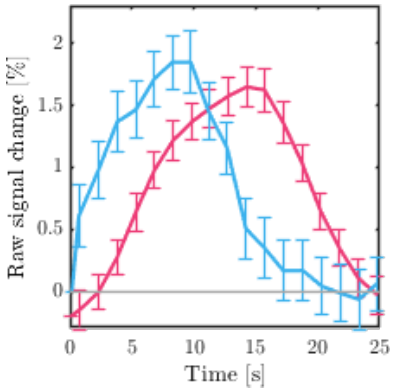

Figure 1.21: Le Bihan measured the diffusion (red) and BOLD (blue) fMRI responses,[29] showing the relatively faster response function of DW-fRMI at a b-value of $1800/mm^2$.

to the signal,[36] or even a largely vascular origin.[35] Jin *et al* found a diffusion signal change on visual stimulus in the cat, with a more rapid onset than BOLD, however when using a contrast agent to remove intravascular contributions the signal was mostly quenched, leading them to conclude the signal was vascular in origin.[35] DWfMRI signal has also been detected in response to hypercapnia, which elicits a haemodynamic response similar to that of a visual stimulus, but is not caused by neuronal activation.[36] There is a possibility of neuronal firing changes or reductions during hypercapnia, however it has not been shown to increase firing rates as would be needed to explain their results.

DWfMRI has been investigated in model systems without haemodynamic artefacts. A study using diffusion MR microscopy showed diffusion accompanying stimulation of snail ganglia without blood.[37] Their results suggested the signal was driven by cellular swelling. Another study looked at the correlation between activity and the DW-fMRI signal *in vitro* by using concurrent Ca^{2+} fluorescence imaging, for detection of spiking neuronal activity.[34] They used rat brain cortical cultures, which shows spontaneous neuronal activity but is without haemodynamic artefacts. They found a simultaneous increase in DW-fMRI signal with the prolonged depolarisation of neurons using pharmacological manipulators, and the swelling of cells was shown to play an important role in this case. They could however not find evidence of correlation between DW-fMRI and normal spontaneous neuronal activity, concluding that DW-fMRI is able to detect hyperexcitability, but that it is not sensitive enough to detect normal neuronal activity. It has

been argued that the lack of observable diffusion changes could be due to the lower density of functional synapses in slices compared to brain tissue.[37] There has also been evidence of DW-fMRI signal originating in activity in live hippocampal slices[17] and in rat spinal cord,[134] both of which are without vasculature and free of haemodynamic effect. One study[33] by the Le Bihan group used an inhibitor of neurovascular coupling, nitroprusside, in an attempt to remove potential haemodynamic contributions to the measured diffusion. They discovered that although the haemodynamic response to stimulation disappeared, they were able to maintain the field potentials in the area, and detect a diffusion response on stimulation. They concluded that DW-fMRI is not vascular in origin.

In early work the rapid onset was attributed to heamodynamic effects; one study detected a diffusion signal preceding the BOLD response by a second, and suggested the signal originated in arteries.[135] The increased delay with b-value was thought to reflect a weighting of the signal towards arterioles and capillaries.[136] A 2009 paper from Kohno *et al* recorded DWfMRI and BOLD simultaneously with non-invasive Near Infrared Spectroscopy in human visual cortex.[137] They found that the diffusion MRI signal had a shorter rise time than both the BOLD signal and total haemoglobin content optical signal, which is assumed to be the fastest observable vascular signal. They therefore concluded the diffusion decrease was driven by events occurring before the vascular responses.

Although conflicting results exist, it is clear that optical imaging of cell structural changes aligned with DWfMRI *in vivo* could provide confidence that that the signal source is related to cell swelling.

1.4 Optical Imaging

Optical imaging encompasses a wide range of techniques. It relies on measuring responses to light, which depending on the method can range from the UV-region through to visible light and into the infrared region. Measurements are made on different scales, including macroscopic 2D or 3D imaging of tissue samples or *in vivo* endoscopic imaging and imaging down to microscopic levels. Some optical imaging techniques have found clinical applications, for example intra-operative imaging[138] and optical brain imaging using near-infrared (NIR) light, which is able to penetrate through the scalp to the brain.[139] In research, optical studies in animal models

have for example provided insight into Alzheimer's disease,[140] stroke[141] and epilepsy,[142] as well as neurovascular coupling.[143–145]

Various optical imaging techniques have been used for the study of brain function. Unlike most functional imaging methods, optical imaging can be be made sensitive to a range of different contrast mechanisms,[146] and is therefore often used concurrently with other techniques to supply complimentary data for interpretation or reduce confounds. Another advantage of optical imaging compared to other methods used to study brain function, is the relatively simple, low-cost setup. Typically the brain tissue is illuminated by a light source, this can be transmitted through a coloured filter to give illumination at a wavelength of interest. The diffusely reflected light from the tissue is imaged with a camera.

Light scattering limits the depth sensitivity of optical methods. As scattering increases, less light is able to reach certain depths, which in turn limits image resolution. Light that travels far through a medium will also undergo more scattering which causes blurring and limits resolution, so sensitivity will depend its baseline absorbing and scattering properties.[147] In clinical optical brain imaging this is normally overcome by using near-infrared (NIR) light, which more efficiently penetrates through the skin and skull to reach brain. In imaging of small animals however, the light is better able to reach into the brain with less loss of resolution, and other wavelengths can be used. Resolution can be further improved by thinning the skull, exposing the cortex to give direct high-resolution imaging of the brain surface.

1.4.1 Optical Imaging Spectroscopy

Optical Imaging Spectroscopy (OIS) is an optical method which is used in studies of brain activity. It is capable of detecting changes in tissue absorption *in vivo* by analysing light remitted from tissue. This is used to infer the concentration of chromophores such as cytochromes or metabolites, but is most often used to measure oxy- and deoxyhaemoglobin. haemoglobin saturation is linked to the processes underlying activity, and are therefore indicative of microscopic functional changes.[146] OIS was originally introduced in a 1977 study, which showed that infrared light could be used to noninvasively monitor changes in cerebral blood oxygenation in an animal model.[139] The method can be used to monitor haemodynamic changes for clinical purposes, but is also used in animal models for imaging of exposed

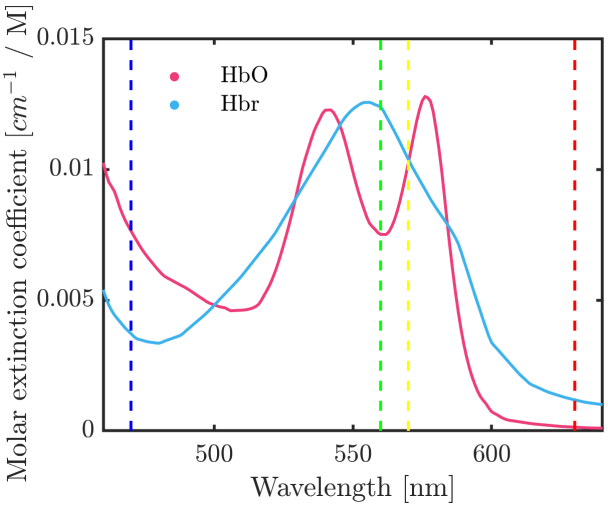

Figure 1.22: Spectra of the molar extinction coefficients for oxy- (red) and deoxy-haemoglobin (blue). The vertical lines show the wavelengths 470, 560, 570 and 630 nm, which were used in OIS.

brain. Imaging the exposed cortex directly can give very high resolution and minimal interference with normal brain activity.[146]

Oxy- and deoxyhaemoglobin (HbO_2 and HbR) are the highest absorbing chromophores in the brain, both at visible and NIR wavelengths. Their molar extinction coefficients are shown in Figure 1.22. When OIS is used to monitor haemodynamics as an indicator of brain activity, the relative concentrations of the two species must be estimated by monitoring absorption at different wavelengths. Early work used a single wavelength to measure total haemoglobin changes. This is sometimes referred to as intrinsic imaging, and the wavelength chosen was an isobestic point, where the HbO_2 and HbR absorption is equal. Illumination at several wavelengths, sometimes called hyperspectral imaging, can be used to infer a relative change in these species. HbO_2 and Hbr have unique absorption spectra, and the baseline values can be assumed.[148] Measurements are typically made at wavelengths where one species is absorbed preferentially over the other, as well as the isobestic point, in order to calculate changes in HbO_2, HbR and HbT. Applications of OIS usually involve illumination at multiple wavelengths. This allows discrimination absorption due to the various absorptive species in the tissue, like oxy- and deoxyhaemoglobin.

OIS uses a relatively simple setup, as shown in Figure 1.23. A white light source projected through a filter illuminates the brain tissue at a chosen

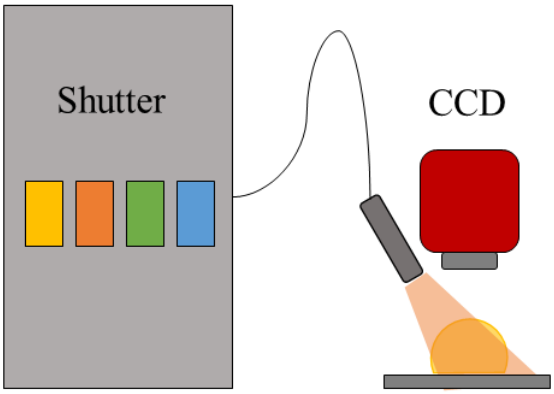

Figure 1.23: Optical Imaging Spectroscopy setup. Illumination at different wavelengths can be achieved with a switching galvanometer. This contains a broad light source, such as a Xe lamp, and an array of filters which can be switched between rapidly. The light remitted from the tissue is captured by the CCD camera

wavelength. A CCD camera captures the remitted light for processing. By adding components such as a mechanical filter wheel, the wavelength of the projected light can be changed rapidly, and remitted light at several wavelengths can be measured at a rate of several frames per second.

OIS measures the attenuation of light, A, which is dependent on the path length L the light travels through a medium, and the concentration c_i and the extinction coefficient E_i of the absorbent species present, Equation 2.2. The path length distribution will have to be estimated, usually through a simulation. Baseline concentrations can be assumed, but the signal change is usually calculated instead. If it is assumed that the effect of changes in the concentration of the other chromophores in the tissue is negligible in the visible spectrum, the attenuation becomes dependent on the concentrations of only oxy- and deoxygenated haemoglobin, HbO_2 and Hbr,[149] giving Equation 1.12. This equation has two unknowns, so measurements must be made with at least two wavelengths for spectroscopic deconvolution.

$$A(\lambda) = L \sum_i E_i(\lambda) c_i \tag{1.11}$$

$$A(\lambda) = L(\lambda)(e_{HbO_2}(\lambda)\Delta HbO_2 + e_{Hbr}(\lambda)\Delta Hbr) \tag{1.12}$$

OIS can therefore measure the haemodynamic response that underlies BOLD and confounds DWfMRI. By concurrently measuring Hbr and HbO_2 concentrations, the Mayhew group made predictions for blood flow changes,

and used it to estimate the oxygen consumption ($CMRO_2$).[150] This showed that $CMRO_2$ increases early during stimulation, with a peak around 2 seconds after onset, even at low stimulation intensities. Another concurrent study investigated the negative BOLD response.[126] They used OIS haemodynamic data to generate predictions of the BOLD response through a biophysical model, showing the negative response originating in deep cortical layers. BOLD fMRI can also provide an estimate of the total blood volume, and be used to parameterise the OIS calculations. Interpretation of OIS measurements often requires estimates of blood saturation, blood volume fraction and the wavelength dependent distributions of pathlengths of the remitted photons. The first two can be estimated with MRI and MRI V_f maps respectively.[151]

A disadvantage of OIS is that in the visible spectrum the technique is invasive. There have been human studies from surgery,[148] however in humans however most studies are done in animal models. The requirement to use anaesthesia could be a potential downside, as there is evidence to suggest the haemodynamics may change under anaesthesia, with the responses to stimulation decreasing.[148] OIS can however be used non-invasively in humans if done in the infrared region, as this wavelength is able to reach into the cortex, through the scalp. OIS has the advantage of a spatial resolution of microns and a temporal resolution of milliseconds, which is better than fMRI can currently achieve.[148]

Path lengths must be estimated with Monte Carlo simulations (MCS). These simulations (detailed in Section 4) can include tissue parameters such as absorption and scattering, and may consist of one or more layers. The brain is heterogeneous, with vessel density[48] and function[95,152] varying by location. A layered simulation model can account for this by assigning different optical properties by depth.

For OIS measurements of brain activity it is often assumed that scattering does not change significantly during activation, there is however likely to be a change in scattering caused by microstructural changes during activity. This was observed already in 1968, when Cohen *et al* studied nerve fibers, detecting changes in scattering and birefringence during stimulus.[24] If cell swelling occurs during measurements this will affect the path length, and should be accounted for in analysis. Scattering changes can be monitored simultaneously with absorption changes using spatial frequency do-

main imaging.

1.4.2 Spatial frequency domain imaging

Spatial Frequency Domain Imaging (SFDI) is an *in vivo* optical imaging technique which, like OIS, can measure wavelength dependent optical properties. It specifically measures the frequency dependent reflectance of spatially modulated light.[39] Light remitted from a tissue will be affected by absorption and scattering, and the effect will vary with the spatial frequency of the illumination. SFDI takes advantage of this to separate the effects of these two processes, providing measurements of absorption and scattering simultaneously. Like in OIS, the wavelength dependence of light absorption can be used to determine the concentration of chromophores and indicate haemodynamic changes. In addition to this, the scattering parameter detected with SFDI can be used to monitor tissue structural changes, which could potentially help confirm the signal source of DWfMRI.

A typical setup is shown in Figure 1.24. A spatial light modulator is used to generate a sinusoidal pattern. The pattern illuminates the object, and the remitted light is measured with a CCD camera. Remission of light is a function of time and space, and so gives two groups of techniques: time-resolved and spatially resolved measurements, Figure 1.25. Time-resolved techniques are again divided into time-domain and frequency-domain techniques through Fourier transform equivalency. Similarly, spatially resolved techniques can be divided into the real spatial domain and the Fourier transform equivalent; spatial frequency domain measurements. SFDI therefore concerns properties which depend on spatial frequency, a measure of the level of detail per degree of visual angle.

Time-domain techniques measure the temporal point-spread function (t-PSF), which is the spreading of a propagated pulse in time. Frequency domain techniques measure the temporal modulation transfer function (t-MTF), which is the attenuation and phase delay of a periodically varying photon density wave. The spatial real domain techniques use the spatial point spread function (s-PSF) which tracks the spatial dependence of reflected or transmitted light generated from a point-like illumination. In SFD, the spatial modulation transfer function (s-MTF) encodes both the depth and optical property information about a turbid media. This allows for quantitation and tomographic imaging of the optical properties changing

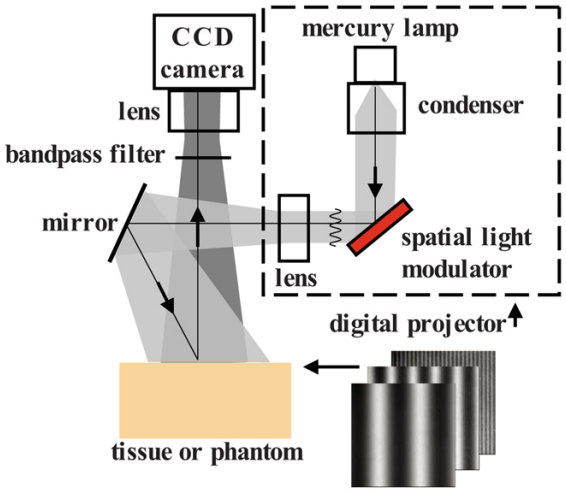

Figure 1.24: Spatial frequency domain imaging setup.

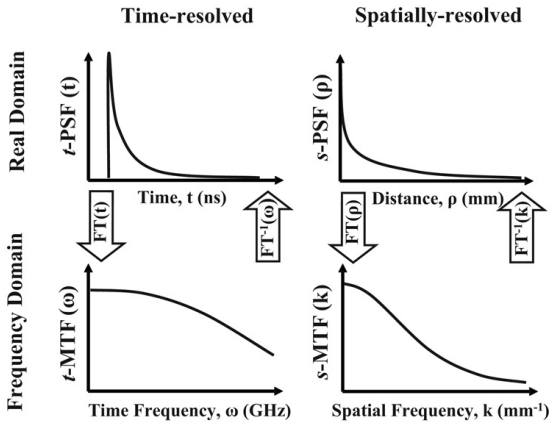

Figure 1.25: Spatial frequency domain imaging is related by Fourier Transform to spatially resolved imaging methods, similarly to how frequency domain methods are related to time domain methods. Figure adapted from Cuccia *et al*, 2009

throughout the media.[38]

Cuccia *et al* first presented 'Modulated Imaging' as a method for optical property mapping of turbid media in 2005.[153] They implemented considerations of steady-state diffusion to show that modulated light of different frequencies could be used to extract optical properties. Using phantoms with a range of properties to validate their SFDI measurements, the group showed they could extract maps of absorption and scattering, achieving a 6 % and 3 % accuracy respectively.[38] Although shown previously using similar methods, this approach also allowed sampling at different depths by varying the spatial frequency, providing a new approach to tomography of turbid media. By varying the spatial frequency of the illumination pattern, the depth of detection can be controlled, this differs from planar illumination (such as in OIS) which relates to a fixed mean depth.[153] Mahzaar *et al* showed that increased spatial frequency enhanced the fluorescence of structures near the surface, while suppressing signal from deeper structures.[154] This is important for studies of brain tissue, as the properties monitored change at different rates throughout the brain.

The early work by Cuccia separated the AC and DC components of remitted light using a demodulation technique which required images acquired at three phase shifts per processed image.[153] Vervandier and Gioux[155] suggested the use of an alternative demodulation, which requires only one image at the given spatial frequency, reducing acquisition time. Each line of the image is Fourier transformed, and the AC and DC components of the line are separated in frequency space by a cutoff frequency. The AC and DC images are then determined by applying an inverse Fourier transform to each line. In Vervandier's work the cutoff frequency is determined automatically for each line, by smoothing the Fourier transformed line and locating the highest AC frequency. The spectrum is then divided at the closest local minimum. The Tromberg group, imaging at a single spatial frequency set a cutoff frequency for all lines to get best quality images for the given spatial frequency.[156] For imaging with only a single spatial frequency, the Vervandier method enables the use of static spatial light modulators; since there is no need to apply a phase shift these can replace dynamic but potentially expensive instruments like digital micromirror devices.[156]

The Tromberg group showed how SFDI could be performed in the visible range using a microprojector,[157] which is the approach used in this thesis.

They demonstrated the setup on a mouse brain, achieving an accuracy of less than 11 % deviation from known phantom μ_a values and 3% from known μ_s' as measured with a spectrophotometer. This demonstrates that SFDI can be a relatively cheap method, and still be capable of achieving good accuracy. Optical property mapping has also been done via endoscope;[158] Angelo *et al* showed this can be used for real-time applications with a maximum error of 0.004 mm^{-1} for absorption and 0.05 mm^{-1} for scattering.

Previous imaging studies[88,159] have indicated that Alzheimer's disease leads to a lessened ability for vasodilation during oxygen deficiency. This could lead the neurons to experience hypoxic stress causeing the production of Aβ oligomers, which themselves have been suspected of damaging vascular function.[39] A study by Lin *et al* used SFDI to measure scattering and absorption values in brain tissue of mice, comparing results from Alzheimer's disease models and controls.[39] They used 17 wavelengths, and the skull was not thinned, in an attempt to avoid potential artefacts. The group was able to find quantifiable differences between the two groups, demonstrating this methods sensitivity to structural changes. The work did not account for different gross brain anatomy between models however, which could account for some differences. Building on Vervandiers demodulation method, the Tromberg group suggested combining this more rapid SFDI with Laser Speckle Imaging (LSI).[156] LSI is a technique used to measure blood flow, based on the random interference by laser light illuminating tissue, known as a speckle pattern. Changes in flow change the intensity in the pattern due to interactions between the incident light and the moving red blood cells. The accuracy of LSI is limited by the non-uniform distribution of μ_a and μ_s', but since SFDI is able to distinguish the effect of the two, the combined approach could correct for some of this error. SFDI has been also used to detect functional changes in absorption and scattering in the rat cortex during spontaneous CSD events.[160] The study found scattering changes which preceeded the haemodynamic response, borth in space and time. The reduction in μ_S' was attributed to neuronal depolarisation.

1.5 Thesis overview

This thesis develops a concurrent *in vivo* optical and fMR imaging technique to detect haemodynamic and microstructural changes in activated brain tissue and explore their correlation with the Diffusion Weighted fMRI signal.

The rat barrel cortex is used as model for neuronal activation, and the stimuli are presented using well-known activation pathways. The optical data is acquired through a triggered acquisition setup within the MR bore, in order to monitor and distinguish both the haemodynamic and the cell volume responses during acquisition of DWfMRI or BOLD data.

Objectives

1 **Collection of BOLD and DWfMRI data from human volunteers**
Human functional data will be collected with the initial aim of reproducing results in the literature. This will allow for comparing the measured activation maps and time courses of the response to activation for the two methods. By collecting and comparing data from both human and animal studies, results collected in the animal will be transferable, and be likely to reflect dynamics present in humans. The DWfMRI data is expected to show a more rapid onset, smaller activation region more specific to layer 4, and to have lower correlation with the location of blood vessels compared with BOLD. The parameters in the analysis pipeline will be carefully considered, and the sensitivity to the results on these parameters will be evaluated.

2 **Collection of BOLD and DWfMRI data from an animal model**
The animal model allows for experiments to be performed with increased number of repetitions, as the anaesthetised model can be kept stable for several hours. The model can therefore be used to test a variety of experimental conditions and stimulus designs. The time course of the responses may depend on stimulus duration and intensity, and could help explain the differing observations of the DWfMRI signal in the literature. The interval between stimulus repeats can also be varied, to look for oscillatory effects; perhaps the shape of the response can be influenced by not allowing enough time for the signal to return to baseline. The effect of different b-values on response shape will also be investigated, as the rapid onset is expected to be prevalent only at high b-values.[30,161] The pre-clinical system has readily adjustable scan protocols, and can be set up to measure the depth profile of the response. This is interesting because DWfMRI is reported to be better

localised to layer 4,[162] and less weighted by vessel architecture than BOLD.

3 **Optical measurements of heamodynamic and structural changes**
With OIS and SFDI, changes in oxygenated and deoxygenated blood and in scattering properties can be measured during activity and used to monitor their time courses relative to stimulus onset. The dynamics will be correlated between these signals and the responses observed with DWfMRI and BOLD, to supply additional information about the processes occurring during the fMRI signal change. Optical methods allow for more rapid imaging which will give increased temporal resolution of the dynamics. The optical methods require building a forward model of light transport through tissue via simulation as well as design and calibration of an optical imaging system capable of implementation into the magnet bore.

4 **Concurrent optical and fMRI measurements**
Concurrent measurements allow the time courses to be compared for the same neuronal event. The biological response can vary between repeats and between animals, so direct comparison of concurrent signals avoids possible bias from averaged separate trials. The concurrent and measurements will confirm whether or not the pathway is activated and if the fMRI should show a response to an individual stimulus, acting as a ground truth when comparing DWfMRI and BOLD responses. Previous experiments in slices and cell cultures have shown correlation between cellular changes and diffusion during hyprexcitability, but not during normal spontaneous neuronal activity. The concurrent model will allow for measurements during a well-known reproducible stimulus, and with more repetitions which will increase the signal. The data will be analysed to deconvolve the measured haemodynamic signals from the DWfMRI signal, to determine the extent to which these contributes to the measured response.

The data collected will aid in the interpretation of the DWfMRI functional data, and potentially validate the biophysical origin of the measured response. As well as improving our understanding of existing work, it could support the further development of DWfMRI and the expansions of its applications in research and in a clinical context.

2 Methods

This chapter describes the methods used for acquisition of MRI data, for both preclinical studies of an animal model (7T) and human responses to visual stimuli (3T). It outlines the optical methods used, including instrument setup, acquisition parameters and analysis methods, and the implementation of the optical setup within the magnet bore. The *in vivo* model is described, including model preparation and presentation of stimulus. Image and signal processing methods are presented, which are used for analysis of both optical and fMRI data.

Method development was a key aspect to this work, and the setup, acquisition parameters and analysis methods were iteratively adapted during testing. In this chapter, the final version of the setup is described, with motivations for the choices made, as well as a discussion of limitations imposed by the setup, with suggestions for improvements that could be made in future work.

2.1 *In vivo* model

MRI and Optical Imaging experiments were performed using a rat model of neuronal activation. Electrical stimulation of the rat whisker pad is a well-known paradigm, which produces rapid and laminar specific responses in the whisker barrel cortex.[163] Each whisker is represented by a 'barrel' in the rodent primary somatosensory cortex.[164] The barrels are discrete units located in layer 4, which are arranged almost identically to the layout of the whiskers on the snout (Figure 2.1).[165] When the whiskers are deflected, it initiates an action potential in sensory neurons, which release glutamate at the synapse located in the brain stem. The information is then passed to the thalamus, where thalamocortical neurons are excited, triggering a response in the primary somatosensory barrel cortex.[164] The neuronal activity will occur on the opposite side of the electrode site, and electrodes are therefore placed on the opposite side of the cranial window in the case of optical imaging.

For the *in vivo* work involved in this study it is necessary to anaesthetise the animal, visualise the rat brain, apply a stimulus to evoke a neuronal response, and to closely monitor the animal throughout the experiment. Blood pressure, temperature and breathing is monitored to ensure the welfare of

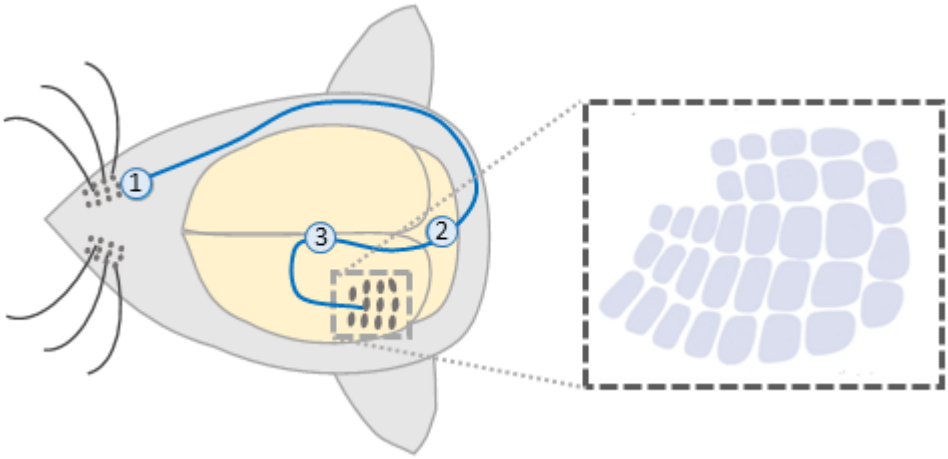

Figure 2.1: The whisker model pathway. When stimulated, the sensory neurons (1) generates an action potential, which initiates release of glutamate in the brain stem (2). The thalamocortical neurons are excited (3), which triggers a response in the primary somatosensory barrel cortex. The barrel's layout is near identical to the whisker positions, with each whisker represented by a barrel.

the animal and to ensure stable experimental conditions. Brain visualisation requires a surgery to expose and thin the skull.

All experimental work was performed with UK Home Office approval under a valid project license. Before commencing work using animal models, the required Home Office course was undertaken, including modules PIL A, B and C for work with rat and mice. Further training on anaesthesia and surgery was done through the in-house biological services facility. Key techniques used are the induction and maintenance of anaesthesia, cannulation of the femoral artery and vein, injection of substances, tracheotomy and thinning of the cranial window using a stereotactic frame. These procedures are required for preparation of the animal and for monitoring of the animal during surgery and during data acquisition. After the experiment an overdose of anaesthesia is administered.

2.1.1 Preparation and monitoring

All animals (Female Hooded Lister rat, $>$ 70 days old) were kept in a day-night cycle for at least 14 days and provided food *ad libitum* before experiments. The animal was weighed prior to starting, and the required doses of administered substances calculated based on its weight (160-250g). The anaesthesia protocol began with isofluorane (2% in 2L/min O_2) sent to the

induction chamber of an anaesthetic machine, where flow meters could be used to set the required flow rates. Once the anaesthesia took effect and the animal was asleep, 25% Urethane (1.25g/kg) was administered through intraperitoneal (IP) injection. The Urethane was made up from 12.5g $>$ 99% crystals dissolved in 50 mL distilled water. The rat was left in the holding cage under observation until toe pinch reflexes are lost. The analgesic Buprevet (Buprenorphine, 0.3 mg/mL, dosage 0.5 mg/kg) was injected subcutaneously (SC). Atropine sulphate (600 μg/mL, dosage $0.4 - 0.8$ mg/kg) was injected SC to reduce mucous secretion.

Cannulation of the femoral artery and vein was performed for the monitoring of blood pressure, as well as for drug infusion and optionally the administration of MRI contrast agents. Cannula were prepared from Portex fine-bore polythene tubing (inner diameter 0.4 mm, 750 mm length) fitted onto a 1 mL syringe filled with saline containing heparin (500 I.U/mL). During surgery, the animal was kept at its body temperature of $(36.5 \pm 1.5)^\circ$ using a heating blanket (TC-1000 Temperature controller, CWE, INC) controlled by a temperature probe. Before incision the area was whetted with saline. The incision was made along the natural angle of the hind leg and the underlying fat layer opened up. The vein, artery and nerve were carefully separated. A suture was tied around the vein close to the leg, and pulled back slightly by a clamp. A cut was made diagonally into the vein, scissors pointing towards the heart. The cannula was inserted through the opening and tied into place with suture thread at both ends of the vein. The process was repeated for the artery, but the artery was clamped closest to the heart prior to the diagonal cut.

In order to prepare the cranial window, the animal was secured in place using a Kopf Instruments small animal stereotaxic frame. The skull was exposed by blunt dissection and thinned to translucency using a micro drill (Cadrim Nail Drill, 38000 rpm) fitted with 2.35 mm shank tungsten carbide ball burrs with 1 mm head, while wetting with saline to cool. An acetal ring (2 cm inner diameter, 0.5 cm height) was positioned over the cranial window, and secured into place with dental cement to create a well. The well was filled with saline, this keeps the thinned skull wet and therefore transparent. Figure 2.2 shows the visibility through the thinned skull under saline.

During the experiment the blood pressure was recorded using a monitor-

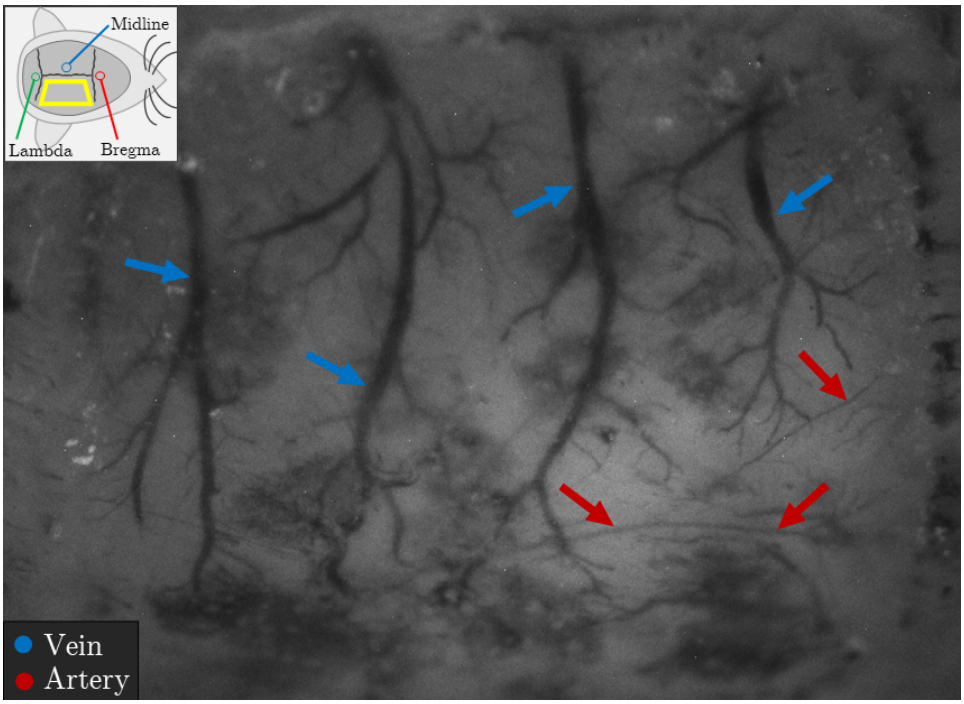

Figure 2.2: The cranial window. The window, shown in yellow in the diagram in the top left corner, approaches the midline at the top of the image, and extends between the lambda line on the left and the bregma line on the right. Four veins are indicated by the blue arrows, these appear dark, branching laterally from the midline. A set of arteries are just visible as thin, brighter lines near the lower right corner, indicated by the red arrows.

ing device attached to the arterial cannula, with the mean arterial pressure (MAP) expected to be in the range $75 - 105$ mmHg.[166] Phenylephrine ($0.13 - 0.26$ mg/hr) was administered through the venous cannula during experiments to maintain blood pressure between the physiological limits. Blood gas analysis was performed using Abaxis VetScan i-STAT1. This provides oxygen content (pO_2) and CO_2 content (pCO_2) of the blood as an indicator of the physiological state of the animal. The temperature was monitored throughout the experiment using the temperature probe. For MRI experiments the temperature was regulated by heated water running along the inside of the holding bed floor, as well as by a heating blanket placed over the animal.

In order to maintain a steady breathing rate and to control the oxygen levels, the animal was kept on a Harvard Apparatus VentElite ventilator. This was done to keep the physiology of the animal consistent across data acquisition. The rat lung volume is estimated as 7 mL per kg,[167] and the ventilator tidal volume was set accordingly, calculated based on the individual animal's weight. The breathing rate was set to 70 breaths per minute. Breathing was monitored using a breathing pad placed under the animals chest. Air was supplied at a rate of 4 L/min, either using medical air or a mixture consisting of 20% O_2 and 80% N_2.

Temperature, blood pressure and breathing data were recorded with the CED and displayed on screen. An example of these traces are shown in Figure 2.3. This allowed vitals to be monitored throughout the experiment, and conditions could be adjusted if necessary. The traces were also logged to file.

For Optical Imaging on the bench, the animal remains in the stereotactic frame. The camera is mounted onto the adjustable stand using a custom 3D-printed mount and positioned into place. The projector is clamped onto a stand and aligned until the projected image (FOV 15×15 mm) is in focus over the cranial window. For MRI experiments, the animal is placed prone in a holding bed (Figure 2.4). The head is supported at a natural elevation via adjustable pads, and by the use of a bite bar. A 3D-printed scaffolding is mounted over the bed to secure the optical components in place over the head, as shown in Figure 2.4. The optical well slots into the front end of the optics rig and ensures the rat's head is secured in place. To allow for concurrent optical imaging and fMRI, a custom surface coil was created,

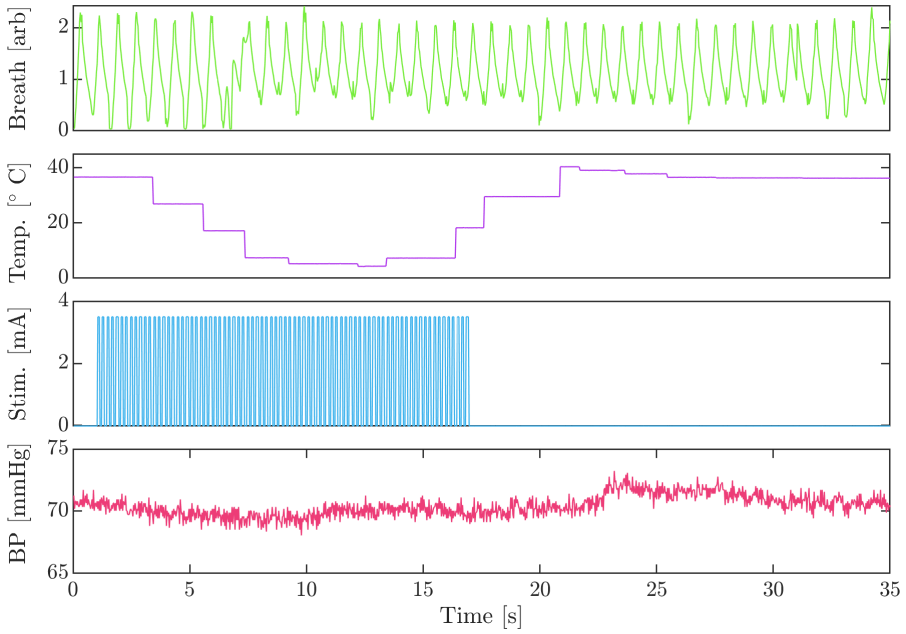

Figure 2.3: Example trace of vitals recorded during an experiment. The blue trace shows the applied stimulus, which is a 5 Hz oscillation with a duration of 16 seconds. The green plot shows the breathing, which should proceed at a steady rate before the start of an experiment. The temperature measurement was affected by the application of the stimulus, but returned to function normally between repeats.

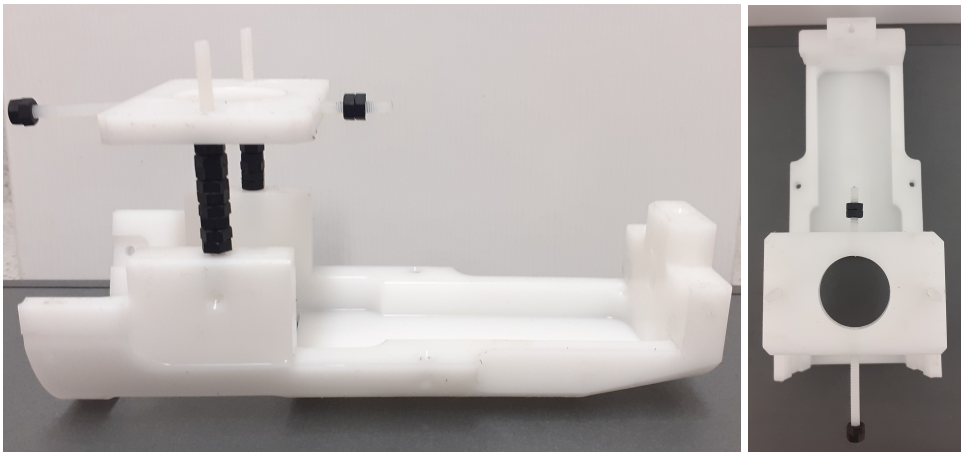

Figure 2.4: A custom holding bed was designed and used to hold the animal during MRI. The animal is placed prone facing towards the right, or front of the bed. For optical imaging, the scaffolding is placed over the animal's head, and the optical well is slotted into the circular opening and fastened using the attachment screws.

which attached to the optical well so that it could be secured in place over the head, while providing visibility to the cranial window. The bed is aligned to place the animal cortex at the center of the bore.

2.1.2 Activation paradigm

A neuronal response was generated via an electrical whisker stimulus. Two electrodes were made from thin tungsten wires (0.25 mm diameter). The tungsten is non-magnetic and therefore suitable for use in MRI, and the connectors allowed for flexibility in moving the animal during setup without removing the wires. Just before use, the electrode tips were scraped to remove any oxide formed on the surface, in order to ensure good conductivity. They were implanted in the whisker pad in a posterior direction, one just below the top whisker row, and the other just above the bottom row, to allow them to activate a large region of the whisker pad. The electrodes were connected via a BNC cable to a DAC channel on the CED, with a 1 kOhm resistor and ammeter connected in series for displaying the applied current. The stimulus waveform is specified on the PC, and played to the CED via custom MATLAB code. The CED had a 5V range over a 16-bit DAC, with the target voltage converted to a DAC value in the code, and just over 2V output producing a targeted 2 mA current.

Hypercapnia challenge was used to elicit a change in blood flow and vol-

ume. This is an abnormal increase in CO_2 levels in the blood, which causes an increase both in the breathing rate and circulation.[168] During a hypercapnic experiment, the gas mixture used for artificial ventilation is adjusted to include 10% CO_2 using a flow meter. The CO_2 was added after a one minute baseline, and kept up for a maximum of 2 minutes before turning it off and allowing the physiological response to return to baseline. Hypercapnia is thought to involve no change in the rate of oxygen consumption,[169] and is therefore detectable using BOLD fMRI even if no neuronal activity is triggered. The signal changes associated with hypercapnia tend to be significant and detected widely throughout the brain, and is therefore useful as a confirmation of the viability of the setup. The respiratory and circulatory changes might also have an improving effect on the animal condition, and therefore improve the signal detected from stimuli.

2.2 Optical Imaging

The optical imaging methods used, Optical Imaging Spectroscopy (OIS) and Spatial Frequency Domain Imaging (SFDI), are similar in set-up, with the main difference being the presentation of incident light. This section outlines the implementation of these methods, including trigger sequencing between camera and light source and image projection. It discusses integration of the optical acquisition setup within the MRI bore, optimisation and validation of each method, and the methods used for analysis of the optical data.

2.2.1 Optical data acquisition

Optical imaging requires a camera and a light source to illuminate the sample. Here, images were acquired using a Thorlabs Quantalux sCMOS CS2100M-USB monochrome camera. It was capable of recording images of 1920 x 1080 pixels, supported up to 87 dB dynamic range, and could provide a maximum frame rate of 50 fps when using the full sensor. The camera had functionality accessible via an SDK, and could therefore be controlled via script. This provided control over parameters such as exposure time, image size and binning, as well as allowing for triggering exposure and for the images to be collected.

The sample is illuminated using a Sutter Lambda DG-4 PLUS/USB ultra-high speed wavelength switching galvanometer (World Precision In-

struments). It contains a Xenon arc lamp operating as a broad light source, and has four slots for replaceable wavelength filters, which it can switch between at a speed of 0.5 or 1 ms for nearby or distant filters. Settings can be controlled via PC and script using a serial port.

Spatial Frequency Domain Imaging requires the projection of a pattern of spatially modulated light onto the sample. This is achieved using an LED pico-projector (Contrast 800:1, supporting a resolution of 1920×1080 pixels). The images to be projected are generated using MATLAB and displayed on full screen using the projector as a second monitor.

Updating the projected image takes time, and doing so between each frame in the acquisition would reduce the achievable frame rate. The projector was therefore modified to use the switching galvanometer output as light source, rather than the pre-installed LED. On the projector side, the guide was secured in place with a 3D-printed holder, which was glued onto the interior of the projector casing. With this setup, the projector can display a single image for the duration of the experiment. The alternation between illumination wavelengths can also be easily controlled using the galvanometer, and wavelengths will be the same across OIS and SFDI, so that results can be compared. To focus the image over the cranial window, the lenses in the projector were removed, and the opening instead fitted with a 50 mm focal length lens (Thorlabs) in a lens tube, which was held in place by a 3D-printed adapter.

In order to record fMRI and optical imaging data simultaneously, the the light must be projected to and recorded from within the MR bore. As the optical equipment contains metal and must be kept outside the scanner room, imaging fibres are used to transmit light across the distance from the source to the bore. An imaging fibre was repurposed from an Avotec MRI Projector system. The fibre was coupled to the projector output using a suitable objective and custom 3D printed supports, as shown in Figure 2.7. The other fibre end was fitted with lenses and an angled mirror, to produce a projected image of dimensions 15mm $\times$ 15mm. Remitted light from the sample was collected using a non-magnetic Endoscan endoscope (following Kennerley et al.[151]). The endoscope consisted of a 50K fiber optic bundle and prisms to provide perpendicular imaging. It allowed for adjustable focus, and connected to the camera C-mount.

Optical data is acquired at set intervals to provide a time series, which

can then be compared across experiments and across optical and MRI modalities. In order to compare time courses of the optical and fMRI responses, the setup should acquire images at known intervals throughout the experiment. For the optical acquisition this requires control over the duration and the sampling rate of an acquisition. For concurrent measurements it is also vital to get a matching time stamp between the MRI and optical data sets, which requires a trigger pulse to ensure the two time courses are correlated. This is handled by a trigger sequence, which is demonstrated in Figure 2.6.

In order to monitor the dynamics of neuronal activity biophysical changes, the optical data must be acquired rapidly. Like a typical BOLD response in humans, the response to whisker stimulation in the rat model has a long time course of several seconds, and can take up towards a minute to return to baseline. The functional MRI signal is acquired at a speed of one frame per second, see Section 2.3. Optical imaging however, can achieve significantly faster rates without loss of resolution. Higher temporal resolution not only provides a more accurate time course, but is also more sensitive to fast dynamics, such as the cell structural changes. A user-controlled triggered setup was constructed to ensure reliable and rapid acquisition.

To measure changes in chromophore concentrations concurrently with MRI data, images should be acquired rapidly at four repeating wavelengths. The optical set-up therefore requires a switching galvanometer to switch between wavelengths, in coherence with the camera acquisition. This sequence is externally triggered by the MRI system so that images are acquired at known time points relative to the MRI measurements. A trigger sequence was set up to control data acquisition, according to the schematic shown in Figure 2.5 and the sequence in Figure 2.6.

The acquisition is controlled using a CED 1401 (Cambridge Electronic Design Limited). This is a device capable of receiving and recording trigger signals. Remote control via PC is possible, here MATLAB is used. A preconfigured output can be loaded, to be played on command or optionally when receiving an external trigger. This is used to initiate a custom trigger sequence, which can run camera acquisitions at the required frequency. The CED is also used to record vitals during the experiment. The camera has pin-outs which are accessed using the recommended Thorlabs I/O cable and breakout board. This provides a trigger-in pin to start acquisition of an image.

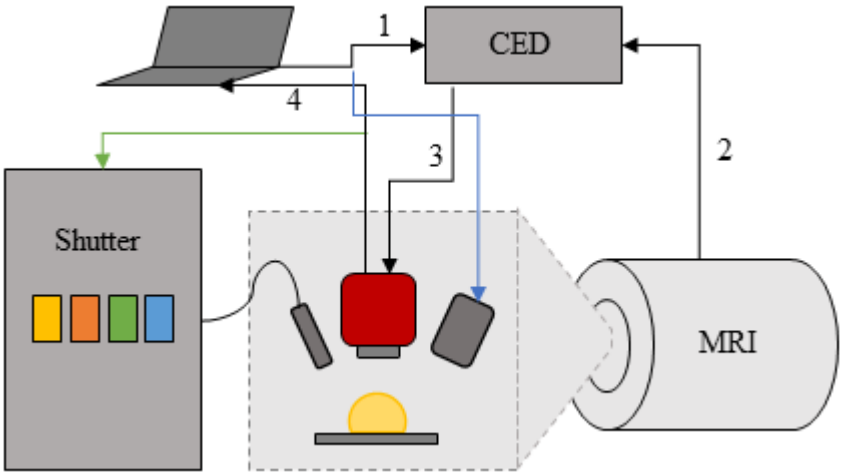

Figure 2.5: Acquisition setup. The computer loads a pre-configured trigger sequence to the CED (1). Once the MRI acquisition begins, it triggers the CED (2) to start playing the pre-configured sequence which runs the camera at the desired frequency (3). For an OIS acquisition, the camera triggers the switching galvanometer to switch filter between each image (Green). For an SFDI acquistion, the computer controls the image displayed onto the sample (Blue). The images are collected on the computer (4).

In order to acquire concurrent MRI and optical data, the trigger sequence can be initiated by the MRI system. The 7T Bruker Bio MRI machine gives the option of sending a trigger pulse for a given pulse sequence, on the start of acquisition, for each volume, or for each slice. The trigger pulse was collected via a BNC cable, and transmitted to the E3 input on the Events socket on the CED via a home-made connector. For the DtiEpi sequence used for diffusion functional imaging there is no trigger out option in the scan card, so the RF blanking pulse was used instead. On triggering the CED drives the camera at a set frequency so that images are acquired at known time points relative to the MRI measurements. Figure 2.6 shows a trigger sequence set up for *in vivo* experiments.

The data acquisition is handled through MATLAB. The triggering sequence is prepared using a custom made GUI. It enables the hardware triggering mode of the CCD camera and sets the exposure time. It enables remote control of the switching galvanometer, loads in the ring buffer which defines the filter sequence, and sets it up for strobe triggering via the camera trigger. It also loads in the CED trigger sequence, which can be modified to the required frequency, and sets this to be played at an external trigger. During an experiment, a script is run to grab frames from the camera and

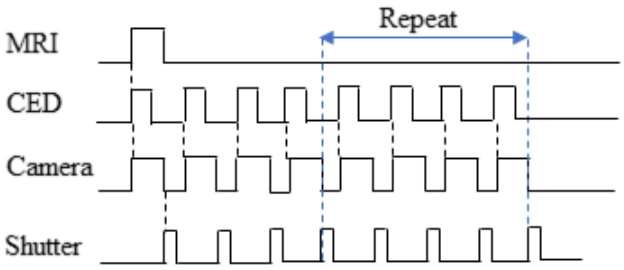

Figure 2.6: The trigger sequence used to control the set-up. When the MRI acquisition starts, a TTL pulse is sent to the CED, triggering a pre-loaded custom trigger sequence. The end of the camera exposure window triggers the switching galvanometer to move to the next filter. There can then be a gap in camera acquisition to save the data.

write these to file.

For imaging under an illumination pattern, the updating of the projected image could become a bottle neck for the achievable imaging rate. The sine pattern images to be displayed could be pre-generated with the desired colours by given RGB values, but drawing the frame to the displayed figure is slower than the fast switching rate of the galvanometer. It would also require additional processing power during the acquisition, which detracts from the work of grabbing the camera frames and storing these to disk, reducing the maximum imaging rate. The projector was therefore modified to use the switching galvanometer light guide as a light source, rather than the inbuilt bright white LED. This enables reliable rapid switching, and the projection image can be updated once, prior to starting the acquisition, freeing the script up to focus exclusively on rapid data capture. This also means the exact same wavelength filters can be used in both OIS and SFDI, enabling direct comparisons.

2.2.2 Optical Imaging Spectroscopy

OIS was used to determine the concentration of oxy- and deoxygenated hemoglobin (HbO and Hbr), by measuring the degree of absorption as light propagates through the tissue. Light travelling through a medium will be attenuated due to the medium's absorption and scattering properties, this is detailed in Chapter 4. In OIS, the attenuation of light by tissue is calculated under illumination at different wavelengths. Attenuation is found from images I relative to 'white' images I_W at the respective wavelengths, where

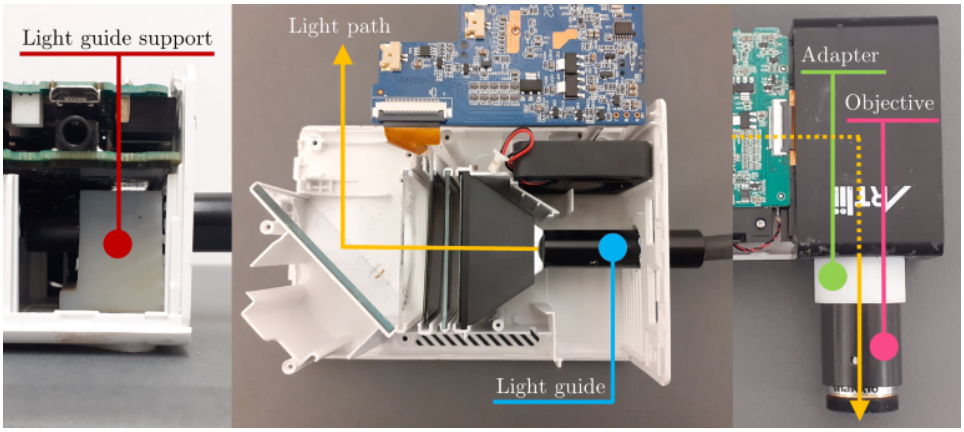

Figure 2.7: A readily available pico-projector was modified to generate the illumination pattern required for SFDI. Originally, the casing housed a bright white LED (positioned in the right chamber in the middle image), and the light passed through the polarisers and image forming elements to reflect of the mirror (on the left in the middle image) and out through a set of magnifying lenses. The LED was replaced with the light guide by creating an opening through the back wall, and a custom holder was 3D-printed and glued to the casing base, to support the light guide in place as shown in the left image. To produce the small FOV required for illuminating the optical window, the magnifying lenses were removed from the front of the projector and replaced with an objective (shown in the image on the right), which was secured onto the casing with another 3D-printed adapter. The adapters required in the modification of the projector were modelled in Blender according to the required dimensions.

there is no sample and all the light is reflected. In each case dark images, I_D and I_{WD} are acquired with no illuminating light, and used as a correction; subtracting them from the lit images removes any signal measured by the pixels which does not belong to the reflected light from the light source.

$$A = log \frac{I(\lambda) - I_D(\lambda)}{I_W(\lambda) - I_{WD}(\lambda)} \tag{2.1}$$

The wavelengths are chosen so that the light is absorbed to different extents by the different chromophores. Of particular interest is oxygenated and deoxygenated haemoglobin, their absorption spectrum is shown in Figure 2.8, with the filter wavelengths highlighted. They cover an isobestic point and points with a large difference in absorption, both with HbO higher and with Hbr higher, as reference points. Other chromophores such as cytochrome could be taken into account, but are only present in very low concentrations.

OIS therefore relies on measuring attenuation changes in remitted light to calculate absorption properties of the tissue, which can be related back to chromophore concentrations. The Beer-Lambert law, Equation 2.2, relates the attenuation of light A to the the concentration c_i and the extinction coefficient ε_i of the absorbent species present via the path length L travelled by the light through the medium.

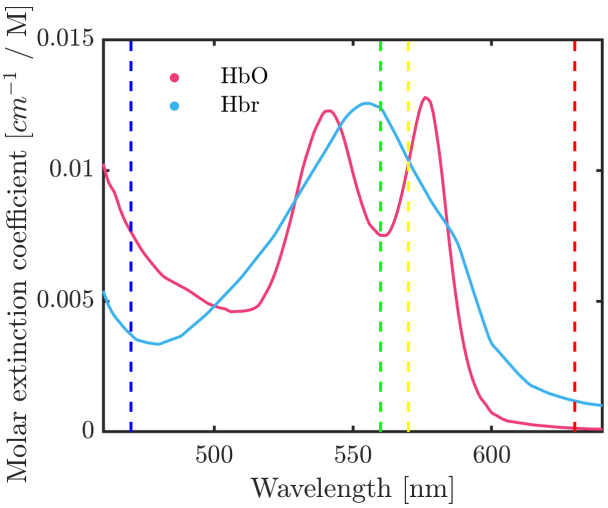

Figure 2.8: Spectra of the molar extinction coefficients for oxy- (red) and deoxy-haemoglobin (blue). The vertical lines show the wavelengths 470, 560, 570 and 630 nm, which were used in OIS.

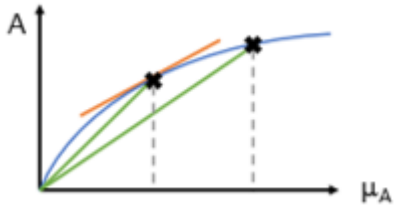

Figure 2.9: The differential path length (red) gives the change in attenuation per change in μ_a. A change in μ_a, such as the difference between the two marked points, will have a more significant impact on the total path length (green), than on the differential path length.

$$A(\lambda) = L\mu_A = L\sum_i \varepsilon_i(\lambda)c_i \tag{2.2}$$

The path length is not known. As light moves through the tissue, scattering causes it to disperse. Only some of the photons are remitted back out of the tissue, and these will have travelled along a distribution of path lengths. OIS therefore relies on the modified Beer-Lambert law, Equation 2.3 which provides the *changes* in chromophore concentration from attenuation changes.[170] Here, G is a function which depends on scattering, but is independent of μ_A.

$$\Delta A = -ln\frac{I}{I_0} = \Delta L \cdot \mu_A + G \approx \Delta L \cdot \mu_A \tag{2.3}$$

This expression involves the differential path length L_d, which is defined as the local gradient of the attenuation against the absorption coefficient as shown in Equation 2.4. The implications of the differential path length is demonstrated in Figure 2.9. The change in L_d is less affected by a change in μ_A than the overall path length L is, and is therefore more robust to minor changes in wavelength than the total path length.

$$\Delta L = ln(10) \cdot \frac{\Delta A}{\Delta \mu_A} \tag{2.4}$$

Most of the light entering tissue will only reach the surface layers before being absorbed or remitted due to scattering. Only a small amount of the remitted light will have reached deeper, and deeper objects will therefore contribute less to the detected signal. The possible path lengths will therefore form a probability distribution, which depends on the tissue's optical

properties.

The differential path length can be found by determining the average path length travelled by light through the tissue.[170] If the possible path lengths are represented by a probability distribution, this is equivalent to the mean or expected value of that path length distribution, as given by Equation 2.5.

$$\Delta L =< L >= E[X] = \sum_{i=1}^{k}(x_i \cdot p_i) \tag{2.5}$$

The path length distribution can be determined for a given tissue using a Monte Carlo simulation, which is discussed in Section 4. Using this estimate, changes in μ_A are determined from attenuation changes:

$$ln\frac{I_1}{I_2} = \Delta A = \Delta L \Delta \mu_A \tag{2.6}$$

Once the attenuation data ΔA is converted into $\Delta \mu_A$, the chromophore concentrations are determined. If two wavelengths are used to determine two chromophore concentrations (typically of HbO_2 and HbR), the equation for μ_A

$$\Delta \mu_A = \epsilon_{HbO_2} \Delta c_{HbO_2} + \epsilon_{Hbr_2} \Delta c_{Hbr_2} \tag{2.7}$$

can be rewritten as a set of simultaneous equations

$$\Delta c_{HbO_2} = \frac{\varepsilon_{Hbr}^{\lambda_1} \cdot \Delta \mu_A(2) - \varepsilon_{Hbr}^{\lambda_1} \cdot \Delta \mu_A(1)}{\varepsilon_{Hbr}^{\lambda_1} \varepsilon_{HbO_2}^{\lambda_2} - \varepsilon_{Hbr}^{\lambda_1} \varepsilon_{HbO_2}^{\lambda_2}} \tag{2.8}$$

where $\Delta \mu_A(i)$ refers to the change at the given wavelength i

$$\Delta \mu_A(i) = \frac{\Delta A(\lambda_i)}{L(\lambda_i)} \tag{2.9}$$

If more than two wavelengths are used, the concentration changes can be determined using a linear least-squares fit.[171] The matrix form of this calculation is shown in Equation 2.10.

$$K = \alpha C + E \tag{2.10}$$

Here C is a vector representing the unknown concentration changes, and K is a vector containing the i observations of the dependent variable, here μ_A changes. α is a matrix with i observations (one for each wavelength) of the

j independent variables (extinction coefficients). E represents the residual errors in the fit for each wavelength.

The changes in concentration can be determined by rearranging to the form shown in Equation 2.11. Here α' denotes the transpose and $(\alpha'\alpha)^{-1}$ is the pseudo-inverse of α. The residual errors of the fit is given by Equation 2.12.

$$C = (\alpha'\alpha)^{-1}\alpha' K \tag{2.11}$$

$$E = K - \alpha C \tag{2.12}$$

In practice, the attenuation data A is used to generate K, using the differential path length estimate for the relevant wavelength.

$$K(w,i) = \frac{log(10) \cdot A(w,i)}{L_w / log(10)} \tag{2.13}$$

C can then be found using Equation 2.11, and the error in this result is found by substituting the residual error E;

$$\delta C = (\alpha'\alpha)^{-1}\alpha' E \tag{2.14}$$

It is important to keep in mind the assumptions made in OIS during analysis. The modified Beer-Lambert Law has been determined to be incorrect,[172] but the differential form applies if attenuation changes are relatively small, G is constant and μ_A change is homogeneous. This means that the differential modified Beer-Lambert law assumes homogeneous absorption change in the tissue, and that intensity loss from scattering is constant. As discussed in Chapter 1, this is not generally the case however, as scattering changes have been widely reported during neuronal activation and CSD events, and tissue absorption changes are typically not spatially homogeneous. It has been estimated that for a tissue with optical properties similar to that of the cerebral cortex, a 1% change in scattering coefficient will cause the calculated chromophore concentration changes to increase by around 0.5 μM.[172]

Concurrent measurements can help to mitigate these errors. By measuring both absorption and scattering changes during activity, Spatial Frequency Domain Imaging not only provides a fuller picture of the underly-

ing biophysical changes, but can provide better estimates of the absorption changes than if scattering is ignored.

2.2.3 Spatial frequency domain imaging

SFDI measured diffuse reflectance R_d, which is dependent upon both scattering and absorption. In order to separate these, more than one diffuse reflectance value is required. The images are demodulated in order to determine the components of R_d caused by the high reference frequency of the illumination pattern and by the low frequency planar components of the light. These are typically referred to as the AC and DC components respectively.

The spatially modulated light S is represented using Equation 2.15, where S_0 is the planar illumination source, M is the modulation depth, α is the phase shift and f_x is the spatial frequency.[153]

$$S = S_0[\frac{1}{2} + M\sin(2\pi f_x + \alpha)] \tag{2.15}$$

The original work used an illuminating sine pattern, and their demodulation method based on three images (I_1, I_2 and I_3) per spatial frequency. These were acquired at phase offsets 0, $2/3\pi$ and $4/3\pi$ radians. M_{AC} can then be determined using Equation 2.19. This represents the amplitude envelope of the reflected photon density standing wave at the given frequency, Figure 2.10.

$$M_{AC}(x_i, f_x) = \frac{2^{1/2}}{3}([I_1(x_i)-I_2(x_i)]^2+[I_2(x_i)-I_3(x_i)]^2+[I_3(x_i)-I_1(x_i)]^2)^{1/2} \tag{2.16}$$

This demodulation removes the average image noise, as this is common to the three images, and removes any constant ambient light. It also does not require knowledge of the spatial frequency, removing any spatial calibration errors.

Once the data is separated into its components, it is calibrated against a phantom of known optical properties, Equation 2.17. $M_{AC}(f_x)$ is the product of the intensity of the light source, I_0 and the modulation transfer functions of the optical system, $MTF_{system}(x_i, fx)$ and of the turbid medium, $R_d(x_i, f_x)$ as shown in Equation 2.18, so this calibrates for the system dependent properties. Using the known properties, the diffuse re-

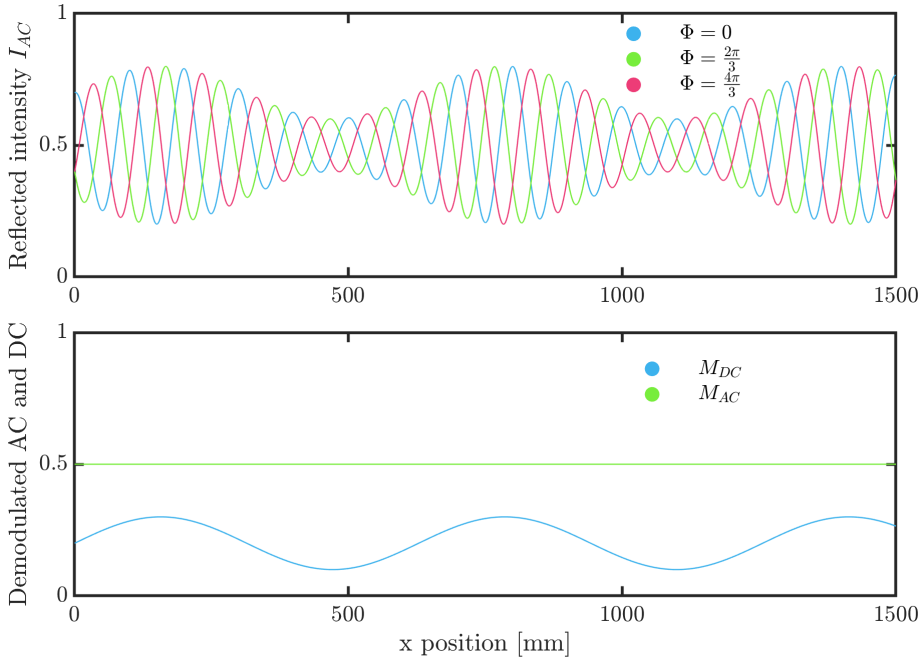

Figure 2.10: Adapted from Cuccia *et al.* 2009. The modulated reflectance (above) and the demodulated *AC* and *DC* components (below).

flectance of the phantom is modelled as $R_d(x_i, f_x)$. The reference measurement $M_{AC,ref}(x_i, f_x)$ is then used to find the diffuse reflectance at each point in the image. The modular transfer function represents the system's spatial frequency response. It represents the contrast at different frequencies.

$$R_d(x_i, f_x) = \frac{M_{AC}(x_i, f_x)}{M_{AC,ref}(x_i, f_x)} \times R_{d,ref,pred}(f_x) \tag{2.17}$$

$$M_{AC}(x_i, f_x) = I_0 \cdot MTF_{system}(x_i, f_x) \cdot R_d(x_i, f_x) \tag{2.18}$$

$$M_{AC}(i, j, fx) = I_0(i, j, fx)(i, j, fx) \tag{2.19}$$

A reference measurement on a turbid media with known optical properties will therefore calibrate for the absolute intensity of the source and the MTF of the imaging system. This avoids PSF deconvolution which could amplify noise and uncertainties

Vervandier and Gioux[155] suggested the use of an alternative demodulation, requiring only one image at the given spatial frequency, reducing acquisition time. Each line of the image is Fourier transformed, and the

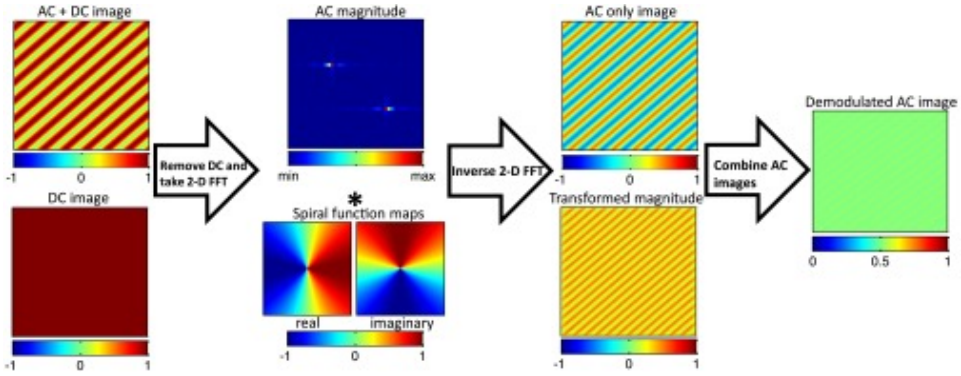

Figure 2.11: The Hilbert transform deconvolution process as described by Nadeau et al.[173] After subtracting the DC map, the AC component of the image is Fourier transformed and multiplied by a spiral phase function map, which contains real and imaginary parts as shown. When the inverse FFT is applied to the product, the sine pattern in the transformed image has become shifted by 90°. This shifted image can be combined with the unshifted AC to give the demodulated AC image.

AC and *DC* components of the line are separated in frequency space by a cutoff frequency, which is determined automatically. The *AC* and *DC* images are then determined by applying an inverse Fourier transform to each line. In Vervandier's work[155] the cutoff frequency is determined automatically for each line, by smoothing the Fourier transformed line and locating the highest *AC* frequency. The spectrum is then divided at the closest local minimum. In their further work using this method, the Tromberg group opted to set a cutoff frequency for all lines to get best quality images for a given spatial frequency.[156]

Another alternative approach suggested by the Tromberg group relies on a Hilbert transform.[173] They were able to extract optical properties from a single frame, with differences of 1% in μ_A and μ'_S compared with the 3-phase demodulation. Here, a complex-valued spiral phase function is generated, according to Equation 2.20, where u and v are the coordinates in the Fourier space. This gives a map with real and imaginary parts. This process is demonstrated in Figure 4.2

$$S(u,v) = \frac{u + iv}{\sqrt{u^2 + v^2}} \tag{2.20}$$

The authors formulate the demodulation problem in terms of Equation 2.21, with the goal being to extract R_{AC}, the *AC* diffuse reflectance term

from the original data I.

$$\begin{aligned} I(x,y) &= 0.5 \cdot R_{DC}(x,y) + 0.5 \cdot M(x,y) \\ M(x,y) &= R_{AC}(x,y) \cdot cos\{2\pi f_{x,y} + \oslash_{x,y}\} \end{aligned} \tag{2.21}$$

The Hilbert transform is obtained with Equation 2.22. First, the DC component is removed from original data I, to give the AC image. A 2-D fast Fourier transform is applied to the AC image to give M. M is multiplied by the phase function map S, which is made to have the same dimensions. The inverse FFT is applied to this product, this has the effect of shifting the modulating sine wave by 90°. This can be thought of as converting the modulating cosine into a sine function. The Hilbert transform of the AC image M is the magnitude of this image.

$$H(x,y) = |FFT^{-1}\{FFT[M(u,v)] \cdot S(u,v)\}| \tag{2.22}$$

The Hilbert transform H is multiplied by i, the complex unit, and added to M. The magnitude of the result is the demodulated AC diffuse reflectance.

$$R(x,y) = |M(x,y) + iH(x,y)| \tag{2.23}$$

The Hilbert demodulation, and indeed other Fourier based approaches, are susceptible to ringing artefacts. This stems from the cut-off around the edges of the image, which causes the projected pattern to be finite. The edges have the effect of a sharp cut-off filter, adding a smoother filter such as a Butterworth filter would reduce this effect.

In this project, both the 3-phase and Hilbert demodulation methods are used, this is to aid development of the optical acquisition an processing. For *in vivo* experiments, a demodulation method based on 1 or 2 images can provide faster sampling speed. During development and testing on phantoms, dynamics are less important, and 3-phase demodulation is used alongside Hilbert-demodulation for comparison.

2.3 MRI acquisition in the animal model

MRI of the rat model was performed using a small-bore (30 cm diameter) 7T Bruker Biospec 70/30 USR scanner, fitted with a 200 mm diameter actively shielded gradient (200 mT/m, 640 T/m/s slew rate). For experiments with

only MRI, a phased array surface coil suitable for rat brain imaging was secured over the head of the rat. A custom made circular surface coil was used for concurrent imaging experiments, which was needed for visualisation of the brain for optical imaging. This was made from a non-conducting copper wire, attached to the surface of the acetal well (20 mm diameter) around the cranial window.

The animal was positioned with the brain area centered in the bore. An initial localiser scan was run. The coil was then 'wobbled' to account for the magnetic field distortion caused by the presence of the animal. Susceptibility effects cause small changes to the magnetic field and Larmor frequencies in the animal, and the electronics should be 'tuned' to its specific resonance frequency. The animal also changes the impedance of the transmit and receive coils, which reduces the energy transfer between the coil and the animal. To account for this, the RF coil impedance should be changed to 'match' that of the wires between the RF amplifier and coil. These adjustments are made by manually turning the 'tune' and 'match' handles on the coil until the RF power is optimised as indicated by an on-screen display. This process provides better signal and reduces noise.

The stimulus is expected to generate a response in a position around 3 cm posterior to bregma. To identify this region, a coronal T2 scan (T2 TurboRARE) was performed, with a slice barely touching the top of the brain as shown on the localiser scan. Bregma was identified from this scan, and an axial slice centered over it. The slice was then shifted by an offset of 3 cm.

Once the slice position was determined, the magnetic field was shimmed. Saturation slices were added diagonally on either side of the brain, as well as under it, as shown in Figure 2.12. A B0 map was collected, (FOV $50 \times 50 \times 50$ mm, 3 averages) which gives a measure of the spatial variation in the magnetic field. This was used as the basis for a map shim, using an iterative correction over the area of interest, defined as an ellipsoid positioned over the brain as shown in the Figure.

GRE-BOLD fMRI data was acquired with a T2star FID EPI sequence, and DWfMRI with a DtiEpi sequence. For both functional measurements the slice thickness was set to 1 mm, and the repetition time was one second. Ten dummy scans were added at the beginning of the sequence, this allows the system magnetisation to reach a steady state before starting data col-

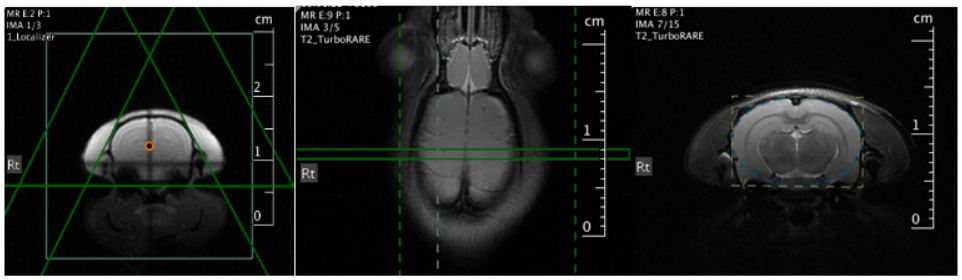

Figure 2.12: Left: Saturation slices. Middle: The positioning of the slices, 3 mm back from bregma. Right: The positioning of the B0 map used for shimming.

lection, and the duration of these scans was accounted for when setting the initial delay for the stimulus onset. Structural scans were performed using the same slice position as the functional scans. These included T1-weighted images (T1 FLASH) and T2-weighted images (T2TurboRARE).

2.4 Data analysis methods

Optical and fMRI data can be analysed in order to determine active sites, to reduce artefacts and in order to extract and understand the time-domain signal. A wide range of signal processing tools are available for these purposes. In this project a combination of tools are used, including both standard processing packages and custom analysis pipelines.

Concurrent data from the animal model is not mapped to the anatomy, as is common in most fMRI processing pipelines. The motivation for this is to avoid potentially introducing artefacts through fitting of the data, and because the focus of the experiments is the dynamic response of the functional signal, rather than on the location of the response.

2.4.1 Statistical Parametric Mapping

Functional MRI data, and other types of functional data such as MEG, EEG or PET data, is often analysed using Statistical Parametric Mapping (SPM). In broad terms, this process realigns a time series of voxel data to account for any shift in the anatomical locations relative to the voxels, then warps the data to match a standard anatomical template and smooths it. Then, General Linear Modelling (GLM) is used to determine the statistical correlation of each voxel to test parameters.

Motion during data acquisition will cause voxel signal changes over time

which are not caused by brain function. Realignment is done to minimise this effect. The motion is represented by an affine transformation of a rigid body. It is parametrised by minimising the sum of the squared differences between each scan and a reference, which is usually taken to be the first scan or the average of all scans in the series. To apply the transformation, the data is re-sampled using a tri-linear, sinc or spline interpolation. The transformation can realign the data to within around hundred microns, but there may still be residual motion artefacts.

Residual motion artefacts after realignment can be caused by non-linear effects, where the motion artefact is not linear with respect to displacement throughout the scans. Examples of this include movement that occurs between the acquisition of different slices, artefacts from interpolation, effects of inhomogeneities in the magnetic field, and spin-excitation history effects. This can be accounted for by fitting the time series data to a function of the estimated movement, as determined by the realignment. The estimate is then subtracted from the data.

In addition to these spatial realignments, there could exist temporal effects caused by a slight delay between acquisition of the different slices. Temporal realignments are sometimes performed using a sinc interpolation. The artefact would cause small delays in functional responses, these are usually small compared to the time course of the biophysical delay of response, so this realignment is therefore usually only performed if the temporal dynamics are important.

For this thesis, functional data was largely analysed using custom MATLAB code. This was useful during data acquisition, because it allowed for quickly analysing animal fMRI data between experiments to check if activity can be detected. This way, the animal's condition or the experimental parameters could be improved before starting comparative experiments, to optimise the chance of seeing a consistent stimulus response. This approach was also used in analysing the results, as it gave full control over which analysis steps to include, and how to parameterise them. By varying the processing pipeline, the effect of each step on the result could be considered, and the results critically analysed.

2.4.2 General Linear Modelling

General linear modelling (GLM) can be used to determine the active region of the brain from functional MRI data. If a repeating stimulus is applied, the time-base signal measured in the active region should be a repeated response following the progression of the stimulus. By comparing the stimulus signal with the time-dependent signal in an MRI voxel, such a response could be found.

GLM estimates the linear equation

$$Y = b_0 + b_1 \cdot x_1 + b_2 \cdot x_2 ... b_n \cdot x_n \tag{2.24}$$

where the coefficients b_i represents the contributions of each of the variables x_i to the prediction of the dependent variable Y. If Y represents the time-dependent signal in a voxel, and x_1 the applied stimulus, the coefficient b_1 is the number of stimulus functions required to make up the signal. A map of b_1 for all voxels in the MRI image can therefore be seen as a map of where the signal best matches the time course of the stimulus, indicating a response.

The GLM regression can be represented in matrix notation as

$$Y = Xb + e, Y = \begin{bmatrix} Y_1 \\ \vdots \\ Y_n \end{bmatrix}, X = \begin{bmatrix} 1 & x_{11} & \dots & x_{1k} \\ \vdots & \vdots & & \vdots \\ 1 & x_{n1} & \dots & x_{nk} \end{bmatrix} e = \begin{bmatrix} e_1 \\ \vdots \\ e_n \end{bmatrix} \tag{2.25}$$

where e contains the residual value, and indices 1 to n relate to the i-th observation of the variables. The column vector b will contain k unknown regression coefficients, and 1 for the intercept. The sum of the squared residuals is minimised bu finding the coefficients which satisfy

$$\left[X'Xb = X'Y\right] \tag{2.26}$$

which has a unique solution if the X variables are linearly independent and the inverse of $X'X$ exists:

$$\left[(X'X)^{-1}X'Xb = (X'X)^{-1}X'Y, b = (X'X)^{-1}X'Y\right] \tag{2.27}$$

In GLM, a generalised inverse is used instead of an inverse. A^g is the gen-

eralised inverse of A if

$$AA^gA = A \tag{2.28}$$

$$YM = Xb + eX'Xb = X'YMb = (X'X)^{-1}X'YM \tag{2.29}$$

M is an $m \times s$ matrix of coefficients defining s linear transformations of the dependent variables.

The MRI data can be analysed to determine the region of activity, and the result overlaid onto the structural image. The active region is found through general linear modelling, GLM. This provides a fit to the time series data at different locations in the image through combining different functions according to Equation 2.30.

$$data = a \cdot f1 + b \cdot f2 + c \cdot f3... + \sigma \tag{2.30}$$

where σ is an error term. The different functions, or 'design matrix', can contain for example a DC offset, a ramp and the applied stimulus. The coefficients $a, b, c...$ are then adjusted to minimise the error. The result will be a map containing the value of each coefficient in each location of the image. The map representing the coefficient for the stimulus function will indicate the regions of the image where the temporal data is most correlated to the stimulus. This can be used to select the active region, for example by thresholding. GLM also provides a method for de-trending the data; since one term, here $b \cdot f2$ depends on the ramp, this term can be removed:

$$data = data - b \cdot f2 \tag{2.31}$$

It is also possible to convolve the stimulus with the haemodynamic response function (HRF), a curve which shows the expected shape of the response to stimulus. The convolved stimulus function would likely follow the shape of the signal in the active region more closely. The HRF is however only an approximation, as neurovascular coupling varies throughout the brain, it should not be assumes that the HRF would be the same throughout data.[18] As the response shapes are compared between BOLD and DWfMRI, is is also important not to assume a response function, as this would introduce bias into the results.

2.4.3 Registration

Registration refers to the process of aligning image data to ensure spatial correspondence between images. This can be performed on a set of functional data to account for the effects of motion. By registering EPI images to each other, shifts due to participant movement, as well as the effect of breathing can be reduced. It can also be used to transform functional data into the same space as structural data acquired with different slice geometry from the same participant. Also know as co-registration, this allows activation maps to be overlaid onto the corresponding structures in the higher resolution anatomical data. Functional data from a one or more participants can also be aligned with a standard anatomical template, a process referred to as normalisation. This requires more extensive deformations, but can be useful in cross-participant comparisons and averaging.

In this work, registration was used to move EPI data into the same space as structural SWI data, collected as part of the human fMRI study described in Chapter 3. The data sets were acquired during the same scan sessions, with the same slice orientation, the transformation was therefore minimal and linear. Registration was limited to this application; to avoid any potential data loss from fitting errors, motion correction was instead only done on the temporal data. Co-registration was also not performed, as the focus of the data analysis was on the temporal dynamics of activation rather than its anatomical location, as well as on the spatial differences between DWfMRI and BOLD functional data, which were acquired with the same slice geometry and therefore compared directly. For fMRI experiments in the animal model, described in Chapter 5, registration was not performed as the animal is under anaesthesia and the head secured in place, so movement was assumed to be minimal.

2.4.4 Frequency filtering

Frequency filtering was performed to reduce the effects of motion on the fMRI time series. Over the course of an experiment, the baseline may drift if the subject moves, and this can be seen as a low frequency change. A high-pass filter, which removes frequencies below a given cut-off frequency, was applied to remove this effect, with the cut-off value set to be significantly lower than the repetition time of the stimulus, so as to avoid interfering with

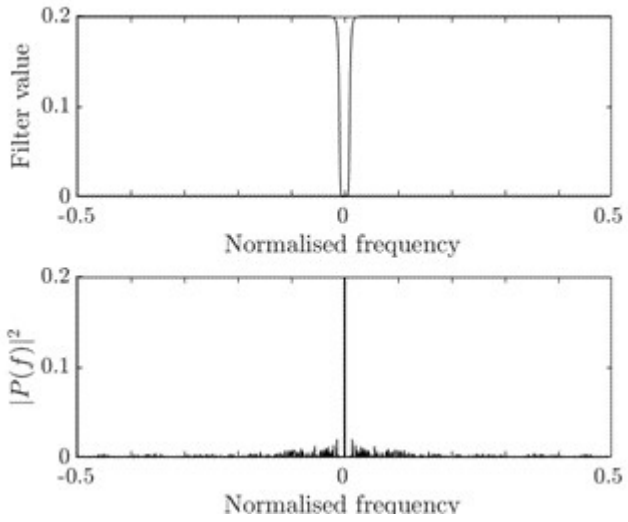

Figure 2.13: Butterworth filter (above) and a frequency representation of a recorded MR time course (below). The frequency-space multiplication of the two removes the central frequencies, filtering out slow drifts in intensity, which are likely caused by motion.

the functional response.

A Butterworth filter was applied to the data, and the filter value is given by Equation 2.32. The filter profile is shown in Figure 2.13, and can be adjusted by changing the order n and cut-off frequency f_c. In order to use this as a high-pass filter, the value at each point was subtracted from 1.

$$|H(f)| = \frac{1}{\sqrt{1 + (\frac{f}{f_c})^{2n}}} \tag{2.32}$$

Figure 2.13 shows an example of frequency filtering. The time series from each voxel in the data set was Fourier transformed to give its representation in frequency space. It was then multiplied by the filter before applying an inverse Fourier transform to convert the data back into a time series.

2.4.5 Spatial smoothing

Spatial smoothing is a process which averages voxels with their neighbours. This results in blurred edges in the images, removing higher frequencies and enhancing low frequencies, acting as a low-pass filter. In the smoothed images, spatial correlations are more pronounced. In fMRI, this is justified by the degree of spatial correlation inherent in the data due to adjacent brain regions having similar function.

Spatial smoothing is achieved by convolving the data with a function referred to as a kernel. The kernel is often given by a Gaussian, Equation 2.33. This forms a symmetric bell curve, where a gives the height of the peak, b is the peak position, and c gives the curve width, or standard deviation.

$$f(x) = a \cdot exp(-\frac{(x-b)^2}{2c^2} \tag{2.33}$$

This has a specific width, expressed as the full width at half maximum (FWHM), which will determine the degree of smoothing. The FWHM is given by

$$FWHM = 2\sqrt{2 \cdot \ln 2}c \tag{2.34}$$

Whether to use smoothing, or which size of filter to use, needs to be considered in relation to the application. Spatial smoothing reduces spatial resolution of the data, and therefore the spatial specificity of a signal's location. This could cause a problem, for example by reducing sensitivity to activation expected to have a narrow spatial extent. Signal peaks that lie close together may also be merged, caused them to appear as a single peak, or appear to be shifted.[174]

The benefits of smoothing include an improvement of the SNR, which increases sensitivity. If the target signal has a Gaussian shape with a FWHM of close to 8 mm, smoothing with an 8 mm Gaussian filter would spread out noise with a smaller spatial extent, faster than it would affect the signal. SNR will be optimised by adjusting the filter width to correspond to the width of the expected signal,[175] which will depend on the functional area of interest in the brain. The size of a signal is not always known, and filter width might be based on pilot data or published observations. If the filter size is too large, narrow activations could become reduced and lose significance, however if it is too small, the gain in SNR will be minimal, but it will still reduce resolution. Liu et al. showed that spatial smoothing causes a reduction in noise, which goes on to cause an expansion of the estimated region of neuronal activity.[176] They suggest a smoothing kernel with a FWHM of maximum two voxels for mapping function with correlation based methods, such as GLM. A similar FWHM of 2-3 voxels was suggested by Chen and Calhoun,[177] who used Independent Component Analysis (ICA) and found this kernel size suitable for single subject analysis.

3 Functional diffusion MRI in human

This chapter presents a study of DW-fMRI in human at 3T. It provides theoretical background about diffusion and describes how diffusion measurements are made with MR. It outlines uses of diffusion for functional contrast in the literature, and perspectives drawn from this work about the origin of the signal. The present study is then presented, including the study aims, and its design as it intends to compare and explore the contrast mechanisms of DW-fMRI and BOLD, with an outline of the analysis process and an exploration of its effect on the results.

3.1 Introduction

Diffusion Weighted functional MRI has been suggested as an alternative approach to the standard BOLD method for the measurement of brain activity. It is important to note that the BOLD response is an *indirect* measure of activity, with a BOLD map reflecting a complex haemodynamic response to activation, affected by blood flow, oxygenation and volume, which is not easily interpreted. BOLD is limited in both its spatial and temporal resolution due to its origin in haemodynamics. The increase in local blood flow will depend on a large area of vessels which can generate a signal from regions of neurons not necessarily involved in the active process.[14] The time taken for the typical BOLD signal to emerge after activation is around 4 seconds, which could limit the temporal accuracy.[29]

A functional MRI technique based on diffusion has been considered based on the idea that water diffusion could be made sensitive to dynamic structural changes occurring on a cellular scale during activity. The diffusion weighted signal has indeed been shown to decrease during stimulus,[30,33] and changes in cell size have been observed in optical studies of brain slices and cultures.[24,103,104] Early DW-fMRI studies attributed observed signal changes directly to neuronal activity,[34] however the relationship between the DW-fMRI signal and cellular swelling is still contested.[17,31,34] This is likely a reason why diffusion fMRI has not become as widely used as BOLD. A motivation for using diffusion weighted fMRI is that cellular swelling would provide a more direct measure of neuronal activity than the ensuing haemodynamic response. However, there is still a need for research into brain cellular swelling, and more information is required to establish the link be-

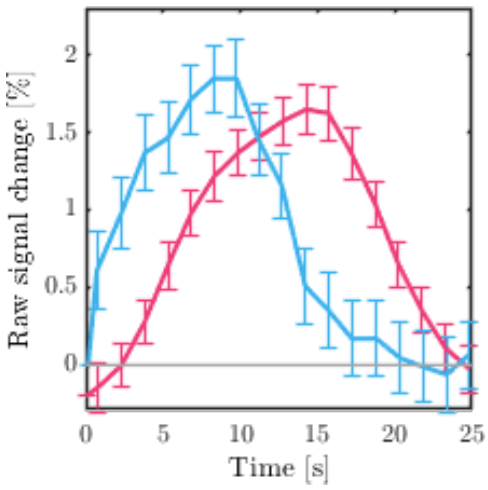

Figure 3.1: Diffusion (blue) and BOLD (red) fMRI responses averaged across repetitions, adapted from Le Bihan 2007.[29] Their results clearly show the DWfMRI response preceeding the BOLD response by several seconds, and featuring a relatively rapid onset. This was taken as an indication that the diffusion weighted response was driven by a mechanism more directly linked to neuronal activity than the slower hemodynamic mechanism underlying the BOLD response.

tween DW-fMRI and its proposed biophysical origin.[34]

One notable and well cited article[29] exploring diffusion weighted MRI as a functional imaging tool was published by Le Bihan *et al* in 2006. In this work they compared responses obtained during a visual stimulus with DW-fMRI and BOLD, as shown in Figure 3.1. Their results show that the diffusion weighted fMRI signal occurs seconds before the BOLD signal. This could suggest that the diffusion response is linked either directly to neuronal activity or to it through a fast coupling mechanism.[33] The activation maps also show smaller active regions, which they suggest reflects DW-fMRI's sensitivity being weighted towards a cellular mechanism, rather than a haemodynamic one. If the link between this signal and activity mediated cellular swelling could be confirmed, the method could become a valuable competitor to BOLD, with the potential to provide higher spatial and temporal specificity.[29]

Here, a study is devised to further investigate the DW-fMRI signal. It aims to confirm the fast response, and investigate the dynamics of the response to visual stimulus under different stimulus designs. It outlines considerations for the acquisition and analysis of DWfMRI data, and discusses what the results might tell us about the underlying mechanism driving the

measured signal.

3.1.1 Free diffusion

Diffusion describes the net movement of a substance from a region of high concentration to a region of low concentration. From a macroscopic view, the particles spread more evenly over time, with the distribution of displacements forming a bell curve. This takes the shape of a bell curve, which gradually flattens out over time, as shown in Figure 3.2.

In pure water, the molecules diffuse freely and randomly. On a microscopic level, their behaviour follows Brownian motion, which describes the random motion of particle movement in a fluid. The directions from which the particles experience interactions are constantly changing, which means there is no preferred direction of flow.

Using Fick's laws of diffusion, Einstein showed[178] that particle displacements in Brownian motion was related to the diffusion coefficient ($m^2 s^{-1}$), connecting microscopic Brownian motion to the macroscopic concept of diffusion. For N particles starting at the origin at a time $t = 0$, the displacements form a probability density function with the form

$$\rho(x,t) = \frac{N}{\sqrt{4\pi Dt}} e^{-\frac{x^2}{4Dt}} \tag{3.1}$$

The equation describes a normal distribution with mean, or center point, μ=0, and a variance of $\sigma^2 = 2\mathrm{Dt}$. Based on this expression, the diffusion coefficient was shown to be dependent on the mean square displacement of the particles, Equation 3.2, where n is the dimension of Brownian motion.

$$\bar{x^2} = 2nDt \tag{3.2}$$

3.1.2 Diffusion in MRI

Diffusion Weighted MRI (DW-MRI) can be used to study the diffusion of water within tissue. In tissues, the water molecules are restricted, as they interact with cell membranes and macromolecules which change their motion. Cell membranes create barriers which limit the available extracellular and intracellular space. The more cells are present, the more restricted the motions become. With few cells, the extra-cellular space is large and

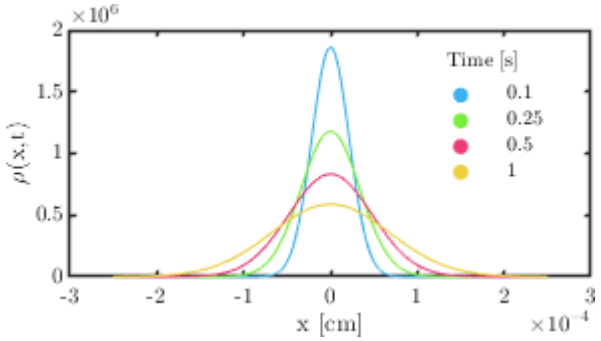

Figure 3.2: The displacement of particles undergoing Brownian motion can be described by a bell curve, which flattens out over time.

water molecules can diffuse more freely, and move through damaged cell membranes.

Diffusion MRI measures a macroscopic quantity which relates to the probability distribution of particle displacement over time. The Einstein equations assume free diffusion, where the distribution of molecular displacements follows a Gaussian law. However in tissues, this is not generally the case, therefore, diffusion is no longer described accurately by the true diffusion coefficient.[179] To account for this concept in diffusion MRI, the Apparent Diffusion coefficient, or ADC was defined.[180]

The diffusion distance in tissue is on the scale of micrometers, with the root mean square of the displacement of water molecules during a DWI acquisition estimated to be around 8 μm.[181] This is similar to the average size of a human cell, which measures around 10 μm, and is therefore on the right scale to explore tissue structure on a cellular scale.[133,179] The DWI signal from tissue contains contributions from motion of water molecules in extracellular space, intracellular space and intravascular space.[182133]

The sensitivity to the cellularity of tissue means DW-MRI has found use for example for imaging tumors. Tumor tissue is highly cellular with many intact cell membranes, so the extra-cellular space is reduced and motions restricted. This is an efficient technique for this purpose because it is not too time consuming and does not require any contrast agent.[133]

3.1.3 The diffusion sequence

A diffusion weighted MR sequence is shown in Figure 3.3. It is based on a T_2-weighted spin-echo sequence, where a 90° pulse is followed after a given time

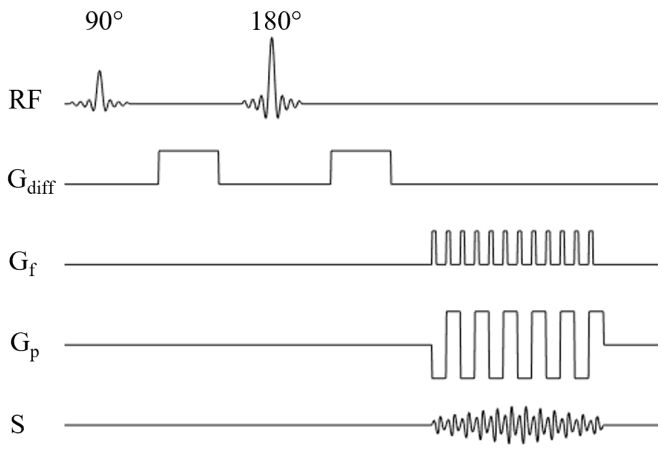

Figure 3.3: A diffusion weighted MRI sequence. A pair of diffusion gradients, G_{diff}, are included before and after the refocusing pulse, and the signal S is read out with EPI.

by a 180° pulse. DW-MRI adapts this by applying a sequence of symmetric or bipolar gradients on either side of the refocusing pulse. Static molecules will receive phase information from the first gradient and be rephased by the second, leaving the signal intensity preserved. Moving molecules are not completely rephased by the second gradient, so signal intensity is lost. DW-MRI measures the degree of signal attenuation, which is proportional to the degree of water motion.[133]

The sequences sensitivity to diffusion can be changed through adjustment of the diffusion gradients. This is characterised by the b-value, originally defined in 1965 by Stejskal and Tanner,[183] which is given in Equation 3.3. It describes the relationship between the gradients' magnitude G, their duration δ and the spacing between the gradients Δ, as shown in Figure 3.4.

$$b = \gamma^2 G^2 \delta^2 (\Delta - \frac{\delta}{3}) \tag{3.3}$$

The b-value therefore indicates the gradient strength and duration, with a higher b-value giving stronger diffusion weighting. It is typically $0 - 4000 s/mm^2$, and the units are the inverse of the units in D. The value used depends on the anatomy to be imaged, as well as on the field strength. A large b-value gives more pronounced attenuation, but also limits the signal-to-noise ratio. Clinical DWI of the brain is typically done with a b-value between 0 and 1000 s/mm^2. Two sequences might have the same b-value, but different sequence timings. This could give different time for water

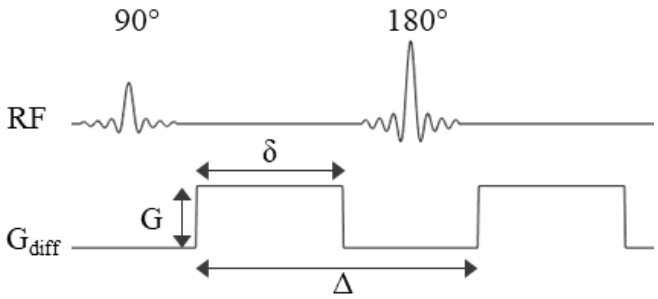

Figure 3.4: The Stejskal and Tanner diffusion sequence with the variable parameters highlighted.

to diffuse, with more diffusion time providing more chance to interact with obstacles, and reducing ADC.[184] The gradient pulse timings should therefore be specified along with the b-value.

Diffusion weighted sequences typically start with acquiring a b0 image, this is acquired with the b-value set to zero, providing a T2-weighted image which can be used as a baseline in analysis. The sequence includes fat suppression to reduce chemical shift artefacts. Since fat molecules have high restriction they produce a high signal, which can obscure useful information.[185] This also reduces the high chemical shift artefacts from EPI, which is the most commonly used DW imaging technique.[185]

Diffusion requires high intensity gradients with longer duration than many other common sequences, and therefore create relatively large Eddy currents.[186] This effect interferes with the readout gradients, effectively reducing the region over which the gradients vary linearly, which can lead to image distortions. EPI is sensitive to Eddy currents, and since the currents depend both on the magnitude and the direction of the gradients, images acquired with different b-values or diffusion encoding directions will be inconsistently affected. Uncorrected, this causes problems with registration, leading to artefacts such as ghosting, and errors in calculated diffusion properties.[187,188] Corrections can be applied in post processing,[188] and the sequence timings can also be adjusted to reduce Eddy currents, as equal and opposite Eddy currents created from switching on or off gradients respectively can be effectively cancelled out.[186]

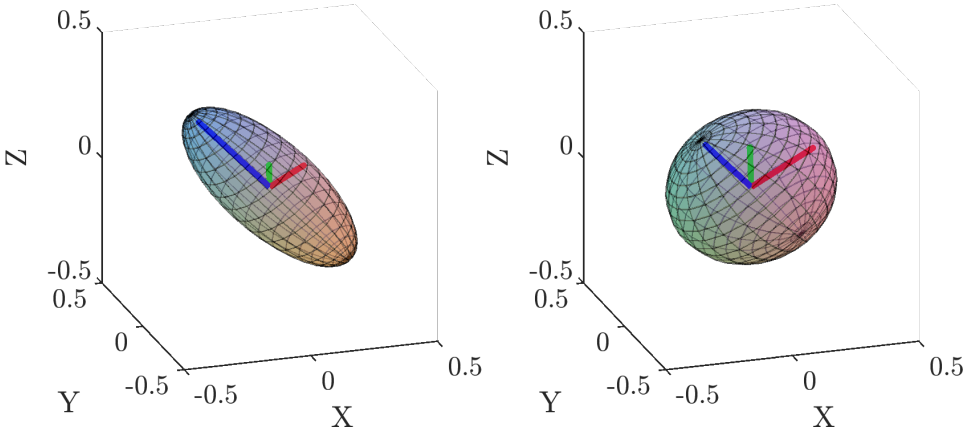

Figure 3.5: Diffusion can be described by a tensor, which specifies a value along each of its eigenvectors. The example shows the isotropic (left) and anisotropic case (right)

3.1.4 Applications

The development of the EPI technique in the early 1990s made DWI a possibility in a clinical setting, because the fast acquisition significantly reduced the sensitivity to motion artefacts. Early works established DWI as a method for detection of acute stroke,[189,190] showing that DWI could be used to detect infarcts sooner than conventional T2-imaging. DWI could identify stroke after less than an hour and the imaging time was less than two minutes, while T2 imaging was unable to show it for 2-3 hours, and sometimes did not show the infarct at all.

The direction of diffusion can be measured by applying diffusion gradients along a set of coil combinations in turn. The diffusion information from each voxel can be described by a diffusion tensor, as demonstrated in Figure 3.5. The directions are given by the eigenvectors, with lengths given by the eigenvalue λ indicating the degree of diffusion along the given direction. Isotropic diffusion gives a spherical ellipsoid, where $\lambda_1 = \lambda_2 = \lambda_3$. Anisotropy leads to a more elongated shape, as diffusion occurs more readily along certain axes. Anisotropy will reduce the degree of diffusion, and therefore gives a brighter region of the image. Anisotropy is high for example in bundles of fibre in white matter, and DWI can be used to map out the white matter tracts, providing insight into connectivity and brain maturation.[191]

DWI results are sometimes represented as a trace image, which shows the sum of the eigenvalues. By averaging across the number of directions used, this provides an image referred to as an ADC map. Measuring along

for example three perpendicular directions, this map approximates the mean diffusivity, but is in fact likely to give an overestimate of the true mean ADC, which requires measurements along 6 directions.[192]

Diffusion Tensor Imaging (DTI)[193] uses the eigenvalues individually, and can be used for example to study white matter connectivity in the brain. The diffusion tensor is a mathematical description of the displacement of the molecules, modelled as a 3D Gaussian distribution. It can be represented in various ways depending on application. Fractional anisotropy (FA) maps represent the amount of diffusion asymmetry in each voxel. This is calculated using the eigenvalues as shown in Equation 3.4, which gives a value between 0 and 1.[194]

$$FA = \sqrt{\frac{1}{2}}\sqrt{\frac{(\lambda_1 - \lambda_2)^2 + (\lambda_2 - \lambda_3)^2 + (\lambda_3 - \lambda_1)^2}{\sqrt{({\lambda_1}^2 + {\lambda_2}^2 + {\lambda_3}^2)}}} \tag{3.4}$$

These FA values can also be used to present a principal diffusion direction map, which is used to show fiber bundle orientation. The voxels are coloured by anisotropy and direction; conventionally the orientation determines the colour and the brightness is determined by the FA value. For example given angles α β and γ with respect to the x, y and z directions, the voxel colour is weighted by $Red = FA * \cos(\alpha)$, $Green = FA * \cos(\beta)$, and $Blue = FA * \cos(\gamma)$.

Diffusion weighted images can be used to generate a fiber tracking map. Here, tracts are traced out starting from a selected seed voxel by following the primary eigenvector of each subsequent voxel to determine the next neighbouring voxel, and for each step changing direction to the new voxel's eigenvector. This progresses until a termination condition is reached, such as the FA value reaching a lower threshold, or a minimum fiber length is reached. Results may vary depending on termination condition and the exact seed voxel selected, as well as on acquisition parameters, with a high number of diffusion directions required for reliable results, and high b-values giving more angular contrast, but lower snr.[195,196] For clinical use, the requirement for shorter acquisition times means resolution is limited and therefore some fibers are too small to be imaged. This can be improved with longer imaging times, which are used in research.[197]

3.1.5 Signal equation

The signal S obtained with a DWfMRI sequence is given by Equation 3.5. Here S_0 is the baseline signal intensity, TR the repetition time and TE the echo time. The effective transverse relaxation rate is given by $\Delta R_2* = \Delta(1-Y)V$, where V is the volume and Y is the saturation of O_2. With the inclusion of the diffusion gradients, the signal obtained becomes dependent on the b-value, and the diffusion constant D:

$$S = S_0(1 - e^{\frac{-TR}{T1}}) \cdot e^{\frac{TE}{R_2^*}} \cdot e^{-bD} \tag{3.5}$$

When the diffusion gradients are turned off and $b = 0$, the final diffusion exponential term becomes 1 and cancels out, the signal obtained therefore becomes the a spin-echo BOLD signal. During a DWfMRI acquisition on the other hand, b can be varied and the other variables are assumed to be constant.

Diffusion weighted images will contain T1 and T2 contrast in addition to the diffusion contrast. Areas in an image can therefore become bright even without highly restricted diffusion, because of high T2 values. This is known as T2 shine-through effect.[198] The effect can be reduced to some extent by keeping the TE short, and the b-value large, but the diffusion gradients and the refocusing pulse extends the TE, therefore it could still be present and cause difficulties with interpretation. A solution to this problem is to divide the diffusion weighted image by the corresponding unweighted image acquired with b = 0 s/mm^2. By rearranging the signal Equation 3.5 to the form

$$ln\left(\frac{S}{S_0}\right) \propto -b \cdot D \tag{3.6}$$

it predicts that the natural log of the signal intensity ratio is proportional to the b-value, decreasing linearly from the baseline signal. The division therefore converts the image into an ADC map, and removes the shine-through effect, as the ADC is independent of the magnetic field strength.[133,198] The signal generally becomes more attenuated for larger b-values, however highly cellular environments will continue to show high signal intensity. This means the slope, and therefore the ADC value, is smaller for highly cellular areas, such as tumors, compared with normal tissue. While the DW images have high signal in areas of restricted diffusion, the resulting ADC image is there-

fore darker, or low in signal, in these areas.[133] By imaging with different b-values, the ADC value can be determined per voxel using Equation 3.6. Measurements using at least two b values are required, and the fit to the slope can be improved by using more, reducing the error in the ADC calculation, and improving the signal-to-noise in the resulting ADC map.[133]

From the equation 3.6, a plot of the signal fraction $ln(\frac{S}{S_0})$ against b would be expected to give a straight line, with a slope equal to the apparent diffusion coefficient ADC. When the diffusion does not follow free Gaussian diffusion as in a homogeneous medium however, this is not generally the case. In the brain, the signal typically deviates from this linear relationship for high and low b-values, as shown in Figure 3.6.

For low b-values of 300-500 s/mm^2, the signal is lower than expected due to the influence of Intravoxel incoherent motion, or IVIM. IVIM was first described by Le Bihan as molecular diffusion and microcirculation in capillaries (known as perfusion), which causes a distribution of phases within a single voxel.[180] In gradients are applied in an MRI experiment, this causes spins to de-phase within a voxel, and some of the signal is lost. With strong gradients the signal loss from IVIM is largely caused by diffusion, but at weaker gradients blood microcirculation in capillaries contributes, as with very low b-values the pseudo-diffusion coefficient associated with blood flow is higher than that of water diffusion. Large vessels tend to have fast flow, which means they have high diffusion values. Their signal is therefore easily attenuated by including diffusion gradients with low b-values, but smaller vessels with slower flow may still contribute above b-values of 200 s/mm^2. For high b-values of 1000-1500 s/mm^2 the signal often shows kurtosis effect. Kurtosis is measured as the degree of deviation of diffusion from Gaussian law, this has diagnostic applications, and has been used for example in the characterisation of ischemic stroke[199] and tumors.[200]

The water in the intravascular space will diffuse further in a given time frame than that in the extracellular or intracellular space, due to blood flow.[133] If diffusion is slow relative to the flow of blood, it will be masked by the flow. For functional measurements in this study, measurements will be done every second. The flow changes with stimulation and could affect measurements.

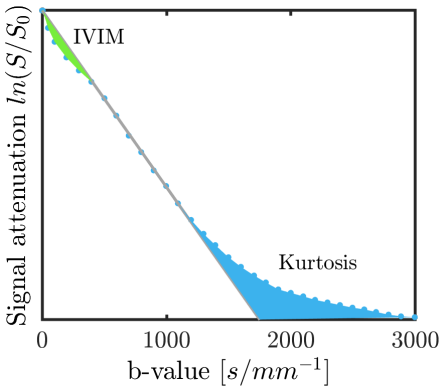

Figure 3.6: For diffusion following Gaussian law, the plot of signal attenuation against b-value would be expected to form a straight line, with a slope equal to the diffusion coefficient. In tissue however, with hindered diffusion, this is not generally the case. Deviations are caused by IVIM at low b-values of 300-500 s/mm^2, and at high b-values of 1000-1500 s/mm^2 due to the kurtosis effect. (Adapted from Le Bihan et al)

3.1.6 Biexponential model

Measurements done on brain and other tissues appear to show two distinct slopes of different gradient D. This can be fitted with a biexponential function, and the analysis method proposed by the Le Bihan group therefore describes diffusion of water in the cortex using a biphasic model.[30] This relates the two slopes to two separate diffusion pools, one with fast and one with slow diffusion, which are in slow exchange with each other.[29] The signal equation can then be written as

$$S = S_0 f_{slow} e^{-bD_{slow}} + S_0 f_{fast} e^{-bD_{fast}} \tag{3.7}$$

where f describes the volume fractions, 70% for the fast diffusing pool and 30% for the slow, with $f_{slow} + f_{fast} = 1$, and D the diffusion coefficients for each of the two phases. If the variations in the signal are small, the signal change dS/S can be modeled as

$$\frac{dS}{S} = F_{slow} df_{slow} + F_{fast} df_{fast}, \tag{3.8}$$

where df is the change in volume fraction of the given diffusion phase.

Several considerations of these two 'pools' have been proposed, for instance relating the fast diffusing pool with extracellular water and the slow with the intracellular. The volume fractions do not agree with the ratio

between intra- and extracellular water however, with evidence suggesting the ADC change in both pools is driven by water in intracellular space.[201] Though the biexponential continues to provide a good fit for measurements, no biophysical origin has been established for the two pools.[29] Despite this, the volume *changes* in the two phases have been shown to correlate well with the volume changes in the intra- and extracellular spaces which occur during the cell size changes observed in different experiments.[202,203]

The intra- and extracellular contributions to the BOLD signal vary with field strength. Simulations have shown that in the case of larger vessels (25 μm radius), the extravascular signal contributes 68% of the signal at 3T, and is the only contributor at 7T, with intravascular contributions nulled out.[204] For smaller radius vessels (3 mum) the values change to 58% and 93% respectively. This is consistent with estimates of intravascular contribution being around 1/3 at 3T and negligible at higher field strengths.

3.1.7 Diffusion functional imaging

Diffusion weighted imaging was developed in 1985, prior to fMRI, and had already been established for clinical applications in stroke detection and ischemia and tumor evaluation. Early observations included detection of apparent diffusion coefficient change during epileptic activity in rats, which causes large, extraphysiological neuronal activation.[205] It was not until the early 2000s that DW imaging was used for functional imaging.

Several early studies employing diffusion weighting in a functional imaging context, aimed to use this to measure blood flow. This was based on the concept of IVIM,[180,206] which some groups have attempted to use to improve fMRI spatial specificity.[207,208] This has been a limitation of BOLD fMRI, as the flow increase due to activity occurs in a wide area, involving remote large arteries or veins supplying the active neuronal region. By including diffusion gradients with low b-values in the sequence, the sequence can "crush" the contributions to the MR signal which originate in the largest vessels.[209][210] The larger vessels have fast flow, and their signal therefore disappears even at low b-values. The remaining signal is weighted towards that from capillaries, which are in close proximity to the activated tissue. This provides more spatially specific activation maps, which has been attributed to a selective sensitivity towards arterial blood flow.[207,208] The method has been used for example to study the contribution from different vasculature to the BOLD

signal.[211] The Song group also identified that the ADC-contrast preceeded the BOLD response with around 1 second, taking this as an indication that it was sensitive to blood flow changes in arteries, as these would have a different spatial location than the veins and be engaged prior to them.[135]

As hardware improved, and higher b-values could be achieved, diffusion weighted imaging was explored as a contrast in itself. A 2001 study[23] by the Le Bihan group showed a change in the diffusion signal during activation of human visual cortex with a 8 Hz flickering checkerboard. The observed transient decrease in ADC was small (<1%), but followed the time course of the stimulus, and was tentatively ascribed to cortical cell swelling. Their 2006 study[30] described a diffusion model based on slow and fast diffusion water compartments, and this analysis suggested the water diffusion decrease was caused primarily by a water phase transition, rather than from a decrease in diffusion coefficient, which could have been caused by a tortuosity increase in the extracellular space.

A key concern for DWfMRI is the potential hemodynamic contribution to the measured signal. The DW-fMRI signal has been ascribed to cell swelling from neuronal activation alone, to residual vascular effects, or to a combination of these.[17,34] Aso et al. modelled the diffusion response as consisting of a haemodynamic response function (HRF) and a diffusion response function, concluding the HRF contributed around a quarter of the signal at peak, while only the DRF contributed at the response onset, showing a rapid initial rise.[212] he early onset of DWfMRI relative to BOLD has been reported by several groups. Using bipolar diffusion gradients with a b-value of 1800 s/mm^2, one group[137] used a checkerboard stimulus of 4 x (10.5 s on + 21 s off) and GLM analysis with a box car function, concluding diffusion slowdown preceeded the vascular response by 2.9 second. The BOLD time course more strongly correlated to concurrent NIRS optical measures of hemodynamics than DWfMRI, suggesting diffusion changes were driven by earlier events.

Some groups have attempted to remove the effects of haemodynamic changes in tissue to clarify the biophysical basis of diffusion changes. Several studies have used model systems without blood or vasculature to exclude any hemodynamic confounds. To investigate activity induced swelling at a cellular level, one study[37] used diffusion MR microscopy. To avoid any vascular contributions to the measured signal, they investigated snail ganglia without

blood. Their results suggested diffusion changes under stimulation arising from cellular swelling, and indicated the ganglia were involved in swelling. Water diffusion was shown to be significantly reduced during activity in rat spinal cord[134] One study[34] by Bai *et al* looked at the interplay between activity and the DW-fMRI signal *in vitro* by using DW-fMRI together with calcium fluorescence imaging. Their model was cortical cultures from rat brains, which shows spontaneous neuronal activity, and is without haemodynamic, respiratory and other physiological artefacts. The fluorescence imaging can detect intracellular Ca^{2+} concentrations which follow neuronal action potentials, detecting neuronal activity. They found a simultaneous increase in DW-fMRI signal with the prolonged depolarisation of neurons using pharmacological manipulators, and the swelling of cells was shown to play an important role in this case. They could however not find evidence of correlation between DW-fMRI and normal spontaneous neuronal activity, concluding it is not sensitive enough to detect it. It has been argued that the lack of observable diffusion changes could be due to the slices lower density of dendritic spines and functional synapses. This points to a need for further studies into which parts of cells undergo swelling.[31]

Another approach to removing the effects of hemodynamics, is by the use of drugs which can inhibit neurovascular coupling. In this model, the link between neurovascular coupling and water microscopic diffusion can be compared between inhibited and non-inhibited stimulation. In one such study[33] by the Le Bihan group, they used nitroprusside as an inhibitor of neurovascular coupling during rat forepaw stimulation, and discovered that although the hemodynamic response to stimulation disappeared, they were able to maintain the local field potentials in the area, and detect a diffusion response on stimulation. With the b-values 250, 1000 and 1800 s/mm^2 the DWfMRI showed a slightly higher peak amplitude than BOLD, and occurred earlier by about 3 seconds. They concluded that DW-fMRI is not vascular in origin.

If DWfMRI is dependant upon cellular rather than purely hemodynamic mechansims, the region of activation should have a closer dependence on the location of the activated neurons than BOLD. Layer dependent fMRI has gained interest in the last twenty years, with early work based on animal studies and the first human study taking place in 2007.[213] This first study by Ress *et al*[214] showed it is possible to obtain a profile of the fMRI

response indicating its size along the neocortical laminae by sampling on a sub-millimeter scale. For BOLD, the signal peaks in the superficial part of the grey matter and declines for deeper layers. Layered fMRI has been used to study the negative BOLD response. The Logothetis group measured BOLD, CBV and CBF in macaque visual cortex and showed that neurovascular coupling differed not only between layers, but also between the positive and negative BOLD responses, with the positive signal coming from regions of increased CBV and CBF, while areas of negative BOLD showed increase in CBV but a decrease in CBF.[152] Layered fMRI has started being used to study the flow of information between cortical regions. By using fMRI method sensitive to cerebral blood volume (CBV-fMRI) as well as BOLD, one group showed input and output of a task localised to superficial and deep laminae respectively, in agreement with anatomical studies.[215] The diffusion functional signal is also dependent on depth,[216] and has been shown to be significantly higher in the middle cortical layers, indicating better localisation of neuronal activity than BOLD. A 2019 study was able to show layer specific connectivity with DW-fMRI during forepaw stimulus in the rat.[162] They achieved a significant improvement in sensitivity by imaging at 9.4T using cryocoils, and imaged under isotropic diffusion weighting with b = 1500 s/mm^2. The group later obtained a temporal response along a depth profile of the rat brain[217] by using an approach known as line scanning.[218] This was achieved by removing the phase encoding dimension, which effectively means each phase encoding step instead samples along the read direction. They defined the imaging region by adding saturation bands to suppress signal from outside the area of interest, removing motion artefacts, and achieved fast acquisition rates with Large Tip Angle scanning,[219] replacing the 90 excitation pulse with a single 150 pulse, which avoids problems of strong T1 weighting.

One key concern about DWfMRI is whether the method is sensitive enough to reliably detect neuronal activity.[34,161] Some of the work showing the relationship between diffusion changes and neuronal activation have used drugs to generate epileptic responses, which can cause more marked tissue structural changes than those obtained from a stimulus response. A 2016 study showed that DWfMRI measures at a range of b-values from 0 to 2400 s/mm^2 corresponded well with the depolarisation of rat cortical neurons by drugs, however they concluded the method was not sensitive enough to

detect normal spontaneous activity.[34] On the other hand, a 2019 study reported DWfMRI showing sensitivity similar to that of BOLD for a finger-tapping stimulus paradigm, with responses measured with a b-value of 1200 s/mm^2 slightly preceeding those with 0 s/mm^2.[161] They compared signal time series of IVIM and apparent diffusion coefficient fMRI while selectively suppressing perfusion and free-water diffusion, and concluded that DWfMRI is sensitive to a decrease in intra or extracellular diffusion.

3.1.8 Aims

A study was been undertaken for the acquisition of DWfMRI and BOLD data from healthy volunteers. The aim was threefold. First, to attempt to replicate key results from the original study published by Le Bihan et al.[30] This was to confirm that the diffusion response can be obtained on the current scanner using the same method as outlined in their work, and to confirm the rapid onset and smaller activation region they observed. Secondly, data collected from humans could provide transferability of the analogous fMRI data collected on rats to the human clinically applicable context. This is needed to validate the model system to be used for the concurrent optical and MR measurements. Thirdly, this comparative study of DW-fMRI and BOLD allows for further exploration of the DW-fMRI signal. The goal was to test different experimental designs to determine the sensitivity of this method to activation compared to BOLD, and to further investigate diffusion-dependent dynamics by varying stimulation paradigms.

In the original study, the stimulation protocol (dartboard, 8Hz) consisted of 3 repeats of 20s (or 16s) stimulus and a 20s (or 24s) intervals. The activation maps based on raw diffusion-sensitised data clearly showed activation (Figure 3.7). The voxels indicated to be active by DWfMRI appeared to be more localised to the cortical ribbon than the broader BOLD activation. In the original work the BOLD response appeared filtered out at b = 1800 s/mm^2 and the DW-fMRI response had a more rapid onset. Their activation maps were calculated using a boxcar basis function to avoid introducing bias from convolving with an expected HRF.

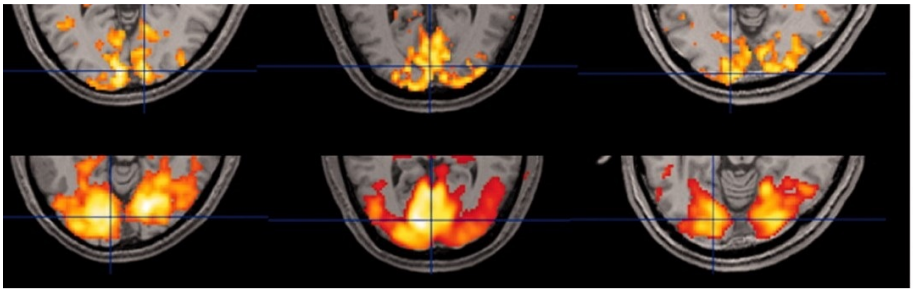

Figure 3.7: DW-fMRI at b = $1800 s/mm^2$ (above) and BOLD fMRI (below) activation maps from the study by Le Bihan et al.,[30] detected with the same acquisition and processing parameters. The SPM activation maps were based on high-resolution data sets. Voxels detected as activated from BOLD fMRI encompasses large subcortical areas beyond the cortex.

3.1.9 Study design

Data was acquired with a SIEMENS MAGNETOM Prisma 3T scanner (80 mT/m @ 200 T/m/s) at the York Neuroimaging Centre (YNiC). Unless otherwise stated, a 32-channel head coil was used. Experimental protocols were approved by the York Neuroimaging Centre ethics committee and were in accordance with the Declaration of Helsinki. The training required to perform scanning on volunteers was completed, including first aid certification. Participants were sought primarily from the local student population and the YNiC volunteer pool (N=53, Age=22-51). The inclusion criteria asked for healthy volunteers with no known vision problems. Volunteers were all provided with a Participant information form. Written consent was obtained from all participants (Study specific consent form). On the day of the scan, investigators aided the participant in completion of the MR safety form immediately prior to scanning. All participant forms are included in the Appendix (7.3)

BOLD was also acquired using an SE-EPI sequence. Since the DW-fMRI sequence is based on an SE-sequence, this provides a comparison of the two methods which is unaffected by using the same sequence, only without the diffusion weighting but SE-BOLD gives lower signal and is not the method of choice for standard BOLD imaging. Additionally, GE BOLD is expected to be more affected by the draining pattern of vessels than SE-BOLD, as it is more affected by contributions of larger vessels. In fact, one simulation study showed SE-BOLD giving highly localised signals to activation, while GE-BOLD gave signals running from the layer of activity up towards the

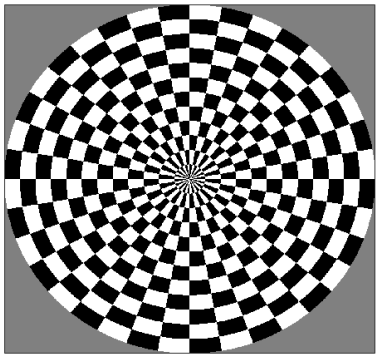

Figure 3.8: The visual stimulus used in the 3T study consisted of a radial checkerboard, flickering at 5 Hz. Between stimulus repeats the screen returns to grey.

surface, with each layers signal containing contributions originating in lower layers.[220] For SE-BOLD, the b-value was simply set to zero.

Diffusion measurements require strong gradients, and especially for functional sequences these are switched on and off rapidly. This can generate heat, the diffusion functional scans were therefore separated in the scan protocol by other scans.

3.1.10 Stimulus presentation

The fMRI study employed a visual stimulus in the form of a radial black-and-white checkerboard (Figure 3.8), flickering at 5 Hz. This was designed to correspond to the stimulus used in the study by Le Bihan *et al.*,[30] and a visual stimulus was chosen because it is a common activation paradigm with a well-known pathway and well-defined region of activation.

The stimulus was created in MATLAB and displayed using functionality provided by the Psychotoolbox (http://psychtoolbox.org/). The custom script is included in Appendix 7.1.6. The image was projected onto a screen visible to the participants within the scanner. The stimulus sequence was initiated by the scanner, which was set to produce a trigger pulse at the beginning of acquisition for each slice.

In the original study, the stimulation protocol (dartboard, 8Hz) consisted of 3 repeats of 20s (or 16s) stimulus and a 20s (or 24s) intervals. A few changes were made to the stimulus design of the original experiment. One was to increase the spacing between repeat stimuli blocks. If the spacing

time is too short, the signal may not fully return to baseline after each section. This might affect the dynamics of the following block, and the interval was therefore increased in an attempt to avoid this. The effect is explored in 3.2.6 below. Another change was the addition of a 60 second baseline before the first stimulus epoch. This was intended to provide a solid estimate of the intensity measured in the absence of stimulus, and help in interpreting whether the response has just been reduced, or fully relaxed back to baseline after the stimulus is switched off. Further repetitions were also added to enhance statistical power, with most experiments consisting of either 10 or 15 repetitions. This should reduce the impact of motion on the averaged response, and potential adaptation effects, which might cause the the response time course to change for later repeated measurements, as the subject becomes accustomed to the stimulus. In the human study the visual stimuli were kept relatively short compared to in the animal model, to reduce the time required for the volunteer in the scanner. Stimuli were therefore prepared with the aim of giving statistical robustness while also keeping overall experiment time within a reasonable duration.

3.1.11 Data collection

After an initial T2 localiser scan, a short DWfMRI setup scan was run to perform the necessary adjustments for the later diffusion functional imaging, including power calibration and shimming. By shimming prior to the functional scans, the functional sequence timings can be kept consistent and set to trigger the stimulus from the first acquired slice. The setup scan was set to acquire 10 slices over the visual cortex, and acted as a positional reference for the subsequent scans. The orientation of the slice packet is shown in Figure 3.9.

Structural scans were acquired using whole-brain isotropic T2-weighted imaging, with voxel size $1.0 \times 1.0 \times 1.0$ mm, FOV 256×256, 128 slices, TR=2500 ms, TE=564 ms, and variable flip angle. In addition, susceptibility weighted imaging (SWI) was performed in plane with the functional scans, with voxel size $0.8 \times 0.8 \times 2.5$ mm ($0.625 \times 0.625 \times 2.5$mm resolution), FOV 290×290, 10 slices and a distance factor of 20%, TR=28 ms, TE=20 ms, and flip angle 15. BOLD responses were collected using a GRE-EPI sequence, with voxel size $3.0 \times 3.0 \times 3.0$mm, base resolution 96, 10 slices, TR=1000 ms, TE=30 ms, FOV 290×290, multiband acceleration factor 2,

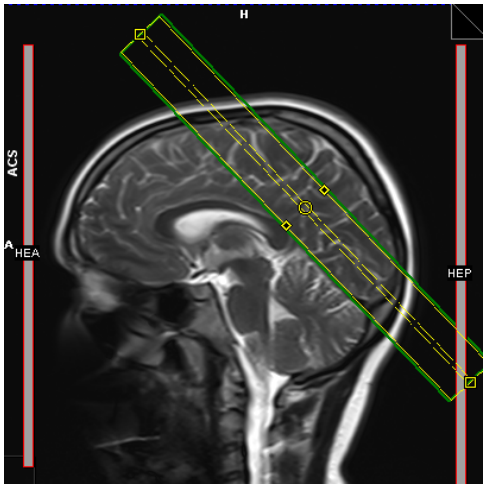

Figure 3.9: The location of the image slice packet, shown outlined in yellow, which is used for functional scans. The slices are positioned over the visual cortex, using the saggital image from the initial localiser scan as a reference. The adjustment volume is outlined in green.

flip angle 90.

DW-fMRI was measured using a monopolar diffusion weighted imaging sequence. To enable repeated measurements for functional imaging, the diffusion directions had to be defined using a table of vectors, with one vector for each repeat measurement, each vector containing values for the diffusion weighting to be used along each of the three main axes. These had to be created beforehand and loaded in to the program. For isotropic diffusion, the three values were all set to $\sqrt{1/3} \approx 0.5574$ to give a unit length vector, according to Equation 3.9. The diffusion weighting was specified by entering the b-value in the scan card.

$$\begin{aligned} |v| &= \sqrt{x^2 + y^2 + z^2} \\ |v| &= 1, x = y = z \\ 1 &= \sqrt{3 \cdot x^2} \\ x &= \sqrt{\frac{1^2}{3}} \end{aligned} \tag{3.9}$$

The functional diffusion sequence acquired an additional frame with b-value 0 s/mm^2 which was collected at the very start of the sequence. The stimulus was therefore adjusted for diffusion scans by adding one second (equal to one TR of 1000 ms) to the initial baseline. The extra frame included for

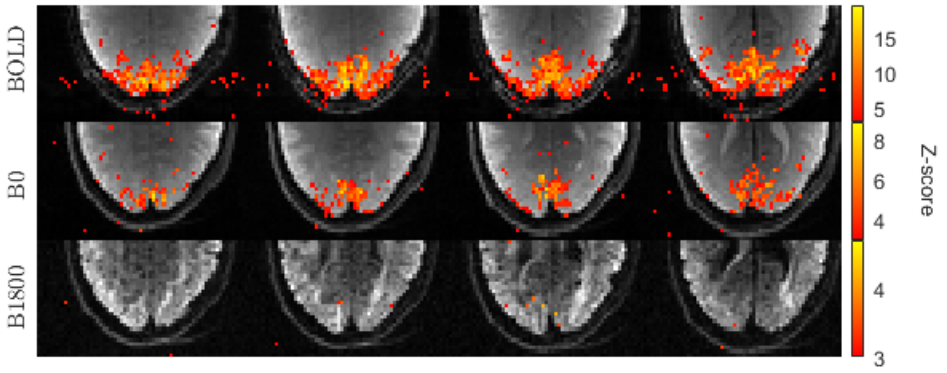

Figure 3.10: Activation maps from GLM analysis of the raw data, using a block stimulus as design matrix. The diffusion weighted data shows very little to no activation, and voxels within the visual cortex appear not to be significantly more correlated to the stimulus than voxels outside the head.

diffusion weighted sequences was later accounted for in analysis.

3.1.12 Detection of activated voxels

Activation maps were generated using GLM (detailed in Chapter 2), using a block representation of the stimulus. Figure 3.10 shows the raw activation maps for BOLD, DWfMRI (b=0) and DWfMRI (b=1800) for a representative set of measurements from the same participant. The DWfMRI data shows considerably smaller activation regions. Although a response can be extracted from the diffusion weighted data, it can be difficult to distinguish active voxels from noisy pixels which appear to correlate with the stimulus. Activation maps can be improved for example by using spatial smoothing, which is discussed later in this chapter.

In subsequent analysis, voxels were considered to be active if the Z-score was above a given cut-off value, and were typically thresholded to have a Z-score of at least 4 for BOLD and 2 for DWfMRI. The GLM results show voxels outside the head, which are clearly due to noise. To avoid these contributions to the signal, the activation maps were multiplied by a brain mask, which is 1 over the brain and 0 anywhere else, this can be made for example by thresholding the raw EPI data. To reduce the contributions of noise within the brain region, these selections were further limited to include only voxels within a cluster size of 3 or larger, which are more likely to represent an active region. These steps are demonstrated in Figure 3.11.

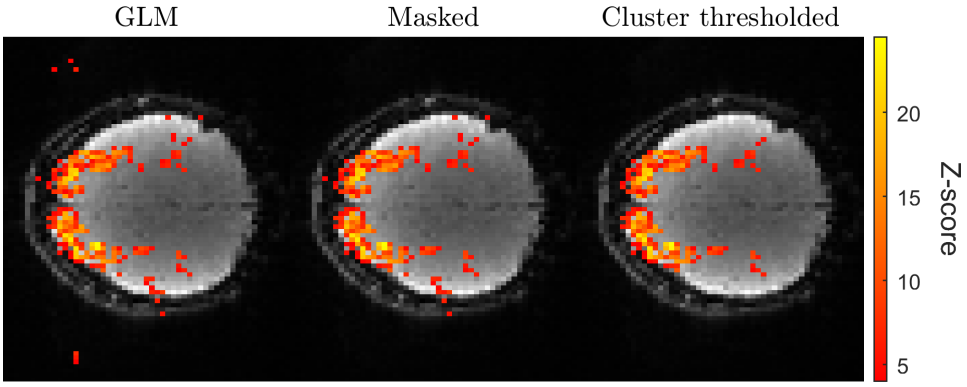

Figure 3.11: An example activation map from GLM analysis of the raw data, using a block stimulus as design matrix (left). The activation data can be masked to exclude data from outside the head, removing noise voxels (middle), and further filtered by minimum cluster size (right), here with removal of any voxels with fewer than 5 neighbours.

The signals were further averaged across the active voxels to extract the time series.

When performing GLM, the resulting Z-scores will reflect how well each voxel's time course correlates with the function representing the stimulus. The choice of this function could therefore determine which voxels are selected as active, influencing the average response extracted from the active region. For BOLD, the heamodynamic response function (HRF) is quite well characterised,[221] and can therefore be convolved with the stimulus train to create a GLM design matrix. This will be a closer match to the measured signal, and accounts for the delay in response onset after the stimulus is applied. For DWfMRI however, the diffusion response function (DRF) is poorly defined, and is expected to differ from the HRF. As this study investigates and compares these response time courses, a block representation was used, with the aim of avoiding bias from convolving with a response function. There are potential drawbacks to this approach. As the DRF is expected to have a more rapid onset, the DWfMRI signal might be more easily extracted than BOLD due to its greater similarity to the design matrix. The BOLD signal is of greater amplitude however, and with more active voxels than DWfMRI, so the average should still be representative. The square input function might also affect the shape of the responses obtained, enhancing the appearance of a rapid onset. The likelihood that this is a real feature would increase if the signal was averaged across a significant number of voxels. Such circularity could be especially affected by any spiking noise

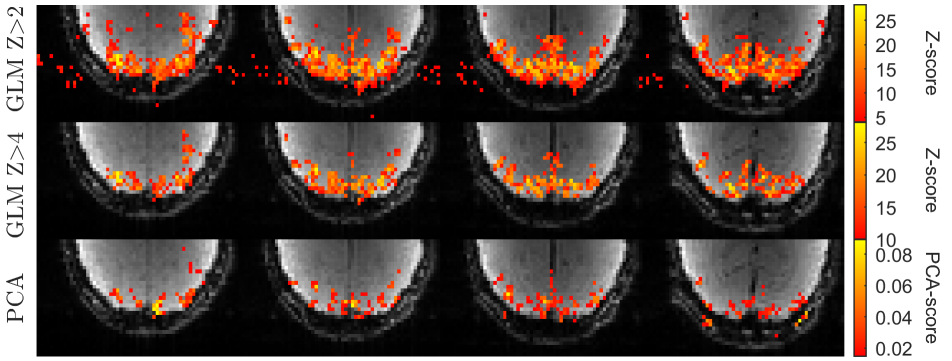

Figure 3.12: Activation maps produced from analysis of a BOLD experiment with GLM and PCA. GLM identifies more voxels as active than PCA, even for high Z-scores, and the activity is indicated in slightly different areas for the two methods.

which correlates to the stimulus onset. To mitigate this, time courses could be obtained by selecting only neighbouring active voxels, as these would be more likely to originate in a real activation.

To avoid assumptions about the response shape altogether, the data can also be processed by principal component analysis (PCA, detailed in Section 2). PCA can be used to generate activation maps and time series like GLM, but the time series is extracted without the need for a design matrix. Figure 3.12 shows a comparison of activation maps resulting from an example analysis with GLM and PCA. The GLM analysis yields significantly more activated voxels, which are reduced by thresholding the Z-score. At a high Z-score of 10 the region highlighted as active can be seen to differ between the two analysis methods. In Figure 3.13, the time course of the voxels selected by PCA analysis appears more noisy than that of GLM. Following from this, the mean response from GLM is smoother than that from PCA, even for the lower Z-score, and plateaus more evenly towards the peak. This could be effected by the square stimulus shape in the design matrix. GLM however gives a time series with peaks that more reliably follow the stimulus, and with a higher average amplitude. GLM was therefore used for the remainder of the analysis unless otherwise stated.

Another option for extracting a response shape from fMRI data is to use Independent component analysis, or ICA. ICA makes no assumptions about the response shape or stimulus design, but can be used to separate a multivariate signal into components. Unlike PCA, which aims to reduce the dimensions of the data by describing it in terms of its principal components,

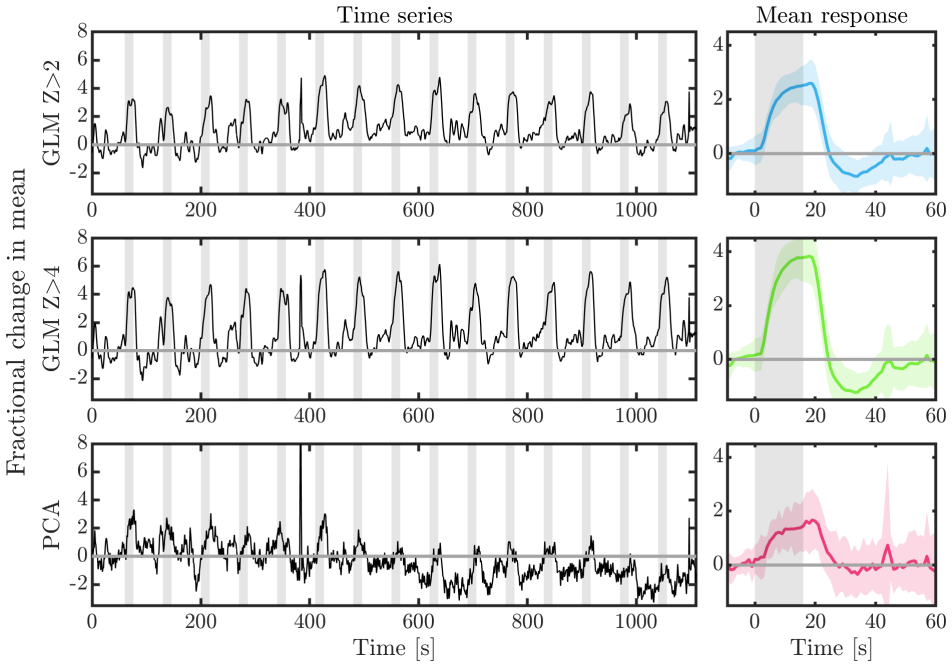

Figure 3.13: The time series (left) and mean responses (right) obtained from analysing the sample functional data using GLM and PCA. GLM provides a less noisy time course, with peaks that more reliably track the stimulus 'on'-periods, resulting in a less noisy mean response than PCA.

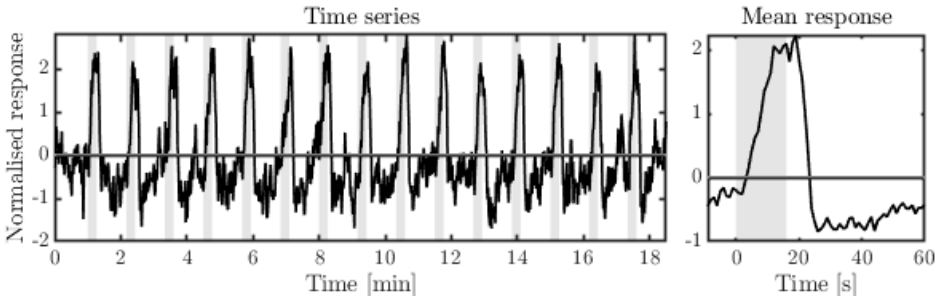

Figure 3.14: The time series of an example BOLD signal as determined using ICA. The method can be used to obtain a mean response function (right) without the requirement for assumptions about the stimulus.

ICA decomposes the data into statistically independent components, finding a maximally independent basis. ICA was performed on the BOLD and DWfMRI data using MELODIC from the FSL toolbox.[222] The results for a representative BOLD experiment is shown in Figure 3.14. Here, ICA produces a clear time course, and the mean response takes on a typical HRF shape.

Although the method works well for BOLD, the DWfMRI data shows no clear activation, this is demonstrated in Figure 3.15. The BOLD power spectrum shows a strong component at the repetition frequency of the stimulus as one would expect, with harmonic components present at multiples of this frequency. This could not be found in the DWfMRI (b=1800) data however. The figure shows an example power spectrum from the same participant acquired in the same session as the BOLD data, but no clear activation could be seen for any of the components extracted, or for any level of spatial smoothing (FWHM = 0, 4), even for participants showing strong BOLD activation with ICA. The activation maps also indicate only noise, even though the BOLD maps show activity localised to the visual regions. This disparity is likely due to the smaller signal magnitude and the greater relative noise of DWfMRI compared with BOLD. A potentially shorter and steeper response shape could also make the DWfMRI signal harder to detect by ICA, spanning fewer time points reducing statistical weight, and having greater resemblance to noise. A GLM-based signal extraction was therefore used for the functional data analysis.

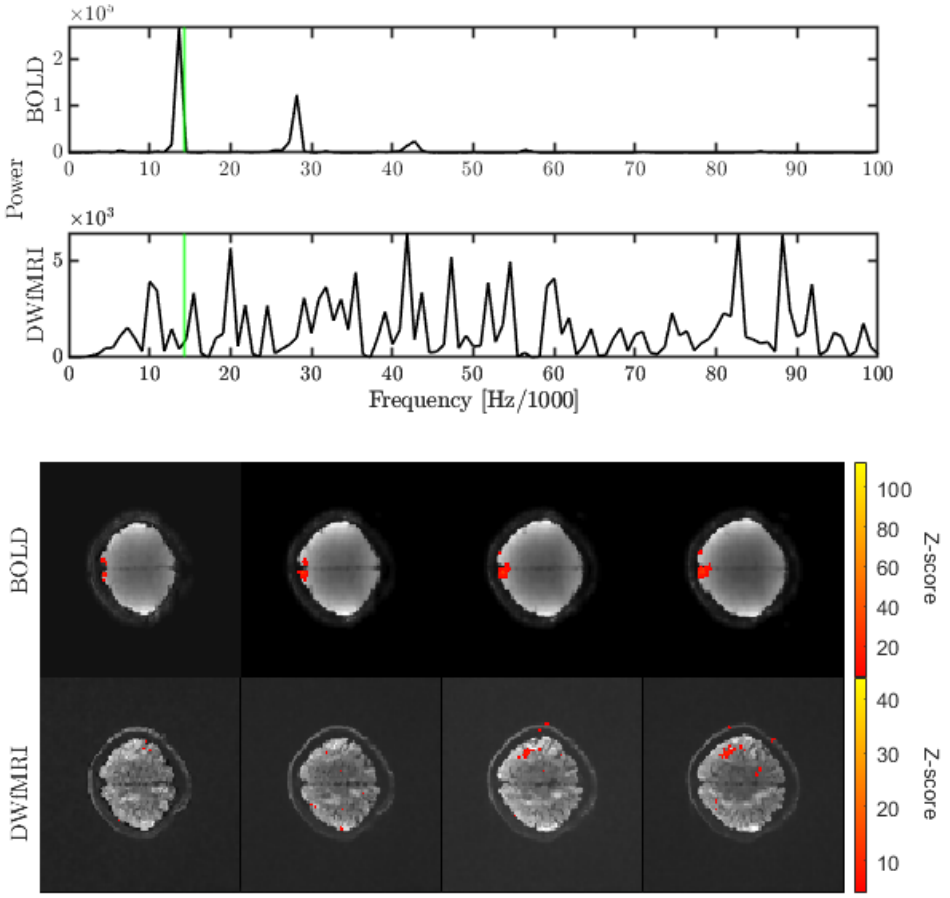

Figure 3.15: The power spectra obtained by independent component analysis of BOLD (above) and DWfMRI raw data (below). The repetition frequency of the stimulus (14.285 Hz/1000) is highlighted by the vertical bar in the power spectrum, where BOLD shows a strong component, while DWfMRI does not. The activation maps also show no signs of activation in DWfMRI, but locates the extracted BOLD signal to the visual regions.

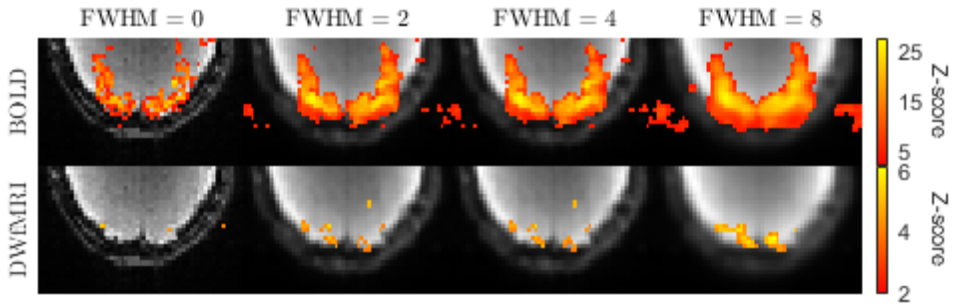

Figure 3.16: The effect of spatial smoothing with a Gaussian kernel of varying width (0, 2, 4 and 8 left to right) for BOLD (top) and DWfMRI data (bottom). For very wide kernels on the right, the area labeled as active bleeds over into areas without activity, such as the CSF and skull. Smoothing also has the effect of amplifying the larger areas of noise outside the head. For DWfMRI, smoothing brings out the very small regions of activation, which can otherwise be hard to distinguish from noise.

3.1.13 Spatial smoothing

Spatial smoothing was performed using a 3D Gaussian kernel of different values of FWHM (2, 4 and 8). The effect of the choice of kernel size on the images is shown in Figure 3.16. Without further processing, The data sets were analysed with GLM and thresholded to select voxels with a Z-score larger than 4. From the BOLD images, it is clear that for a very wide kernel, the area considered activated by this approach bleeds out to include areas which are not activated, as voxels are highlighted over the CSF. Similarly, noisy pixels which are located outside the head in this data set, are extended. For the DWfMRI data set, smoothing appears to have the effect of bringing out narrow active regions that might not be easily identified otherwise. As the signals are expected to be more highly localised compared with BOLD, smoothing could be especially beneficial in exposing such activity. In fact, in the absence of smoothing, 'active' voxels appear quite similar to noise pixels.

The time courses extracted for the smoothed data sets are shown in Figure 3.17. For both measurement methods, spatial smoothing has the effect of reducing signal intensity. This could be explained by the inclusion of more nearby voxels with a lower Z-score, which reduces the average signal. The overall shape of the signal is however largely maintained. For the DWfMRI data set, the response appears to be less noisy after smoothing.

For the following analysis, spatial smoothing was applied with a kernel

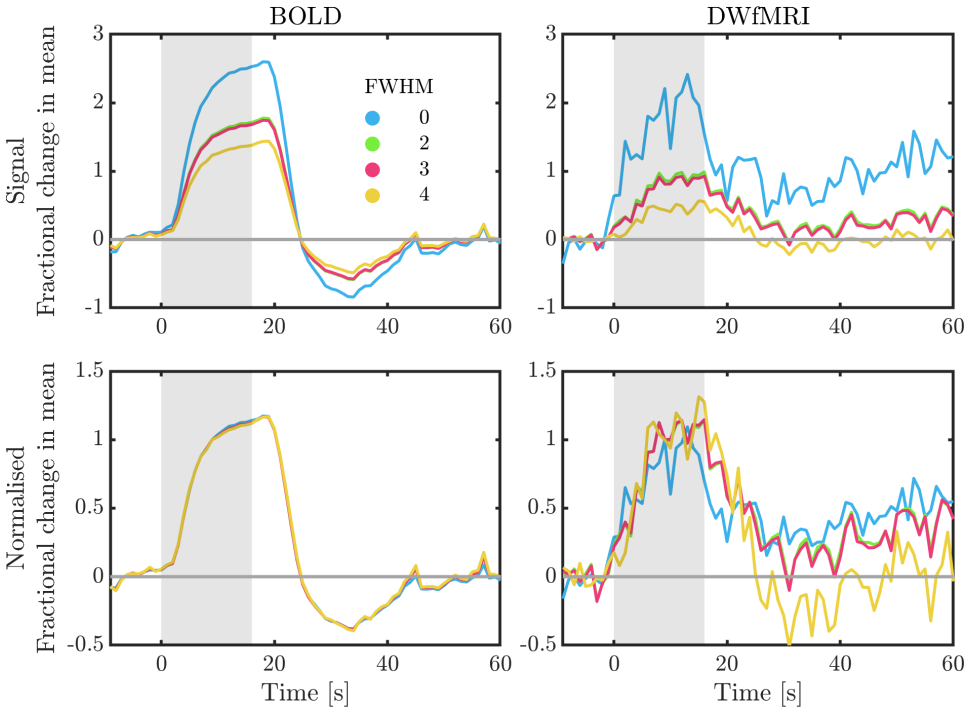

Figure 3.17: Time courses obtained from BOLD (left) and DWfMRI functional data (right) after smoothing with Gaussian kernels of differing FWHM. The responses were extracted from the same set of voxels, namely those labelled as active by the FWHM = 4 case for the given sequence. For each smoothing level, these voxels were thresholded to include those with a Z-score of at least 3.

size of 2 FWHM. This was considered beneficial particularly for the purposes of bringing out the DWfMRI response, as this was often weak, and not easily identified in activation maps otherwise. This should increase confidence in the statistical significance of the voxels identified as activated.

Spatial smoothing should be considered carefully for the purposes of comparing the time courses of the two responses. In some cases the rapid onset became less apparent at larger kernel size.

3.1.14 Temporal filtering

The data was subjected to frequency filtering to reduce the effects of motion on the time series. A Butterworth high-pass filter was used to remove the low-frequency component of the full time series. The filter, with a cutoff frequency of 0.009 rad/s and order 6, was used in all subsequent analysis. The cutoff frequency was chosen to be significantly lower than the repetition time of the stimulus, in order to avoid affecting with the functional

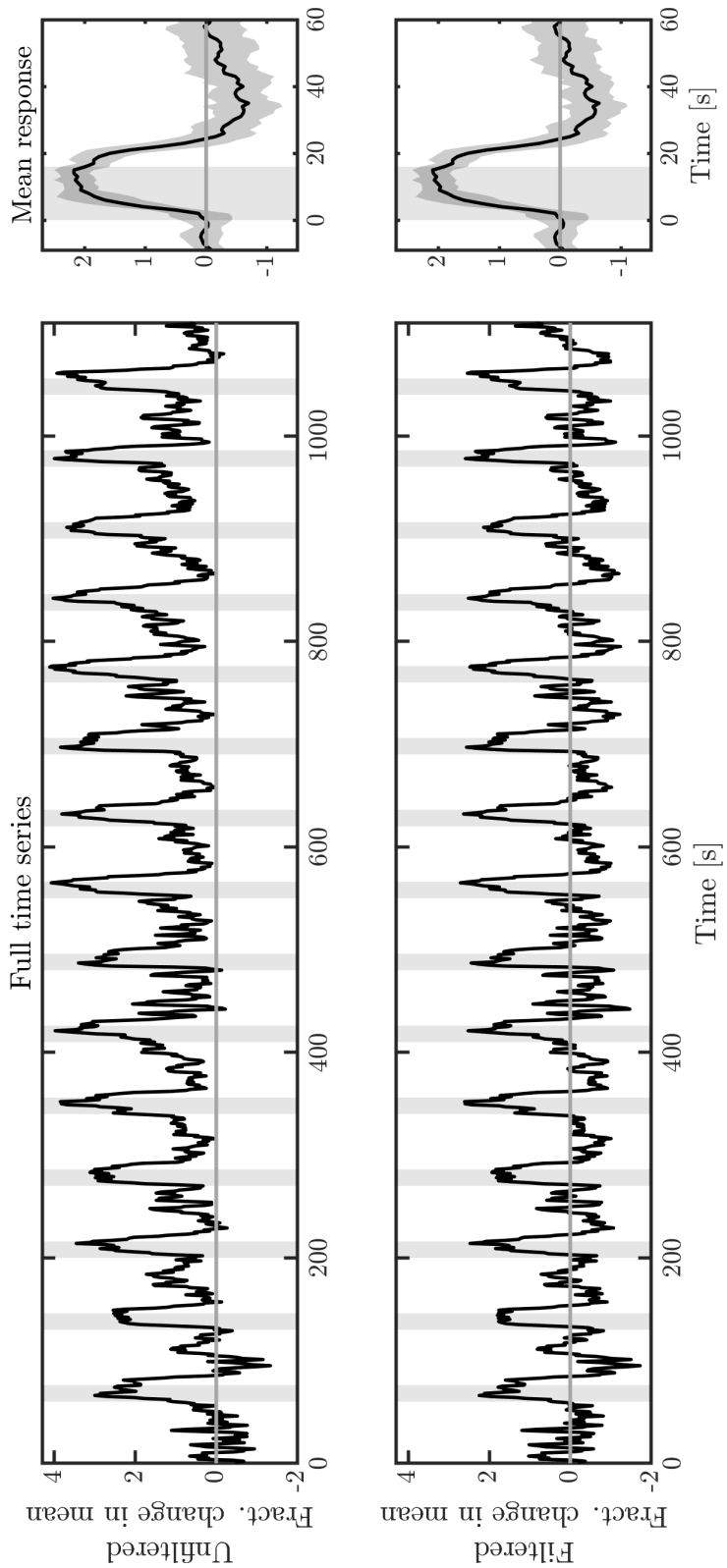

Figure 3.18: An example of the effect of the frequency filtering, with the raw signal above, and the filtered signal below, aligning more consistently with the baseline.

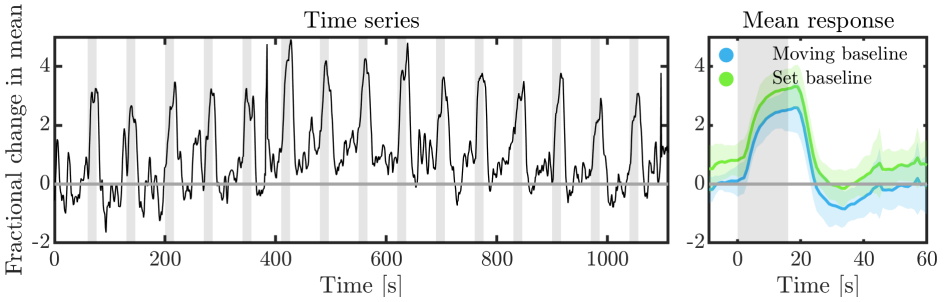

Figure 3.19: Baseline correction using a mean baseline from the initial 60 second delay, and using a moving baseline averaged across the 10 seconds of data points immediately preceding each stimulus trial. By accounting for a slowly drifting signal, the average response begins more reliably follows the expected onset from and return to baseline.

response. A representative example of a filtered time series is shown in Figure 3.18. The overall low-frequency drift within the signal is removed, while the higher frequency changes coinciding with the activation of the stimulus are maintained.

Because the response shape was of significant interest, no low-pass filtering was applied to the time series, as this would could reduce the slope of the onset. The effect of any remaining baseline drift can be countered by using a moving window to calculate the baseline at the relevant point in the time series. For a repeated stimulus, the response to each trial can be determined based on the change relative to the signal in the preceding few seconds. This is demonstrated in Figure 3.19. The example data shows a slow drift in signal, likely due to participant motion. Here, the initial 60 second delay contains some noise, which could affect an estimate of the mean. The 10 seconds prior to each trial are used as a baseline, in an attempt to include enough points for a reasonable mean value, but to avoid including data from the tail-end of the previous response. As can be seen from the figure, using a moving baseline leads to the mean response more closely following the x-axis prior to stimulus onset, and returning to it after relaxation, as one would expect. A moving baseline was therefore used in the subsequent analysis.

The averaged response from repeated stimuli can be further smoothed out using a Savitzky-Golay filter. This involves applying a successive polynomial fitting over a moving window of adjacent data points, with the goal of smoothing the data while maintaining its overall shape. This was applied only if stated, and was set to have order 2 and frame length 5.

3.2 Results

Initial experiments were conducted to ensure the DWfMRI signal could be detected, and parameters were adjusted to improve the measurement. Changes made to hardware configuration and sequence modifications are outlined below. After testing the effect of these parameters, the sequence and was selected and kept for the remaining experiments. Further optimisations might be possible, but the sequence was accepted for the current purposes due to time constraints and considerations of ethical and efficient use of participant time. The data from the remainder of experiments were pre-processed using methods as outlined above, with the various parameters varied to determine their effect on the results. Pre-processing included spatial smoothing with FWHM = 2, and frequency filtering with fc = 0.009, unless otherwise stated.

3.2.1 Hardware

The first 9 sets of experiments were conducted using a 64-channel head coil. The diffusion weighted data appeared not to show much activation, so a 32-channel coil was tested instead. Figure 3.20 shows a comparison of a few examples of the activation maps determined using the two coils. The 32-channel coil appears to show more activation in the DWfMRI data, which is an important factor as there are so few active voxels with this method. The 64-channel coil appears to give more artifact in the DWfMRI images, with show a streak of brighter voxels crossing the left hemisphere, which is not as apparent in the 32-channel data. The 32-channel coil also seemed to provide clearer, more consistent response time courses for DWfMRI, which are shown in Figure 3.21. Following these tests the 32-channel coil was considered a better choice for the purposes of the study, and was used for all subsequent experiments. The impact of coil choice specifically on fMRI has been investigated in the literature, with differences observed dependent on cortical depth,[223] and on brain region,[224] as well as having different effects on tSNR loss observed due to acceleration.[225]

3.2.2 Sequence design

The first two participants were scanned using an available diffusion weighted scan protocol based on a bipolar sequence. The data showed little to no acti-

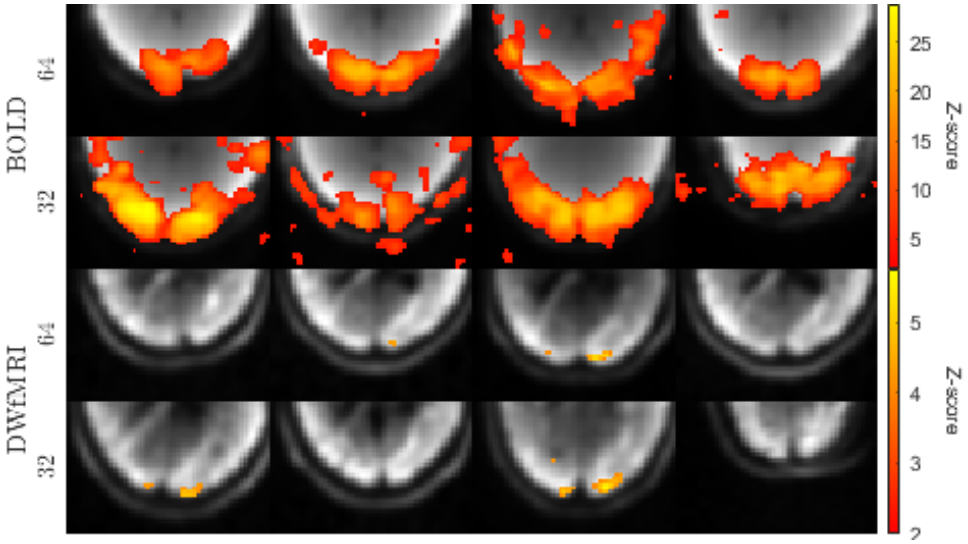

Figure 3.20: Comparison between BOLD (above) and DWfMRI activation maps (below) from a 16 second stimulus using a 64-channel head coil (top) or a 32-channel head coil (bottom). The example data sets have been pre-processed in the same way ($FWHM = 8$, $fc = 0.009$), and the activated voxels determined with GLM using a block-design. Data acquired with the 32-channel head coil yielded a higher number of active voxels. The 64-channel coil appeared to produce more artefacts in the DWfMRI images than the 32-channel coil.

vation as shown in Figure 3.22. For the next participants, this was exchanged for a monopolar sequence. With the same stimulus design, with 16 second stimuli with 24 second spacing, the monopolar data showed similar results. The monopolar images appeared to be of higher quality visually, and this sequence was carried forward for subsequent scans. The key consideration however, was that it allows the TE to be shorter.

3.2.3 The effect of the b-value

The majority of DWfMRI experiments used a b-value of $1800 s/mm^2$, to correspond to the original Le Bihan study.[30] Data was also collected at different b-values, (0, 600, 1200 and 1500 s/mm^2) to demonstrate the effect the degree of diffusion weighting has on the response shape. A greater degree of diffusion weighting has been suggested to 'filter out' the haemodynamic effects from the signal,[30] so the higher values were expected to reduce the influence of the slower plateau effect after the response peak, and the time course tend from resembling the b = 0 s/mm^2 response towards the shape of the response observed using b = 1800 s/mm^2. The average

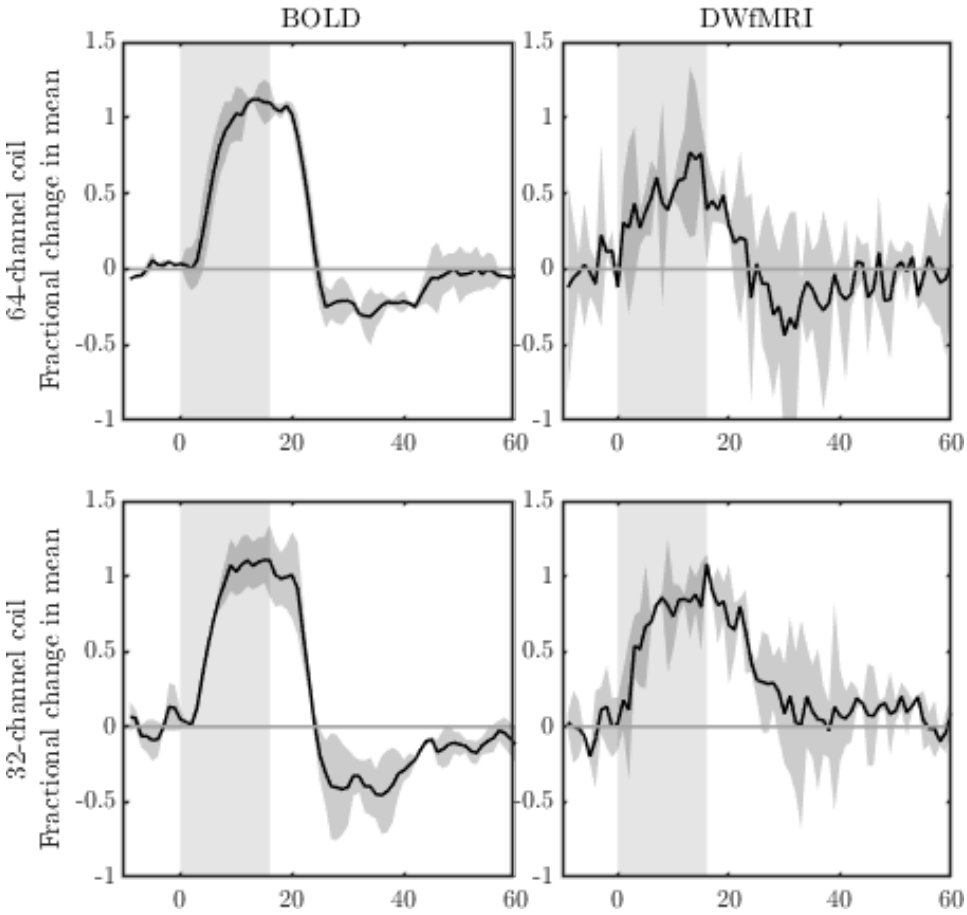

Figure 3.21: The responses collected with BOLD (left) and DWfMRI (right) using the 64-channel (above) and 32-channel coil (below). The 32-channel DWfMRI data appears less noisy, as expected from the higher number of activated voxels, as shown in Figure 3.20.

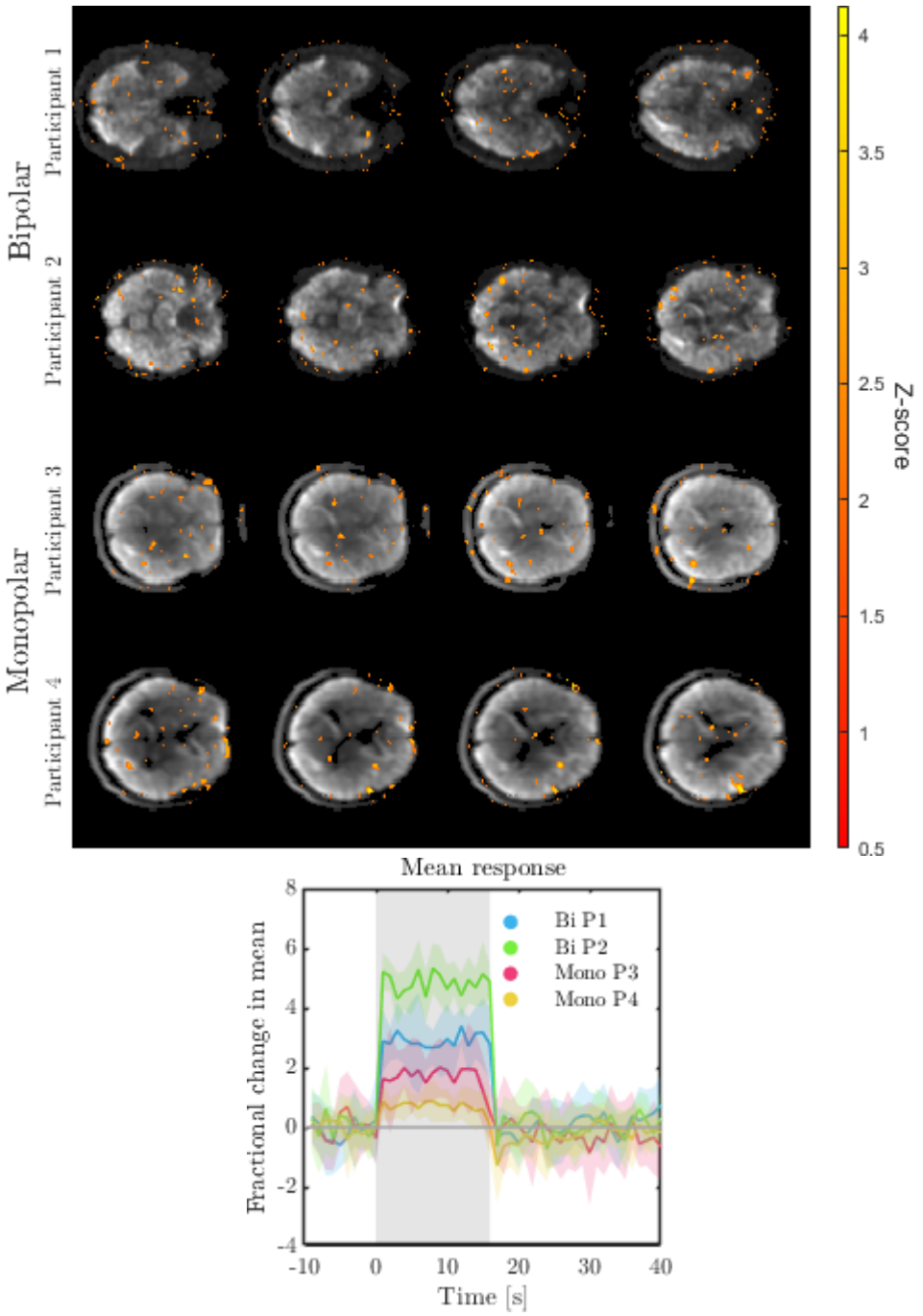

Figure 3.22: DWfMRI b=1800 s/mm^2 activation maps acquired during a visual stimulus with 'on' and 'off' timings 16 and 24 s respectively, using a bipolar (above) and monopolar (below) sequence. The maps show very few voxels labelled as activated, even after spatial smoothing with FWHM = 4, and these voxels are due to noise remote from the visual regions. The signals averaged across trials appear square, with no sign of a response in the noise, and the results are similar across participants.

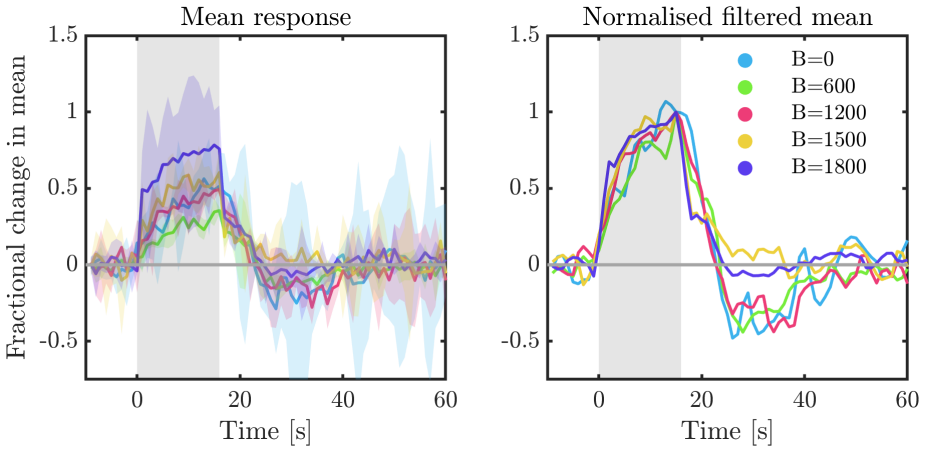

Figure 3.23: Diffusion Weighted fMRI was performed using a range of b-values (0, 600, 1200, 1500 and 1800 s/mm^2). The average responses are shown with shaded errors (left), with larger errors for the b=1800 case. Larger b-values are expected to give lower SNR. The normalised mean responses differ most significantly in the return to baseline, with the appearance of a post-stimulus dip for b=0 and up until b=1200, which is not present for the higher diffusion weightings. The onset appears to become slightly steeper with higher b-values in line with reports in the literature, a trend which is promoted by the application of temporal filtering (right).

responses collected using different b-values are shown in Figure 3.23. The slope of the onset does appear to become steeper with stronger diffusion weighting, however the effect is less marked than in the results reported by Le Bihan et al.. The increase in b-value has a significant effect on the post-stimulus undershoot however. This could be due to a filtering out of a part of the haemodynamic response as suggested, as the return to baseline is more rapid as expected from a fast cellular mechanism. The response is less weighted by the undershoot, which has been linked to an excess of deoxy-hemoglobin.[226] It might however be explained by an arterial origin, with the diffusion weighting removing sensitivity to large draining veins.

3.2.4 Functional response time course

Figure 3.24 shows the average functional responses obtained with the BOLD and DWfMRI ($0s/mm^2$, $1800s/mm^2$) sequences for a 16 second stimulus. The data sets have been spatially smoothed (FWHM=2) and frequency filtered. In accordance with the original study, the diffusion weighted signal shows a rapid onset relative to BOLD, as well as a a reduced appearance of post-stimulus undershoot.

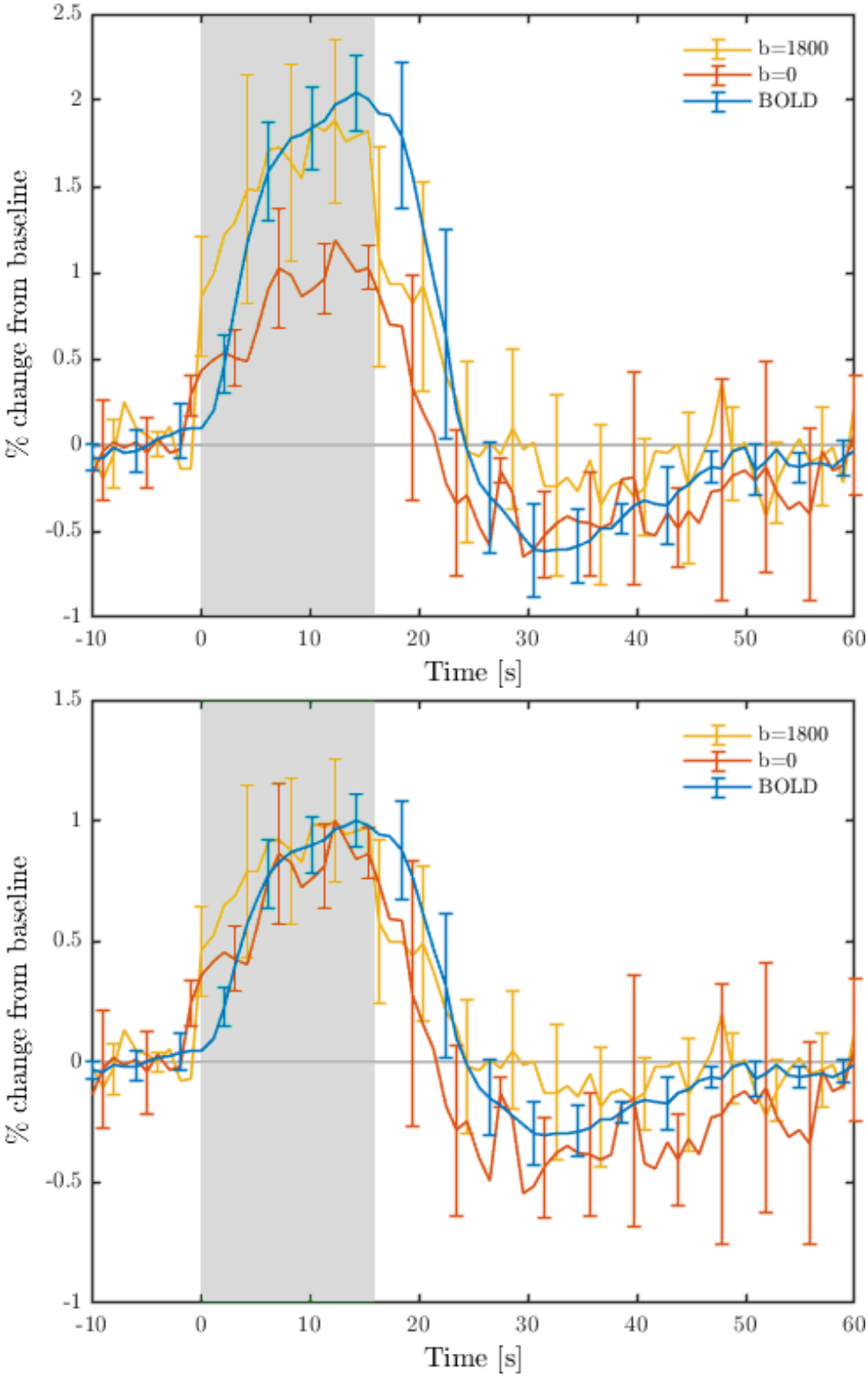

Figure 3.24: The mean responses across 10 stimulus repetitions, averaged across participants for BOLD, and DWfMRI $b = 0s/mm^2$ and $b = 1800s/mm^2$ (N = [5,6,6]). The normalised responses are shown below, and the 16 second stimulus 'on' duration indicated in grey.

3.2.5 Temporal offset

As an indicator of the temporal offset between the DWfMRI and BOLD time series, the responses averaged across participants were compared by shifting the former relative to the latter. For each offset, the normalised root-mean-squares (nRMS) of the two time series x(t) and y(t) was calculated using Equation 3.10, where $\bar{y}$ is the mean of the measured data.

$$RMS = \sqrt{\frac{\sum_{t=1} T(x_t - y_t)^2}{T}} \qquad nRMS = \frac{RMS}{\bar{y}} \tag{3.10}$$

The nRMS is plotted against offset in Figure 3.25. The error is minimised for a 2 second offset. This indicates the b=1800 diffusion response preceeds BOLD as expected from Le Bihan et al.,[30] however their results show an offset closer to 4 seconds. Their results also show that for b=0 and BOLD, nRMS is minimised for the case with no offset, meaning there is approximately no delay between these two time series. This is not the case for the data plotted in the right panel of Figure 3.25. Here there appears to be an offset similar to that of b=1800. This is reflected in the b=0 time courses in Figure 3.24, where the b=0 curve shows a smaller shoulder on the stimulus onset.

3.2.6 Interstimulus spacing

As can be seen in Figure 3.24, the BOLD response to the visual stimulus takes close to a minute to relax back to baseline. Here, the interval between stimuli repeats was chosen to allow the biological response enough time to play out and for the signal to return to baseline. By repeating the stimulus more frequently than this, a later response is likely to be influenced by the tail effects of its predecessor. After the stimulus, the vessels have become dilated to allow the oxygenated blood to flow towards the active site. Pre-dilated vessels could allow the hemodynamic changes to progress more rapidly. DWfMRI shows less post-stimulus undershoot, and if it is largely or in part driven by cellular rather than hemodynamic changes, frequent repeats might not affect the response curve in the same way it would BOLD. However, any vascular effects might contribute to the observed rapid onset. The Le Bihan study, as well as others,[137,161,227] have employed such shorter

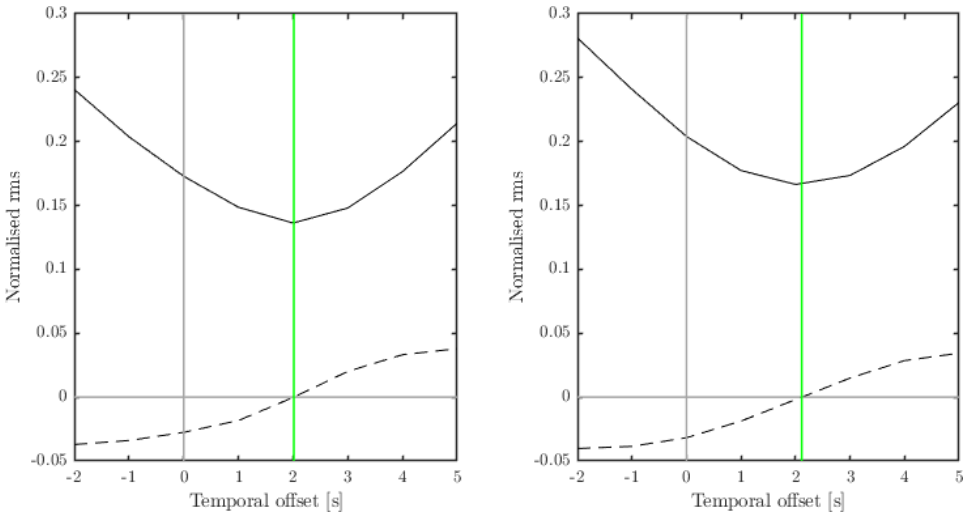

Figure 3.25: The normalised RMS for different offsets of the DWfMRI time series (b=1800 on the left and b=0 on the right) averaged across participants relative to the average BOLD response. For b=1800 the derivative of the nRMS (dashed line) crosses zero at 2.015 s, indicating the approximate relative delay of the BOLD response.

(< 60s) intervals. A benefit of this is that more repeats can be performed without requiring long scan times, and long intervals have been suggested to increase the chance of other cognitive processes confounding the measurements.[228] To investigate the effect of inter-stimulus interval (ISI), the experiment was repeated with a shorter spacing of 24 seconds.

Average responses from the 16 second stimulus with short and long ISI are shown in Figure 3.26. With a shorter stimulus interval, an early signal increase appears in the BOLD response, similar to the rapid onset reported for DWfMRI in the literature. If the driving mechanism for the response is assumed to be equal for the short ISI to that measured with the longer stimulus spacing, this indicates that the later responses are affected by an unrelaxed starting condition. The larger error bars seen for the short ISI data are likely influenced by a smaller sample size, but could be an indication the response is less regular. Unlike BOLD, the DWfMRI response maintains the rapid onset even when the stimulus spacing is long, clearly showing early activation, and a faster return to baseline. This appears in agreement with a different mechanistic sensitivity between the two methods. Notably, the short stimulus spacing appears to exaggerate the onset, indicating DWfMRI too is affected by the unrelaxed conditions, which would indicate a dependence on hemodynamic effects linked to pre-dilated vessels.

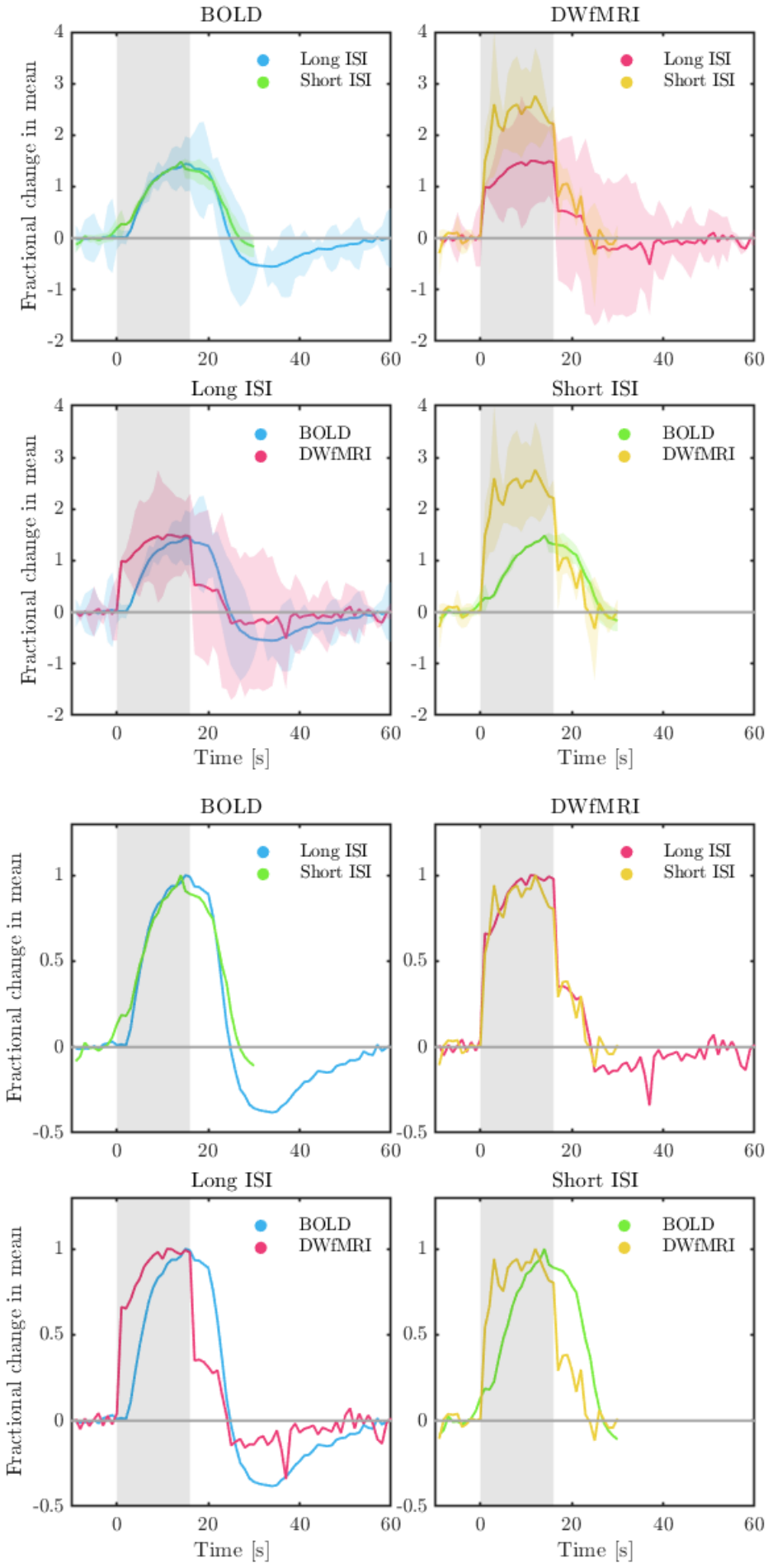

Figure 3.26: Comparison of GRE-BOLD and DWfMRI (b=1800) averaged across participants (above) and normalised (below), for different inter-stimulus intervals, with long ISI: (16s 'on' + 54s off, BOLD: N = 16, DWfMRI: N = 11) and short ISI (16s on + 24s off, BOLD: N = 6, DWfMRI: N = 9). All experiments are averaged across 15 stimulus repetitions. Shaded areas indicate the on duration of the stimulus.

3.2.7 Stimulus duration

Data was acquired using different stimulus durations of 16, 8, 4 and 2 seconds. This was done to investigate the stimulus shape's dependency on the stimulus duration, and to look for differences in this dependency between BOLD and DWfMRI. The slow effects of hemodynamic changes was expected to affect BOLD response shape more for stimuli over a couple of seconds, while DWfMRI should be less affected if hemodynamics plays a smaller role.

Simple GLM with a block design stimulus provided very few activated voxels for the short stimuli (<= 4 seconds). With Z-scores of 4, 3 or even 2, the voxels highlighted clearly corresponded to noise, being located both remote from the visual cortex and also outside the head, and giving temporal responses with a very sharp box-like shape. Lowering the Z-score to 0.5 the responses took on a more plausible shape, but activation maps highlighted the entire dataset without noticeable activation specific to the visual areas.

In order to improve the maps and voxel selection, tests were performed with a wider block stimulus shape as the design matrix. The stimulus was also jittered, this involved adding a small delay (1-3 seconds) to the stimulus train, so that each repeated 'on' period of the design matrix occurs slightly after the corresponding experimental stimulus onset. This should have better resemblance to the response shape and timing of the BOLD response as determined by the previous experiments. Figure 3.27 shows the activation maps of BOLD and DWfMRI data for a stimulus of 4 second duration, determined using varying width and jitter. For the BOLD data, the activation of the visual regions becomes more prominent with increased jitter delay, which is to be expected from the slow rise to peak. Increasing the width is also beneficial. For DWfMRI, a longer jitter time reduces the number of active voxels, but an increased width of the stimulus improves the maps.

Time series were extracted from the data using the design matrix which gave the best activation maps, determined by giving the greatest activation in the visual region: J = 3, W = 2 for BOLD, and J = 1, W = 3 for DWfMRI. The responses are shown in Figure 3.28. The BOLD responses all show a plateau after stimulus end, with the width of this plateau increasing for the longer stimuli. The DWfMRI signal relaxes more rapidly towards the baseline however, with signal intensity declining sharply right after the stimulus 'on' period. For these measurements, the longer the duration of

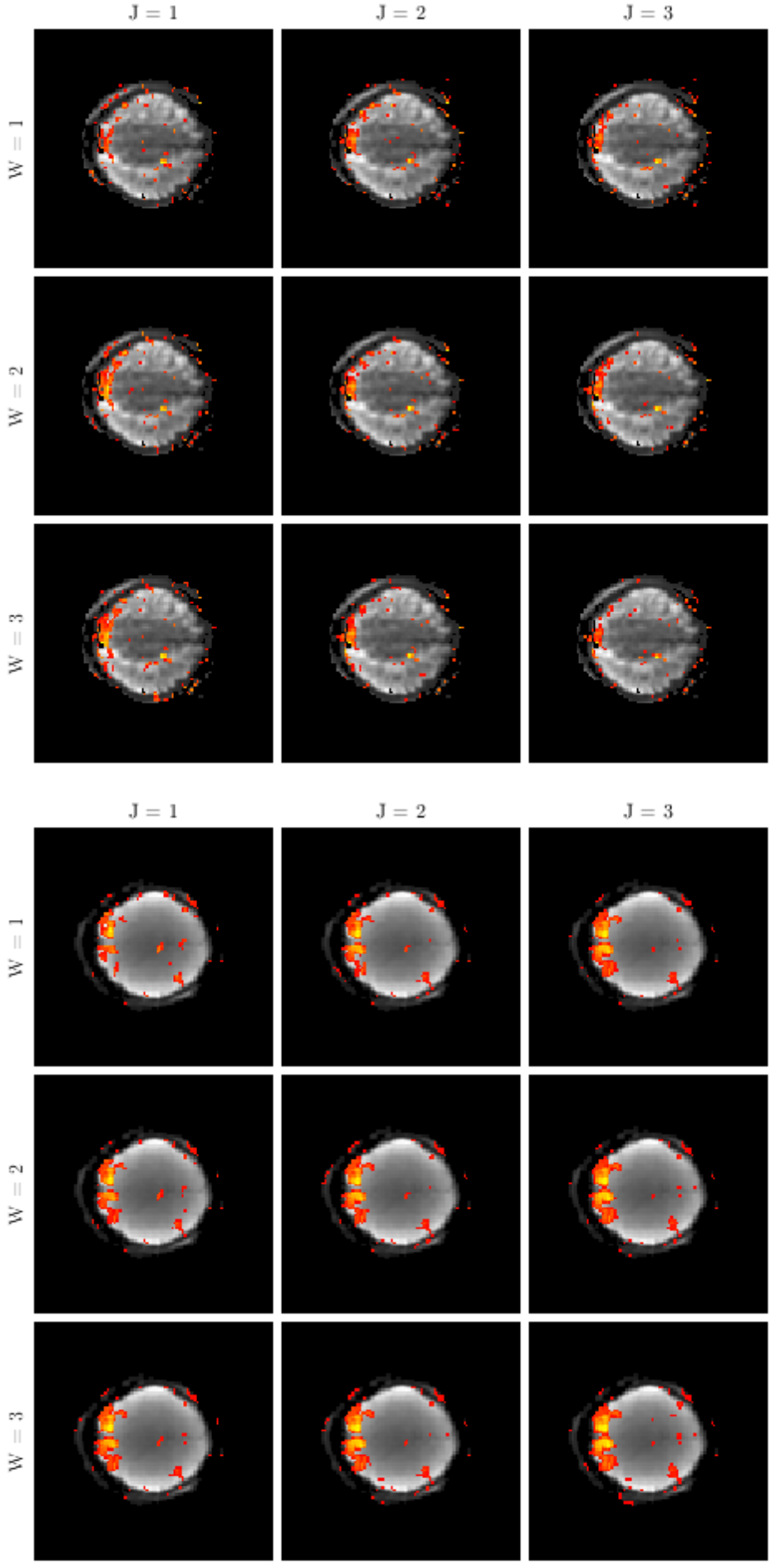

Figure 3.27: Activation maps from a 4 second stimulus acquired using both DWfMRI (above) and BOLD (below) in the same participant (Z = 2). The maps were generated using a design matrix with different jitter delays ($J[s]$) and with extended block widths ($W[s]$).

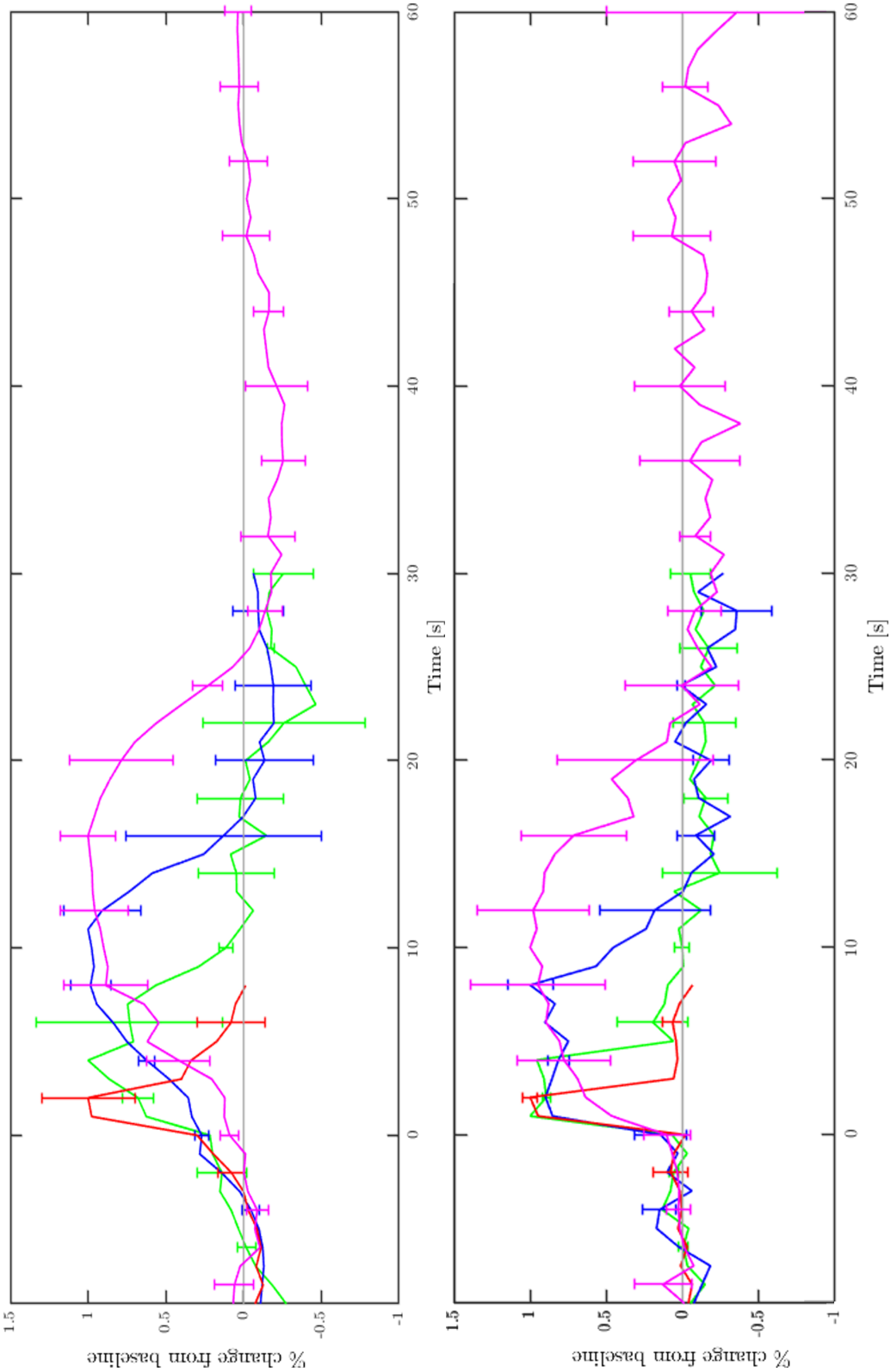

Figure 3.28: BOLD (above) and DWfMRI (below) responses for different stimulus durations of 2, 4, 8 and 16 seconds. The BOLD responses maintain a plateau after stimulus end, which is more pronounced for the longer stimuli, while DWfMRI relaxes more rapidly towards the baseline.

the stimulus, the slower this return to baseline becomes. This mirrors the BOLD behaviour, supporting a hemodynamic contribution also in DWfMRI. Notably, even long duration stimuli do not produce the post-stimulus undershoot in DWfMRI.

3.2.8 Susceptibility weighted imaging

Susceptibility weighted images (SWI) provides a map of magnetic susceptibility differences in tissue.[229] In the clinic, this can be used to detect deoxygenated blood, as well as ferritin and calcium, and to detect levels of iron in the brain, which can provide very useful information on neurological disorders such as multiple sclerosis, stroke, trauma and tumors, as well as ageing.[229] SWI can be used to map out blood vessels, which can be used to spatially correlate the functional responses with the vessel structure.

Susceptibility weighted images were acquired in plane with the functional scans, with more slices so that the functional data lay fully within the region spanned by the images. After acquisition the data is automatically pre-processed, generating an additional output data set in the form of a Minimum Intensity Projection (mIP) map. These maps are used in the clinic to better visualise the veins. The 17 mIP images were generated by considering a rolling window of 7 of the 24 SWI slices at a time, and determining the minimum intensities across each set.

In order to correlate values from the functional data sets and the structural MIP data set, the EPI data was transformed into the coordinate system of the MIP data. Since the SWI and EPI data is acquired in the same position and orientation, this could be achieved by accounting for the voxel size and image dimensions to create a set of coordinates for each of the two data sets, and interpolating the data from one to the other in 3D. Figure 3.29 shows the correlation of the images after processing.

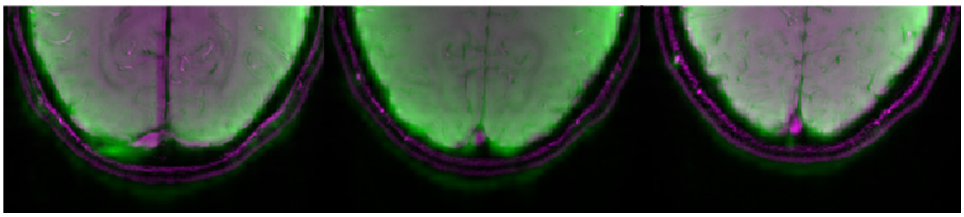

Figure 3.29: The correlation between transformed EPI (green) and SWI images (purple).

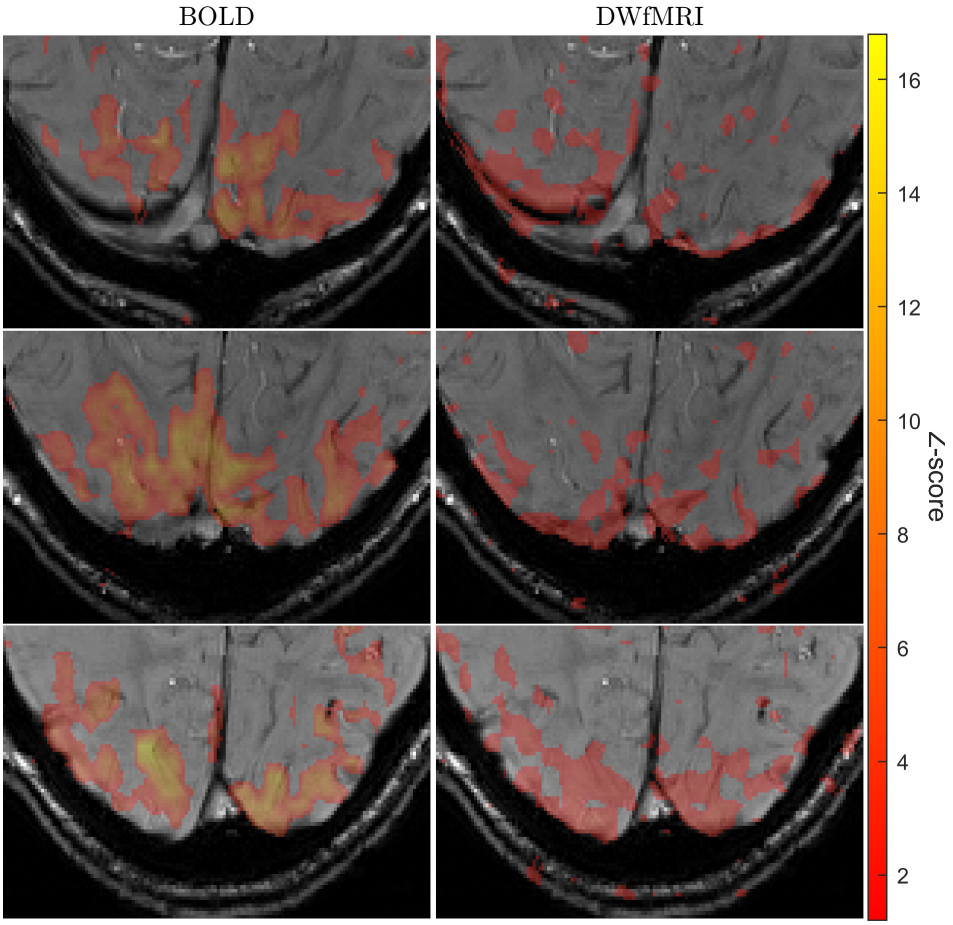

Figure 3.30: The MIP images from three central slices, with the BOLD and DWfMRI (b=1800 s/mm^2) activation maps from a 16 second stimulus overlaid. The DWfMRI activation covers a smaller region, has overall lower Z-scores, and appears to occur closer to the surface.

Figure 3.30 shows the MIP images from three central slices over the visual cortex, with the activation maps from BOLD and DWfMRI (b=1800 s/mm^2) overlaid. The active regions differ visibly between the two methods, with the diffusion weighted response here occurring closer to the surface. This could be indicative of a regionally and biologically differing driving force behind the measured response, however DWfMRI activation near the surface could still be related to the large structures of vasculature present there. The greater area of activation in BOLD is in line with expectations from the literature.

3.3 Discussion

DWfMRI showed overall poorer sensitivity than BOLD, and this represented a challenge in processing. The smaller signal amplitude and presence of noise should be considered in analysis, and care taken not to lose the signal (or induce one) by applying the same conditions as used for BOLD processing. The responses obtained with diffusion weighting were markedly different from standard BOLD, and changes such as a reduction in the post-stimulus dip were apparent also when moving from a b=0 measurement to b=1800, indicating this was diffusion-related and not explainable by the different sequences alone.

Perhaps the most notable results in this chapter are the relatively rapid onsets observed of DWfMRI signals relative to BOLD. Although the larger contributions of noise in diffusion measurements complicates the analysis somewhat, the discrepancies in onset between methods appears reproducible. These experiments also confirmed that the stimulus design could have a significant effect on the response shape. A short inter-stimulus interval of $< 54s$ did cause an appearance of rapid onset in the BOLD data, which was not present for stimuli with longer intervals, however the rapid onset persisted in DWfMRI also when the response was given sufficient time to relax.

Certain barriers remain to researching DWfMRI. The built-in diffusion weighted sequences on a standard scanner are not currently designed for functional imaging, and so set-up for this takes time. Here, a structural sequence had to be used for functional imaging by creating an external file and loading this into the software. There were also limited options available in the settings, which only allowed for changing the b-value and not the sequence timings, which extended the gradient pulses into the TE. Acquiring a suitable sequence and implementing it could be a multi-step process with ethical and administrative requirements, and might require technical expertise beyond standard operator qualifications. The lack of standards in sequence design also means that the method might vary quite significantly between research groups. In the literature the descriptions are also often limited to only reporting the b-value used and not the full timings of the sequence. As explained in this chapter, this leaves room for interpretation, as the same b-value might be produced with different gradient pulse timings. This affects reproducibility, and might lead different groups to report

different observations for the same experimental protocol.

Unlike the 7T scanner, on the 3T scanner is intended for use on humans, which imposes extensive additional safety measures and restricts access to hardware. It was therefore not an option to connect to directly monitor the hardware, for example with the CED, to further monitor the acquisition timings. Custom sequences to be installed on the scanner have to be obtained from recognised sources and pre-approved for use in a clinical context, as part of safety measures put in place to ensure participant and equipment safety. This means there are limited options to adjust sequences for testing purposes. In fact, it can be difficult to determine the exact behaviour of a sequence. The sequence operations are described in documentation, but insight into the scripts themselves are limited, with the inclusion of proprietary code. As such sequences can be purpose-built for specific applications, there is a risk that these have been optimised in ways that are detrimental for use in other contexts, and some care should be taken to ensure the sequence for example does not include unwanted filtering.

4 Light transport modelling

OIS and SFDI both require a forward model of light propagation within tissue in order to interpret the collected data. In OIS, Beer-Lambert law estimation of chromophore concentrations requires an estimate of the path length light has travelled before being remitted back from the tissue and captured by the camera, and the absorption will be wavelength dependent. SFDI requires a pre-calculated look-up table to determine the contributions of absorption and scattering from diffuse reflectance measurements. In both cases a well-defined model is needed to determine the diffuse reflectance for given tissue optical properties.

Properties of photon transport in tissues can alternatively be estimated analytically using radiative transfer theory, however this is complicated to solve without approximations. The diffusion approximation of radiative transfer can be used to determine diffuse reflectance,[230] however it has drawbacks. The diffusion approximation is typically less accurate with an increase in absorption coefficient and with a decrease in scattering coefficient.[231] Several tissues have albedos within this lower range, which means the accuracy of the approximation could be questioned.[232] It also breaks down close to the radiation source.[233] For the applications in this thesis, it is therefore necessary to build a forward model for determining diffuse reflectance. This can be achieved with a Monte Carlo simulation of light transport through the tissue.[234]

This chapter introduces the optical properties of tissues which impact on photon traversal through them, and outlines the simulation of this light transport and some results this can provide.

4.1 Tissue optical properties

The way in which light interacts with a medium is dependent on the medium's optical properties. These properties include absorption and scattering, as well as the refractive index and the anisotropy, which influences the direction of scattering. The refractive index, denoted n, is a measure of the velocity light will travel through a medium, v, relative to the speed of light in vacuum c, with $n = c/v$. It is useful for determining how light is bent when moving from one medium to another (Figure 4.1). If a photon travels through multiple tissue layers, or enters or exits a tissue, the relative refractive indices

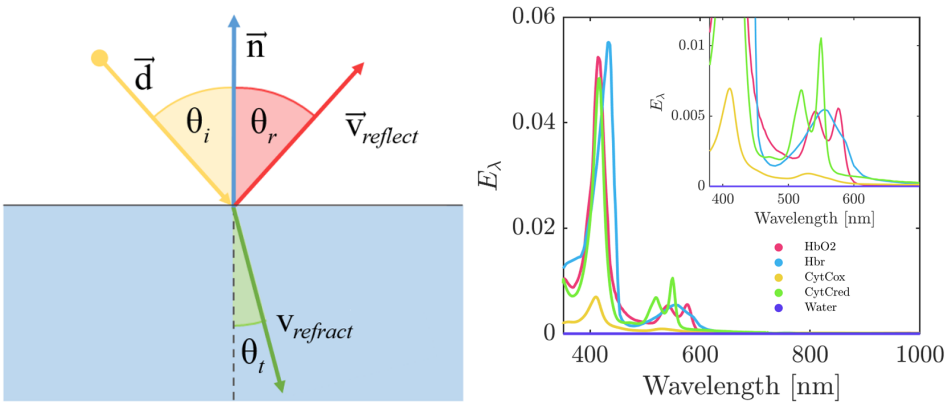

Figure 4.1: Left: Light passing from air into a medium with a higher refractive index, causing the trajectory of the photon to change. Right: The extinction coefficient spectra of chromophores common in tissue. Oxy- and deoxyheamoglobin are significant absorbers in the visible range shown in the inset. Other chromophores such as cytochromes also have high extinction coefficients, but these are present in only comparatively minor concentrations.

therefore influences the trajectory.

Absorption occurs when a photon's energy corresponds to the energy gap of a molecule in the medium; the photon energy is transformed into internal energy in the absorber, exciting it. In tissues, key absorbers include both the oxygenated and deoxygenated forms of haemoglobin (Figure 4.1), with smaller contributions from water, melanin and lipids, depending on the tissue composition. Absorption is quantified by the absorption coefficient $\mu_a[cm^{-1}]$, which is defined as the probability of the photon being absorbed per unit of infinitesimal path length.

Scattering occurs when the light trajectory is changed due to nonuniformities within a medium. It can be thought of as being caused either by particles or regions that have a different refractive index to its surroundings.[235] Like with absorption, the scattering coefficient $\mu_s[cm^{-1}]$ gives the probability of a scattering event occurring as a function of distance. Scattering is often approximated using Mie theory or Rayleigh scattering. Mie theory is used when the atomic or molecular particles the light scatters off are close in size to the light's wavelength, if particles are much smaller, under around a tenth of the wavelength, the Rayleigh regime is used.

After scattering, the new direction of the photon is given by the scattering phase function, which provides the probability of scattering in a given direction relative to the original trajectory. This function is typically de-

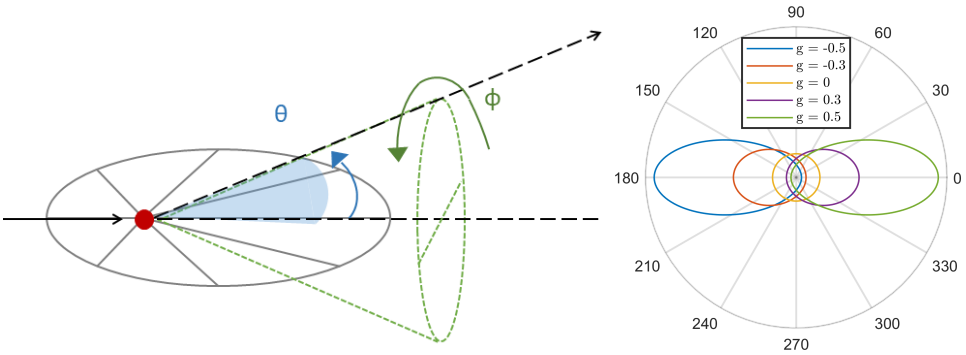

Figure 4.2: Left: a schematic of a scattering event, with the angles of deflection θ and azimuthal angle *phi*. Right: The Henyey-Greenstein phase function for various values of the anisotropy factor g.

noted $p(\theta, \phi)$, where the angles θ and ϕ refer to the deflection angle and azimuthal angle of scattering respectively, as shown in Figure 4.1. However, when the tissue is thick enough that multiple scattering events occur, the scattering structures within the tissue are considered randomly oriented. The ϕ component is therefore averaged, and its contribution can be ignored, and when the θ component is averaged by multiple scattering, the effect can be described $g =< cos\theta >$, the dimensionless anisotropy factor.[235] Scattering can be represented by the Henyey-Greenstein scattering phase function, Equation 4.1. In Figure 4.2, this function is plotted for different values of g, which can take the values $-1 \geq g \leq 1$. A g value close to 1 indicates mainly forward scattering, while isotropic scattering has a value of 0.

$$f(\theta_s) = \frac{1}{4\pi} \frac{1 - g^2}{[1 + g^2 - 2g \cdot \cos(\theta_s)]^{\frac{3}{2}}} \tag{4.1}$$

When significant scattering occurs, this is sometimes denoted in terms of the reduced scattering coefficient $\mu_s' = \mu_s(1 - g)$. This describes the behaviour in the diffusion regime, when multiple scattering events causes light to diffuse through the medium.[235] Biological tissues are optically turbid, with a great degree of scattering occurring with thicknesses larger than the mean free path $1/\mu_s$, which is typically 100 μm or less.[235]

The absorption and scattering coefficients are sometimes combined to give μ_t, the total interaction coefficient. Tissues are also sometimes described by the albedo, which indicates the fraction of extinction which is

caused by scattering.

$$\mu_T = \mu_a + \mu_s \tag{4.2}$$

$$albedo = \mu_s/(\mu_a + \mu_s) \tag{4.3}$$

The overall effect of scattering and absorption on reducing the light intensity over the distance travelled is referred to as attenuation. Depending on the application or field of study, attenuation might be described in terms of the decadic attenuation coefficient, μ_{10}, or the Napierian attenuation coefficient, μ, where

$$\mu_{10} = \frac{\mu}{ln10} \tag{4.4}$$

This is important to be aware of, as the choice is not always made clear in various literature.

The light transport through tissue can be modelled using a Monte Carlo Simulation; as the μ_a, μ_s and scattering angle are all represented by probability distributions, these can be selected for each step based on a random number, until the photon becomes absorbed, remitted or reaches a boundary. By propagating a series of photons through a model tissue, it can generate a probability distribution of the escaped photon's path lengths.

4.2 Monte Carlo methods

The Monte Carlo method is a statistical approach to approximating the solution to a mathematically complex problem by using random numbers. They can be used for either probabilistic or deterministic problems. In the first case, the aim is to find a result of a random process. This is simulated by picking random numbers which enact the random process, and the results is found with the observed random numbers. In the second case, the problem can be formulated theoretically, but the solution can not be found directly; the theoretical steps involved in the process can then be solved with a Monte Carlo simulation.[236] First formulated in 1949 by Metropolis and Ulam,[237] the method has found a wide range of applications in problems requiring sampling, estimation or optimisation. In chemistry, it has been used to study kinetics in chemical processes,[238] and to develop materials such as those used in organic LEDs,[239] as experimenting on models of the material rather than physical samples is often a cheaper and less time-consuming approach to optimise its parameters. Monte Carlo techniques also have

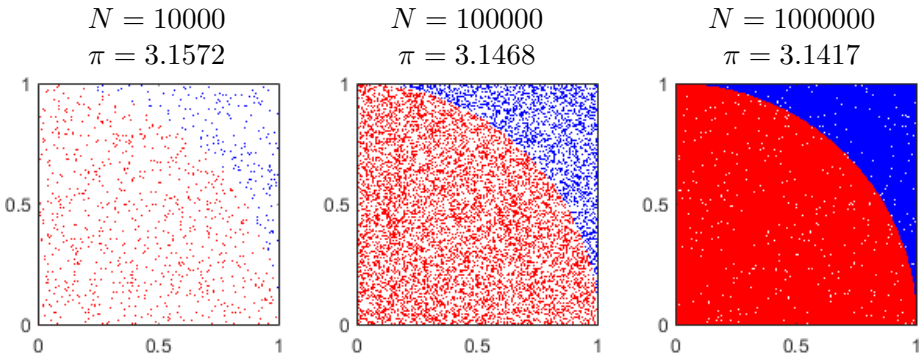

Figure 4.3: Monte Carlo estimates of π. The more points are sampled within the square, the closer the estimate becomes to the true value, which is 3.1416 to four decimal places.

applications in finance,[240] one example is in risk analysis, and in statistics, where it for example can be used in the bootstrap method, to simulate values such as confidence intervals.[241] It can even be used as to perform a tree search, to solve for example the classical traveling salesman problem.[242]

Monte Carlo simulations rely on a large number of samples. The Law of Large Numbers states "*As the number of identically distributed, randomly generated variables increases, their sample mean approaches their theoretical mean.*" This can be demonstrated by a simple example of a Monte Carlo estimate of π. Figure 4.3 shows a quadrant of a circle with radius 1 inside a square with sides of length 1. If a random point is picked inside the square, the probability of a point being within the quadrant is $\pi/4$. For a large number of random points, the fraction of points which fall within the quadrant will be close to the expectation value. Through repeated sampling, ie. as $n \to \infty$, the estimate of π will become closer and closer to the true value. This reliance on repeated measurements is a reason why many Monte Carlo simulations are inherently parallelisable. When each run of the experiment is independent on the others, they can be run simultaneously with the use of parallel computing, significantly increasing efficiency.

Monte Carlo simulations can be used to determine a physical quantity which is equivalent to the expected value of one or several random variables. Light transport is an example of a deterministic problem, where the processes of absorption and scattering can be formulated mathematically, however resulting properties of the photon's trajectory can not be calculated directly from these formulas. The random variable is represented by multiple independent samples, and the expected value is found by averag-

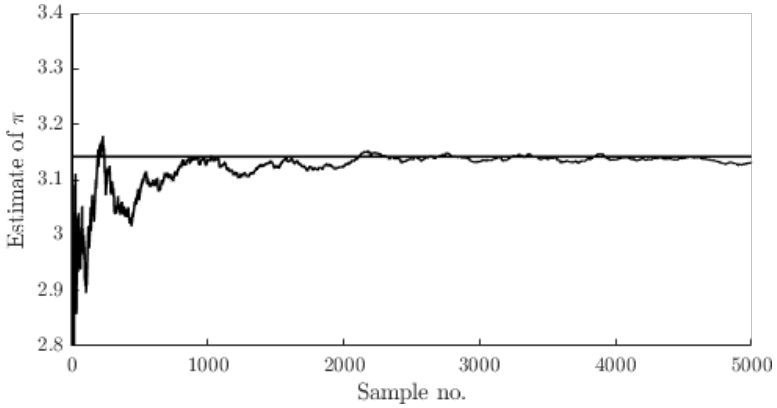

Figure 4.4: Estimated value of π as a function of the number of points used in the estimate, with the true value represented by the horizontal line.

ing these samples. Photon propagation can be expressed in the form of probability distributions which describe the step size of photon movement between sites of photon-tissue interaction, and the angles of deflection after a scattering event.[243] By randomly sampling this distribution each time, the distribution of results after a large number of samples should reflect the expected value. MCS was first used to study light transport in biological materials in 1983.[244] Later work introduced anisotropic scattering,[245] and in 1995 Wang and Jacques implemented a Monte Carlo Multi-Layered program (MCML), which allowed a tissue model to be defined by layers with individual tissue optical properties.[243] The simulation implemented in this project is based on the equations used in their work.

4.3 Monte Carlo Simulation

The scripts were written in MATLAB and are included in 6,**??**. Figure 4.5 shows the simulation model. The incident light is represented by an infinitely narrow photon beam which is directed perpendicularly onto the surface of a tissue. The tissue can consist of multiple layers which are stacked parallel to the x,y-plane, each with its own optical properties.

A layered model is used because it allows for assigning different optical properties depending on the tissue depth. With the layered structural classification and depth dependent vascular density of the brain discussed in Chapter 1, a layered model should provide a more accurate description of the brain optical properties than a homogeneous slab.

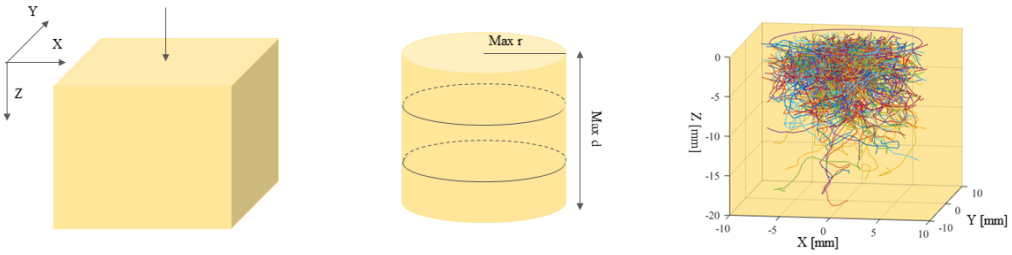

Figure 4.5: The Monte Carlo simulation models a photon beam which is perpendicularly incident on a tissue whose surface is aligned with the X,Y-plane. The tissue is intended to be infinite, but to save computation time a photon will be considered to have escaped the tissue if it has travelled too far to be likely to contribute to the remitted light in the region of interest. The maximum depth d of the tissue and the maximum radius r which define the model boundaries are therefore chosen to be large enough not to interfere with the simulation, but small enough to remain relatively efficient. The tissue can be defined as consisting of multiple layers with the boundaries between them parallel to the surface. On the right of the figure, the photons' simulated paths are shown.

In the simulation, layers are defined by the layer thickness, anisotropy factor, refractive index and absorption and scattering coefficients. The different components that make up brain tissue, such as grey matter, white matter, CSF and blood, can be included in this model by accounting for their properties.

Photons moving through the tissue are treated as classical particles. Statistical sampling is used to determine the step size a photon will move before an interaction occurs, and the angles associated with a change in direction after it undergoes scattering. It is also used to determine whether it internally reflects or transmits at a boundary, and whether a photon with a small weight will be stopped or not.

Figure 4.6 shows a flow diagram of the simulation. The photon starts out with unit weight w, which is reduced by specular reflectance Rsp when it enters the tissue. The step size s is statistically sampled, and as long as the step size is small enough to fit in the current layer, the photon is moved around the layer, undergoing absorption and scattering events after each step. The absorption reduces the weight. If the photon hits a boundary, it will undergo transmission or internal reflection depending on its incidence angle. After each step the step size is reset. The photon will continue to propagate until it leaves the tissue or the weight is 0. If the weight is sufficiently low, the Russian roulette technique determines whether the weight will be set to zero or increased. As each photon terminates, its data

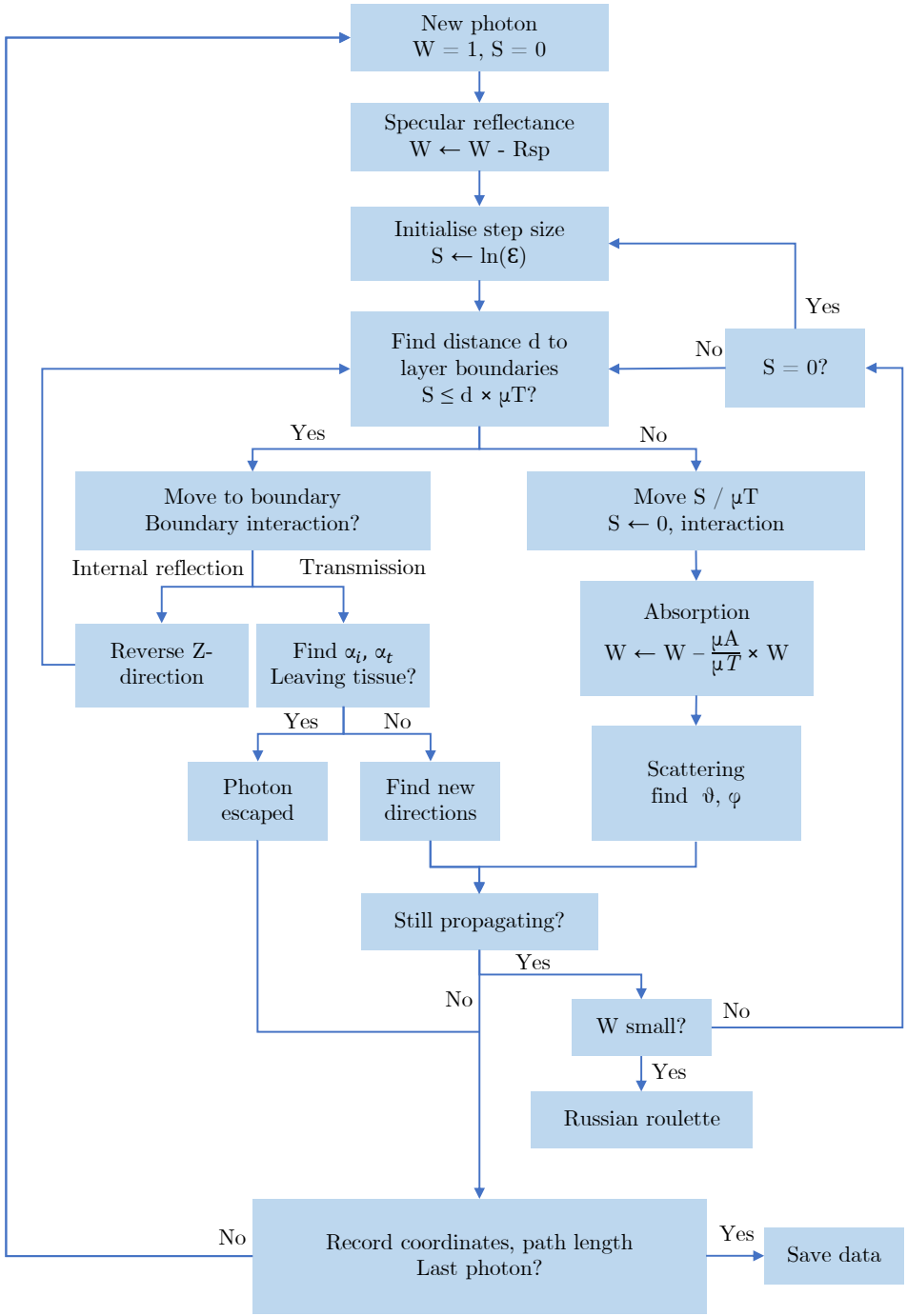

Figure 4.6: A flowchart of the Monte Carlo simulation used in this project.

is stored and the next photon is initialised.

The photon is represented by a class, which keeps track of the photon weight, its current coordinates and directional cosines, its total path length travelled through each tissue layer, and the photon activity, which indicates whether the photon is propagating, has stopped, or has escaped the tissue. The tissue is represented by a structure, which has entries for each layer containing its thickness, absorption coefficient μ_a, scattering coefficient μ_s', refractive indices n, and anisotropy factor g.

In order to reduce computation time, a set of boundary conditions is set for how far a photon can travel. A maximum radius from the Z-axis is set to terminate photons that travel too far away from the source, these photons are unlikely to contribute to the light captured by the camera. There is a depth boundary, as a photon can only travel as deep as the lower limit of the last tissue layer. In some cases where only remitted light will be considered, for example when determining path length distributions for OIS, it can also be beneficial to set a depth boundary within the tissue model to terminate any photon that travels too deeply to be likely to affect the remitted light.

In order to validate the simulation, predictions of diffuse reflectance and transmittance were calculated and compared with the results of Wang et al, as shown in Table 1. The tissue had optical properties relative refractive index $n = 1$, $\mu_a = 10\ cm^{-1}$, $\mu_s = 90\ cm^{-1}$, anisotropy factor $g = 0.75$ and thickness $0.02\ cm$. The results are based on 10 simulations of 50 000 photons each.

Table 1: Simulation results of diffuse reflectance (R_d) and total transmittance (T_t) from turbid medium. The results from the MCS are similar to the values published by Wang *et al.*

Simulation	R_d average	T_t average
Wang et al	0.09734	0.66096
MCS	0.09761	0.66112

Simulations were run on a high-performance computing cluster to speed up processing. Parallel processing allows several CPUs to work on the simulation simultaneously. Because each photon's life cycle is independent of the other photons, they can be simulated in parallel, and the results of individual runs can be combined. Since the simulation results are additive, one simulation can be divided into several independent smaller simulations and processed in parallel on different CPUs. For example, instead of running a

single simulation for 10 000 000 photons, 50 simulations of 200 000 photons each can be ran simultaneously and their results combined, reducing the overall simulation duration to around one 50th of the time.

4.4 Path length distribution

The Monte Carlo simulation can be used to determine how far a photon has travelled through the tissue before being remitted. After each move the photon makes, the distance travelled between interaction sites is recorded into the photons path length for the given tissue layer. If the photon is remitted back out from the tissue, the distance it travelled is added to an array, along with the current photon weight. The results from the simulation are binned to provide a function of the number of photons travelling a given path length. This is then normalised to give a path length probability distribution (Figure 4.7).

Simulations were run to investigate the dependency of the path length distribution on the input optical parameters, and its sensitivity to each. The model was set to mimic brain tissue, and had optical properties $g = 0.85$ and $n = 1.4$. The results are shown in Figure 4.7. The maximum depth of the tissue was set to 50 mm, and the radial limit for the photons propagation in the X,Y-direction was set to 10 mm. The boundary conditions were chosen so that photons would terminate by absorption, lateral escape or remission, to avoid artifacts from photon escape through the deep limit of the tissue, which is assumed to be negligible in the real system. For each experiment, 20 simulations were performed in parallel, each with 50 000 photons, yielding a concatenated result based on 1000 000 photons. The path length results were divided into 100 bins.

The results from simulations at various μ_A values show that a larger absorption coefficient reduces the average depth the photons reach before remitting, and indicate the path length is quite sensitive to this parameter.

4.5 Point-Spread Function

The tissue response to incident light can be described by a point-spread function (PSF). This is a concept frequently used in optics to characterise the response of an imaging system to a point source. The PSF generated by the simulation indicates the probability of photon escape as a function

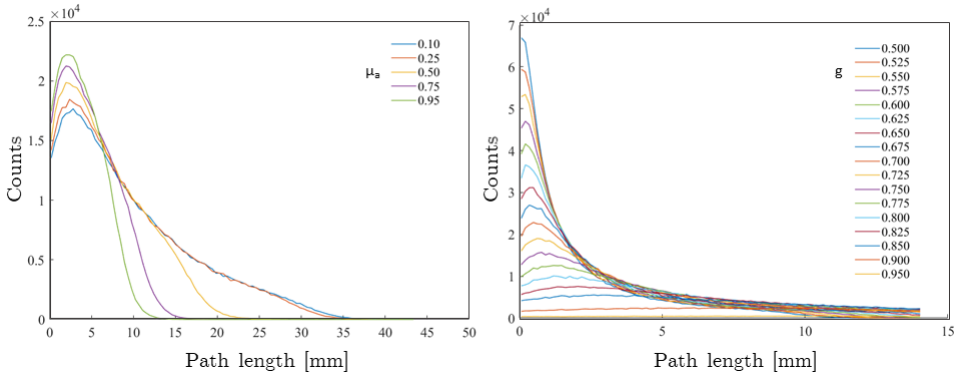

Figure 4.7: Path length distributions as a function of the absorption coefficient μ_a (left) and of the anisotropy factor g (right). Increasing μ_a increases the probability of photon absorption, so remitted photons are less likely to have travelled far through the tissue. A larger g value leads to a flattening of the curve, as the increased forward scattering causes photons to travel deeper before potentially being remitted.

of radial distance from the point of incidence. The Monte Carlo Simulation was set up to produce a PSF from the diffusely reflected light. If a photon escapes back out from the surface of the tissue, the (x,y)-coordinates of the point where it was remitted are stored, along with the current photon weight. Figure 4.8 shows a PSF generated from a simulation of a sample tissue.

SFDI measures the modular transfer function (MTF), which is the Fourier transform of the PSF. For SFDI analysis, it is beneficial to express the diffuse reflectance as a function of radial distance ($R_d(\rho)$). The tissue surface in the simulation was divided into bins along the radial axis ρ, defined by concentric rings originating at the z-axis and with equal spacing (Figure 4.8A). Following the work by Wang et al.,[243] the indices of the radial bins were calculated using Equation 4.5 to minimise error, here Δr represents the bin size.

$$r = [(i + 0.5) + \frac{1}{12(i + 0.5)}]\Delta r \tag{4.5}$$

Upon escaping, the photon's distance from the z-axis was calculated from its coordinates, and its weight added to the corresponding radial bin. At the end of the simulation, the data is normalised (4.8) by dividing each bin by the area of the surface ring, given by Equation 4.6.[243]

$$\Delta a = 2\pi(i + 0.5)(\Delta r)^2 \tag{4.6}$$

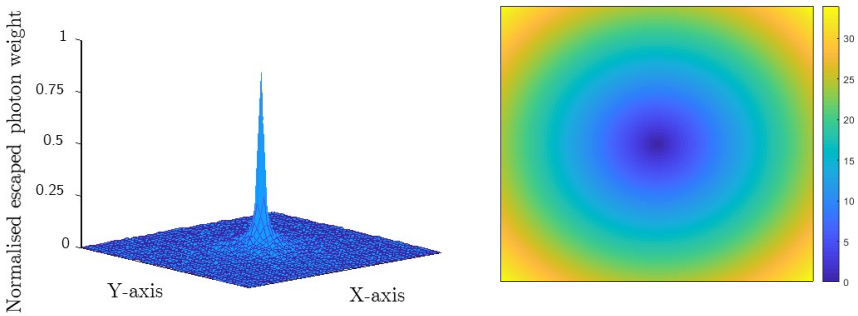

Figure 4.8: Left: 3D view of example PSF data. Right: Radial bins used to normalise PSF, distributed on a 25x25 mm grid. The colour bar shows the radial distance [mm].

4.6 Diffuse reflectance

The diffuse reflectance $R_d(k)$ can be determined by a Fourier transform of the spatial point spread function $R_d(\rho)$ for the given optical properties. If the PSF $R_d(\rho)$ is radially symmetric, this is a 2-D Fourier transform in the x-y plane, which can be reduced to a 1-D Hankel transform of order zero. This is calculated as in Equation 4.7, where $J_0(k\rho)$ is the zeroth-order Bessel function of the first kind. Since ρ is binned into n finite intervals $\Delta\rho_i$, the integral can be expressed in terms of the sum in Equation 4.8.[38]

$$R_d(k) = 2\pi \int \rho J_0(k\rho) R_d(\rho) d\rho \tag{4.7}$$

$$R_d(k) = 2\pi \sum_{i=1}^{n} \rho_i J_0(k\rho_i) R_d(\rho_i) \Delta\rho_i \tag{4.8}$$

Cuccia et al[38] present the diffusion approximation for calculating the spatial frequency dependence of diffuse reflectance at given optical properties. They compare this with results from the Monte Carlo predictions used in SFDI analysis, as shown in Figure 4.9. To validate the calculations, this figure was replicated, using the diffusion approximation calculated for the same transport lengths. Here $l^* = 1/\mu_{tr}$ is the transport mean free path, where $\mu_{tr} = \mu_a + \mu_s'$, and for each curve $\mu_s'/\mu_a = 100$. The bin size Δr was set to 0.09 mm to compare with Cuccia et al. There are minor differences between the two figures, which are mainly noticeable for higher spatial frequencies. It is unclear why this is the case, as the optical properties and the bin size used were the same. The image analysis relying on the dif-

fuse reflectance is however performed at low spatial frequencies (typically $0 - 0.3mm^{-1}$), so the results should still be largely comparable.

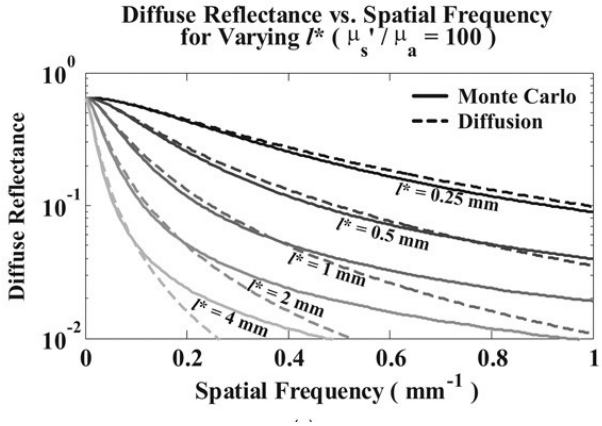

Figure 4.9: Cuccia et al present simulation results of diffuse reflectance dependence on spatial frequency, which correspond with the diffusion approximation

4.7 Look-up table

Analysis of SFDI image data involves determining optical properties from diffuse reflectance data. For each point in the image, reflectance values from two frequencies, f_x and $0mm^{-1}$, are used to determine the optical properties (OP) μ_a and μ_s'. Since the relationship between these values is calculated via a forward model which determines R_d from OPs, the OP values need to be found through interpolation.

The analysis is typically done using a pre-computed look-up table (LUT).

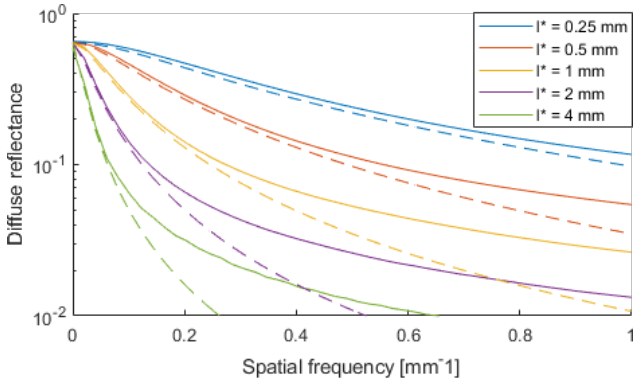

Figure 4.10: Diffuse reflectance dependence on spatial frequency, replicated from Cuccia et al.

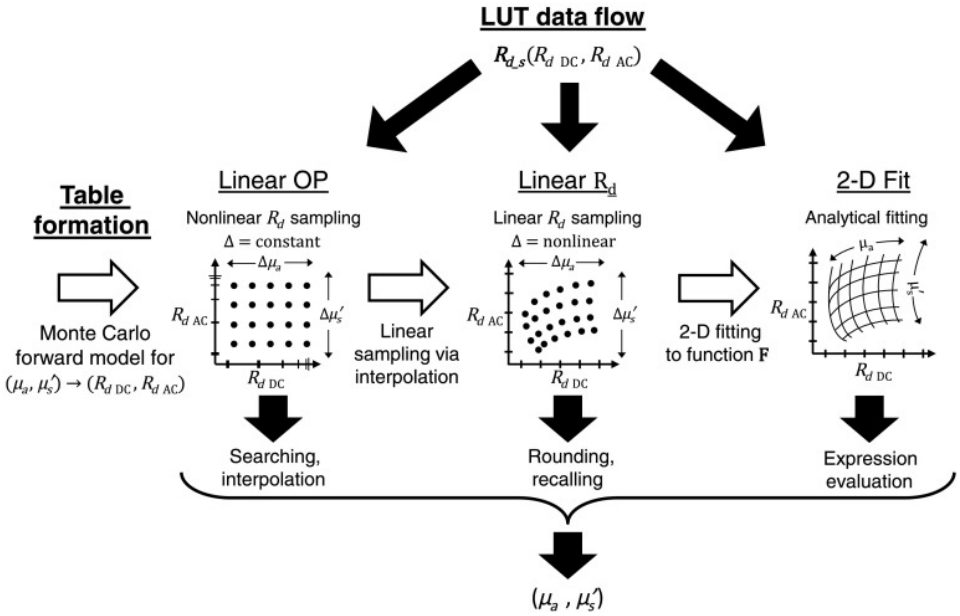

Figure 4.11: The process used to generate the LUT, shown by Angelo et al. in their paper.[246] Monte Carlo simulations provide a map of (R_{AC},R_{AC}) as a function of (μ_a,μ_s'). This data is resampled at linear intervals of diffuse reflectance. They finally determine an analytic fit of the resampled LUT, which can be evaluated for given (R_{AC},R_{AC}) values. For this thesis, the resampled LUT was used directly, without the analytical fitting.

Figure 4.11 demonstrates this process, as proposed by Angelo et al.[246] The Monte Carlo simulation can provide the R_dk and R_d0 values for a range of relevant optical properties. This provides a table where each set of $[\mu_a, \mu_s']$ values acts as indices to the corresponding reflectance values. By interpolating the data linearly with respect to R_dk and R_d0, a new table can be generated. Here, the OPs can be found using the reflectance values as indices. The image values can therefore be rounded to the nearest spacing and found directly, and the values can then be calculated without the need for fitting procedures during analysis of each individual data set. This table can also be used to fit a function, on the form $[\mu_a, \mu_s'] = f(Rdk_AC, Rdk_DC)$.[246] In their paper, the group achieved 0.2% error in μ_a and 0.09% error in μ_s' with the linear Rd LUT and 1.9% error in μ_a and 2.8% error in μ_s' from 2-D fit LUT. For this thesis, the Rd-LUT was sampled directly, without the use of a fitting function.

In order to validate the method, a Look-up table was generated using the diffusion approximation as a forward model. Input optical properties $\mu_a = [0.0001, 0.45]$ and $\mu_s' = [0.001, 4.5]$ were chosen to cover the range typi-

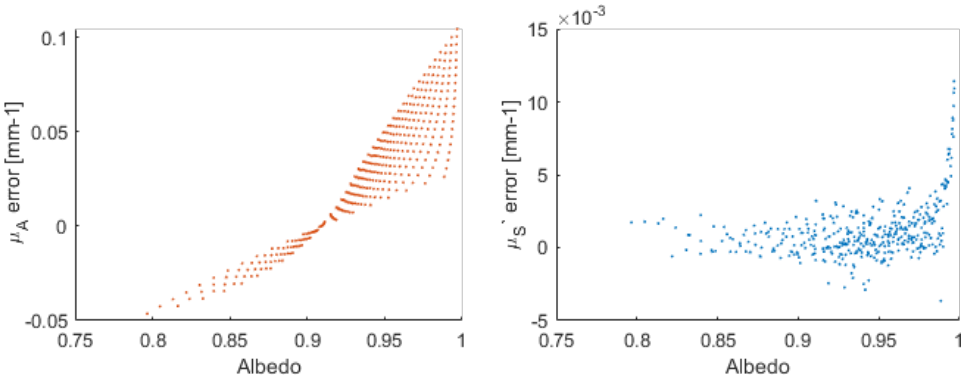

Figure 4.12: The errors in optical properties when sampling the generated LUT, as difference from the true value plotted against the albedo. For μ_a errors are smallest close to an albedo of 0.9, as this is the typical value for input properties used to generate the table. For μ_s', errors are fairly small consistently.

cal for tissues, and to reflect typical tissue albedo, $\mu_s' \approx 10\mu_a$. $R_d(\mu_a, \mu_s', f_x)$ was determined for N absorption coefficients and M reduced scattering coefficients for $f_x = 0.1$, giving a $N \times M$ matrix. Different matrix sizes were tested by increasing the number of input optical property pairs. This data was linearly interpolated to generate two new data sets linear with respect to R_d, one for absorption and one for scattering. The new indices R_d were equally spaced over the range 0 to 1. This allows for indexing the data by rounding to the nearest multiple of the spacing distance.

The errors in the fit were determined by selecting optical property pairs $[\mu_a, \mu_s']$, determining the $[R_d(0), R_d(k)]$ values by the diffusion approximation, and comparing the look-up values at $R_d(0), R_d(k)$ with the input OP pair. The error of the fit for table based on $500\mu_a \times 500\mu_s'$ is shown in Figure 4.12. This shows that estimates of μ_a are most accurate for a 0.9 albedo, which is achieved when $9\mu_a \approx \mu_s'$. This is unsurprising because this is the typical albedo of tissues, and the input values used to generate the fit are chosen within the typical OP range. Errors varied with the input table size, ranging from 15% at a size of 100×100, to 1.5% at 1000×1000.

4.8 Absorption estimates for light therapy

The developed Monte Carlo simulations were used in conjunction with a research study on the therapeutic effects of biophotomodulation (PBM). The study aimed to investigate if the application of light onto the back of the skull could have neuroprotective benefits, as this has been hypothesised to

stimulate mitochondrial production of ATP. As part of the experimental protocol, ^{31}P MRI was used to detect any changes in the rates of ATP production before and after light treatment. The simulations of light transport could provide an estimate of the amount of externally applied light which is able to reach the grey matter, where the mitochondrial cytochrome-C oxidase is thought to absorb it. This can help indicate whether photons even reach the sufficient depth for such a process to be likely to occur, and can show how the grey matter absorption varies with wavelength, which could influence the choice of light source.

4.8.1 Motivation

It has been suggested that red/near infrared light can be used to improve brain cell function in various neurological or psychological conditions such as Alzheimer's Disease,[247,248] brain injury,[249] Parkinson's disease,[250] depression and anxiety[251,252] and age-related cognitive decline.[253] These conditions cause neuronal mitochondria to undergo oxidative stress, increase cell death and reduce the production of adenosine triphosphate (ATP). PBM has been shown to improve mitochondrial function and ATP production in animal models of ageing and neurodegenerative disease,[254,255] however clinical applications have been limited, as the potential mechanism of PBM is not clear. A leading theory suggests that the light can cause excitation of cytochrome-c oxidase within the mitochondria, which in turn increases ATP production.[256,257] It has however been shown that blue light, which is strongly absorbed by cytochrome-c oxidase, actually reduced ATP production.[258]

To investigate the effects on metabolic rate of the PBM technique, ten participants with no known neurodegenerative conditions were scanned with ^{31}P Magnetic Resonance Spectroscopy (MRS) to measure ATP metabolism in the brain before and after treatment with light, applied for 20 minutes each day for four days. To complement these experiments, Monte Carlo simulations were run for a layered model tissue parameterised to represent the human head. The simulations could provide an estimate of the amount of externally applied light which is able to reach the grey matter where the mitochondrial cytochrome-C oxidase is thought to absorb it. This provides an indication of whether photons reach sufficient depth for such a process to be likely to occur. It can also show how the grey matter absorption varies

with wavelength, which could influence the choice of light source.

4.8.2 Tissue optical properties

The tissue model consisted of five layers; skin, skull, CSF, grey matter and white matter. Tissue layer thicknesses were similar to estimates from other models.[259] The thickness of skull however, was initially set to a low estimate of 3 mm, this is because measured values are very dependent on region (and age and gender),[260] and the back of the skull is generally thinner. Refractive indices were all set to equal values as has been done in previous simulations, and the anisotropy factor g were similar to previous models.[259] Wavelength dependent absorption and reduced scattering parameters were estimated for each layer using reported literature values.

Table 2: Tissue layer parameters used in comparative simulations of individual layers and a combination of these layers

Property	Skin	Skull	CSF	Gray	White
thickness [mm]	3	3	2	4	20
refractive index	1.365	1.365	1.365	1.365	1.365
g	0.88	0.94	0.999	0.96	0.87

Scattering properties of skin were calculated by combining the effects of Mie and Rayleigh scattering.[261]

$$\mu'_{sMie} = 2 \cdot 10^5 \cdot \lambda^{-1.5} \tag{4.9}$$

$$\mu'_{sRayleigh} = 2 \cdot 10^{12} \cdot \lambda^{-4} \tag{4.10}$$

$$\mu'_{sskin} = \mu'_{sMie} + \mu'_{sRayleigh} \tag{4.11}$$

The μ'_s value for CSF was set to a constant $3 \cdot 10^{-4}$ for all wavelengths. Studies have indicated values between 0 and 0.3 mm^{-1} will not significantly affect path lengths.[262] The scattering properties of skull, grey matter and white matter were calculated using Equation 4.12. Jacques (2013) provides an overview of tissue optical properties as determined in the literature.[263] The data is converted into fitting parameters according to this equation, where the wavelength (λ) is normalised by a reference wavelength of 500 nm. The value b is referred to as the scattering power, giving the wavelength dependence of μ'_s and a is the value of μ'_s at 500 nm, which is used as a

scaling factor. The listed typical a and b values for bone, brain and white matter were used to determine μ_s' for skull, grey matter and white matter respectively.

$$\mu_s' = a(\frac{\lambda}{500(nm)})^{-b} \tag{4.12}$$

The μ_a values for skin were estimated using Equations 5-8.[261] These provide an estimate for both epidermal and dermal absorption. Epidermal absorption is calculated from melanine absorption and a skin baseline absorption. The melanine fraction was set to 0.04, which is a medium value for the light-skinned range, and likely to be suitable for the participants in the study. Blood fraction in skin (b_f) was set to 0.03, this is typically 2-5% in well-perfused tissue.[261] Epidermal thickness (d_{epi}) was assumed to be 0.1 mm, compared to the 3 mm thickness of skin (d_{skin}), the ratio was used to weight the result.

$$\mu_{abaseline}[mm^{-1}] = \frac{0.244 + 85.3^{\frac{-1\lambda-154}{66.2}}}{10} \tag{4.13}$$

$$\mu_{aderm} = b_f \cdot \mu_{ablood} + (1 - b_f) \cdot \mu_{abaseline}; \tag{4.14}$$

$$\mu_{amelanine}[mm^{-1}] = \frac{(6.6 \cdot 10^{11}) \cdot \lambda^{-3.33}}{10} \tag{4.15}$$

$$\mu_{aepidermal}[mm^{-1}] = f_{melanine} \cdot \mu_{amelanine} + (1 - f_{melanine}) \cdot \mu_{abaseline} \tag{4.16}$$

$$\mu_{askin} = \frac{d_{epi}}{d_{skin}} \cdot \mu_{aepi} + \frac{d_{skin} - d_{epi}}{d_{skin}} \cdot \mu_{aderm} \tag{4.17}$$

The μ_a value for skull was set to a constant 0.04 mm^{-1} for all wavelengths. CSF absorption was assumed to be similar to that of water. Grey matter and white matter μ_a was estimated from extinction coefficients and concentrations of oxyhemoglobin (HbO_2), deoxyhemoglobin (HbR), cytochrome-C oxidase (CytC-Ox), cytochrome-C reductase (CytC-Red) and water. The amounts used are listed in Table 3. These are based on previously estimated concentrations,[264] but adjusted to fit the water content and blood content difference between white and grey matter.[265] The estimated μ_a and μ_s' spectra for each tissue layer are shown on the next page.

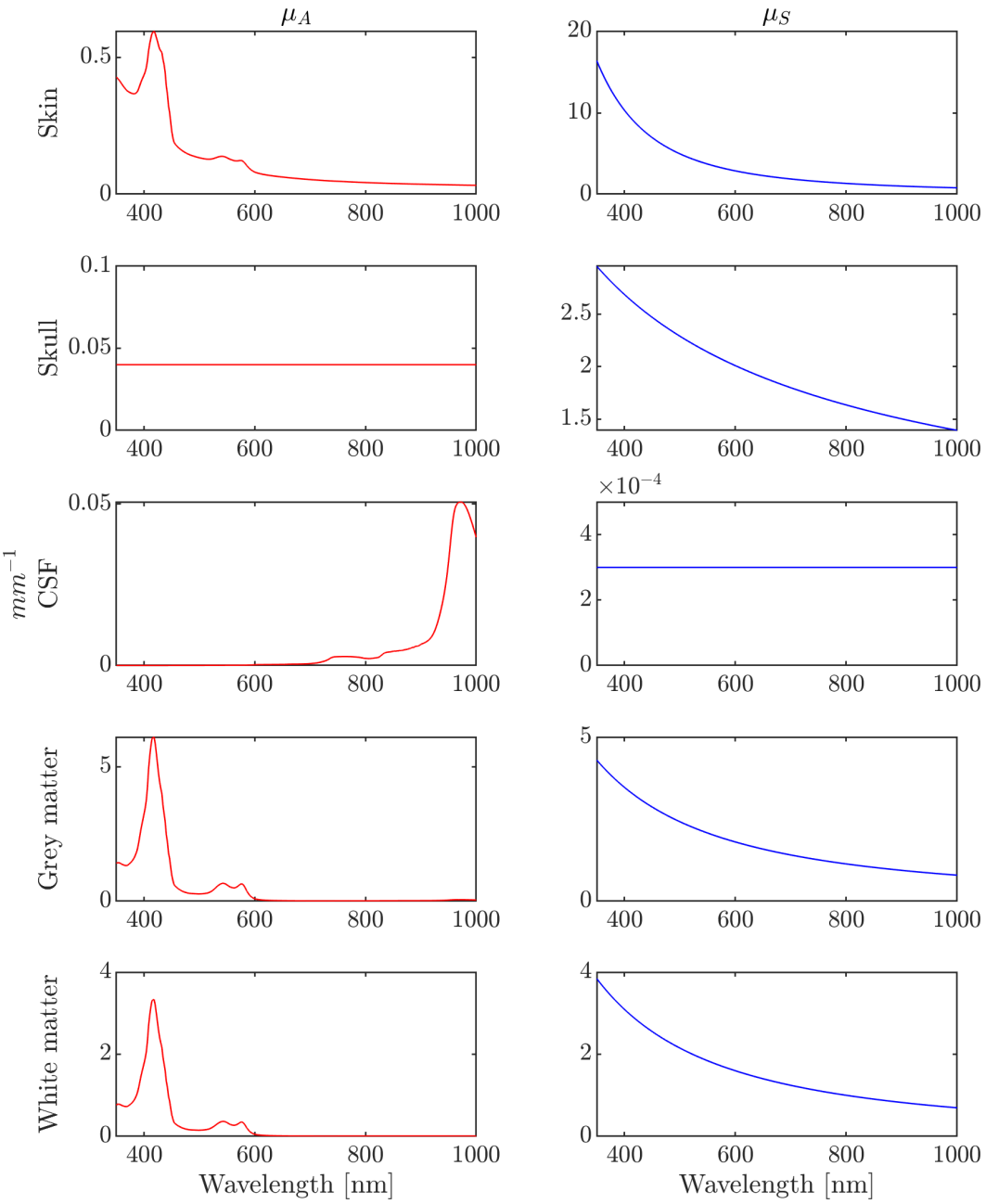

Figure 4.13: The μ_a and μ_s' spectra used for the different tissue layers in the base light transport simulation. The spectra were generated by considering the relative contributions from the different tissue components, using optical property estimates from the literature.

Table 3: Chromophore concentrations used in predictions of μ_a spectra of brain tissue

	Grey matter	White matter
HbO_2 $[\mu M/L]$	88.037	47.40
HbR $[\mu M/L]$	37.73	20.32
CytC-Ox $[\mu M/L]$	8	8
CytC-Red $[\mu M/L]$	1.36	1.36
Water [ml/g]	0.82	0.72

4.8.3 Results

The five layer simulation consists of several separate experiments which cover the wavelength range 350-1000 nm in increments of 5 nm. Each experiments is run on 100 nodes, with 500 photons per node. This gives 50 000 photons per experiment. At lower absorption the jobs are likely to have longer run times, and the photon number was therefore limited to reduce computation time.

Depth dependent absorption results are shown in Figure 1 and the cytochrome absorption in grey matter is shown in Figure 2. Absorption values are expressed as the fractional photon weight (fpw) of the photons incident onto the tissue surface which are absorbed at a given depth.

The simulation was run for different tissue parameters to evaluate their impact on the grey matter absorption, as well as how this effect was reflected in the amount of light absorbed by Cytochrome-C. Skull thickness varies quite significantly by region. A typical maximum skull thickness was selected as 8 mm using the data from Sawosz et al.[260] The CSF thickness would vary with the shape of the cortical surface. Sulci depth and width could be affected by age, but as an estimate large sulci are around 16 mm deep.[266] The thickness of the CSF layer was increased from 2 mm to 7 mm to indicate the effect this would have on absorption.

Figure 4.17 shows the results on changing the melanin fraction in skin, the blood fraction in the grey matter, the thickness of the CSF layer, and the thickness of the skull. The results are compared with the base simulation, which uses the tissue parameters estimated from literature values, and the layer thickness informed by the structural MR data from the participants.

The most significant effect is seen with changing the melanin fraction of skin. For the high end of the range of melanin, ie darker skin tones,

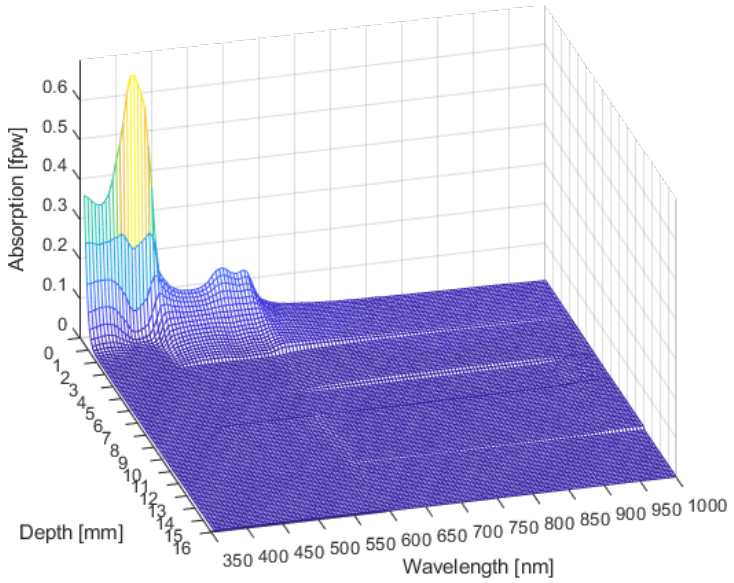

Figure 4.14: Absorption is shown as a function of depth and wavelength for the five layer model. The large absorption in skin in the 350-450 nm range prevents most light from reaching the skull (3-6 mm). Above this limit light starts to be absorbed also in the grey matter.

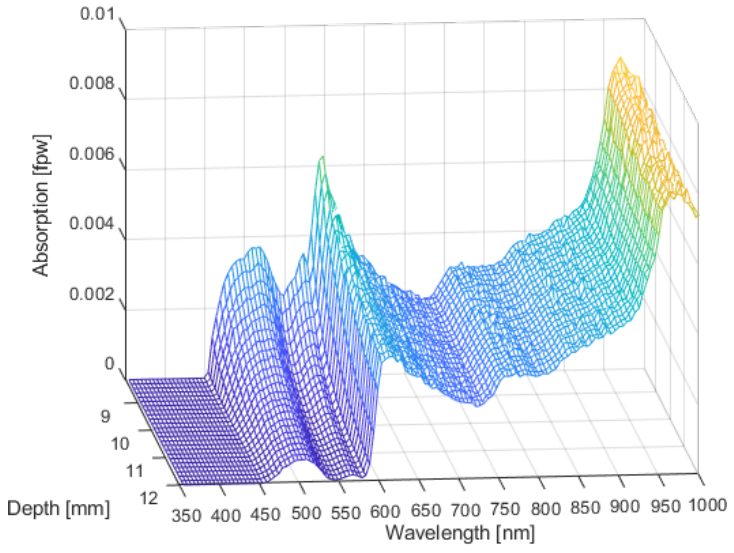

Figure 4.15: Grey matter absorption. Light beyond 450 nm can reach through skin and skull and become absorbed in the grey matter, but this makes up less than 1% of the incident light.

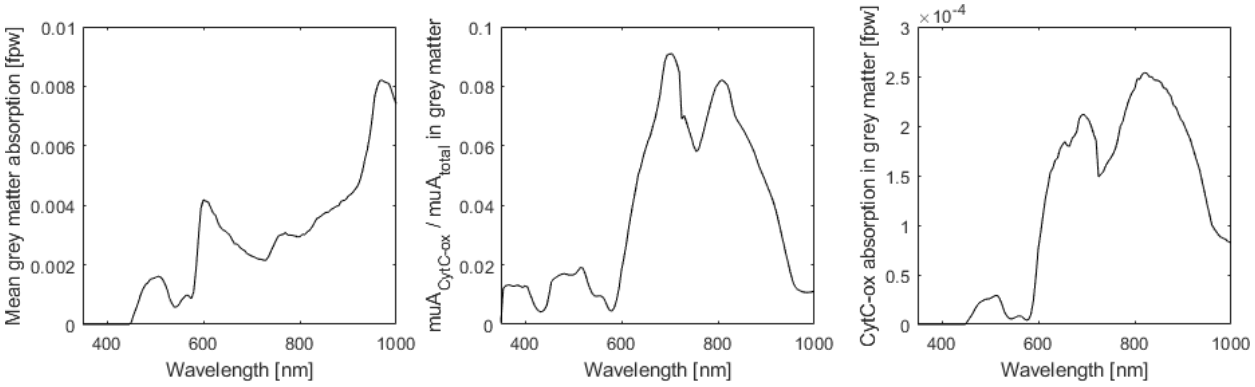

Figure 4.16: The mean grey matter absorption (left) was multiplied by the fractional μ_a of cytochrome-C oxidase in grey matter (middle) to give the fraction of incident photon weight absorbed by cytochrome in the grey matter (right).

the Cytochrome-C absorption is reduced by about half at the peak at 820 nm, and by two thirds at the target wavelength of 670 nm used in the study. This is an important consideration in the design of photobiomodulation treatment, as the potential impact of a given light exposure protocol will vary significantly depending on skin tone. This is an important factor also in other clinically relevant optical techniques, and racial bias in pulse oximetry and functional near-infrared spectroscopy has recently come into focus.[267,268]

The blood fraction has no significant effect on absorption, and the effect of CSF thickness is relatively minor, and mostly seen towards higher wavelengths. The increased skull thickness however, reduces the absorption as expected. As skull thickness varies quite significantly by region, the placement of the bulb and the point of light incidence will likely have an effect on the Cytochrome-C absorption.

4.8.4 A mesh-based light transport simulation

The algorithm implemented by Wang *et al.* has been validated by numerous investigators using phantoms with known optical properties, and is regarded as the gold standard for modelling photon propagation in tissues.[269] The model is limited however, to a tissue model consisting of layers with parallel boundaries between them. In reality the layers might have different thickness in different regions, and they could feature curved or uneven surfaces.

This would have an effect on the photon trajectories, as the angle of a

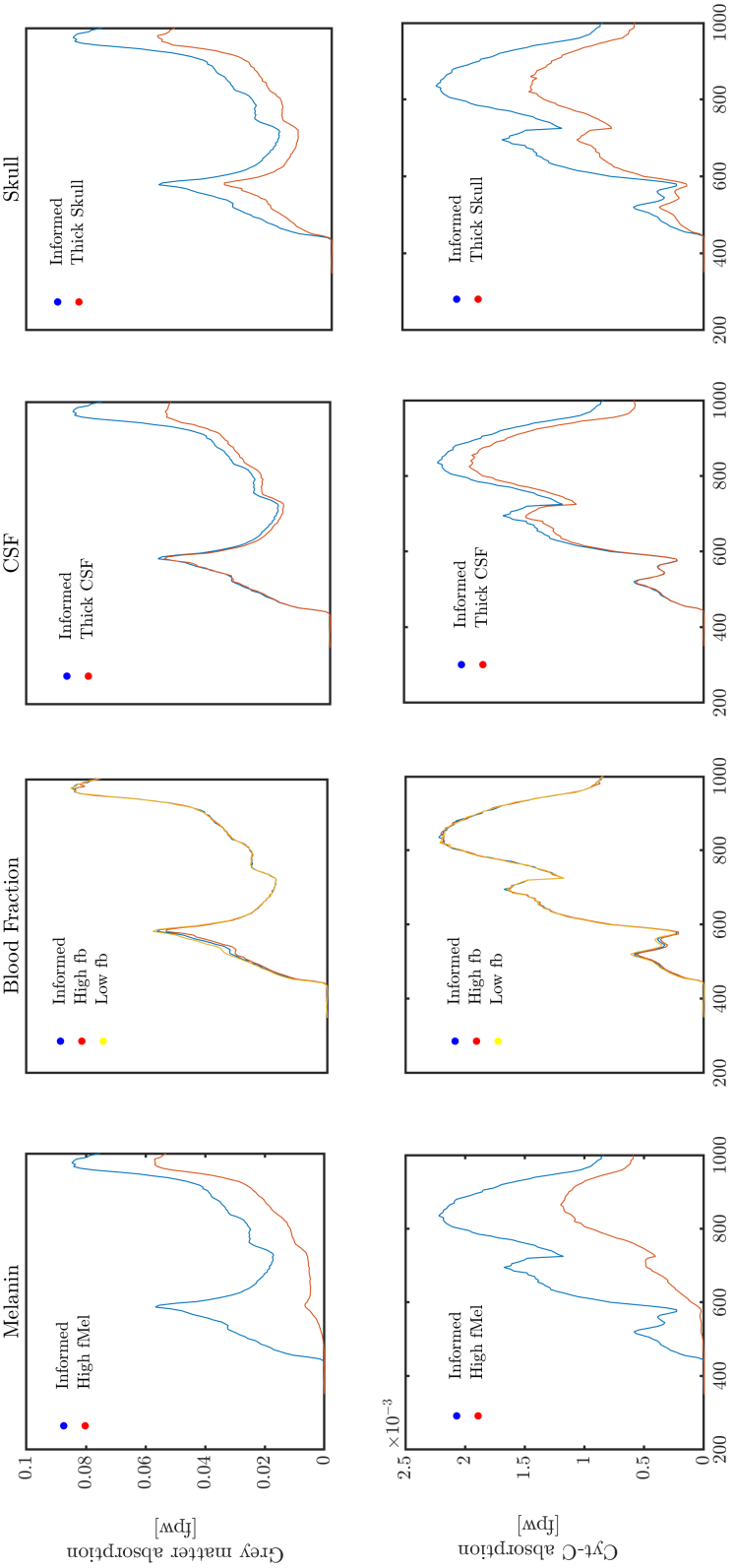

Figure 4.17: The absorption in grey matter (above) and in Cytochrome-C (below) simulated for different tissue parameters. The melanin content in skin has a significant impact on grey matter absorption, nearly halving the absorption in Cytochrome-C.

tissue boundary relative to the photon direction influences the likelihood of transmission. In the case of the brain surface, the presence of for example sulci and gyri might affect the paths of photons to different extents depending on the photon entry point. Sulcal width tends to increase by age, but is typically 2-3 mm.[270] This is well within the horizontal spread of photon absorption events found in the layered simulation results, with photons reaching up to 30 mm from the photon trajectory.

A 3D MCS was developed by Jacques et al. in 2013 based on the MLMC by Wang et al. This model, mcxyc, is available online[271] and performs the simulation in 3D voxel data. The medium is defined as a cube with each voxel containing an integer to denote which tissue it belongs to. Although supporting a more nuanced assignment of tissue properties in three dimensional space, the model assumes matched boundaries, with tissues sharing refractive indices, and does not account for boundary surface orientation.

A new simulation was written by extending the layered simulation, with the goal of accounting for three dimensional tissue features. This method uses a model where each volume is represented by a triangle mesh of the volume surface, and the trigonometric calculations were updated to account for the tissue boundary orientations. Adjustments made to the code included 1) collision tests for photon intersecting with a boundary, 2) calculation of the updated direction of a photon after reflection or refraction with the surface and 3) indexing of absorption events by their layer as well as by the coordinates.

4.8.5 Implementation

In the new simulation, the z-coordinate can no longer be used to detect when the photon reaches a boundary. Instead, a test is done by checking for ray-triangle intersections between the photon's trajectory and the triangles making up the mesh. This approach follows the Möller-Trumbore algorithm introduced in 1997.[272]

The position of a point in the plane of a triangle can be described in terms of its barycentric coordinates. The barycentric coordinates defines a point's position in reference to a simplex (such as a triangle in 2D space), and can be thought of as a weighting towards the simplex vertices. If the

triangle has vertices v_1, v_2 and v_3, the position p is given by

$$p = w \cdot v_1 + u \cdot v_2 + v \cdot v_3 \tag{4.18}$$

where w, u and $v \geq 0$ are the barycentric coordinates. These have the property that $w + u + v = 1$, so there are actually only two degrees of freedom, and the point can be uniquely described by two of the coordinates. The point can therefore be expressed more simply:

$$\begin{aligned} p &= (1 - u - v)v_1 + u \cdot v_2 + v \cdot v_3 \\ &= v_1 + u(v_2 - v_1) + v(v_3 - v_1) \end{aligned} \tag{4.19}$$

A ray intersecting the triangle has origin o and direction $\vec{d}$. The point of intersection p will be given by

$$p = o + t\vec{d} \tag{4.20}$$

where t gives the distance from the ray's origin to the intersection point. Combining this with Equation 4.19, the variable p can be replaced with the point's coordinates expressed in terms of barycentrics, which allows the equation to be rearranged. By doing this, the unknown scalar variables t, u and v can be separated out.

$$\begin{aligned} o + t\vec{d} &= v_1 + u(v_2 - v_1) + v(v_3 - v_1) \\ o - v_1 &= -t\vec{d} + u(v_2 - v_1) + v(v_3 - v_1) \\ \begin{bmatrix} -\vec{d} & (v_2 - v_1) & (v_3 - v_1) \end{bmatrix} &\begin{bmatrix} t \\ u \\ v \end{bmatrix} = o - v_1 \end{aligned} \tag{4.21}$$

This simplified expression can be solved using Cramer's rule, which uses the properties of a determinant, denoted by vertical bars, to solve a set of linear equations. Let $T = o - v_1$, $E_1 = v_2 - v1$ and $E_2 = v_3 - v1$.

$$\begin{bmatrix} t \\ u \\ v \end{bmatrix} = \frac{1}{\left| \begin{bmatrix} -\vec{d} & E_1 & E_2 \end{bmatrix} \right|} \begin{bmatrix} T & E_1 & E_2 \\ -\vec{d} & T & E_2 \\ -\vec{d} & E_1 & T \end{bmatrix} \tag{4.22}$$

Using the solution for the value of a 1x3 matrix, given by

$$|ABD| = -(AxC) \cdot B = -(CxB) \cdot A \tag{4.23}$$

Equation 4.22 can be written on the form

$$\begin{bmatrix} t \\ u \\ v \end{bmatrix} = \frac{1}{(\vec{d} \times E_2) \cdot E_1)} \begin{bmatrix} (T \times E_1) \cdot E_2 \\ (\vec{d} \times E_2) \cdot T \\ (T \times E_1)\vec{d} \end{bmatrix} \tag{4.24}$$

When performing the calculation, the cross products can be pre-computed as $P = (\vec{d} \times E_2)$ and $Q = (T \times E_1)$, and the equation is then solved for t, u, v using Equation 4.25

$$\begin{bmatrix} t \\ u \\ v \end{bmatrix} = \frac{1}{P \cdot E_1} \begin{bmatrix} Q \cdot E_2 \\ P \cdot T \\ Q\vec{d} \end{bmatrix} \tag{4.25}$$

If the determinant $((\vec{d} \times E_2) \cdot E_1)$ in Equation 4.24) is close to zero, there is no intersection, as the photon direction and triangle normal are orthogonal. If u is within 0 to 1 and v is within 0 to 1, there is an intersection.

All the intersections along the current photon direction are stored. The closest triangle is selected by comparing the distances t from the photon origin to the intersection points, and the boundary collision is evaluated using the optical properties of the volume this triangle belongs to.

The surface mesh triangles have a consistent vertex winding order, which causes all the triangle normals to point outwards. This can be used to determine if a photon is entering or leaving a volume. Collisions will only occur if the photon direction is not in the plane of the triangle. If during the collision the photon is approaching the triangle from the direction the triangle normal is facing, the dot product will be positive, otherwise it is negative. The positive or negative dot product therefore indicates that the photon is entering or leaving the volume which the triangle belongs to, respectively. This is also used to keep track of which volume the photon is currently in after escaping a volume; the next intersecting triangle along the photon direction which has a negative determinant will belong to the volume the photon is currently in.

When the photon hits a boundary, it can undergo either reflection or refraction. Figure 4.18 shows the photon's change in direction in each case.

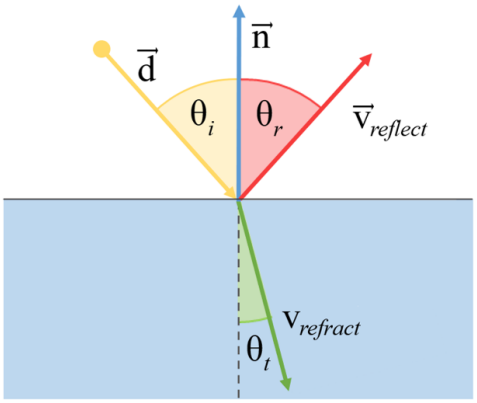

Figure 4.18: Reflection (red) and refraction (green) of a photon $\vec{d}$ incident on a plane with normal $\vec{n}$. The angle of incidence θ_i denotes the angle between the photon direction and the normal of the plane. Here, the angles are calculated using the refractive indices of air and water.

If the normalised directional vector of the light is $\vec{l}$, and $\vec{n}$ represents the normal of the plane facing towards the direction where the light is approaching from, the angle of incidence $\cos\theta_i$ is given by

$$\cos\theta_i = -\vec{n} \cdot \vec{l} \tag{4.26}$$

If the photon is reflected, its new new direction will be given by

$$\vec{v}_{reflected} = \vec{l} + 2\cos\theta_i \vec{n} \tag{4.27}$$

Snell's law can be used to derive the direction of the photon after refraction. Let θ_i and θ_t be the angle relative to the surface normal of the incident

ray and the transmitted ray respectively, as shown in Figure 4.18

$$
\begin{aligned}
sin\theta_t &= \left(\frac{n_i}{n_t}\right)\sin\theta_i \\
&= \left(\frac{n_i}{n_t}\right)\sqrt{1-\cos\theta_i{}^2}
\end{aligned}
$$

$$
\begin{aligned}
cos\theta_t &= \sqrt{1-(\sin\theta_t)^2} \\
&= \sqrt{1-\left(\frac{n_i}{n_t}\right)^2\left(1-\left(\cos\theta_i{}^2\right)\right)}
\end{aligned}
\tag{4.28}
$$

$$
\vec{v}_{refraction} = \left(\frac{n_i}{n_t}\right)\vec{l} + \left(\frac{n_i}{n_t}\cos\theta_i - \cos\theta_t\right)\vec{n}
$$

Let $r = \frac{n_i}{n_t}$ and $c = \cos\theta_i = -\vec{n}\cdot\vec{l}$. The equation can then be expressed without trigonometric function names as

$$
\vec{v}_{refraction} = r\vec{l} + (rc - \sqrt{1-r^2(1-c^2)})\vec{n} \tag{4.29}
$$

As a validation for the updated method, a set of simulations were run for a five-layer model, with identical tissue parameters, but with one using the layered model and the other using the mesh based tissue model. The absorption is plotted as a function of depth in Figure 4.19. As expected, this shows the that two tissue models produce very similar results.

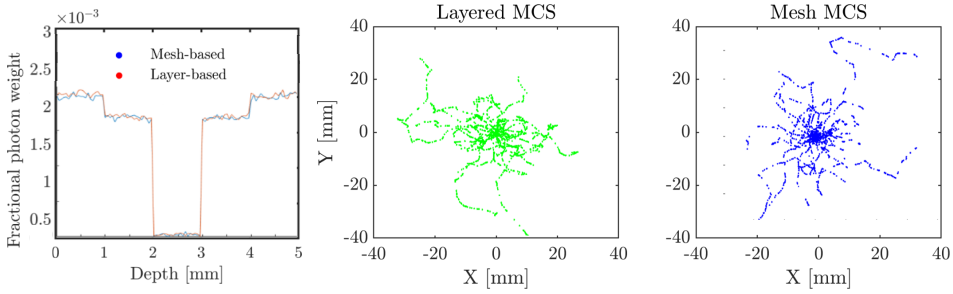

Figure 4.19: Results of two simulations of light transport through a five-layered tissue, with a layered and a mesh-based tissue model. The resulting absorption values across layers are very similar for the two approaches (left). The results were obtained from two simulations with 50 000 photons each. Absorption events plotted according to their [x,y]-coordinates for the layered (middle) and mesh-based (right) simulations. The spread is comparable for the two models as expected.

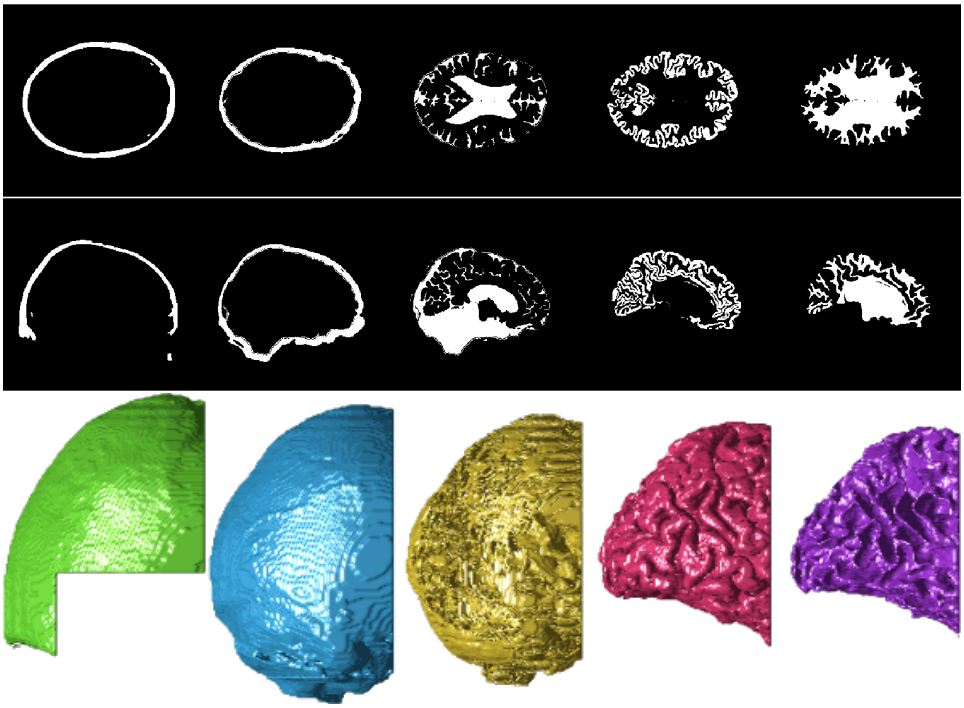

Figure 4.20: Segmentation of skin, skull, CSF, grey matter and white matter from structural MR data, presented left to right. The voxels belonging to the skin, skull, grey matter and white matter were extracted using FreeSurfer,[273] and the CSF defined as remaining voxels, with the exterior of the head thresholded out. The voxel data was limited to only contain the back of the head to reduce mesh size. The surface meshes shown in the bottom row were generated by applying the Marching Cubes algorithm to the segmented voxel data for each layer.

4.8.6 Segmentation and mesh generation

The mesh-based tissue model was generated from MRI structural data. The data was first segmented to create a mask for each of the volumes skin, skull, CSF, grey matter and white matter. Segmentation was performed using the software package FreeSurfer.[273] It produced surfaces identifying the grey matter and white matter from high resolution T1 and T2-weighted structural images. It also generated a 'brain mask' which identifies and removes the skin, skull and background from the images. These three data sets were imported into MATLAB along with the raw data for further processing, where intensity filtering was used generated voxel masks for the skin, skull and CSF.

A 3D mesh was generated based on the voxel data of each mask using the Marching Cubes algorithm. Originally presented by Lorensen and Cline

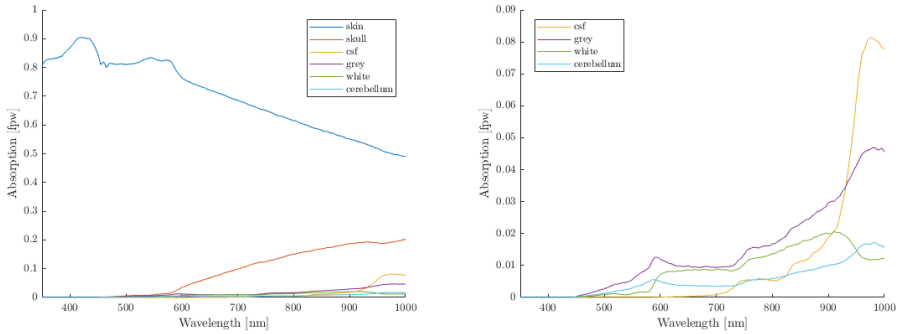

Figure 4.21: 3D mesh-based simulation results showing the wavelength-dependent absorption for each layer. The skin is responsible for the majority of the absorption, with only a few percent of the photon weight reaching the grey matter.

in 1987 for visualising MRI and CT data,[274] the method has undergone development, notably by Chernyaev[275] to improve topology preservation, and is today considered robust and computationally cheap, making it the most popular algorithm for extracting isosurfaces from volumetric data.[276] The segmentation results and reconstructed volume surfaces are shown in Figure 4.20.

4.8.7 Results

The layered model used for comparing model variations originally consisted of layer thicknesses [3, 3, 2, 4, 9] mm for skin, skull, CSF, grey and white matter respectively. To compare layered and mesh-based results, the layer model was rerun for layer thicknesses similar to those in the mesh data. To estimate the 3D model layer thicknesses, intersection tests were done using the participant's extracted mesh data. A photon was represented by a ray corresponding to the original photon launch direction, and the intersection of this ray was determined for each mesh, yielding the separation between subsequent surfaces. The measurement was repeated and averaged across a small region on the surface of the back of the head on the model, here with 11×11 rays covering a 2mm $\times$ 2mm window. These thicknesses, averaged across participants and given in Table 4, were used in a new layered simulation to provide a better comparison. Results shown below were more similar to the mesh model both in shape and magnitude.

The grey matter absorption in the two models is compared in Figure 4.22. The mesh model appears to give ≈ 3 times the absorption in grey matter,

Table 4: Tissue layer thicknesses estimated from 3D MRI data

Tissue	Thickness [mm]
Skin	8.5556
Skull	5.8535
CSF	3.4528
Grey matter	6.0926
White matter	26.0455

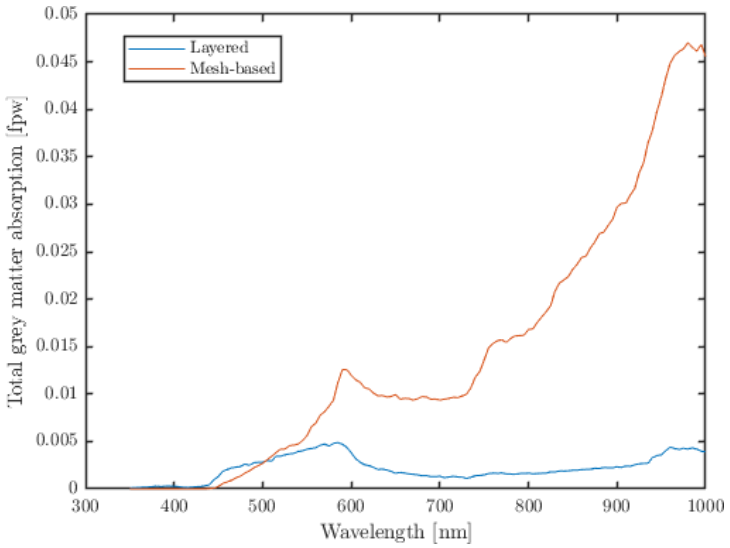

Figure 4.22: A comparison of the grey matter absorption estimated with a layered and a mesh-based simulation. When using layer thicknesses measured from the MRI structural scans to parameterise the layered simulation model, the results are in some agreement for the lower end of the spectrum, with the mesh-based simulation indicating a greater degree of absorption towards the higher wavelengths than the layered model.

with a reduction in absorption around the lower (< 800 nm) wavelengths compared with the layered model results. This is likely due to differences in layer thicknesses, as these will vary spatially for the mesh model, and a thicker skin layer could have a marked effect on absorption, as indicated by the impact of the melanin fraction showed earlier. The more complex surface might also more effectively trap photons, which would undergo more transitions between volumes, potentially increasing overall absorption. Figure 4.23 shows results for the 'informed' layered model, parameterised using the best estimates of layer thicknesses based on participant MR structural data.

The grey matter absorption results are in some agreement with the study

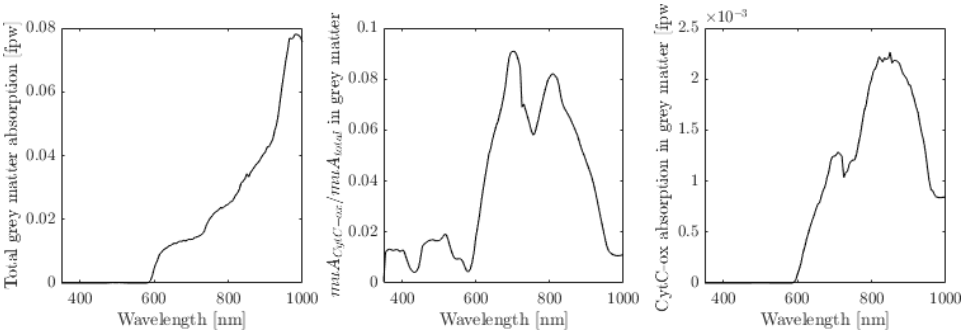

Figure 4.23: Simulation results from a layered model parameterised with layer thicknesses from the structural MRI data. The fractional photon weight absorbed in the grey matter (left), the fraction of μ_a in grey matter which is caused by cytochrome-C oxidase (middle), and the calculated fractional photon weight absorbed by cytochrome-C oxidase within the grey matter (right). Only about 0.1-0.2% of the light applied is estimated to be absorbed by Cytochrome-C oxidase.

Table 5: Variations in scalp and skull thicknesses with bulb positioning for example participants

		Min	Max	Mean ± stdev
Scalp	Participant 1	7.2643	14.0816	8.8938 ± 1.9066
	Participant 2	4.2765	11.9837	7.6447 ± 1.7976
	Participant 3	6.8449	25.6113	12.1934 ± 5.9651
Skull	Participant 1	4.3213	7.4759	5.9057 ± 1.0302
	Participant 2	3.1980	8.8959	5.0131 ± 1.5541
	Participant 3	3.0704	9.1435	5.7416 ± 1.7258

from Wong-Riley et. al (2004).[256] The greatest activation they observed occurred where absorption is high in the figure (830 and 670 nm), and the least activation occurred at 728 nm, where absorption is low, however the absorption was also high for 880 nm.

The layer thickness estimation method was used to test the effect of bulb positioning on the photon trajectory. Similarly to before, $2mm \times 2mm$ regions were sampled using packets of 11×11 rays, and this process was repeated for 3 yaw angles and 5 pitch angles, as indicated in Figure 4.25, with rotations of [-30, 0] degrees and [-30, 30] degrees respectively, relative to the center of the head. As summarised in Table 5, the incidence direction can have a significant effect on the tissue thickness along the line of initial photon trajectory, with layers doubling or more. Seeing as absorption is so dominant in the scalp, this is definitely worth considering when designing such an experiment.

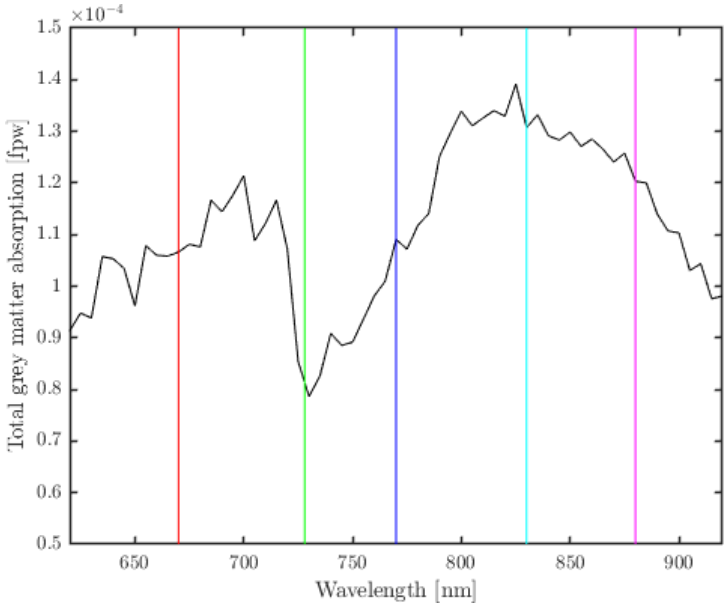

Figure 4.24: Zoom in over the relevant region of the cytochrome absorption with the wavelengths sampled by Wong-Riley et. al[256] highlighted.

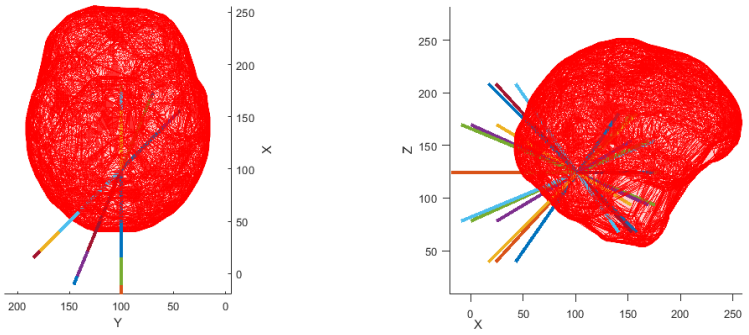

Figure 4.25: The effect of bulb positioning on the effective layer thicknesses was tested through repeated ray intersection tests for 3 yaw angles (left) and 5 pitch angles (right). Only the mesh for grey matter is shown for clarity.

4.8.8 Future work

The mesh-based model is more computationally intensive than a voxel-based model, and there is likely ways to reduce processing time. Simulation time varies significantly across different optical properties, and the overall duration is in practice reliant on the number of computation nodes, photon number and boundary conditions. However as a rough indication, the typical run time for a job from the mesh-based simulation used in this study was 3-4 hours, while for the layered model with the similar tissue thicknesses the duration was 5-15 minutes. This is because the test for interaction between the photon and the mesh surface requires a large number of ray-triangle intersection tests, rather than checking for a layer boundary in only the voxels along the photon step size, which can be found by their coordinates. The intersection test itself is fast, the Möller-Trumbore algorithm has been described as the fastest option for the generic case,[277] however reducing the triangle count for a less detailed surface could help speed up simulation at the cost of model accuracy. The algorithm could be developed further to reduce the number of triangles tested per step, for example by subdividing the meshes by grouping their vertices into 'boxes' by coordinates (like an octree) and only testing boxes within range of the photon, which could reduce computation time.

The simulation assumes the light source is an infinitely narrow photon beam. A more realistic photon launch path could be chosen by representing the light source as a planar or spherical source, which has been done in published simulations. For this study, the photons could for example have parallel starting directions, but the origin of the ray could be picked by randomly sampling points within a circle parallel to the back of the head with radius equal to the lamp. Future work might consider the lamp geometry, as well as its distance from the head surface. The present work does not account for heat, which might become a relevant factor with a closely positioned bulb and over time. It also does not consider the effect of hair, with the participants generally having light hair colours. Hair colour is dependent on the content of melanin, which affected absorption in the case of skin, the effect of hair colour and thickness could therefore have an impact, and should be explored.

5 Functional MRI in the animal model at 7T

This chapter describes the functional MRI experiments performed using a rat model at 7T. The experimental design and data acquisition is outlined, and the analysis process is considered. The results are presented and discussed, with comparisons drawn with analogous functional measurements performed on human volunteers at 3T.

5.1 Introduction

There are several advantages to using an animal model for MR studies. With the application of anaesthesia, the animal can remain in a physiologically stable state for several hours. During this time, vitals can be monitored to ensure consistent physiology across trials and across experiments, and adjustments can be made as needed to maintain breathing, heart rate and temperature. This minimises confounding factors such as movement and changes in alertness, which could affect measurements in awake human subjects. Common routes for eliciting functional responses in the rat include electrical stimulation of the whiskers, fore paw stimulation, or puffing air against the whiskers. With the option for long duration experiments, animal models have the advantage of enabling more repetitions, which increases statistical power. Repeats can be separated by long enough intervals to ensure relaxation back to the baseline.

The model opens up for a wide range of different types of experiments. Contrast agents can for example be administered to increase SNR during experiments, or to achieve a specific contrast to investigate other aspects of the functional response. Hypercapnia experiments can be performed to elicit a change in blood flow and volume, as described in Chapter 2. Some experiments rely on the application of drugs. An example of this is bicuculline, which when applied to the brain or to brain slices generates strong responses similar to a stroke. This is used in studies of epilepsy. It has been used in studies of DWfMRI, as these gross changes are more easily detected than physiological neuronal activity. A wide range of experiments can be performed on the rat model through concurrent imaging with other modalities such as optical imaging.

There are however drawbacks of this method. As discussed in Chapter 1, it is possible for the behaviour of neurovascular coupling to change, and

an example of this is under anaesthesia. Anaesthesia weakens the haemodynamic response to stimulation, as has been shown in concurrent fMRI and OIS studies.[148] This can have an impact on results from BOLD studies, where the signal might decrease by as much as a factor of 5.

The small animal scanner allowed greater flexibility in sequence design than the human scanner. As it cannot be used for scanning humans, the available sequences do not require the same level of validation, so pulse programs can be viewed, and certain changes can be implemented. This for example allowed the phase gradient to be switched off for a given sequence, to perform line scanning, which is discussed in Section **??**. The scanner also features accessible trigger outputs, which can be used for monitoring for example RF via BNC cables. This provided more information on exact sequence timings, as well as the trigger outputs required for running the optical setup. A few considerations should be made however when comparing functional MRI data recorded at different field strengths. Increasing field strength means the magnetic field becomes less homogeneous, which contributes to higher magnetic susceptibility related artifacts in the EPI images.

5.2 Experimental design

All work with animals was performed with UK Home Office approval under the Animals (Scientific Procedures) Act 1986. The necessary accredited training (PIL A, B and C) was completed prior to the start of experiments. Further training was done in-house, with each protocol signed off for competency.

5.2.1 Stimulus presentation

In the animal model, activation was achieved with a whisker stimulus as outlined in Chapter 2. Each experiment began with an initial delay acting as a baseline measurement, where data was collected in the absence of any stimulus. The stimulus was typically applied for a duration of 16 seconds, with an interval of 80 seconds between trials. The stimulus was repeated for a number of trials to increase statistical power. The spacing in between stimuli should be sufficient to allow time for the biological response to play out, which can take over a minute.[149]

The stimulus train was started by a trigger TTL pulse from the scanner. The trigger can be set to fire at the acquisition of a slice or at the start of a new volume, and is enabled controlled via the options in the trigger card of the scan window. For BOLD, the CED was triggered to begin both output and recording at the start of the first slice. The DWfMRI sequence did not have a trigger out option, so for these scans the RF blanking pulse was used instead.

5.2.2 Acquisition of MR data

Structural T1 and T2 images were acquired using the in-built T1Flash and T2TurboRARE scans. These were captured in-plane with the functional scans, with TE 35.32 ms, TR=2500 ms, FOV = 96 × 96 voxels of 35 × 35 mm and slice thickness 1 mm.

Functional BOLD experiments were performed with a T2starFIDEPI sequence (TE=10.88 ms, TR=1000 ms, FOV = 64×64 voxels of 35×35 mm). DWfMRI used the DtiEpi sequence (TE=74.04 ms, TR=1000 ms, FOV = 64 × 64 voxels of 35 × 35 mm, 10 dummy scans). BOLD was typically set to acquire 3 slices, while DWfMRI was single slice, this was done to avoid overexerting the system for higher b-values. With the small region to be imaged and strong gradients required to reach the target b-values, the system was on occasion pushed quite hard towards its capacity. Before running an adjusted EpiDti, the duty cycle was therefore tested using the duty cycle simulation, which was available under the adjustment window of the scanner software. This predicts the gradient strength as a fraction of the maximal achievable output. This prediction is evaluated for several time points throughout the proposed scan, and is used to ensure the gradients will not pushed too far. The b-values and sequence timing parameters were adjusted to make sure the duty cycle did not reach above 70%.

Line scan was based on a modified FLASH sequence. The method requires the phase gradient be turned off, this causes data from the same region to be acquired per phase step, trading in image information for an increased sampling rate across time. No option for this exists in the scan card; the adjustment was made by making a small edit to the pulse program.

5.3 Results

The analysis pipeline for animal MR data was similar to that used for human data, with the changes made being due to the differences in image size and quality. After any spatial smoothing and the temporal filtering to exclude low frequency signal changes, the active voxels were determined and time series extracted. Registration was not used for the animal work. The breathing rate was kept consistent, and the animals' heads were secured in place during experiments, movement should therefore be minimal.

5.3.1 Determination of active voxels

The active voxels were identified using GLM, with a design matrix featuring a square representation of the applied stimulus. The voxels considered active after thresholding with a given Z-score, were then typically filtered to remove noisy data. This was done first by applying a mask to include only the region of the image showing the head, by setting the Z-score to 0 if the image intensity was below a cutoff-value. This removes contributions from noise located in the lower signal background. The active voxels were then filtered to only include clusters of a certain size.

Figure 5.1 shows an example of BOLD and DWfMRI activation maps from a whisker stimulus (16 s on, 80 seconds off, 7 repeats). This demonstrates the level of noise in the data after a simple GLM ($Z > 2$), and the difference made by the mask and cluster size filtering. The diffusion weighted images are somewhat noisier than the BOLD, as expected from the lower SNR, but the activity is still clearly visible in both cases, with a Z-score of up to 9. There is a distinct shift due to distortion. This should be kept in mind for any comparison of the spatial origin of the signals, which would require a spatial transformation.

Figure 5.2 shows the extracted responses from the identified active regions. Again, the DWfMRI time series is noticeably noisier, yet the active epochs can be identified above the noise, with around 2-6% change in signal from baseline.

5.3.2 The effect of different b-values

A 16 second stimulus (80 second interval, 7 repeats) was repeated for BOLD and for DfMRI with different b-values. For comparison, all resulting data

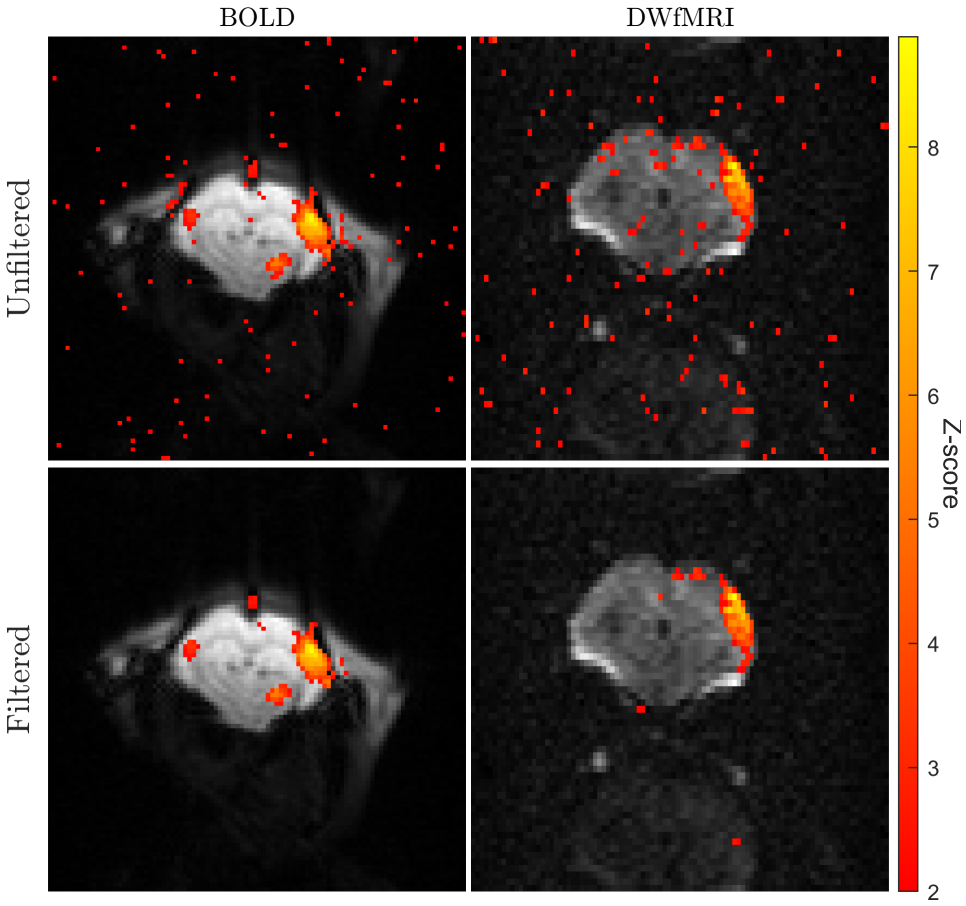

Figure 5.1: Activation maps from a BOLD (left) and a DWfMRI experiment (right) in the same animal. The top row shows the unfiltered maps, after performing GLM with a square stimulus design matrix. For the lower row, the maps have been masked to exclude voxels outside the head, and filtered by cluster size (≥ 5). This removes the majority of the noise.

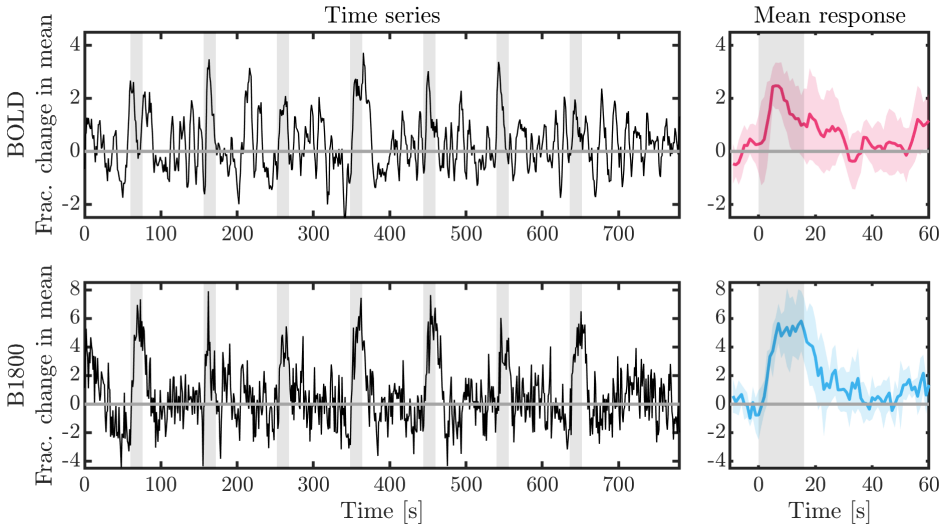

Figure 5.2: The time series and average responses extracted from the BOLD (above) and DWfMRI b=1800 s/mm^{-1} (below) based on the activation maps in Figure 5.1. The DWfMRI time series is more noisy as the diffusion weighting reduces SNR.

sets were analysed using a Z-score of 2, and no cluster size thresholding was performed. The activation maps for the different b-values are shown in Figure 5.3, with the extracted responses from the active regions plotted in Figure 5.4.

The activation maps also appear very similar between experiments, with the activation area for b=0 s/mm^2 appearing somewhat larger, but with all responses occurring in the same location close to the cortical surface. From the averaged time courses shown, it appears the diffusion weighting has very little effect on response shape. This is in contrast to what would be expected from the results from Le Bihan et al. The response from the b=0 s/mm^2 experiment should not have any diffusion weighting, yet the response onset is just as rapid. In fact, there appears to be no broadening or plateau of the b=0 signal or dip beyond the baseline as associated with slower hemodynamic changes, perhaps indicating a sensitivity to primarily arterial components. Vitals could have deteriorated and affected the lower b-value scans done later in the day. Since there is no optical data to compare it with, it is possible that stimulus response differed between experiments. This is a confounding factor which could also apply to the human data in the original work by Bihan et al.

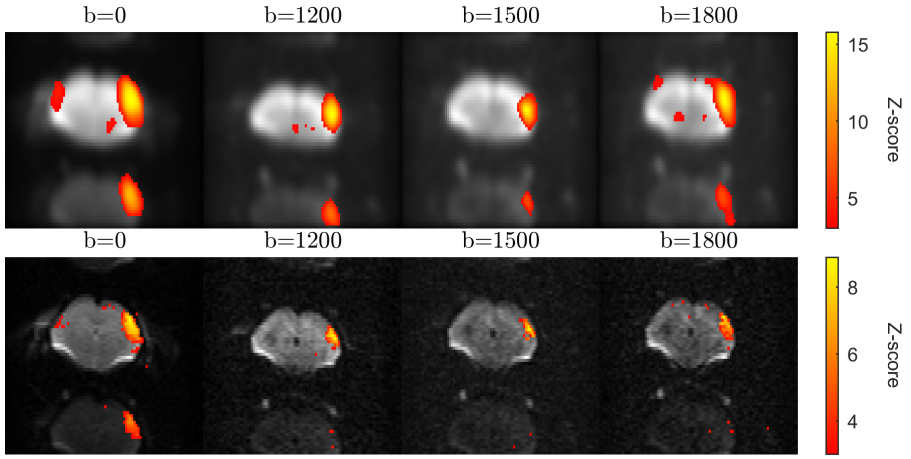

Figure 5.3: Activation maps from DWfMRI experiments with a 16 second stimulus, measured with different b-values in the same animal. The Z-score was thresholded to $Z \geq 3$

5.3.3 Hypercapnia

Hypercapnia experiments were performed using DWfMRI with b=0 and b=1800 s/mm^2. Figure 5.6 shows the activation maps and time series for each case. GLM was performed with a 150s delay rather than 60 seconds baseline used, to better characterise the slow response. As HCN should primarily elicit a hemodynamic response without significant neural activation, the BOLD measurement was expected to show a greater signal change. This can be seen in the figure, however the effect is not removed by the diffusion weighting, and the DWfMRI signal therefore appears to contain hemodynamic components. The signal is less localised to the surface vessels than BOLD, and appears noisy, however the time course corresponds to that of a hemodynamic HCN response. The two experiments were performed on different animals on different days; there could therefore be a difference in baseline physiology between the two responses. The hypercapnic event tends to affect the state of the animal as indicated by the vitals measured, so subsequent experiments on the same animal might still be measured under different physiological conditions however. The experiment also induces changes in breathing rates, and gasping could cause movements in the animal which could affect the response shape. Due to persistent difficulties with noise on the scanner system, only one set of data was collected for each of these experiments.

Hypercapnia results could have been affected by the design of the gas

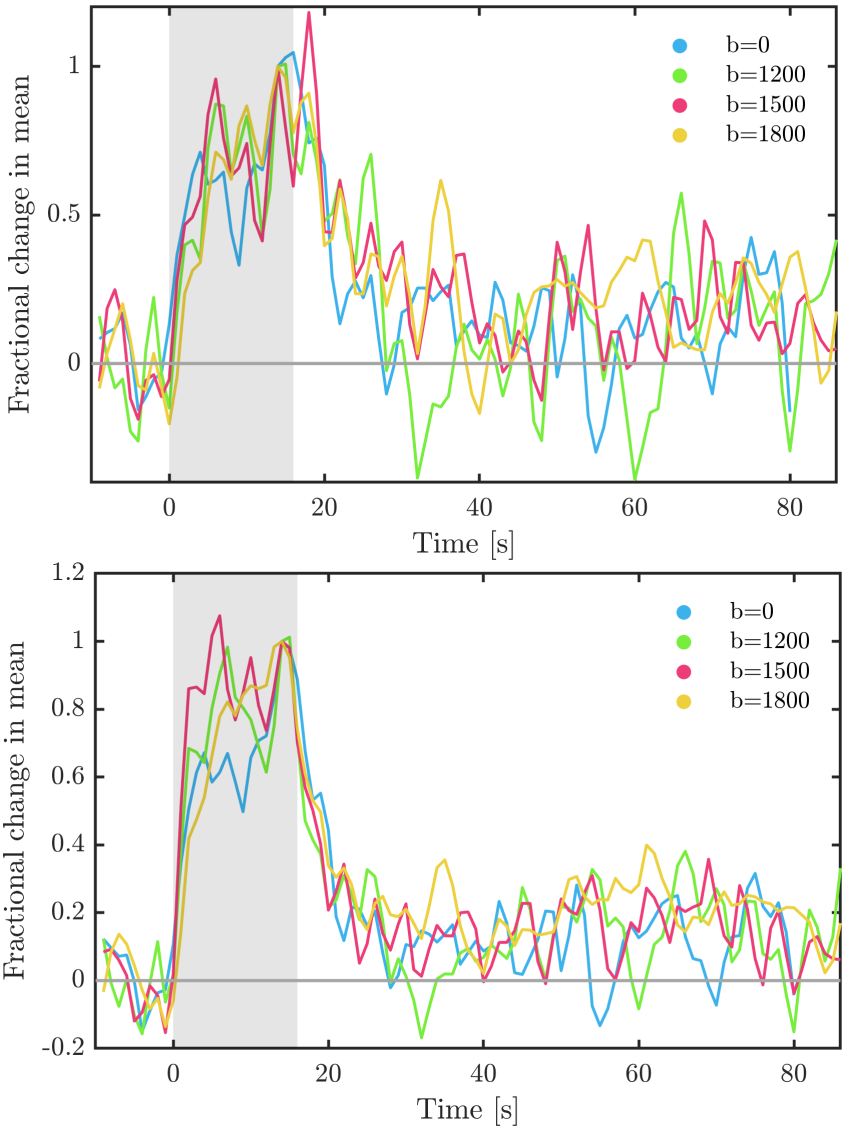

Figure 5.4: The DWfMRI responses to a 16 second stimulus recorded at four different b-values, with normalised amplitude. The responses appear very similar in shape, all with a rapid onset at the start of the stimulus. Notably, this is also the case for the b=0 s/mm^2 experiment, even though there is no diffusion weighting, and the response is hemodynamically driven.

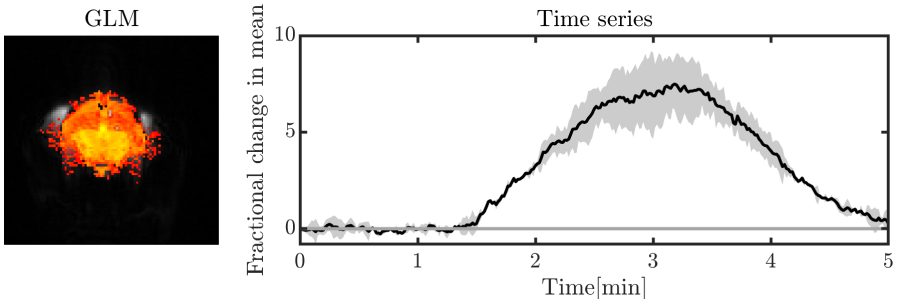

Figure 5.5: Hypercapnia results from BOLD experiments. A representative activation map (left) shows the whole brain responding during the event, with the design matrix consisting of a 120 second square stimulus with a delay of 90 seconds rather than 60, to bring out the delayed response as shown in the time series (right). The time series shows the average response to hypercapnia across 3 animals.

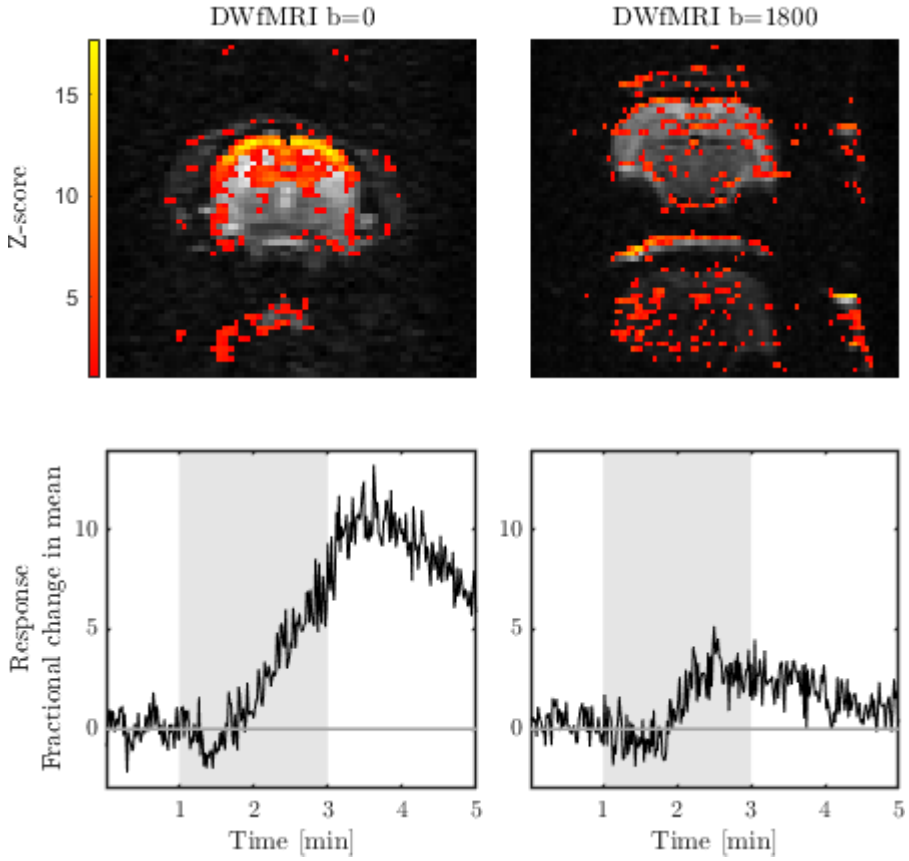

Figure 5.6: Activation maps (above) and time series from hypercapnia experiments using diffusion weightings of b=0 (left) and b=1800 s/mm^2. The timing of the addition of CO_2 into the gas mixture is highlighted by the grey box. Activation maps were produced using a design matrix with a 2 minute square stimulus delayed by 90 seconds (as with BOLD in Figure 5.5). The higher diffusion weighting appears to filter out much of the slow response, and provide a faster return to baseline.

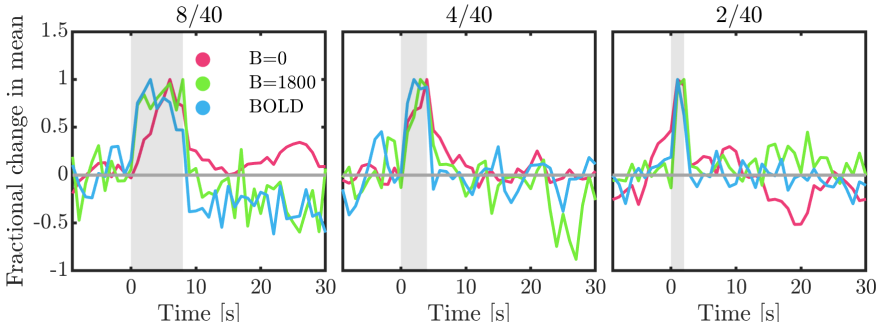

Figure 5.7: The normalised average responses for different stimulus durations, with 8 seconds, 4 seconds and 2 second stimuli left to right.

delivery system. The ventilator is located outside the magnet room, which necessitates the use of a breathing tube long enough to reach into the scanner bore, a distance of close to three meters. The delivery of the CO_2 to the rat is therefor likely to be delayed relative to the start of gas addition into the supplied air. There might also be a delayed effect from the gas travelling through the ventilator itself. This could potentially be alleviated against by moving the gas source closer to the animal.

5.3.4 Stimulus duration

Data was acquired for different stimulus durations, repeating the stimulus timing which were used for the analogous experiments in humans. The responses were acquired with BOLD, and with DWfMRI, using b-values of 0 and 1800 s/mm^2. The averaged time courses are shown in Figure 5.7. Here, the rapid onset is evident in all experiments, except for the b=0 s/mm^2 measurement of the 8 second stimulus. This reading was likely affected by noise, or acquired during a time of irregular physiology, as there was little response on the activation map, which is shown in Figure 5.8. The BOLD and diffusion weighted data otherwise follow very similar time courses for a given stimulus. There is therefore no indication of these methods being driven by different biophysical processes.

The shorter stimuli are likely more sensitive to noise than the 8 second stimulus, especially the 2 second stimulus, whose response width of only two frames is similar to the spiking observed in very noisy data. 10 repeats were used for each of the experiments to increase statistical significance, however the analysis needs to detect the signal occurring for only two frames

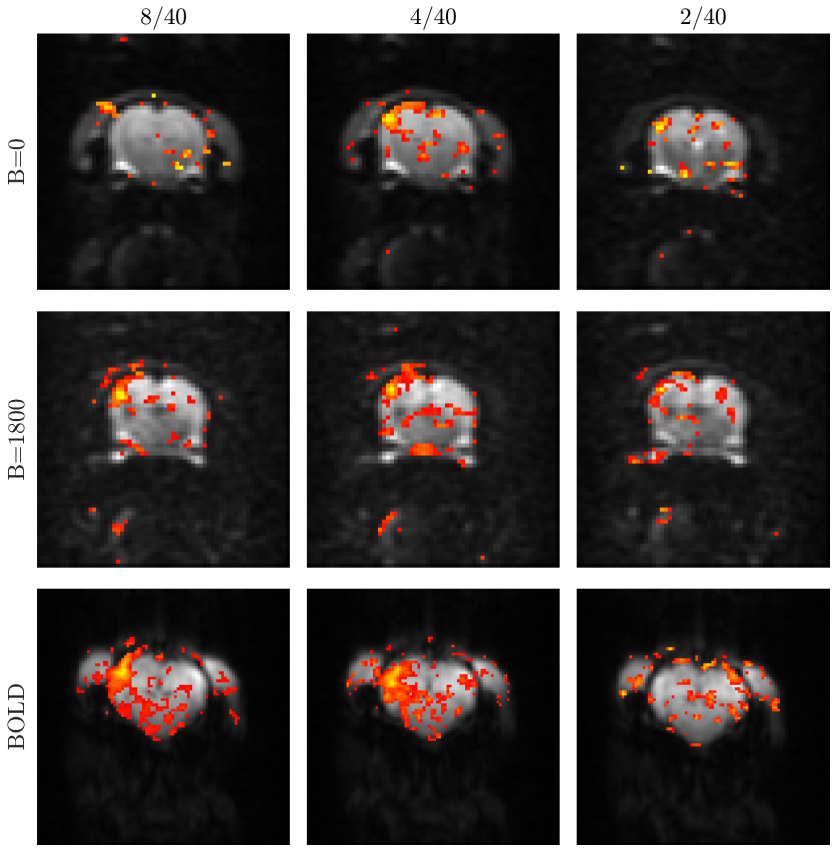

Figure 5.8: The activation maps from b=0 s/mm^2, b=1800 s/mm^2 and BOLD experiments, using different stimulus durations.

per repetition, so the very short stimuli were difficult to extract. From the diffusion activation maps, there appears to be activation in the target region, however the z-score is not much greater than in other areas where noise occurred.

A study by Urban et al performed similar whisker stimulation in rats in 2015, using functional ultrasound.[278] They observed a much faster return of CBV to baseline after a 1 second stimulus than for a 7 second stimulus. This was attributed to a balloon-like effect, which is dependent on the stimulus duration. Here, there is no noticeably slower recovery of the 8 second stimulus. This might be affected by the physiology of the animal during the experiment. Alternatively, the selected region might be weighted toward the arterial parts of the response, as the balloon-effect also varies by depth. Tian et al measured CBV in rat with depth-resolved fMRI, reporting a slow recovery of CBV in higher order arteries in combination with post-stimulus undershoot in lower-order arteries and on the surface.[95] This leads to a smoothing of the sharp arterial response by processes in other parts of the vasculature.[279] Any such depth resolved effect would likely be more apparent with higher imaging resolution.

The 8 second stimulus BOLD experiment appears to show negative BOLD (Figure 5.9). The amplitude is small, but the effect is clearly visible across a region with a significant Z-score. This was not visible for the shorter stimuli, these might have been too short for the negative response to come into effect, as this has been show to be dependent on stimulus duration.[280] Negative Z-scores are also found in the same region in the DWfMRI activation maps, however the relevant voxels are less clustered and could be caused by noise. If there is a negative BOLD effect, this might indicate the diffusion weighted response is weighted by heamodynamics, as the effect is thought to be related to blood flow, and linked to decrease in the local oxygen consumption.[281]

5.3.5 Line scanning

Following the work of Nunes et al,[217] line scanning[218] was performed during stimulus to investigate the cortical depth dependence of the response. They implemented DWfMRI imaging at a temporal resolution of 100 ms for investigation of the fast response.

The line scans benefit from an approach known as Large-Tip-Angle imag-

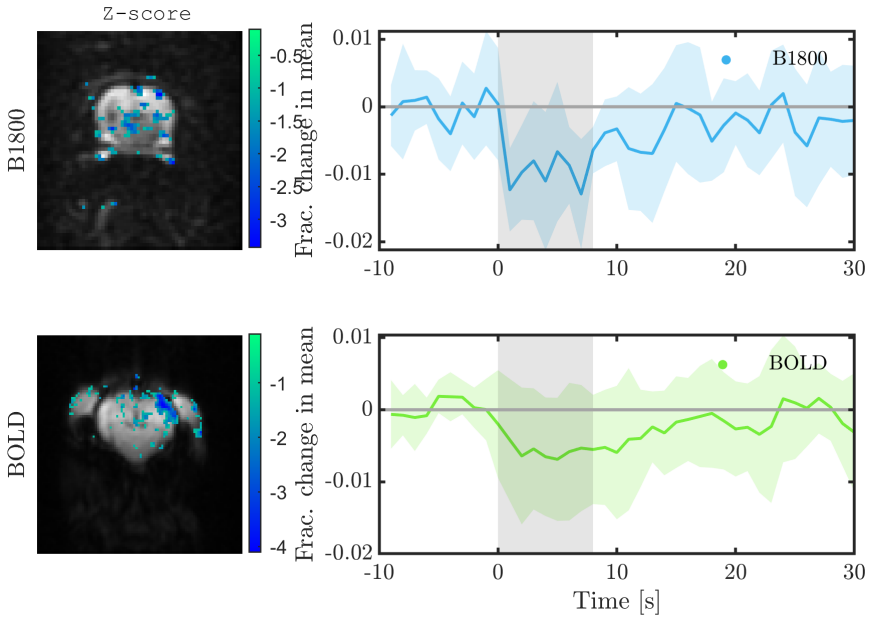

Figure 5.9: The activation maps from the 8 second stimulus BOLD experiment shows a region of signal decrease during activation. This appears to show negative BOLD, which is small in amplitude, but easily distinguishable in the activation map. The DWfMRI maps also have negative z-scores in this region, but it is not clear whether this is significant or an effect of noise. The DWfMRI response on the right was extracted from only the 'active' voxels within the region shown for the BOLD data.

ing.[219] In spin-echo sequences, the TR is restricted by the signal to noise ratio; the SNR reduces as the TR is shortened. This is due to the longditudinal magnetisation magnitude depending on the TR. Standard SE imaging uses a 90° pulse followed by one or more 180° refocusing pulses. By using a large tip angle of more than 90°, the longditudinal magnetisation magnitude will be larger after the initial 180 degree pulse, increasing the signal.[282] The tip angle is optimised between 90 and 180 degrees, and depends on the TR and the tissue T1 value. The angle is optimised so it is equal to the GRE Ernst angle right after the 180 degree refocusing pulse, by subtracting the Ernst angle from 180 degrees. The resulting SE sequence should give a higher signal than a GRE sequence with the same TR and TE values because unlike GRE, SE compensates for the static field heterogeneity. The LTA approach can increase signal in cases where the T1 relaxation is equal to or longer than the TR, and can be used to achieve good contrast even with lowered TR and therefore reduce imaging time.[219]

Line scans were performed using the Ernst angle to increase the signal. The Ernst angle is the flip angle which maximises the T1 weighted signal, and can be determined using Equation 5.1.[283] The optimal flip angle will be 90° only when TR >> T1. In the brain, where the average T1 is 800 msec, the optimal angle changes significantly for low TR. Although it maximises signal, imaging is not necessarily done near the Ernst angle, as with multiple tissues it becomes important to obtain maximum contrast. Here, A T1 of 1939 ms was used, based on measurements of human grey matter T1 at 7T.[284]

$$\alpha_E = \arccos e^{-\frac{TR}{T1}} \tag{5.1}$$

As the pulse program has been changed, the line scan data had to be manually reconstructed from the raw FID data. This was a long set of digits, with the alternating data points representing the real and imaginary parts of the signal. The data is first expressed in complex form, then rearranged into a 2D array to form the image with dimensions equal to the read direction FOV specified in the scan protocol, against the number of repetitions multiplied by the number of phase steps. Then, a Fourier transform is applied to the data and the absolute value determined per pixel.

Figure 5.10 demonstrates the extraction of temporal data recorded in a BOLD line scanning experiment, and the resulting time series is shown

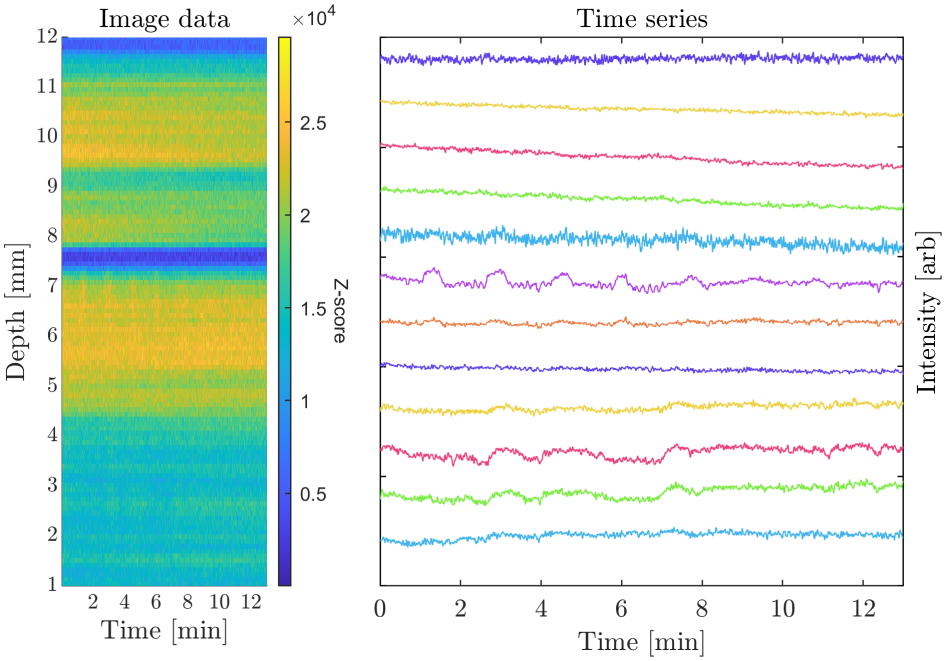

Figure 5.10: Demonstration of data analysis for an example line scanning data set from a BOLD experiment using a 16 second stimulus. The time series (left) were extracted by averaging step-wise across the image data in the phase direction, each window covering 10 lines, corresponding to a depth interval of about 0.94 mm.

in Figure 5.11. The time series was averaged across 4 lines along the read direction, over the indices corresponding to the location of the grey matter at a depth of 0.6-0.8 mm relative to the animal head surface. The DWfMRI line scan experiments did not succeed, implementing the sequence involved making changes to the pulse program, and it was only later discovered that due to an error in this updated sequence the phase gradient had been left on.

5.4 Discussion

A significant challenge to MR acquisition was intermittent external noise. Often, a functional scan would progress fine until the signal suddenly dropped out, causing the images collected to contain only static noise. Data from the unaffected repeats could sometimes be extracted, but the noise tended to cause dropped frames, which prevented reconstruction. Attempts were made to prevent this, including using shielded BNC cables for the equipment outside the magnetically shielded room, and temporarily disconnecting

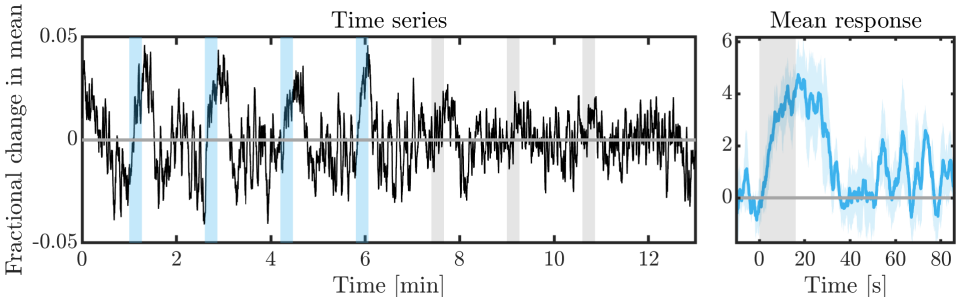

Figure 5.11: Example of a time series and average response extracted from a BOLD Line scan. Only the repetitions highlighted in blue were used to determine the average response.

equipment in turn during scans. The scanner was inspected by a qualified engineer, but the noise persisted despite various modules and the software being swapped out. The source was eventually identified as a damage to the connection between the PSD power board and HPPR module, which had occurred during drilling in connection with construction work outside the building.

Noise was also a hindrance to combining fMRI measurements with optical data acquisition. A concurrent OIS and MRI experiment was performed using a custom surface coil. This was required for visibility through to the cranial window for imaging, which is blocked with the standard setup, and the signal would be much too reduced if no surface coil was used. The coil was made using copper tape, which was attached to the underside of the optical well. The power output of the coil was limited, with the setup not able to generate a 180° pulse, which limited the use of spin echo sequences. The spin echo diffusion sequences therefore gave poor signal. The experiment could potentially work with a better coil design, however the power limitation is especially detrimental to DWfMRI, which already relies on reduced signal from the diffusion weighting.

The activation maps for DWfMRI showed much clearer active regions for the animals compared to the human case. The time courses also appears less dependent on b-value in the animal data, with response shapes remaining quite consistent with the b=0 response, even for high b-values. The differences observed between the rat data and human data could be caused by differences in experimental design. Although visual stimuli in humans and whisker stimuli in rats are standard models of neuronal activation, the measurements made might not directly comparable. Rats use their whisker

sensitivity to a great degree during minute-by-minute activity, as humans do visual perception. The two processes operate via different neural pathways however, and there could be a difference in the underlying biophysical mechanism of the responses. There could also be a difference in sequence timings between the two scanners, and perhaps even differences between the effective b-values. There could also be an effect related to differences in physiology, such as the neuronal cell density, and also structural differences of for example vasculature between rats and humans. Being recorded at different magnetic field strengths, the sensitivity to changes occurring in the different parts of the vasculature could vary.

The physiological state during the experiment could have an impact on the response shape. As discussed in Chapter 2, anaesthesia is likely to impact on the response in the rats. For humans, attention might drift during an experiment, and responsiveness could be affected by factors like sleepiness or caffeine. The effect of basal conditions was investigated by Cohen et al, who applied visual stimuli in humans first by itself, then during a period of hypo- or hypercapnia.[285] While the stimulus produced a fast response under physological conditions, the response to stimulus during hypercapnia was markedly different, with an almost complete exclusion of the arterial part of the response. Although every effort was made to maintain the animal in a stable condition, it can not be ruled out that changes to the physiology occurring over time could have had an impact on the response shape.

There has also emerged evidence, based on a rat model, of brain states having an effect on the functional response shape, and in particular affecting the rapid part of the response. Slack et al.[286] observed that recorded fMRI data could be classified into two different brain states by use of a neural marker based model initialised using LFP recordings. They grouped results from the trials recorded during each of these states, referred to as synchronised and desynchronised. They found that the heamodynamics for the sychronised state showed an early peak around 5 seconds after stimulus onset, followed by a plateau and return to baseline, while this initial peak was not present in the desynchronised state, which instead rises towards the later peak of around 16 seconds after onset.

Although line scanning was not fully explored in this thesis, this method has the potential to provide some very interesting information on the DWfMRI signal. Imaging with faster acquisition rates could help detection of the short

duration stimuli. It also offers valuable depth-dependent information which could be explored further. On activation the arteries dilate rapidly, and the venous response is much slower. The BOLD response is delayed relative to the arterial dilation because the oxygenated blood takes time transferring into the capillaries and veins.[287] The BOLD fMRI response has been measured as a function of cortical depth in the rat model.[95] This showed a greater 'dip' in signal post stimulus from the cortical layers close to the surface, along with a more significant initial dip and larger amplitude at the peak of the response. Their acquisition protocol used a 1 second TR, but the stimulus onset was jittered between stimulus repeats. This way the data could be collected at different time points along the stimulus time course, which allowed them to estimate the response with a higher temporal resolution. When acquiring signal from a cortical region which spans across these layers, the functional MR temporal signal might become smoothed out to include contributions from both ends of this behaviour. Line scanning could provide the rapid imaging required by such an experiment without the need for jittering, ensuring the same biological response is sampled at all depths for a given time point.

6 Conclusion

This thesis presents experimental design and acquisition of fMRI and optical imaging data, the steps and considerations made in analysis of this data, and the implementation of modelling tools used to interpret results and theoretically explore the method limitations. The work has had a particular focus on method developments, and has therefore highlighted some of the challenges involved with functional MR imaging, optical imaging and the attempt to apply these methods concurrently.

There are certain barriers which complicate research on DWfMRI, with key challenges being the lower signal compared with BOLD, and the lack of a standardised sequence design. Several articles in the field leave out details when describing their acquisition protocols, for example regarding the choice between monopolar or bipolar gradients, or reporting only the b-value and not full sequence timings, which is not sufficient information to characterise the sequence. Changes in this design could be particularly impactful on the lower SNR signal. This makes the work harder to replicate and validate, and has likely contributed to the variation in observations and conclusions reported in the literature.

The built-in diffusion based sequences on MR systems are not set up to be used for functional imaging, and investigators must therefore rely on importing or developing custom sequences, requiring additional time or specialised expertise to set up. Such sequences can be purpose-built for specific applications, and there is a risk that these have been optimised in ways that are detrimental for use in other contexts, for example by including unwanted filtering. If a sequence is built on proprietary code which is not publicly accessible, it might hide unwanted or poorly optimised features. The sequence might also not be easily tested, as the safety measures and restrictions on direct hardware access prevents direct monitoring. If parameters are not exposed in the scan card or made understandable, this could lead to different groups potentially obtaining quite different results from similar experiments.

The 7T scanner provided great flexibility, however measurements were often disrupted by significant noise due to a fault with the imaging system, which limited the amount of data that could be collected. Further complications arose from the inclusion of the concurrent optical setup, as the surface coil had to be replaced with a less efficient coil to allow for optical imaging.

Future work aiming to combine imaging modalities would benefit from an improved coil design.

Optical imaging was explored, and while hemodynamic changes could be measured with OIS, no scattering changes could be detected with SFDI. Any tissue structural changes occurring during normal brain activity may be too subtle to detect with the optical acquisition setup described in this thesis. Although SFDI has been shown to be sensitive to gross changes induced by the application of drugs, further experiments would be required to determine if the method is capable of discerning a scattering effect from physiologically normal response to stimuli. Improvements to the optical setup would likely be a good starting point. A higher caliber projection system could be developed to provide better resolution of the projection pattern, as well as higher intensity illumination, which could provide a greater amount of diffusely reflected light to base analysis on.

Challenges were highlighted both for imaging on the bench and within the bore. A key problem to solve for concurrent imaging is the transmission of light in and out of the bore, and in particular the challenge of retaining a structured illumination pattern with both good resolution and high enough intensities from outside the magnetically shielded room. Despite these challenges, concurrent imaging holds promise as a tool for understanding fMRI in the animal model. There was often great variation observed for repeat fMRI measurements in a single experiment, and concurrently collected optical and fMRI data would be ideal to understand how this related to variations in the underlying biophysical processes. This would provide a better basis to compare fMRI results between experiments. Additional information about the underlying mechanisms of activity is required to understand the measured DWfMRI signals, and concurrent imaging has great potential to provide this. Further concurrent work would therefore be beneficial as it could help establish the biophysical driver of the signal.

The overall poorer sensitivity of DWfMRI to activation than BOLD should be considered in data processing, as the effects of for example spatial smoothing was shown to differ between the two methodologies. From the results presented in the 3T study, it appears stimulus design can have great effect on the response shape. When recording repeat measurements of a response, time should be allowed time for the biological response to play out between repetitions. This is important for any interpretation of the response

time course, and it is especially important for comparison across experiments with different stimuli. Response shapes are also sensitive to stimulus duration, and this warrants further study. With the 1 second repetition time used, extracting the time course was not straight forward. Imaging with faster acquisition rates could help detection and improve characterisation of the short duration stimuli.

The DWfMRI results seem to suggest the response contains hemodynamic components, and that the shape is driven in part by arterial weighting. A fast response was observed, however no clear indication could be found of this early onset being independent of the heamodynamics. The early onset could be somewhat affected by noise. As seen in GLM activation maps, the square stimulus often shows correlation with noise, and voxels with spiking noise could be present in the DWfMRI data, giving additional square weighting. The rapid onset appeared reproducible however, being observed both in human and animal data and persisting for a variety of stimulus durations and intervals. The post-stimulus undershoot in the human BOLD data was significantly reduced or removed in DWfMRI showing reduced sensitivity to this slower vascular effect, indicating the hemodynamic components affecting the signal are related to earlier events. For shorter stimuli, both in human and animal, the rapid onset persisted in DWfMRI, but there was also great resemblance between the response shapes of DWfMRI and BOLD. There was therefore no definite proof that the rapid component of the DWfMRI signal was driven by a non-hemodynamic component which BOLD was not sensitive to, this effect might be present also in BOLD, but be occluded for longer stimulus durations by other longer-range parts of the composite signal.

The differences between animal and human results for similar experiments raise the question of how applicable observations of animal DWfMRI are to the human case. There is a need to consider the validity of direct comparison between responses from the visual stimulus versus the whisker stimulus, both in terms of potential differences in the underlying biophysical mechanism of the responses, and the impact of physiological states, particularly anaesthesia. Both factors relating to experimental design and physiology represent possible barriers to transferability. A key challenge here lies in the sequence design. Preclinical DWfMRI research, like research involving human participants, would benefit from a standardised protocol.

A standardised protocol would be an important step to making DWfMRI a clinically viable alternative. Currently BOLD is much easier to implement due to available sequences commonly being installed in most scanner systems, and the various settings are already in-place or well documented. Combined with the higher signal-to-noise ratio and activation maps which more clearly show active regions, BOLD maintains a clear advantage as long as no definite argument can be made for how DWfMRI might be a more direct measure of neuronal activity.

References

[1] Daniel A. Orringer, David R. Vago, and Alexandra J. Golby. Clinical applications and future directions of functional MRI. *Seminars in Neurology*, 32(4):466–475, 2012.

[2] Walter A. Hall, Peter Kim, and Charles L. Truwit. Functional magnetic resonance imaging-guided brain tumor resection. *Topics in Magnetic Resonance Imaging*, 19(4):205–212, 2008.

[3] Frédérique Liégeois, J. Helen Cross, David G. Gadian, and Alan Connelly. Role of fMRI in the decision-making process: Epilepsy surgery for children. *Journal of Magnetic Resonance Imaging*, 23(6):933–940, jun 2006.

[4] Seyed Hani Hojjati, Ata Ebrahimzadeh, and Abbas Babajani-Feremi. Identification of the Early Stage of Alzheimer's Disease Using Structural MRI and Resting-State fMRI. *Frontiers in Neurology*, 10(AUG):904, aug 2019.

[5] Franck Amyot, Kimbra Kenney, Emily Spessert, Carol Moore, Margalit Haber, Erika Silverman, Amir Gandjbakhche, and Ramon Diaz-Arrastia. Assessment of cerebrovascular dysfunction after traumatic brain injury with fMRI and fNIRS. *NeuroImage: Clinical*, 25:102086, jan 2020.

[6] Scott M. Hayes, Lee Ryan, David M. Schnyer, and Lynn Nadel. An fMRI study of episodic memory: Retrieval of object, spatial, and temporal information. *Behavioral Neuroscience*, 118(5):885–896, oct 2004.

[7] Morton Ann Gernsbacher and Michael P. Kaschak. Neuroimaging Studies of Language Production and Comprehension, 2003.

[8] Jerzy P. Szaflarski, Vincent J. Schmithorst, Mekibib Altaye, Anna W. Byars, Jennifer Ret, Elena Plante, and Scott K. Holland. A longitudinal functional magnetic resonance imaging study of language development in children 5 to 11 years old. *Annals of Neurology*, 59(5):796–807, may 2006.

[9] Eleanna Varangis, Christian G. Habeck, Qolamreza R. Razlighi, and Yaakov Stern. The Effect of Aging on Resting State Connectivity of

Predefined Networks in the Brain. *Frontiers in Aging Neuroscience*, 11:234, sep 2019.

[10] J. Jean Chen. Functional MRI of brain physiology in aging and neurodegenerative diseases. *NeuroImage*, 187:209–225, feb 2019.

[11] S Ogawa, T M Lee, A R Kay, and D W Tank. Brain magnetic resonance imaging with contrast dependent on blood oxygenation. *Proceedings of the National Academy of Sciences of the United States of America*, 87(24):9868–72, dec 1990.

[12] Marcus E. Raichle. Behind the scenes of functional brain imaging: A historical and physiological perspective. *Proceedings of the National Academy of Sciences of the United States of America*, 95(3):765–772, feb 1998.

[13] Richard D. Hoge, Jeff Atkinson, Brad Gill, Gérard R. Crelier, Sean Marrett, and G. Bruce Pike. Linear coupling between cerebral blood flow and oxygen consumption in activated human cortex. *Proceedings of the National Academy of Sciences of the United States of America*, 96(16):9403–9408, aug 1999.

[14] Robert Turner. How Much Cortex Can a Vein Drain? Downstream Dilution of Activation-Related Cerebral Blood Oxygenation Changes. *NeuroImage*, 16(4):1062–1067, aug 2002.

[15] Aaron A Phillips, Franco Hn Chan, Mei Mu Zi Zheng, Andrei V Krassioukov, and Philip N Ainslie. Neurovascular coupling in humans: Physiology, methodological advances and clinical implications. *Journal of cerebral blood flow and metabolism : official journal of the International Society of Cerebral Blood Flow and Metabolism*, 36(4):647–64, apr 2016.

[16] David Attwell, Alastair M. Buchan, Serge Charpak, Martin Lauritzen, Brian A. MacVicar, and Eric A. Newman. Glial and neuronal control of brain blood flow. *Nature*, 468(7321):232–243, nov 2010.

[17] Jeremy Flint, Brian Hansen, Peter Vestergaard-Poulsen, and Stephen J. Blackband. Diffusion weighted magnetic resonance imaging of neuronal activity in the hippocampal slice model. *NeuroImage*, 46(2):411–418, jun 2009.

[18] Ian M. Devonshire, Nikos G. Papadakis, Michael Port, Jason Berwick, Aneurin J. Kennerley, John E.W. Mayhew, and Paul G. Overton. Neurovascular coupling is brain region-dependent. *NeuroImage*, 59(3):1997–2006, feb 2012.

[19] J. Duncombe, R. J. Lennen, M. A. Jansen, I. Marshall, J. M. Wardlaw, and K. Horsburgh. Ageing causes prominent neurovascular dysfunction associated with loss of astrocytic contacts and gliosis. *Neuropathology and Applied Neurobiology*, 43(6):477–491, oct 2017.

[20] Helene Girouard and Costantino Iadecola. Neurovascular coupling in the normal brain and in hypertension, stroke, and Alzheimer disease. *Journal of Applied Physiology*, 100(1):328–335, jan 2006.

[21] Osman Shabir, Jason Berwick, and Sheila E. Francis. Neurovascular dysfunction in vascular dementia, Alzheimer's and atherosclerosis, oct 2018.

[22] Kayoung Han, Jiwoong Min, Myunghee Lee, Bok Man Kang, Taeyoung Park, Junghyun Hahn, Jaeseung Yei, Juheon Lee, Junsung Woo, C. Justin Lee, Seong Gi Kim, and Minah Suh. Neurovascular Coupling under Chronic Stress Is Modified by Altered GABAergic Interneuron Activity. *The Journal of neuroscience : the official journal of the Society for Neuroscience*, 39(50):10081–10095, dec 2019.

[23] Anne Darquié, Jean-Baptiste Poline, Cyril Poupon, Hervé Saint-Jalmes, and Denis Le Bihan. Transient decrease in water diffusion observed in human occipital cortex during visual stimulation. *Proceedings of the National Academy of Sciences*, 98(16):9391–9395, jul 2001.

[24] L. B. Cohen, R. D. Keynes, and Bertil Hille. Light scattering and birefringence changes during nerve activity. *Nature*, 218(5140):438–441, may 1968.

[25] Kunihiko Iwasa, Ichiji Tasaki, and Robert C. Gibbons. Swelling of nerve fibers associated with action potentials. *Science*, 210(4467):338–339, oct 1980.

[26] Knut Holthoff and Otto W. Witte. Intrinsic optical signals in rat neocortical slices measured with near-infrared dark-field microscopy reveal changes in extracellular space. *Journal of Neuroscience*, 16(8):2740–2749, apr 1996.

[27] P. G. Aitken, D. Fayuk, G. G. Somjen, and D. A. Turner. Use of intrinsic optical signals to monitor physiological changes in brain tissue slices. *Methods: A Companion to Methods in Enzymology*, 18(2):91–103, jun 1999.

[28] R.D. Andrew and B.A. Macvicar. Imaging cell volume changes and neuronal excitation in the hippocampal slice. *Neuroscience*, 62(2):371–383, sep 1994.

[29] Denis Le Bihan. The wet mind': water and functional neuroimaging. *Physics in Medicine and Biology*, 52(7):R57–R90, apr 2007.

[30] Denis Le Bihan, Shin-ichi Urayama, Toshihiko Aso, Takashi Hanakawa, and Hidenao Fukuyama. Direct and fast detection of neuronal activation in the human brain with diffusion MRI. *Proceedings of the National Academy of Sciences of the United States of America*, 103(21):8263–8, may 2006.

[31] Yoshifumi Abe, Tomokazu Tsurugizawa, and Denis Le Bihan. Water diffusion closely reveals neural activity status in rat brain loci affected by anesthesia. *PLOS Biology*, 15(4):e2001494, apr 2017.

[32] Kevin C. Chen and Charles Nicholson. Changes in brain cell shape create residual extracellular space volume and explain tortuosity behavior during osmotic challenge. *Proceedings of the National Academy of Sciences of the United States of America*, 97(15):8306–8311, jul 2000.

[33] Tomokazu Tsurugizawa, Luisa Ciobanu, and Denis Le Bihan. Water diffusion in brain cortex closely tracks underlying neuronal activity. *Proceedings of the National Academy of Sciences of the United States of America*, 110(28):11636–41, jul 2013.

[34] Ruiliang Bai, Craig V Stewart, Dietmar Plenz, and Peter J Basser. Assessing the sensitivity of diffusion MRI to detect neuronal activity

directly. *Proceedings of the National Academy of Sciences of the United States of America*, 113(12):E1728–37, mar 2016.

[35] Tao Jin and Seong Gi Kim. Functional changes of apparent diffusion coefficient during visual stimulation investigated by diffusion-weighted gradient-echo fMRI. *NeuroImage*, 41(3):801–812, jul 2008.

[36] Karla L. Miller, Daniel P. Bulte, Hannah Devlin, Matthew D. Robson, Richard G. Wise, Mark W. Woolrich, Peter Jezzard, and Timothy E.J. Behrens. Evidence for a vascular contribution to diffusion FMRI at high b value. *Proceedings of the National Academy of Sciences of the United States of America*, 104(52):20967–20972, dec 2007.

[37] Yoshifumi Abe, Khieu Van Nguyen, Tomokazu Tsurugizawa, Luisa Ciobanu, and Denis Le Bihan. Modulation of water diffusion by activation-induced neural cell swelling in Aplysia Californica. *Scientific Reports*, 7(1):6178, dec 2017.

[38] David J Cuccia, Frederic Bevilacqua, Anthony J Durkin, Frederick R Ayers, and Bruce J Tromberg. Quantitation and mapping of tissue optical properties using modulated imaging. *Journal of biomedical optics*, 14(2):024012, 2009.

[39] Alexander J. Lin, Maya A. Koike, Kim N. Green, Jae G. Kim, Amaan Mazhar, Tyler B. Rice, Frank M. Laferla, and Bruce J. Tromberg. Spatial frequency domain imaging of intrinsic optical property contrast in a mouse model of alzheimer's disease. *Annals of Biomedical Engineering*, 39(4):1349–1357, apr 2011.

[40] Costantino Iadecola. The Neurovascular Unit Coming of Age: A Journey through Neurovascular Coupling in Health and Disease. *Neuron*, 96(1):17–42, sep 2017.

[41] V. Muoio, P. B. Persson, and M. M. Sendeski. The neurovascular unit - concept review. *Acta Physiologica*, 210(4):790–798, apr 2014.

[42] David Attwell and Costantino Iadecola. The neural basis of functional brain imaging signals, dec 2002.

[43] Nikos K. Logothetis and Brian A. Wandell. Interpreting the BOLD signal, 2004.

[44] K. K. Kwong, J. W. Belliveau, D. A. Chesler, I. E. Goldberg, R. M. Weisskoff, B. P. Poncelet, D. N. Kennedy, B. E. Hoppel, M. S. Cohen, R. Turner, H. M. Cheng -, T. J. Brady, and B. R. Rosen. Dynamic magnetic resonance imaging of human brain activity during primary sensory stimulation. *Proceedings of the National Academy of Sciences of the United States of America*, 89(12):5675–5679, 1992.

[45] Ravi S. Menon, Seiji Ogawa, Xiaoping Hu, John P. Strupp, Peter Anderson, and K??mil U??urbil. BOLD Based Functional MRI at 4 Tesla Includes a Capillary Bed Contribution: Echo-Planar Imaging Correlates with Previous Optical Imaging Using Intrinsic Signals. *Magnetic Resonance in Medicine*, 33(3):453–459, mar 1995.

[46] Angelo Mosso. Concerning the circulation of the blood in the human brain. *Leipzig: Verlag von Viet & Company*, 1881.

[47] C. S. Roy and C. S. Sherrington. On the Regulation of the Bloodsupply of the Brain. *The Journal of Physiology*, 11(1-2):85–158, jan 1890.

[48] E. HORNE CRAIGIE. THE ARCHITECTURE OF THE CEREBRAL CAPILLARY BED. *Biological Reviews*, 20(4):133–146, oct 1945.

[49] Dale Purves, George J Augustine, David Fitzpatrick, Lawrence C Katz, Anthony-Samuel LaMantia, James O McNamara, and S Mark Williams. Electrical Potentials Across Nerve Cell Membranes. 2001.

[50] A. L. Hodgkin. The local electric changes associated with repetitive action in a nonmedullated axon. *The Journal of Physiology*, 107(2):165–181, mar 1948.

[51] E M GLASER and G C WHITTOW. Evidence for a non-specific mechanism of habituation. *The Journal of physiology*, 122(Suppl):43–4P, jan 1953.

[52] Barrie Condon, Robert McFadzean, Donald M. Hadley, Michael S. Bradnam, and Uma Shahani. Habituation-like effects cause a significant decrease in response in MRI neuroactivation during visual stimulation. *Vision Research*, 37(9):1243–1247, may 1997.

[53] B Pfleiderer, J Ostermann, N Michael, and W Heindel. Visualization of Auditory Habituation by fMRI. *NeuroImage*, 17:1705–1710, 2002.

[54] Joachim W. Deitmer, Shefeeq M. Theparambil, Ivan Ruminot, Sina I. Noor, and Holger M. Becker. Energy Dynamics in the Brain: Contributions of Astrocytes to Metabolism and pH Homeostasis, dec 2019.

[55] Fahmeed Hyder, Douglas L. Rothman, and Maxwell R. Bennett. Cortical energy demands of signaling and nonsignaling components in brain are conserved across mammalian species and activity levels, feb 2013.

[56] Chase R. Figley and Patrick W. Stroman. The role(s) of astrocytes and astrocyte activity in neurometabolism, neurovascular coupling, and the production of functional neuroimaging signals. *European Journal of Neuroscience*, 33(4):577–588, feb 2011.

[57] PierreJ. Magistretti and Igor Allaman. A Cellular Perspective on Brain Energy Metabolism and Functional Imaging. *Neuron*, 86(4):883–901, may 2015.

[58] Simonetta Camandola and Mark P Mattson. Brain metabolism in health, aging, andneurodegeneration. *The EMBO Journal*, 36(11):1474–1492, jun 2017.

[59] Yoshiaki Itoh, Takanori Esaki, Kazuaki Shimoji, Michelle Cook, Mona J. Law, Elaine Kaufman, and Louis Sokoloff. Dichloroacetate effects on glucose and lactate oxidation by neurons and astroglia in vitro and on glucose utilization by brain in vivo. *Proceedings of the National Academy of Sciences of the United States of America*, 100(8):4879–4884, apr 2003.

[60] Hannah M. Gibbons and Mike Dragunow. Adult human brain cell culture for neuroscience research, jun 2010.

[61] Dennis A. Turner and David Cory Adamson. Neuronal-astrocyte metabolic interactions: Understanding the transition into abnormal astrocytoma metabolism, mar 2011.

[62] Thomas Misje Mathiisen, Knut Petter Lehre, Niels Christian Danbolt, and Ole Petter Ottersen. The perivascular astroglial sheath provides a

complete covering of the brain microvessels: An electron microscopic 3D reconstruction. *Glia*, 58(9):1094–1103, jul 2010.

[63] Mireille Bélanger, Igor Allaman, and Pierre J. Magistretti. Brain energy metabolism: Focus on Astrocyte-neuron metabolic cooperation, dec 2011.

[64] Gary Yellen. Fueling thought: Management of glycolysis and oxidative phosphorylation in neuronal metabolism. *The Journal of cell biology*, 217(7):2235–2246, jul 2018.

[65] Heather L. McConnell, Cymon N. Kersch, Randall L. Woltjer, and Edward A. Neuwelt. The translational significance of the neurovascular unit, jan 2017.

[66] Marilyn J. Cipolla. Anatomy and Ultrastructure. 2009.

[67] David Attwell, Anusha Mishra, Catherine N Hall, Fergus M O'Farrell, and Turgay Dalkara. What is a pericyte? *Journal of cerebral blood flow and metabolism : official journal of the International Society of Cerebral Blood Flow and Metabolism*, 36(2):451–5, feb 2016.

[68] Ramon y Cajal. *Histology of the nervous system of man and vertebrates (trans. Swanson N, Swanson LW)*. Oxford University Press, New York, 1995.

[69] Stewart Shipp. Structure and function of the cerebral cortex, jun 2007.

[70] George S. Bloom. Amyloid-β and tau: The trigger and bullet in Alzheimer disease pathogenesis. *JAMA Neurology*, 71(4):505–508, 2014.

[71] K. R. Ko, A. C. Ngai, and H. R. Winn. Role of adenosine in regulation of regional cerebral blood flow in sensory cortex. *American Journal of Physiology - Heart and Circulatory Physiology*, 259(6 28-6), 1990.

[72] Ralph D. Freeman and Baowang Li. Neural Metabolic coupling in the central visual pathway, oct 2016.

[73] Helen Shinru Wei, Hongyi Kang, Izad Yar Daniel Rasheed, Sitong Zhou, Nanhong Lou, Anna Gershteyn, Evan Daniel McConnell,

Yixuan Wang, Kristopher Emil Richardson, Andre Francis Palmer, Chris Xu, Jiandi Wan, and Maiken Nedergaard. Erythrocytes Are Oxygen-Sensing Regulators of the Cerebral Microcirculation. *Neuron*, 91(4):851–862, aug 2016.

[74] PT Fox, ME Raichle, MA Mintun, and C Dence. Nonoxidative glucose consumption during focal physiologic neural activity. *Science*, 241(4864):462–464, jul 1988.

[75] Richard B. Buxton. The physics of functional magnetic resonance imaging (fMRI). *Reports on Progress in Physics*, 76(9):096601, sep 2013.

[76] Declan G. Lyons, Alexandre Parpaleix, Morgane Roche, and Serge Charpak. Mapping oxygen concentration in the awake mouse brain. *eLife*, 5(FEBRUARY2016), feb 2016.

[77] Barbara Lykke Lind, Alexey R. Brazhe, Sanne Barsballe Jessen, Florence C.C. Tan, and Martin J. Lauritzen. Rapid stimulus-evoked astrocyte Ca2+ elevations and hemodynamic responses in mouse somatosensory cortex in vivo. *Proceedings of the National Academy of Sciences of the United States of America*, 110(48):E4678–E4687, nov 2013.

[78] Brian A MacVicar and Eric A Newman. Astrocyte regulation of blood flow in the brain. *Cold Spring Harbor perspectives in biology*, 7(5):a020388, mar 2015.

[79] Grant R.J. Gordon, Hyun B. Choi, Ravi L. Rungta, Graham C.R. Ellis-Davies, and Brian A. MacVicar. Brain metabolism dictates the polarity of astrocyte control over arterioles. *Nature*, 456(7223):745–750, dec 2008.

[80] Krystal Nizar, Hana Uhlirova, Peifang Tian, Payam A. Saisan, Qun Cheng, Lidia Reznichenko, Kimberly L. Weldy, Tyler C. Steed, Vishnu B. Sridhar, Christopher L. MacDonald, Jianxia Cui, Sergey L. Gratiy, Sava Sakadžić, David A. Boas, Thomas I. Beka, Gaute T. Einevoll, Ju Chen, Eliezer Masliah, Anders M. Dale, Gabriel A. Silva, and Anna Devor. In vivo stimulus-induced vasodilation occurs without

IP3 receptor activation and may precede astrocytic calcium increase. *Journal of Neuroscience*, 33(19):8411–8422, may 2013.

[81] Norio Takata, Terumi Nagai, Katsuya Ozawa, Yuki Oe, Katsuhiko Mikoshiba, and Hajime Hirase. Cerebral Blood Flow Modulation by Basal Forebrain or Whisker Stimulation Can Occur Independently of Large Cytosolic Ca2+ Signaling in Astrocytes. *PLoS ONE*, 8(6):e66525, jun 2013.

[82] S. E. Dore. On The Contractility and Nervous Supply of the Capillaries. *British Journal of Dermatology*, 35(11):398–404, nov 1923.

[83] Andrea Trost, Simona Lange, Falk Schroedl, Daniela Bruckner, Karolina A Motloch, Barbara Bogner, Alexandra Kaser-Eichberger, Clemens Strohmaier, Christian Runge, Ludwig Aigner, Francisco J Rivera, and Herbert A Reitsamer. Brain and Retinal Pericytes: Origin, Function and Role. *Frontiers in cellular neuroscience*, 10:20, 2016.

[84] Catherine N Hall, Clare Reynell, Bodil Gesslein, Nicola B Hamilton, Anusha Mishra, Brad A Sutherland, Fergus M O'Farrell, Alastair M Buchan, Martin Lauritzen, and David Attwell. Capillary pericytes regulate cerebral blood flow in health and disease. *Nature*, 508(7494):55–60, apr 2014.

[85] Claire M Peppiatt, Clare Howarth, Peter Mobbs, and David Attwell. Bidirectional control of CNS capillary diameter by pericytes. *Nature*, 443(7112):700–704, oct 2006.

[86] Costantino Iadecola. The Pathobiology of Vascular Dementia, nov 2013.

[87] Matthew R. Halliday, Sanket V. Rege, Qingyi Ma, Zhen Zhao, Carol A. Miller, Ethan A. Winkler, and Berisla V. Zlokovic. Accelerated pericyte degeneration and blood-brain barrier breakdown in apolipoprotein E4 carriers with Alzheimer's disease. *Journal of Cerebral Blood Flow and Metabolism*, 36(1):216–227, jan 2016.

[88] Konstantin Kotliar, Christine Hauser, Marion Ortner, Claudia Muggenthaler, Janine Diehl-Schmid, Susanne Angermann, Alexander

Hapfelmeier, Christoph Schmaderer, and Timo Grimmer. Altered neurovascular coupling as measured by optical imaging: A biomarker for Alzheimer's disease. In *Scientific Reports*, volume 7, pages 1–11. Nature Publishing Group, dec 2017.

[89] Peter Toth, Stefano Tarantini, Anna Csiszar, and Zoltan Ungvari. Functional vascular contributions to cognitive impairment and dementia: Mechanisms and consequences of cerebral autoregulatory dysfunction, endothelial impairment, and neurovascular uncoupling in aging, 2017.

[90] F. M. Faraci and D. D. Heistad. Regulation of large cerebral arteries and cerebral microsvascular pressure, 1990.

[91] RobertA. Hill, Lei Tong, Peng Yuan, Sasidhar Murikinati, Shobhana Gupta, and Jaime Grutzendler. Regional Blood Flow in the Normal and Ischemic Brain Is Controlled by Arteriolar Smooth Muscle Cell Contractility and Not by Capillary Pericytes. *Neuron*, 87(1):95–110, jul 2015.

[92] W. Kuschinsky and O. B. Paulson. Capillary circulation in the brain., jan 1992.

[93] Antal G. Hudetz. Regulation of oxygen supply in the cerebral circulation. In *Advances in Experimental Medicine and Biology*, volume 428, pages 513–520. Springer New York LLC, 1997.

[94] Francisco Fernández-Klett, Nikolas Offenhauser, Ulrich Dirnagl, Josef Priller, and Ute Lindauer. Pericytes in capillaries are contractile in vivo, but arterioles mediate functional hyperemia in the mouse brain. *Proceedings of the National Academy of Sciences of the United States of America*, 107(51):22290–22295, dec 2010.

[95] Peifang Tian, Ivan C. Teng, Larry D. May, Ronald Kurz, Kun Lu, Miriam Scadeng, Elizabeth M.C. Hillman, Alex J. De Crespigny, Helen E. D'Arceuil, Joseph B. Mandeville, John J.A. Marota, Bruce R. Rosen, Thomas T. Liu, David A. Boas, Richard B. Buxton, Anders M. Dale, and Anna Devor. Cortical depth-specific microvascular dilation underlies laminar differences in blood oxygenation level-dependent

functional MRI signal. *Proceedings of the National Academy of Sciences of the United States of America*, 107(34):15246–15251, aug 2010.

[96] Jernej Vidmar Ae, Igor Serša, Ae Eduard Kralj, A E Gregor, Tratar Ae, and Aleš Blinc. Discrimination between red blood cell and platelet components of blood clots by MR microscopy.

[97] Kâmil Uluda, Bernd Müller-Bierl, and Kâmil Uurbil. An integrative model for neuronal activity-induced signal changes for gradient and spin echo functional imaging. *NeuroImage*, 48(1):150–165, oct 2009.

[98] Claus Mathiesen, Kirsten Caesar, Nuran Akgören, and Martin Lauritzen. Modification of activity-dependent increases of cerebral blood flow by excitatory synaptic activity and spikes in rat cerebellar cortex. *Journal of Physiology*, 512(2):555–566, oct 1998.

[99] Seiji Ogawa, Tso Ming Lee, Ray Stepnoski, Wei Chen, Xiao Hong Zhu, and Kamil Ugurbil. An approach to probe some neural systems interaction by functional MRI at neural time scale down to milliseconds. *Proceedings of the National Academy of Sciences of the United States of America*, 97(20):11026–11031, sep 2000.

[100] N. K. Logothetis, J. Pauls, M. Augath, T. Trinath, and A. Oeltermann. Neurophysiological investigation of the basis of the fMRI signal. *Nature*, 412(6843):150–157, jul 2001.

[101] Nikos K. Logothetis. What we can do and what we cannot do with fMRI, jun 2008.

[102] Jakob Heinzle, Peter J. Koopmans, Hanneke E.M. den Ouden, Sudhir Raman, and Klaas Enno Stephan. A hemodynamic model for layered BOLD signals. *NeuroImage*, 125:556–570, jan 2016.

[103] Hana Inoue, Shin-ichiro Mori, Shigeru Morishima, and Yasunobu Okada. Volume-sensitive chloride channels in mouse cortical neurons: characterization and role in volume regulation. *European Journal of Neuroscience*, 21(6):1648–1658, mar 2005.

[104] Niklas Hübel and Ghanim Ullah. Anions Govern Cell Volume: A Case Study of Relative Astrocytic and Neuronal Swelling in Spreading Depolarization. *PLOS ONE*, 11(3):e0147060, mar 2016.

[105] Jolanda M. Spijkerman, Esben T. Petersen, Jeroen Hendrikse, Peter Luijten, and Jaco J.M. Zwanenburg. T 2 mapping of cerebrospinal fluid: 3t versus 7t. *Magnetic Resonance Materials in Physics, Biology and Medicine*, 31:415–424, 6 2018.

[106] Jorge Zavala Bojorquez, Stphanie Bricq, Clement Acquitter, Franois Brunotte, Paul M. Walker, and Alain Lalande. What are normal relaxation times of tissues at 3 t?, 1 2017.

[107] Clarence P. Davis, Graerne C. McKinnon, Jorg F. Debatin, Stefan Duewell, and Gustav K. Von Schulthess. Singleshot versus interleaved echoplanar MR imaging: Application to visualization of cardiac valve leaflets. *Journal of Magnetic Resonance Imaging*, 5(1):107–112, 1995.

[108] Shujun Ding, Steven D. Wolff, and Frederick H. Epstein. Improved coverage in dynamic contrast-enhanced cardiac MRI using interleaved gradient-echo epi. *Magnetic Resonance in Medicine*, 39(4):514–519, 1998.

[109] Roland Bammer, Stephen L. Keeling, Michael Augustin, Klaas P. Pruessmann, Roswitha Wolf, Rudolf Stollberger, Hans Peter Hartung, and Franz Fazekas. Improved diffusion-weighted single-shot echo-planar imaging (EPI) in stroke using sensitivity encoding (SENSE). *Magnetic Resonance in Medicine*, 46(3):548–554, 2001.

[110] Reidar P Lystad and Henry Pollard. Functional neuroimaging: a brief overview and feasibility for use in chiropractic research. *The Journal of the Canadian Chiropractic Association*, 53(1):59–72, mar 2009.

[111] Elizabeth M.C. Hillman. Coupling Mechanism and Significance of the BOLD Signal: A Status Report. *Annual Review of Neuroscience*, 37(1):161–181, jul 2014.

[112] Christoph M. Michel and Denis Brunet. EEG source imaging: A practical review of the analysis steps. *Frontiers in Neurology*, 10(APR):325, apr 2019.

[113] Karen J. Mitchell, Marcia K. Johnson, Carol L. Raye, and Mark D'Esposito. fMRI evidence of age-related hippocampal dysfunction in

feature binding in working memory. *Cognitive Brain Research*, 10(1-2):197–206, sep 2000.

[114] J. V. Haxby, M. I. Gobbini, M. L. Furey, A. Ishai, J. L. Schouten, and P. Pietrini. Distributed and overlapping representations of faces and objects in ventral temporal cortex. *Science*, 293(5539):2425–2430, sep 2001.

[115] Mark D'Esposito, Andrew Kayser, and Anthony Chen. Functional MRI: Applications in cognitive neuroscience. In *Neuromethods*, volume 119, pages 317–353. Humana Press Inc., sep 2016.

[116] Fraser Aitken, Georgios Menelaou, Oliver Warrington, Renee S. Koolschijn, Nadège Corbin, Martina F. Callaghan, and Peter Kok. Prior expectations evoke stimulus-specific activity in the deep layers of the primary visual cortex. *PLoS Biology*, 18(12), dec 2020.

[117] José M. Soares, Ricardo Magalhães, Pedro S. Moreira, Alexandre Sousa, Edward Ganz, Adriana Sampaio, Victor Alves, Paulo Marques, and Nuno Sousa. A Hitchhiker's guide to functional magnetic resonance imaging, nov 2016.

[118] Varsha Jain, Osheiza Abdulmalik, Kathleen Joy Propert, and Felix W. Wehrli. Investigating the magnetic susceptibility properties of fresh human blood for noninvasive oxygen saturation quantification. *Magnetic Resonance in Medicine*, 68(3):863–867, sep 2012.

[119] John Martindale, John Mayhew, Jason Berwick, Myles Jones, Chris Martin, Dave Johnston, Peter Redgrave, and Ying Zheng. The hemodynamic impulse response to a single neural event. *Journal of Cerebral Blood Flow and Metabolism*, 23(5):546–555, may 2003.

[120] Xiaoping Hu and Essa Yacoub. The story of the initial dip in fMRI, aug 2012.

[121] R. D. Frostig, E. E. Lieke, D. Y. Ts'o, and A. Grinvald. Cortical functional architecture and local coupling between neuronal activity and the microcirculation revealed by in vivo high-resolution optical imaging of intrinsic signals. *Proceedings of the National Academy of Sciences of the United States of America*, 87(16):6082–6086, aug 1990.

[122] Nikos K Logothetis. The underpinnings of the BOLD functional magnetic resonance imaging signal. *The Journal of neuroscience : the official journal of the Society for Neuroscience*, 23(10):3963–71, may 2003.

[123] Gunnar Krüger, Andreas Kleinschmidt, and Jens Frahm. Dynamic MRI sensitized to cerebral blood oxygenation and flow during sustained activation of human visual cortex. *Magnetic Resonance in Medicine*, 35(6):797–800, 1996.

[124] Richard B. Buxton. Dynamic models of BOLD contrast, aug 2012.

[125] Richard B. Buxton, Eric C. Wong, and Lawrence R. Frank. Dynamics of blood flow and oxygenation changes during brain activation: The balloon model. *Magnetic Resonance in Medicine*, 39(6):855–864, 1998.

[126] Aneurin J. Kennerley, John E. Mayhew, Luke Boorman, Ying Zheng, and Jason Berwick. Is optical imaging spectroscopy a viable measurement technique for the investigation of the negative BOLD phenomenon? A concurrent optical imaging spectroscopy and fMRI study at high field (7T). *Neuroimage*, 61(1-6):10, 2012.

[127] Luke Boorman, Aneurin J. Kennerley, David Johnston, Myles Jones, Ying Zheng, Peter Redgrave, and Jason Berwick. Negative blood oxygen level dependence in the rat: A model for investigating the role of suppression in neurovascular coupling. *Journal of Neuroscience*, 30(12):4285–4294, mar 2010.

[128] Geoffrey M. Boynton, Stephen A. Engel, Gary H. Glover, and David J. Heeger. Linear systems analysis of functional magnetic resonance imaging in human V1. *Journal of Neuroscience*, 16(13):4207–4221, 1996.

[129] Beau M. Ances, Eric Zarahn, Joel H. Greenberg, and John A. Detre. Coupling of neural activation to blood flow in the somatosensory cortex of rats is time-intensity separable, but not linear. *Journal of Cerebral Blood Flow and Metabolism*, 20(6):921–930, jun 2000.

[130] Geon Ho Jahng, Michael W. Weiner, and Norbert Schuff. Improved arterial spin labeling method: Applications for measurements of cere-

bral blood flow in human brain at high magnetic field MRI. *Medical Physics*, 34(11):4519–4525, 2007.

[131] Ajna Borogovac and Iris Asllani. Arterial Spin Labeling (ASL) fMRI : Advantages , Theoretical Constrains and Experimental Challenges in Neurosciences. 2012, 2012.

[132] Hanzhang Lu and Peter C.M. van Zijl. A review of the development of Vascular-Space-Occupancy (VASO) fMRI, aug 2012.

[133] Dow Mu Koh and David J. Collins. Diffusion-weighted MRI in the body: Applications and challenges in oncology. *American Journal of Roentgenology*, 188(6):1622–1635, 2007.

[134] Nitzan Tirosh and Uri Nevo. Neuronal activity significantly reduces water displacement: DWI of a vital rat spinal cord with no hemodynamic effect. *NeuroImage*, 76:98–107, aug 2013.

[135] Stacey L. Gangstead and Allen W. Song. On the timing characteristics of the apparent diffusion coefficient contrast in fMRI. *Magnetic Resonance in Medicine*, 48(2):385–388, aug 2002.

[136] Todd B. Harshbarger and Allen W. Song. B factor dependence of the temporal characteristics of brain activation using dynamic apparent diffusion coefficient contrast. *Magnetic Resonance in Medicine*, 52(6):1432–1437, 2004.

[137] Satoru Kohno, Nobukatsu Sawamoto, Shin Ichi Urayama, Toshihiko Aso, Kenji Aso, Akitoshi Seiyama, Hidenao Fukuyama, and Denis Le Bihan. Water-diffusion slowdown in the human visual cortex on visual stimulation precedes vascular responses. *Journal of Cerebral Blood Flow and Metabolism*, 29(6):1197–1207, jun 2009.

[138] Floris J. Voskuil, Jasper Vonk, Bert van der Vegt, Schelto Kruijff, Vasilis Ntziachristos, Pieter J. van der Zaag, Max J.H. Witjes, and Gooitzen M. van Dam. Intraoperative imaging in pathology-assisted surgery. *Nature Biomedical Engineering*, 6:503–514, 5 2022.

[139] Frans F. Jöbsis. Noninvasive, infrared monitoring of cerebral and myocardial oxygen sufficiency and circulatory parameters. *Science*, 198(4323):1264–1266, 1977.

[140] Ge Song, Zachary A. Steelman, Stella Finkelstein, Ziyun Yang, Ludovic Martin, Kengyeh K. Chu, Sina Farsiu, Vadim Y. Arshavsky, and Adam Wax. Multimodal Coherent Imaging of Retinal Biomarkers of Alzheimer's Disease in a Mouse Model. *Scientific Reports*, 10(1):1–11, dec 2020.

[141] Cenk Ayata, Andrew K. Dunn, Yasemin Gursoy-Özdemir, Zhihong Huang, David A. Boas, and Michael A. Moskowitz. Laser speckle flowmetry for the study of cerebrovascular physiology in normal and ischemic mouse cortex. *Journal of Cerebral Blood Flow and Metabolism*, 24(7):744–755, jul 2004.

[142] Sonya Bahar, Minah Suh, Mingrui Zhao, and Theodore H. Schwartz. Intrinsic optical signal imaging of neocortical seizures: The 'epileptic dip'. *NeuroReport*, 17(5):499–503, apr 2006.

[143] Anna Devor, Andrew K. Dunn, Mark L. Andermann, Istvan Ulbert, David A. Boas, and Anders M. Dale. Coupling of total hemoglobin concentration, oxygenation, and neural activity in rat somatosensory cortex. *Neuron*, 39(2):353–359, jul 2003.

[144] J. Berwick, D. Johnston, M. Jones, J. Martindale, P. Redgrave, N. McLoughlin, I. Schiessl, and J. E.W. Mayhew. Neurovascular coupling investigated with two-dimensional optical imaging spectroscopy in rat whisker barrel cortex. *European Journal of Neuroscience*, 22(7):1655–1666, oct 2005.

[145] Elizabeth M.C. Hillman, Anna Devor, Matthew B. Bouchard, Andrew K. Dunn, G. W. Krauss, Jesse Skoch, Brian J. Bacskai, Anders M. Dale, and David A. Boas. Depth-resolved optical imaging and microscopy of vascular compartment dynamics during somatosensory stimulation. *NeuroImage*, 35(1):89–104, mar 2007.

[146] Elizabeth M C Hillman. Optical brain imaging in vivo: techniques and applications from animal to man. *Journal of biomedical optics*, 12(5):051402, 2007.

[147] Elizabeth M. C. Hillman, Cyrus B. Amoozegar, Tracy Wang, Addason F. H. McCaslin, Matthew B. Bouchard, James Mansfield,

and Richard M. Levenson. In vivo optical imaging and dynamic contrast methods for biomedical research. *Phil. Trans. R. Soc. A*, 369(1955):4620–4643, nov 2011.

[148] Chris Martin, Jason Berwick, Dave Johnston, Ying Zheng, John Martindale, Michael Port, Peter Redgrave, and John Mayhew. Optical imaging spectroscopy in the unanaesthetised rat. *Journal of Neuroscience Methods*, 120(1):25–34, oct 2002.

[149] Aneurin J. Kennerley, Jason Berwick, John Martindale, David Johnston, Ying Zheng, and John E. Mayhew. Refinement of optical imaging spectroscopy algorithms using concurrent BOLD and CBV fMRI. *NeuroImage*, 47(4):1608–1619, 2009.

[150] John Mayhew, David Johnston, Jason Berwick, Myles Jones, Peter Coffey, and Ying Zheng. Spectroscopic Analysis of Neural Activity in Brain: Increased Oxygen Consumption Following Activation of Barrel Cortex. *NeuroImage*, 12(6):664–675, dec 2000.

[151] Aneurin J. Kennerley, Jason Berwick, John Martindale, David Johnston, Nikos Papadakis, and John E. Mayhew. Concurrent fMRI and optical measures for the investigation of the hemodynamic response function. *Magnetic Resonance in Medicine*, 54(2):354–365, 2005.

[152] Jozien Goense, Hellmut Merkle, and NikosK. Logothetis. High-Resolution fMRI Reveals Laminar Differences in Neurovascular Coupling between Positive and Negative BOLD Responses. *Neuron*, 76(3):629–639, nov 2012.

[153] David J. Cuccia, Frederic Bevilacqua, Anthony J. Durkin, and Bruce J. Tromberg. Modulated imaging: quantitative analysis and tomography of turbid media in the spatial-frequency domain. *Optics Letters*, 30(11):1354, 2005.

[154] Amaan Mazhar, David J Cuccia, Sylvain Gioux, Anthony J Durkin, John V Frangioni, and Bruce J Tromberg. Structured illumination enhances resolution and contrast in thick tissue fluorescence imaging. *Journal of biomedical optics*, 15(1):010506, 2010.

[155] Jean Vervandier and Sylvain Gioux. Single snapshot imaging of optical properties. *Biomedical optics express*, 4(12):2938–44, 2013.

[156] Michael Ghijsen, Bernard Choi, Anthony J Durkin, Sylvain Gioux, and Bruce J Tromberg. Real-time simultaneous single snapshot of optical properties and blood flow using coherent spatial frequency domain imaging (cSFDI). *Biomedical optics express*, 7(3):870–82, mar 2016.

[157] Alexander J Lin, Adrien Ponticorvo, Soren D Konecky, Haotian Cui, Tyler B Rice, Bernard Choi, Anthony J Durkin, and Bruce J Tromberg. Visible spatial frequency domain imaging with a digital light microprojector. *Journal of biomedical optics*, 18(9):096007, sep 2013.

[158] Joseph P Angelo, Martijn van de Giessen, and Sylvain Gioux. Real-time endoscopic optical properties imaging. *Biomedical optics express*, 8(11):5113–5126, nov 2017.

[159] Giuseppe Querques, Enrico Borrelli, Riccardo Sacconi, Luigi De Vitis, Letizia Leocani, Roberto Santangelo, Giuseppe Magnani, Giancarlo Comi, and Francesco Bandello. Functional and morphological changes of the retinal vessels in Alzheimer's disease and mild cognitive impairment. *Scientific Reports*, 9(1):1–10, dec 2019.

[160] David Cuccia, Bruce Tromberg, Ron Frostig, and David Abookasis. Quantitative In Vivo Imaging of Tissue Absorption, Scattering, and Hemoglobin Concentration in Rat Cortex Using Spatially Modulated Structured Light. In Frostig RD, editor, *In Vivo Optical Imaging of Brain Function.*, chapter 12, pages 339–361. CRC Press/Taylor & Francis, 2nd editio edition, may 2009.

[161] Alberto De Luca, Lara Schlaffke, — Jeroen, C W Siero, Martijn Froeling, and — Alexander Leemans. On the sensitivity of the diffusion MRI signal to brain activity in response to a motor cortex paradigm. 2019.

[162] Daniel Nunes, Andrada Ianus, and Noam Shemesh. Layer-specific connectivity revealed by diffusion-weighted functional MRI in the rat thalamocortical pathway. *NeuroImage*, 184:646–657, jan 2019.

[163] Jennifer Li, Diego S. Bravo, A. Louise Upton, Gary Gilmour, Mark D. Tricklebank, Marianne Fillenz, Chris Martin, John P. Lowry, David M.

Bannerman, and Stephen B. McHugh. Close temporal coupling of neuronal activity and tissue oxygen responses in rodent whisker barrel cortex. *European Journal of Neuroscience*, 34(12):1983–1996, dec 2011.

[164] Carl C.H. Petersen. The functional organization of the barrel cortex., oct 2007.

[165] Thomas A. Woolsey and Hendrik Van der Loos. The structural organization of layer IV in the somatosensory region (S I) of mouse cerebral cortex. The description of a cortical field composed of discrete cytoarchitectonic units. *Brain Research*, 17(2):205–242, jan 1970.

[166] Ying Wang, Yushuang Cong, Jun Li, Xueting Li, Bing Li, and Sihua Qi. Correction: Comparison of Invasive Blood Pressure Measurements from the Caudal Ventral Artery and the Femoral Artery in Male Adult SD and Wistar Rats. *PLoS ONE*, 8(9), sep 2013.

[167] C. Saiki, T. Matsuoka, and J. P. Mortola. Metabolic-ventilatory interaction in conscious rats: Effect of hypoxia and ambient temperature. *Journal of Applied Physiology*, 76(4):1594–1599, 1994.

[168] Leonard Hill and Martin Flack. The effect of excess of carbon dioxide and of want of oxygen upon the respiration and the circulation. *The Journal of Physiology*, 37(2):77–111, jun 1908.

[169] S. S. Kety and C. F. Schmidt. The effects of altered arterial tensions of carbon dioxide and oxygen on cerebral blood flow and cerebral oxygen consumption of normal young men. *The Journal of clinical investigation*, 27(4):484–492, jul 1948.

[170] M. Hiraoka, M. Firbank, M. Essenpreis, M. Cope, S. R. Arridge, P. Van Der Zee, and D. T. Delpy. A Monte Carlo investigation of optical pathlength in inhomogeneous tissue and its application to near-infrared spectroscopy. *Physics in Medicine and Biology*, 38(12):1859–1876, 1993.

[171] Mark Cope. The development of a near infrared spectroscopy system and its application for non invasive monitory of cerebral blood and

tissue oxygenation in the newborn infants. *Diss. University of London*, page 342, 1991.

[172] L. Kocsis, P. Herman, and A. Eke. The modified Beer-Lambert law revisited. *Physics in Medicine and Biology*, 51(5), 2006.

[173] Kyle P Nadeau, Anthony J Durkin, and Bruce J Tromberg. Advanced demodulation technique for the extraction of tissue optical properties and structural orientation contrast in the spatial frequency domain. *Journal of biomedical optics*, 19(5):056013, may 2014.

[174] Michal Mikl, Radek Mareček, Petr Hluštík, Martina Pavlicová, Aleš Drastich, Pavel Chlebus, Milan Brázdil, and Petr Krupa. Effects of spatial smoothing on fMRI group inferences. *Magnetic Resonance Imaging*, 26(4):490–503, may 2008.

[175] AC Rosenfeld, A. and Kak. *Digital Picture Processing*. New York, 2nd edition, 1982.

[176] Peng Liu, Vince Calhoun, and Zikuan Chen. Functional overestimation due to spatial smoothing of fMRI data. *Journal of Neuroscience Methods*, 291:1–12, nov 2017.

[177] Zikuan Chen and Vince Calhoun. Effect of Spatial Smoothing on Task fMRI ICA and Functional Connectivity. *Frontiers in Neuroscience*, 12(FEB):15, feb 2018.

[178] Albert Einstein. *Investigations on the theory of the Brownian movement*. New York, N.Y. : Dover Publications, Mineola, NY, 1956.

[179] Denis Le Bihan and Mami Iima. Diffusion Magnetic Resonance Imaging: What Water Tells Us about Biological Tissues. *PLOS Biology*, 13(7):e1002203, jul 2015.

[180] D Le Bihan, E Breton, D Lallemand, P Grenier, E Cabanis, and M Laval-Jeantet. MR imaging of intravoxel incoherent motions: application to diffusion and perfusion in neurologic disorders. *Radiology*, 161(2):401–7, nov 1986.

[181] Jeffrey J. Neil. Measurement of water motion (apparent diffusion) in biological systems. *Concepts in Magnetic Resonance*, 9(6):385–401, jan 1997.

[182] D. Le Bihan, E. Breton, D. Lallemand, M. L. Aubin, J. Vignaud, and M. Laval-Jeantet. Separation of diffusion and perfusion in intravoxel incoherent motion MR imaging. *Radiology*, 168(2):497–505, 1988.

[183] E. O. Stejskal and J. E. Tanner. Spin diffusion measurements: Spin echoes in the presence of a time-dependent field gradient. *The Journal of Chemical Physics*, 42(1):288–292, jan 1965.

[184] Nadya Pyatigorskaya, Denis Le Bihan, Olivier Reynaud, and Luisa Ciobanu. Relationship between the diffusion time and the diffusion MRI signal observed at 17.2 tesla in the healthy rat brain cortex. *Magnetic Resonance in Medicine*, 72(2):492–500, 2014.

[185] D. Hernando, D. C. Karampinos, K. F. King, J. P. Haldar, S. Majumdar, J. G. Georgiadis, and Z. P. Liang. Removal of olefinic fat chemical shift artifact in diffusion MRI. *Magnetic Resonance in Medicine*, 65(3):692–701, 2011.

[186] Timothy G. Reese, O. Heid, R. M. Weisskoff, and V. J. Wedeen. Reduction of eddy-current-induced distortion in diffusion MRI using a twice-refocused spin echo. *Magnetic Resonance in Medicine*, 49(1):177–182, jan 2003.

[187] Rachel W. Chan, Constantin Von Deuster, Daniel Giese, Christian T. Stoeck, Jack Harmer, Andrew P. Aitken, David Atkinson, and Sebastian Kozerke. Characterization and correction of eddy-current artifacts in unipolar and bipolar diffusion sequences using magnetic field monitoring. *Journal of Magnetic Resonance*, 244:74–84, jul 2014.

[188] Peter Jezzard, Alan S. Barnett, and Carlo Pierpaoli. Characterization of and correction for eddy current artifacts in echo planar diffusion imaging. *Magnetic Resonance in Medicine*, 39(5):801–812, 1998.

[189] M. E. Moseley, Y. Cohen, J. Mintorovitch, L. Chileuitt, H. Shimizu, J. Kucharczyk, M. F. Wendland, and P. R. Weinstein. Early detection of regional cerebral ischemia in cats: Comparison of diffusion and T2weighted MRI and spectroscopy. *Magnetic Resonance in Medicine*, 14(2):330–346, 1990.

[190] Steven Warach, D. Chien, W. Li, M. Ronthal, and R. R. Edelman. Fast magnetic resonance diffusionweighted imaging of acute human stroke. *Neurology*, 42(9):1717–1723, 1992.

[191] Denis Le Bihan. Looking into the functional architecture of the brain with diffusion MRI. *Nature Reviews Neuroscience*, 4(6):469–480, 2003.

[192] Denis Le Bihan, Jean-Franois Mangin, Cyril Poupon, Chris A. Clark, Sabina Pappata, Nicolas Molko, and Hughes Chabriat. Diffusion tensor imaging: Concepts and applications. *Journal of Magnetic Resonance Imaging*, 13(4):534–546, apr 2001.

[193] P. J. Basser, J. Mattiello, and D. LeBihan. MR diffusion tensor spectroscopy and imaging. *Biophysical Journal*, 66(1):259–267, 1994.

[194] Tomokazu Numano, Kazuhiro Homma, Nobuaki Iwasaki, Koji Hyodo, Naotaka Nitta, and Takeshi Hirose. In vivo isotropic 3D diffusion tensor mapping of the rat brain using diffusion-weighted 3D MP-RAGE MRI. *Magnetic Resonance Imaging*, 24(3):287–293, apr 2006.

[195] Qi Zhao, Rees P. Ridout, Jikai Shen, and Nian Wang. Effects of Angular Resolution and b Value on Diffusion Tensor Imaging in Knee Joint. *Cartilage*, 13(2):295S–303S, dec 2021.

[196] Stephanie Crater, Surendra Maharjan, Yi Qi, Qi Zhao, Gary Cofer, James C. Cook, G. Allan Johnson, and Nian Wang. Resolution and b value dependent structural connectome in ex vivo mouse brain. *NeuroImage*, 255:119199, jul 2022.

[197] Wolfgang Gaggl, Andrzej Jesmanowicz, and Robert W. Prost. High-resolution reduced field of view diffusion tensor imaging using spatially selective RF pulses. *Magnetic Resonance in Medicine*, 72(6):1668–1679, dec 2014.

[198] Geetha Soujanya Chilla, Cher Heng Tan, Chenjie Xu, and Chueh Loo Poh. Diffusion weighted magnetic resonance imaging and its recent trend-a survey. *Quantitative imaging in medicine and surgery*, 5(3):407–22, jun 2015.

[199] Farida Grinberg, Ezequiel Farrher, Luisa Ciobanu, Françoise Geffroy, Denis Le Bihan, and N. Jon Shah. Non-Gaussian Diffusion Imaging

for Enhanced Contrast of Brain Tissue Affected by Ischemic Stroke. *PLoS ONE*, 9(2):e89225, feb 2014.

[200] Jing Yuan, David Ka Wai Yeung, Greta S.P. Mok, Kunwar S. Bhatia, Yi Xiang J. Wang, Anil T. Ahuja, and Ann D. King. Non-Gaussian analysis of diffusion weighted imaging in head and neck at 3T: A pilot study in patients with nasopharyngeal carcinoma. *PLoS ONE*, 9(1), jan 2014.

[201] Jonathan V. Sehy, Joseph J.H. Ackerman, and Jeffrey J. Neil. Evidence that both fast and slow water ADC components arise from intracellular space. *Magnetic Resonance in Medicine*, 48(5):765–770, nov 2002.

[202] Jacqueline M. O'Shea, Stephen R. Williams, Nick van Bruggen, and Anthony R. Gardner-Medwin. Apparent diffusion coefficient and mr relaxation during osmotic manipulation in isolated turtle cerebellum. *Magnetic Resonance in Medicine*, 44:427–432, 9 2000.

[203] Thoralf Niendorf, Rick M. Dijkhuizen, David G. Norris, Menno Van Lookeren Campagne, and Klaas Nicolay. Biexponential diffusion attenuation in various states of brain tissue: Implications for diffusion-weighted imaging. *Magnetic Resonance in Medicine*, 36(6):847–857, dec 1996.

[204] John Martindale, Aneurin J. Kennerley, David Johnston, Ying Zheng, and John E. Mayhew. Theory and generalization of monte carlo models of the BOLD signal source. *Magnetic Resonance in Medicine*, 59(3):607–618, mar 2008.

[205] J. Zhong, O. A. C. Petroff, J. W. Prichard, and J. C. Gore. Changes in water diffusion and relaxation properties of rat cerebrum during status epilepticus. *Magnetic Resonance in Medicine*, 30(2):241–246, aug 1993.

[206] Denis Le Bihan. What can we see with IVIM MRI? *NeuroImage*, 187:56–67, feb 2019.

[207] Allen W. Song and Tianlu Li. Improved spatial localization based on flow-moment-nulled and intral-voxel incoherent motion-weighted fMRI. *NMR in Biomedicine*, 16(3):137–143, 2003.

[208] Tao Jin, Fuqiang Zhao, and Seong Gi Kim. Sources of functional apparent diffusion coefficient changes investigated by diffusion-weighted spin-echo fMRI. *Magnetic Resonance in Medicine*, 56(6):1283–1292, 2006.

[209] Allen W. Song, Marty G. Woldorff, Stacey Gangstead, George R. Mangun, and Gregory McCarthy. Enhanced Spatial Localization of Neuronal Activation Using Simultaneous Apparent-Diffusion-Coefficient and Blood-Oxygenation Functional Magnetic Resonance Imaging. *NeuroImage*, 17(2):742–750, oct 2002.

[210] Denis Le Bihan. Diffusion, confusion and functional MRI, aug 2012.

[211] Jerrold L. Boxerman, Peter A. Bandettini, Kenneth K. Kwong, John R. Baker, Timothy L. Davis, Bruce R. Rosen, and Robert M. Weisskoff. The intravascular contribution to fmri signal change: monte carlo modeling and diffusionweighted studies in vivo. *Magnetic Resonance in Medicine*, 34(1):4–10, 1995.

[212] Toshihiko Aso, Shin ichi Urayama, Cyril Poupon, Nobukatsu Sawamoto, Hidenao Fukuyama, and Denis Le Bihan. An intrinsic diffusion response function for analyzing diffusion functional MRI time series. *NeuroImage*, 47(4):1487–1495, oct 2009.

[213] David G. Norris and Jonathan R. Polimeni. Laminar (f)MRI: A short history and future prospects, aug 2019.

[214] David Ress, Gary H. Glover, Junjie Liu, and Brian Wandell. Laminar profiles of functional activity in the human brain. *NeuroImage*, 34(1):74–84, jan 2007.

[215] Laurentius Huber, Daniel A. Handwerker, David C. Jangraw, Gang Chen, Andrew Hall, Carsten Stüber, Javier Gonzalez-Castillo, Dimo Ivanov, Sean Marrett, Maria Guidi, Jozien Goense, Benedikt A. Poser, and Peter A. Bandettini. High-Resolution CBV-fMRI Allows Mapping of Laminar Activity and Connectivity of Cortical Input and Output in Human M1. *Neuron*, 96(6):1253–1263.e7, dec 2017.

[216] Trong-Kha Truong and Allen W. Song. Cortical depth dependence and implications on the neuronal specificity of the functional apparent diffusion coefficient contrast. *NeuroImage*, 47(1):65–68, aug 2009.

[217] Daniel Nunes, Rita Gil, and Noam Shemesh. A rapid-onset diffusion functional MRI signal reflects neuromorphological coupling dynamics. *NeuroImage*, 231:117862, may 2021.

[218] Xin Yu, Chunqi Qian, Der Yow Chen, Stephen J. Dodd, and Alan P. Koretsky. Deciphering laminar-specific neural inputs with line-scanning fMRI. *Nature Methods*, 11(1):55–58, 2014.

[219] Allen D. Elster and Terry J. Provost. Large-tip-angle spin-echo imaging: Theory and applications. *Investigative Radiology*, 28(10):944–953, 1993.

[220] Irati Markuerkiaga, Markus Barth, and David G. Norris. A cortical vascular model for examining the specificity of the laminar BOLD signal. *NeuroImage*, 132:491–498, may 2016.

[221] Richard B. Buxton, Kâmil Uluda, David J. Dubowitz, and Thomas T. Liu. Modeling the hemodynamic response to brain activation. In *NeuroImage*, volume 23. Neuroimage, 2004.

[222] FSL toolbox: MELODIC. `https://fsl.fmrib.ox.ac.uk/fsl/fslwiki/MELODIC/`.

[223] J. Albrecht, M. Burke, K. Haegler, V. Schöpf, A. M. Kleemann, M. Paolini, M. Wiesmann, and J. Linn. Potential Impact of a 32-Channel Receiving Head Coil Technology on the Results of a Functional MRI Paradigm. *Clinical Neuroradiology*, 20(4):223–229, dec 2010.

[224] Jessica L. Panman, Yang Yang To, Emma L. van der Ende, Jackie M. Poos, Lize C. Jiskoot, Lieke H. H. Meeter, Elise G. P. Dopper, Mark J. R. J. Bouts, Matthias J. P. van Osch, Serge A. R. B. Rombouts, John C. van Swieten, Jeroen van der Grond, Janne M. Papma, and Anne Hafkemeijer. Bias Introduced by Multiple Head Coils in MRI Research: An 8 Channel and 32 Channel Coil Comparison. *Frontiers in Neuroscience*, 13(JUL):729, jul 2019.

[225] Philipp Seidel, Seth M. Levine, Marlene Tahedl, and JensV V. Schwarzbach. Temporal Signal-to-Noise Changes in Combined

Multislice- and In-Plane-Accelerated Echo-Planar Imaging with a 20- and 64-Channel Coil. *Scientific Reports*, 10(1):1–9, dec 2020.

[226] Matthias L Schroeter, Thomas Kupka, Toralf Mildner, Kâmil Uludag, and D Yves Von Cramon. Investigating the post-stimulus undershoot of the BOLD signal-A simultaneous fMRI and fNIRS study. 2005.

[227] R. Nicolas, H. Gros-Dagnac, F. Aubry, and P. Celsis. Comparison of BOLD, diffusion-weighted fMRI and ADC-fMRI for stimulation of the primary visual system with a block paradigm. *Magnetic Resonance Imaging*, 39:123–131, jun 2017.

[228] Chun Siong Soon, Vinod Venkatraman, and Michael W.L. Chee. Stimulus repetition and hemodynamic response refractoriness in event-related fMRI. *Human Brain Mapping*, 20(1):1–12, sep 2003.

[229] E. M. Haacke, S. Mittal, Z. Wu, J. Neelavalli, and Y. C.N. Cheng. Susceptibility-weighted imaging: Technical aspects and clinical applications, part 1, jan 2009.

[230] Michael S. Patterson, B. Chance, and B. C. Wilson. Time resolved reflectance and transmittance for the noninvasive measurement of tissue optical properties. *Applied Optics*, 28(12):2331, jun 1989.

[231] Tuan H Pham, Frederic Bevilacqua, Thorsten Spott, Jan S Dam, Bruce J Tromberg, and Stefan Andersson-engels. Quantifying the absorption and reduced scattering coefficients of tissuelike turbid media over a broad spectral range with noncontact Fourier-transform hyperspectral imaging. *Applied Optics*, 39(34):6487–6497, 2000.

[232] Erik Alerstam, Stefan Andersson-Engels, and Tomas Svensson. White Monte Carlo for time-resolved photon migration. *Journal of Biomedical Optics*, 13(4):041304, 2008.

[233] Alwin Kienle and Michael S Patterson. Determination of the optical properties of turbid media from a single Monte Carlo simulation. *Physics in Medicine and Biology*, 41(10):2221–2227, oct 1996.

[234] steve Lihong Wang. Monte Carlo Modeling of light transport in multilayer tissue.pdf.

[235] Steven L. Jacques. Optical properties of biological tissues: A review, jun 2013.

[236] Monte Carlo Methods - J. Hammersley - Google Books.

[237] Nicholas Metropolis and S. Ulam. The Monte Carlo Method. *Journal of the American Statistical Association*, 44(247):335–341, 1949.

[238] Michail Stamatakis and Dionisios G. Vlachos. Unraveling the complexity of catalytic reactions via kinetic monte carlo simulation: Current status and frontiers, dec 2012.

[239] Murat Mesta, Marco Carvelli, Rein J. De Vries, Harm Van Eersel, Jeroen J.M. Van Der Holst, Matthias Schober, Mauro Furno, Björn Lüssem, Karl Leo, Peter Loebl, Reinder Coehoorn, and Peter A. Bobbert. Molecular-scale simulation of electroluminescence in a multilayer white organic light-emitting diode. *Nature Materials*, 12(7):652–658, apr 2013.

[240] Paul Glasserman. *Monte Carlo Methods in Financial Engineering*. Springer-Verlag, New York, 2004.

[241] Dirk P. Kroese and Joshua C. C. Chan. *Statistical Modeling and Computation*. Springer, New York, 2014.

[242] Minh Anh Nguyen, Kazushi Sano, and Vu Tu Tran. A Monte Carlo tree search for traveling salesman problem with drone. *Asian Transport Studies*, 6:100028, jan 2020.

[243] Lihong Wang, Steven L. Jacques, and Liqiong Zheng. MCML-Monte Carlo modeling of light transport in multi-layered tissues. *Computer Methods and Programs in Biomedicine*, 47(2):131–146, jul 1995.

[244] B. C. Wilson and G. Adam. A Monte Carlo model for the absorption and flux distributions of light in tissue. *Medical Physics*, 10(6):824–830, 1983.

[245] Marleen Keijzer, Steven L. Jacques, Scott A. Prahl, and Ashley J. Welch. Light distributions in artery tissue: Monte Carlo simulations for finitediameter laser beams. *Lasers in Surgery and Medicine*, 9(2):148–154, 1989.

[246] Joseph Angelo, Christina R. Vargas, Bernard T. Lee, Irving J. Bigio, and Sylvain Gioux. Ultrafast optical property map generation using lookup tables. *Journal of Biomedical Optics*, 21(11):110501, 2016.

[247] Luis De Taboada, Jin Yu, Salim El-Amouri, Sebastiano Gattoni-Celli, Steve Richieri, Thomas McCarthy, Jackson Streeter, and Mark S. Kindy. Transcranial laser therapy attenuates amyloid-β peptide neuropathology in amyloid-β protein precursor transgenic mice. *Journal of Alzheimer's Disease*, 23(3):521–535, 2011.

[248] Daniel M. Johnstone, Cécile Moro, Jonathan Stone, Alim Louis Benabid, and John Mitrofanis. Turning on lights to stop neurodegeneration: The potential of near infrared light therapy in Alzheimer's and Parkinson's Disease, 2016.

[249] Takahiro Ando, Weijun Xuan, Tao Xu, Tianhong Dai, Sulbha K. Sharma, Gitika B. Kharkwal, Ying Ying Huang, Qiuhe Wu, Michael J. Whalen, Shunichi Sato, Minoru Obara, and Michael R. Hamblin. Comparison of therapeutic effects between pulsed and continuous wave 810-nm wavelength laser irradiation for traumatic brain injury in mice. *PLoS ONE*, 6(10), oct 2011.

[250] Abid Oueslati, Blaise Lovisa, John Perrin, Georges Wagnières, Hubert Van Den Bergh, Yanik Tardy, and Hilal A. Lashuel. Photobiomodulation suppresses alpha-synuclein-induced toxicity in an AAV-based rat genetic model of Parkinson's disease. *PLoS ONE*, 10(10), oct 2015.

[251] Fredric Schiffer, Andrea L Johnston, Caitlin Ravichandran, Ann Polcari, Martin H Teicher, Robert H Webb, and Michael R Hamblin. Psychological benefits 2 and 4 weeks after a single treatment with near infrared light to the forehead: a pilot study of 10 patients with major depression and anxiety. *Behavioral and Brain Functions*, 5(1):46, 2009.

[252] Farzad Salehpour and Seyed Hossein Rasta. The potential of transcranial photobiomodulation therapy for treatment of major depressive disorder. *Reviews in the Neurosciences*, 28(4):441–453, may 2017.

[253] Farzad Salehpour, Nahid Ahmadian, Seyed Hossein Rasta, Mehdi Farhoudi, Pouran Karimi, and Saeed Sadigh-Eteghad. Transcranial

low-level laser therapy improves brain mitochondrial function and cognitive impairment in D-galactoseinduced aging mice. *Neurobiology of Aging*, 58:140–150, oct 2017.

[254] Pardis Kaynezhad, Ilias Tachtsidis, Asmaa Aboelnour, Sobha Sivaprasad, and Glen Jeffery. Watching synchronous mitochondrial respiration in the retina and its instability in a mouse model of macular degeneration. *Scientific Reports*, 11(1):3274, dec 2021.

[255] Despoina Gkotsi, Rana Begum, Thomas Salt, Gerassimos Lascaratos, Chris Hogg, Kai Yin Chau, Anthony H.V. Schapira, and Glen Jeffery. Recharging mitochondrial batteries in old eyes. Near infra-red increases ATP. *Experimental Eye Research*, 122:50–53, 2014.

[256] Margaret T.T. Wong-Riley, Huan Ling Liang, Janis T. Eells, Britton Chance, Michele M. Henry, Ellen Buchmann, Mary Kane, and Harry T. Whelan. Photobiomodulation directly benefits primary neurons functionally inactivated by toxins: Role of cytochrome c oxidase. *Journal of Biological Chemistry*, 280(6):4761–4771, feb 2005.

[257] Noriko Mochizuki-Oda, Yosky Kataoka, Yilong Cui, Hisao Yamada, Manabu Heya, and Kunio Awazu. Effects of near-infra-red laser irradiation on adenosine triphosphate and adenosine diphosphate contents of rat brain tissue. *Neuroscience Letters*, 323(3):207–210, may 2002.

[258] Maria G. Mason, Peter Nicholls, and Chris E. Cooper. Re-evaluation of the near infrared spectra of mitochondrial cytochrome c oxidase: Implications for non invasive in vivo monitoring of tissues. *Biochimica et Biophysica Acta - Bioenergetics*, 1837(11):1882–1891, 2014.

[259] M. S. Wróbel, A. P. Popov, A. V. Bykov, M. Kinnunen, M. Jędrzejewska-Szczerska, and V. V. Tuchin. Multi-layered tissue head phantoms for noninvasive optical diagnostics. In *Journal of Innovative Optical Health Sciences*, volume 8. World Scientific Publishing Co. Pte Ltd, may 2015.

[260] P. Sawosz, S. Wojtkiewicz, M. Kacprzak, W. Weigl, A. Borowska-Solonynko, P. Krajewski, K. Bejm, D. Milej, B. Ciszek, R. Maniewski, and A. Liebert. Human skull translucency: post mortem studies. *Biomedical Optics Express*, 7(12):5010, dec 2016.

[261] Skin Optics Summary. *https://omlc.org/news/jan98/skinoptics.html*.

[262] Anna Custo, William M. Wells, Alex H. Barnett, Elizabeth M.C. Hillman, and David A. Boas. Effective scattering coefficient of the cerebral spinal fluid in adult head models for diffuse optical imaging. *Applied Optics*, 45(19):4747–4755, jul 2006.

[263] Optical properties of biological tissues: a review - IOPscience. *https://iopscience.iop.org/article/10.1088/0031-9155/58/11/R37/meta*.

[264] Aleh Sudakou, Stanislaw Wojtkiewicz, Frédéric Lange, Anna Gerega, Piotr Sawosz, Ilias Tachtsidis, and Adam Liebert. Depth-resolved assessment of changes in concentration of chromophores using time-resolved near-infrared spectroscopy: estimation of cytochrome-c-oxidase uncertainty by Monte Carlo simulations. *Biomedical Optics Express*, 10(9):4621, sep 2019.

[265] *Quantitative MRI of the Brain: Measuring Changes Caused by Disease - Google Libri*.

[266] Kaide Jin, Tianqi Zhang, Marnie Shaw, Perminder Sachdev, and Nicolas Cherbuin. Relationship Between Sulcal Characteristics and Brain Aging. *Frontiers in Aging Neuroscience*, 10:339, nov 2018.

[267] Owen Dyer. Pulse oximetry may underestimate hypoxaemia in black patients, study finds, dec 2020.

[268] Martin J. Tobin and Amal Jubran. Unreliable pulse oximetry in dark-skin patients: a plea for algorithm disclosure, dec 2022.

[269] Daniel Wangpraseurt, Steven L. Jacques, Tracy Petrie, and Michael Kühl. Monte Carlo Modeling of Photon Propagation Reveals Highly Scattering Coral Tissue. *Frontiers in Plant Science*, 7(September):1404, sep 2016.

[270] Christopher R. Madan. Robust estimation of sulcal morphology. *Brain Informatics*, 6(1):1–11, dec 2019.

[271] Monte Carlo Light Scattering Programs. `https://omlc.org/software/mc/`.

[272] Tomas Möller and Ben Trumbore. Fast, Minimum Storage Ray-Triangle Intersection. *Journal of Graphics Tools*, 2(1):21–28, jan 1997.

[273] FreeSurfer. `https://surfer.nmr.mgh.harvard.edu/`.

[274] William E. Lorensen and Harvey E. Cline. Marching cubes: A high resolution 3D surface construction algorithm. In *Proceedings of the 14th Annual Conference on Computer Graphics and Interactive Techniques, SIGGRAPH 1987*, volume 21, pages 163–169, New York, New York, USA, aug 1987. Association for Computing Machinery, Inc.

[275] E. V., Chernyaev. *Marching Cubes 33 : construction of topologically correct isosurfaces : presented at GRAPHICON '95, Saint-Petersburg, Russia, 03-07.07.1995.* CERN. Computing and Networks Division, 1995.

[276] Lis Custodio, Sinesio Pesco, and Claudio Silva. An extended triangulation to the Marching Cubes 33 algorithm. *Journal of the Brazilian Computer Society*, 25(1):6, dec 2019.

[277] Juan J Jiménez, Carlos J Ogáyar, José M Noguera, and Félix Paulano. Performance Analysis for GPU-based Ray-triangle Algorithms.

[278] Alan Urban, Clara Dussaux, Guillaume Martel, Clément Brunner, Emilie Mace, and Gabriel Montaldo. Real-time imaging of brain activity in freely moving rats using functional ultrasound. *Nature Methods*, 12(9):873–878, aug 2015.

[279] Kâmil Uluda and Pablo Blinder. Linking brain vascular physiology to hemodynamic response in ultra-high field MRI. *NeuroImage*, 168:279–295, mar 2018.

[280] João Jorge, Patrícia Figueiredo, Rolf Gruetter, and Wietske van der Zwaag. Mapping and characterization of positive and negative BOLD responses to visual stimulation in multiple brain regions at 7T. *Human Brain Mapping*, 39(6):2426–2441, jun 2018.

[281] Alex R. Wade. The negative BOLD signal unmasked, dec 2002.

[282] Gino DiIorio, Jeffrey J. Brown, Joseph A. Borrello, William H. Perman, and Hui Hua Shu. Large angle spin-echo imaging. *Magnetic Resonance Imaging*, 13(1):39–44, jan 1995.

[283] R. R. Ernst and W. A. Anderson. Application of fourier transform spectroscopy to magnetic resonance. *Review of Scientific Instruments*, 37(1):93–102, 1966.

[284] P. J. Wright, O. E. Mougin, J. J. Totman, A. M. Peters, M. J. Brookes, R. Coxon, P. E. Morris, M. Clemence, S. T. Francis, R. W. Bowtell, and P. A. Gowland. Water proton T1 measurements in brain tissue at 7, 3, and 1.5T using IR-EPI, IR-TSE, and MPRAGE: Results and optimization. *Magnetic Resonance Materials in Physics, Biology and Medicine*, 21(1-2):121–130, 2008.

[285] Eric R. Cohen, Kamil Ugurbil, and Seong Gi Kim. Effect of basal conditions on the magnitude and dynamics of the blood oxygenation level-dependent fMRI response. *Journal of Cerebral Blood Flow and Metabolism*, 22(9):1042–1053, 2002.

[286] R. Slack, L. Boorman, P. Patel, S. Harris, M. Bruyns-Haylett, A. Kennerley, M. Jones, and J. Berwick. A novel method for classifying cortical state to identify the accompanying changes in cerebral hemodynamics. *Journal of Neuroscience Methods*, 267:21–34, jul 2016.

[287] Patrick J. Drew. Vascular and neural basis of the BOLD signal, oct 2019.

[288] Rolf B Saager, David J Cuccia, and Anthony J Durkin. Determination of optical properties of turbid media spanning visible and near-infrared regimes via spatially modulated quantitative spectroscopy. *Journal of biomedical optics*, 15(1):017012, 2010.

[289] Hugo J. van Staveren, Christian J. M. Moes, Jan van Marie, Scott A. Prahl, and Martin J. C. van Gemert. Light scattering in lntralipid-10% in the wavelength range of 4001100 nm. *Applied Optics*, 30(31):4507, nov 1991.

[290] Ryan P. Vetreno, Richard Yaxley, Beatriz Paniagua, G. Allan Johnson, and Fulton T. Crews. Adult rat cortical thickness changes across age and following adolescent intermittent ethanol treatment. *Addiction Biology*, 22(3):712–723, may 2017.

[291] K. L. Leenders, D. Perani, A. A. Lammertsma, J. D. Heather, P. Buckingham, T. Jones, M. J.R. Healy, J. M. Gibbs, R. J.S. Wise, J. Hatazawa, S. Herold, R. P. Beaney, D. J. Brooks, T. Spinks, C. Rhodes, and R. S.J. Frackowiak. Cerebral blood flow, blood volume and oxygen utilization: Normal values and effect of age. *Brain*, 113(1):27–47, feb 1990.

[292] Egill Rostrup, Gitte M. Knudsen, Ian Law, Søren Holm, Henrik B.W. Larsson, and Olaf B. Paulson. The relationship between cerebral blood flow and volume in humans. *NeuroImage*, 24(1):1–11, jan 2005.

7 Appendix

7.1 Optical Imaging

This chapter discusses the optical imaging experiments and results. This includes the development and validation of the optical acquisition setup, with testing of camera performance, acquisition data rate for storing, calibrations, and validation using phantoms. It also details the process for making phantoms used in method calibration. The results from OIS and SFDI experiments are presented, and discussed in context with the fMRI results from previous chapters.

7.1.1 Acquisition development and validation

Acquisitions were designed to balance fast imaging rates with memory requirements. Images acquired at full resolution would give a rapidly increasing file size, which could require the data to be stored across different files, or result in long loading times and slow down analysis. For OIS, the temporal resolution was considered important, but image resolution was reduced, as changes occur in a large area of the well, and the precise location was not a focus. By setting image resolution to 256×256 and using 2-factor binning during functional imaging, the area of interest could be covered while achieving 16 Hz frame rates, but producing manageable file sizes. Several protocols were tested for saving data, settling on saving each frame directly to a .mat-file for the purposes of these experiments. This allowed an experiment of typically 13 minutes to be saved to a single file. For higher frame rates or longer experiments, it would alternatively be possible to save data after each trial, with time allotted to the saving process being factored into the trigger timings. The frame size could be reduced to fit more time points into a memory buffer. An experiment could further be divided into sections, such that the frames from a given trial of the stimulus could be kept in active memory and written to file before starting a new trial.

Figure 7.1 shows camera intensity over time from imaging a white background, as a test of stability. There is a slight drift in recorded intensity over time most likely due to gradual heating of the camera components, and the inclusion of a heat sink does not have a significant effect on the magnitude of the drift. This could potentially affect readings for very long experiments, and such experiments may benefit from the addition of a cool down time

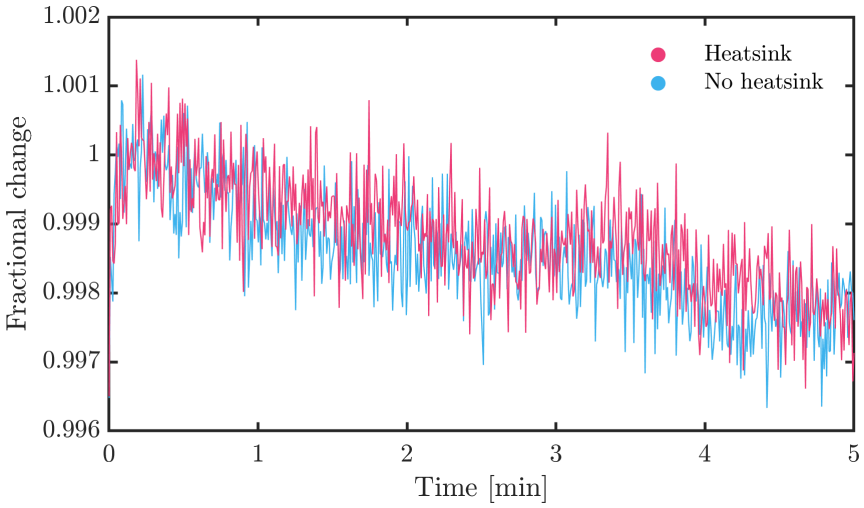

Figure 7.1: Camera drift over time. The average intensity readings from the camera decrease somewhat over the course of minutes, however the effect is slow, fairly regular and on the scale of less than a percent, and therefore not likely to affect the results. The inclusion of a heat sink had little effect on the trend during testing.

between trials. The error for the time interval shown represents around 2% of the measured intensity, and with further reductions in overall measured intensity it could become difficult to detect any (likely very small) change in cellular scattering. The effect per experiment should however be minimal, as low-frequency changes are corrected for in analysis.

Projector calibration In this experiment, the illuminating image is displayed using an AAXA Technologies P2 Jr pico projector. Projectors typically have a non-linear output, meaning that an input computer grey scale value is not linearly proportional to the output intensity. This was corrected for in order to produce more sine shaped output. An intensity response function was measured by acquiring a series of images of a flat white surface illuminated by the projector while incrementing the computer generated image grey scale from black to white. The averaged intensity for each image is shown in Figure 7.2. The displayed sine images were adjusted in accordance with the intensity response function to provide a recorded sine wave image. The baseline of the intensity curve was removed, the was data normalised, and a function was fitted to the curve, using recorded intensity as the independent variable. This provided an expression giving the computer value required (0-100) to give a desired recorded intensity. As a test, each image in the intensity response test was adjusted in this manner, and the

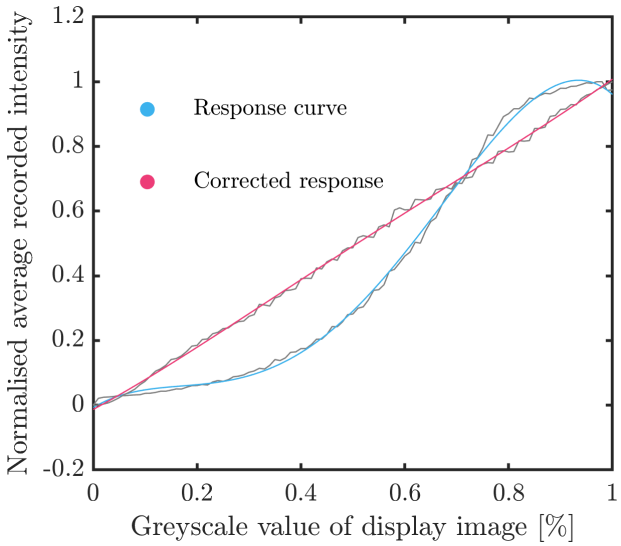

Figure 7.2: Instrument response function for the projector used in this project (Blue). The red curve shows the same measurement after adjusting the white levels of each image according to the calibration procedure, giving a straight line as expected.

resulting curve in shown in red in Figure 7.2. Shown in Figure 7.3 is the recorded sine wave from illuminating a flat white surface with the adjusted and unadjusted sine wave images.

Distortion correction The lens can cause radially symmetric distortion of the projected image. Radial distortion is sometimes described as barrel or pincushion distortion, which refer to the degree of magnification increasing towards the center or towards the periphery of the image respectively. This is easily visualised with a grid pattern as shown in the Figure 7.4. The distortion follows Equation 7.1, where (x_c, y_c) are the coordinates of the distortion center, (x_d, y_d) is the distorted point and (x, y) the point after correction. The radial distortion coefficient k_1 is negative for barrel distortion and positive for pincushion distortion.

$$\begin{aligned} x &= x_c + \frac{x_d - x_c}{1 + k_1 r^2 + k_2 r^4 ...} \\ y &= y_c + \frac{y_d - y_c}{1 + k_1 r^2 + k_2 r^4 ...} \end{aligned} \tag{7.1}$$

The barrel distortion created by the setup lens can be corrected for by applying a pincushion correction to the generated image before projection. This counteracts the effect, giving a final image where the straight lines of

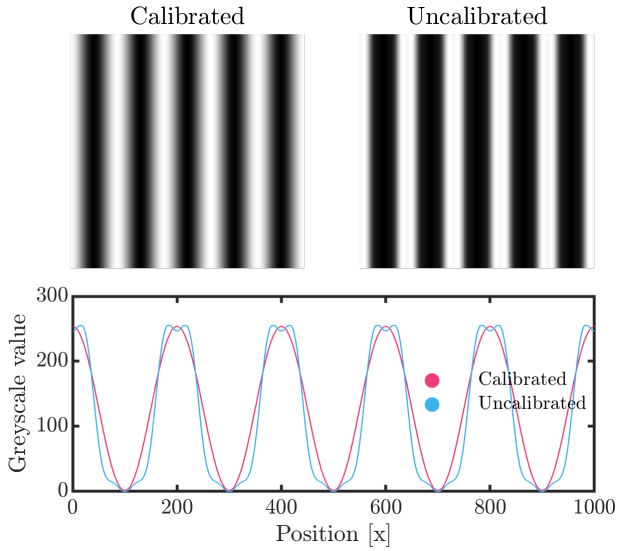

Figure 7.3: The sine pattern after (left) and before calibration (right), and the cross-section of the sine pattern for each image. The instrument response function causes the displayed pattern to be sharp and square if left uncorrected.

the sine pattern appear parallel as intended. The required correction was determined before experiments by projecting the grid pattern and adjusting the k until the lines were parallel.

A few factors could impact on the measurements performed at different wavelengths. Firstly, the camera quantum efficiency varies across the operating wavelengths. The quantum efficiency is a measure of the ability of the camera to convert incoming photons to electrons, and is therefore a measure of how the electrical signals or readout response correlates to the input light intensity for a given wavelength. The manufacturer has provided measurements of this efficiency, which is shown in Figure 7.5. As the optical imaging analysis relies on combining measurements made at several wavelength, it is worth noting the variation across the wavelengths chosen. Here, the quantum efficiency is fairly consistent for the target wavelengths as shown on the right panel of the figure, with the exception of 470 nm, where efficiency is somewhat lower. This will lead the intensities measured under the blue filter to be slightly underestimated in comparison with the other data.

Another consideration is the filter profiles. The Thorlabs filters have a center wavelength of $\pm$ 2nm and FWHM 10 $\pm$ 2nm. As can be seen from Figure 7.6 however, the filter profiles are not all Gaussian as expected, and

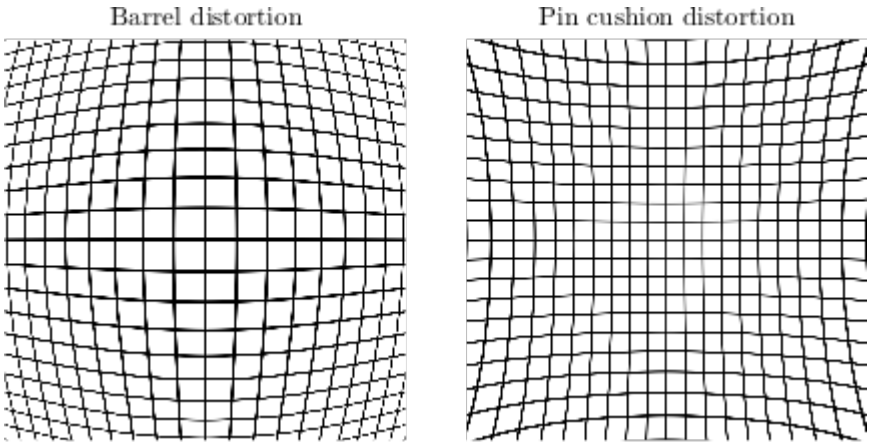

Figure 7.4: Radial distortion can cause the image to warp, and is described by barrel (left) or pincushion distortion (right). This effect can be caused by lenses, but a correction can be applied to the digital image so that the projected image appears undistorted. Barrel distortion (left) is caused by a positive value of k, pin cushion distortion by a negative k, here k is 0.6 and -0.2 respectively.

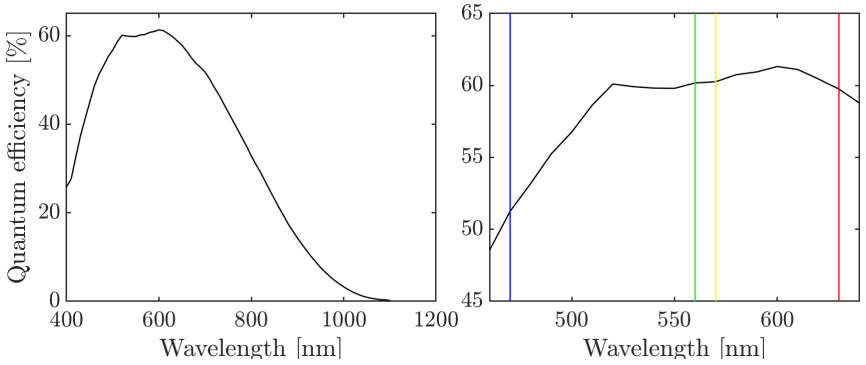

Figure 7.5: The quantum efficiency of the camera used for optical imaging.

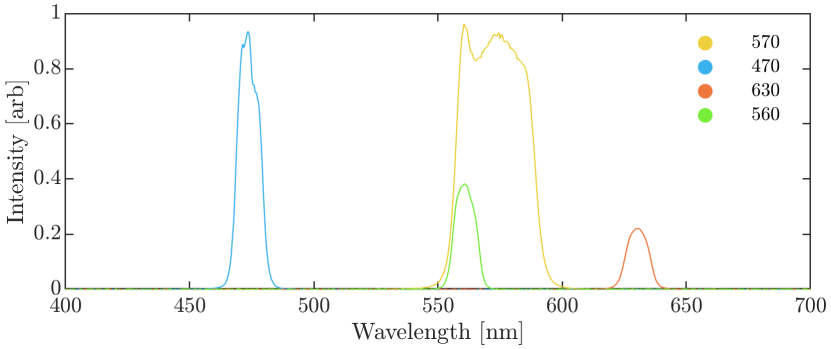

Figure 7.6: The spectral profiles of the four filters used for OIS. Corrections should be made in analysis to account for the shape of the filter profiles to avoid errors in relative intensity scaling in the different channels.

the 570 nm filter is significantly wider than the others. The shape and width of each filter profile should be included in the analysis to account for the absorption within that range. Here, the area under the curve was normalised to one for each filter, and the resulting profile multiplied by the extinction coefficient spectrum during analysis.

7.1.2 Phantoms

During development, the optical methods were tested using phantoms. The aim of using these systems is to mimic some behaviours of real tissue, but they offer more flexibility or have known properties. In order to provide quantitative results, SFDI must be calibrated using images acquired of samples with known optical properties. Liquid phantoms were prepared, and used to test and calibrate the SFDI acquisition and analysis.

There are several options for tissue simulating phantoms described in the literature. These can be either liquid or solid samples, and are made from substances which are well characterised. Cuccias original work used 16 turbid phantoms made up of Liposyn lipid emulsion and water-soluble nigrosin dye for scattering and absorption properties respectively. The properties were determined by frequency domain photon migration measurements. Another alternative for a solid phantom is polymethyldisiloxane, using India ink and TiO_2 for absorption and scattering properties.

Although solid phantoms are more easily transported and last longer, liquid phantoms are convenient because they are easily prepared from readily available materials, and their optical properties are more easily determined.

Here, liquid phantoms phantoms were prepared using nigrosin dye as absorbing media and intralipid 20% as scatteing media, following the work of Saager et al.[288] Intralipid is well characterised and therefore suitable for use as scatterer. For easily achievable concentrations it has scattering properties which are similar to those of tissue, and relatively low absorbance. Water-soluble nigrosin dye was used as the absorbing agent, as it has a broad absorption spectrum in the visible range, similar to tissue. As scattering and absorption is dependent only on the concentration of each of the two components, the optical properties are easily determined. By selecting suitable concentrations, the absorption and scattering properties can be set to a sufficiently broad range of values to span the ranges of properties typical for tissue in the visible region. Here the values were matched to those used by Cuccia et al.,[38] with $\mu_A = [0.002 - 0.12]mm^{-1}$ and $\mu'_S = [0.32 - 1.8]mm^{-1}$.

The wavelengths used in this project are [630,570,560,470]. In order to make phantoms with a sensible range of absorption coefficients within this range, solutions of nigrosin dye were made up at different concentrations. Absorber solutions were made up to have absorbances close to the targets, and the true absorption coefficients were calculated from the measured absorbances. Concentrations were adjusted to give suitable absorbances at 560 nm, as given by the equation 7.2

$$\begin{aligned} T = e^{-\mu_A L} &= 10^{-A} \\ -\mu_A L &= ln(10^{-A}) \\ \mu_A &= \frac{A \cdot ln(10)}{L} \end{aligned} \tag{7.2}$$

Stavern *et al* showed that the scattering properties of intralipid-10% closely follow Mie scattering, and can therefore be approximated to by Equation 7.3 to within 6% error.[289] Saager confirmed these findings with separate measurements.[288] The wavelength (λ) is here given in nm.

$$\mu_S(\lambda)[\mathrm{mL}^{-1}\mathrm{Lmm}^{-1}] = 0.016 \cdot (\lambda \cdot 10^{-4})^{-2.4} \tag{7.3}$$

$$g(\lambda) = 1.1 - 0.58 \cdot (\lambda \cdot 10^{-4}) \tag{7.4}$$

They showed this equation holds for concentrations of around 17% at 400 nm to 4% at 1100 nm. For the desired scattering coefficients, the intralipid

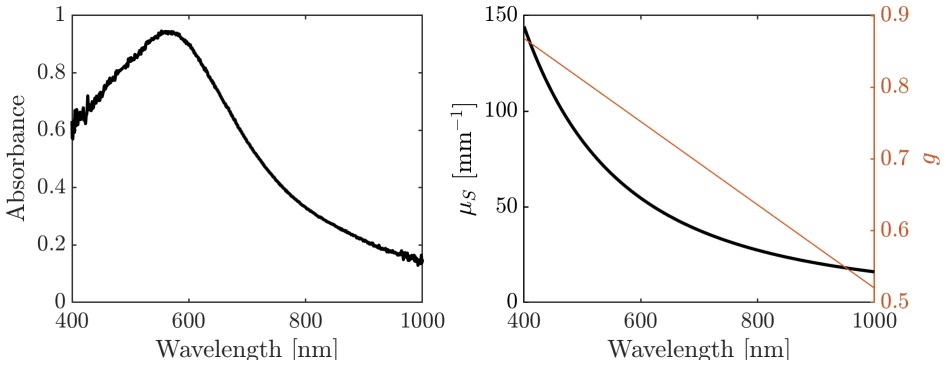

Figure 7.7: Optical properties of the components used to make the phantoms. The nigrosin dye provides broad absorption in the visible range, as seen to the left. The intralipid scattering can be approximated by Mie scattering, as shown to the right.

had to be diluted with deionised water to a suitable percentage, following

$$\mu'_S[\text{mm}^{-1}] = \sigma C_{\%}, \sigma = \mu_s(1-g)/10 \tag{7.5}$$

where $C_{\%}$ is the intralipid concentration in percent volume ($< 10\%$).

7.1.3 OIS analysis

The path lengths required to calculate chromophore concentrations from attenuation data were determined by simulation as detailed in Chapter 4. As discussed in Chapter 2, the calculation is done using the differential path length, as this is less sensitive to small errors in the path length estimate. The resulting conversion relates a change in attenuation to a change in path length, according to Equation 7.6.

$$\begin{aligned} A &= \mu_A \cdot L \\ \delta\mu_A &= \int \frac{\delta A}{\delta L} \end{aligned} \tag{7.6}$$

Practically, the differential path lengths δL were determined from the histogram H of the path length distribution across bins x and bin width δq.

$$L = \frac{\sum_{i=1} x_i \cdot (i-1) \cdot \delta q \cdot H(x_i)}{\sum_{i=1} x_i \cdot H(x_i)} \tag{7.7}$$

The μ_A before stimulus is used as a baseline, this is estimated using the baseline blood volume V (eg. 100 uM) and the baseline blood oxygen satu-

ration Y (eg. 50%). Concentrations of oxy- and deoxy-hemoglobin are given as

$$\begin{aligned} [HbO] &= V * Y \\ [Hbr] &= V(1-Y) \end{aligned} \tag{7.8}$$

During analysis, the attenuation data is divided through by the differential path lengths, these therefore affect the magnitude of the HbO, Hbr and HbT signals, as well as the relative magnitude between the three. A good estimate of the path length distribution is therefore necessary for interpretetation of the results. Simulations were parameterised using optical properties typical of grey matter, as detailed in Section 4. It was assumed that the effects of skull and CSF would be negligible, as these layers were so thin. 100 parallel simulations were run, each with 10000 photons, for each of the four target wavelengths.

As the density of blood vessels varies significantly by cortical depth, the model was divided into layers, with each layers absorption properties affected by a specified blood volume fraction. The haemoglobin, being the main absorber in the cortical tissue, will have a significant effect on the path length, with the superficial layers being likely to absorb an incoming photon before it has travelled very far. The blood volume fractions were based on the depth profile presented by Kennerley et al,[151] which shows experimentally determined values from rat cortex. Their data is shown in Figure 7.8, along with the profile which was used in the path length simulations. For deeper layers literature values were used, assuming white matter below a cortical thickness of 1.75 mm.[290] The transition was smoothed using Savitzky-Golay filtering to avoid a sharp change. Blood volume fraction has been measured by PET to be $5.2 \pm 1.4\%$ in grey matter and $2.7 \pm 0.6\%$ in white matter.[291] It can vary during hypo- or hypercapnia, within 5.1 to 6.9 % and 2.0 to 2.8 % in grey and white matter respectively.[292] Figure 7.9 shows the impact of including the depth-variation in blood volume fraction, as opposed to keeping it constant at the literature value.

The OIS data is expected to show a peak for HbO with an amplitude of around 15 % change with respect to baseline. This is the degree of change reported in concurrent OIS and fMRI studies using an electrical stimulus to activate the rat whisker barrel cortex.[151] This amplitude of response is also required to explain the BOLD response observed in that study. The

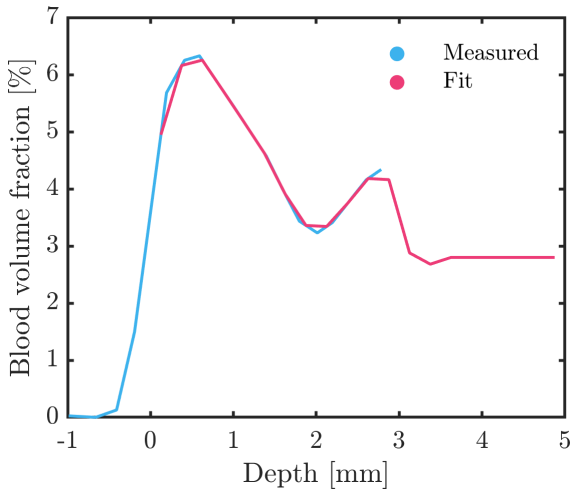

Figure 7.8: The profile of blood volume fraction per depth, used for simulations of path length estimates. MR measurements of the blood volume fraction as a function of cortical depth (blue), were adapted from Kennerley et al.[151] Values for the deeper layers were estimated using literature values, and the transition was smoothed using Savitzky-Golay filtering.

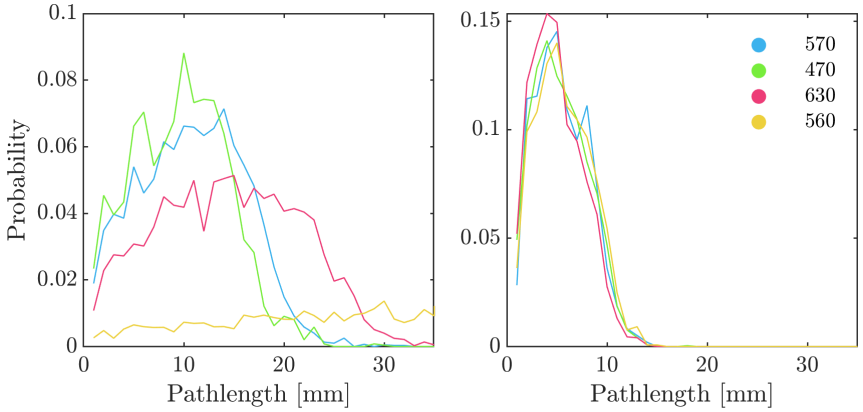

Figure 7.9: Path length distributions simulated using optical properties typical for grey matter (left), and using the same properties but introducing a layer-dependent variation in blood volume fraction. As would be expected, the greater absorption in the superficial layers of cortex reduces the typical path length, as the photons become more readily absorbed early on.

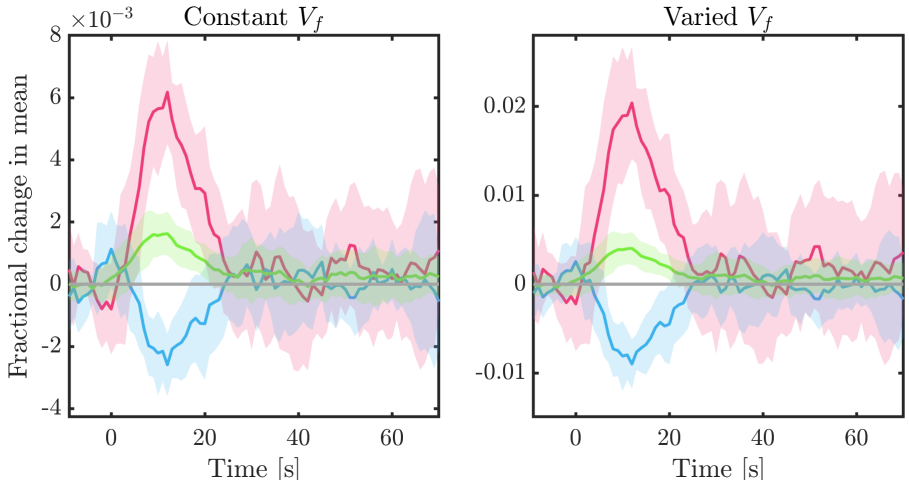

Figure 7.10: Response from an example 8 second stimulus, showing the effect of considering the variation of blood volume fraction by depth. Signal amplitudes are greatly increased as the differential pathlength is approximately halved.

pathlength effect on the responses are shown in Figure 7.10. Here the differences in path lengths have had a significant effect on the amplitude of the responses, while the relative amplitudes of HbO, Hbr and HbT remain fairly similar between the two data sets. By including the variation in blood volume fraction, the differential pathlengths have all been reduced to half or less relative to those of the single-layer grey matter slab, resulting in a 3-fold increase in signal amplitude.

7.1.4 Simulation for optical analysis

The sensitivity of μ_s' measurements are dependent on the spatial frequency. Simulations were run at μ_s' values in the range $[0.30 - 2.50] mm^{-1}$, which is quoted as typical for tissue,[231] and repeated for small changes in μ_s'. The value of μ_a was held constant at 0.02 mm^{-1}, and 10^7 photons were used per simulation. Figure 7.11 shows that sensitivity to μ_s' is greatest close to 0.1 mm^{-1}. This agrees with results shown by Cuccia et al.[38] The cranial window has a diameter of 15mm, so this frequency would give only 1.5 waves to cover the area. For a 5% change in scattering, changes predicted at 0.1 mm^{-1} of around $1.5 \cdot 10^{-2}$ relative to 0.3 diffuse reflectance, would correspond to a 5% change in diffuse reflectance, which should be detectable. The sensitivity is however quite sensitive to the spatial frequency, and light levels remitted from tissue are limited, so the camera must be sensitive to

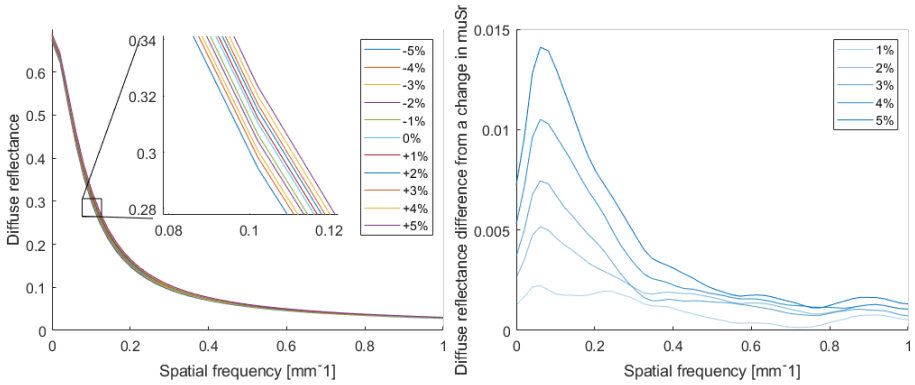

Figure 7.11: Left: Rdk predictions for small changes in μ_s'. The overall curves are very similar, with differences on a 10^{-3} scale. Right: The differences in Rdk caused by % changes in μ_s', as a function of spatial frequency. The peak shown for 0.1 mm^{-1} would indicate the spatial frequency with the highest sensitivity to scattering changes.

these changes. For small scattering changes it might be challenging to pick up the subtle differences in diffuse reflectance, this could well be the case for neuronal activity related tissue changes.

7.1.5 Results

Results from an example OIS experiment is shown in Figures 7.12 and 7.13. The activation maps show clear activation, and the averaged response across stimulus repeats follows a typical time course. Figure 7.14 shows an SFDI response to a standard 16 seconds stimulus, averaged over 7 repeats. Although the stimulus is clearly in effect, the scattering measurement did not show any changes on activation. From the SFDI results, it appears that only muA, not muSr changes during the activation. Scattering properties of the tissue remain constant throughout the stimulus, and remains at baseline for the duration of the experiment.

If tissue structural changes are activated by the stimulus, it may be that these changes are too subtle to be detected with this method. Work in the literature using SFDI to monitor scattering changes within rat brain, have demonstrated significant changes during gross neuronal changes.[160] The signals in their study were recorded during cortical spreading depression (CSD), a heamodynamic event which can occur in response to stroke, which was induced by the application of KCl solution onto the cortex. The effect if this would be not just a greater change in scattering, but the changes were sustained over time. In the case of neuronal activity-related changes,

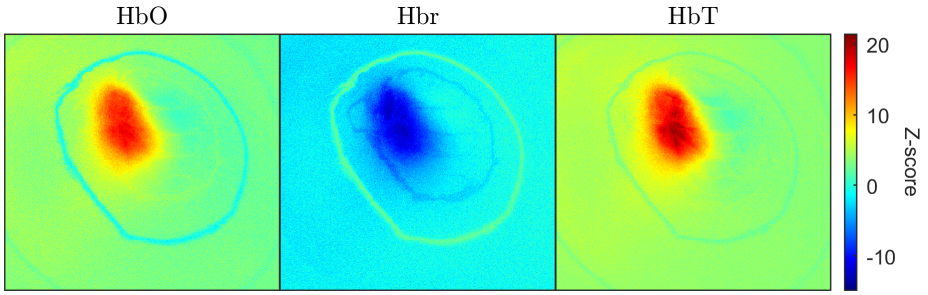

Figure 7.12: GLM results from an example OIS experiment with an 8 second stimulus.

any scattering effect would likely be smaller and could be relatively short lived, making it harder to detect. Their measurements were performed under projections with a 0.26 mm^{-1} spatial frequency, similar to the values used here. They attribute the scattering changes to neuronal depolarisation, noting they preceed both spatially and temporally the heamodynamic changes.

7.1.6 Discussion

SFDI results did not show any scattering changes during stimulus. Any scattering effects may be lost in analysis. Both the deconvolution step and the LUT could introduce fitting errors, which could reduce the scattering measures. Design of the LUT and look-up method might lead to a lowered sensitivity towards scattering. Even subtle dicrepancies could affect the result, if the scattering effect is very small.

A challenge in performing optical imaging within the bore is the light loss which occurs when transmitting the projection in and out of the bore. A crude test was set up to estimate the transmission efficiency through the fibre optics. The camera intensity was measured while illuminating a white background with the light guide output directly, and averaged across data from a one minute acquisition at 4 Hz. The ambient light levels were determined through repeating the experiment with the light guide turned off, and the result was subtracted from the original data, before dividing by the exposure time to get a value for intensity per uS. The measurement was repeated, first when illuminating with the light guide through the MRI fibre and then while illuminating through the endoscope, keeping the distance between light source and target constant. The results indicated only around 0.34% of light was transmitted through the endoscope, and 0.42% through

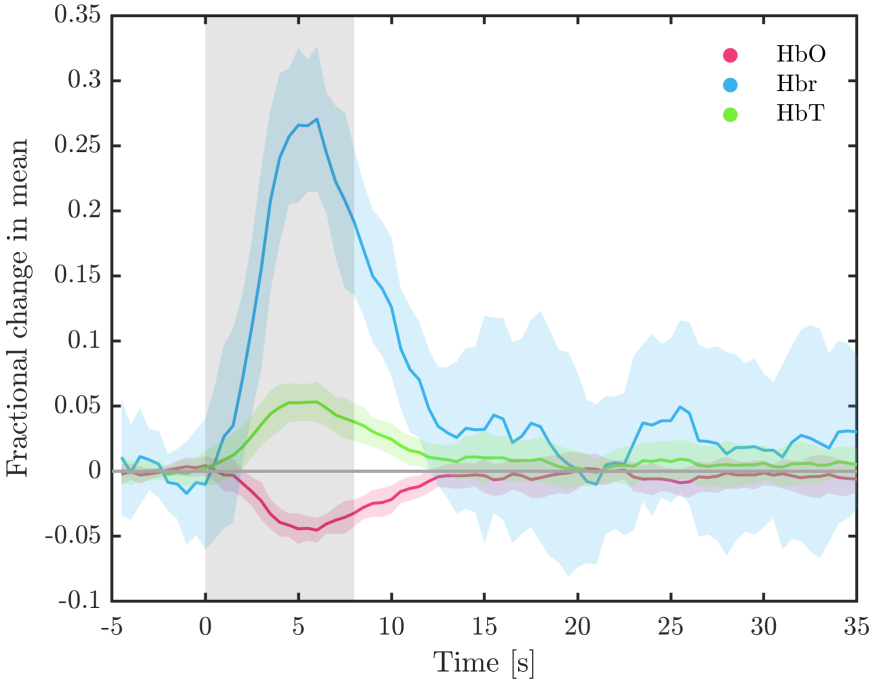

Figure 7.13: Mean response from an example OIS experiment with an 8 second stimulus

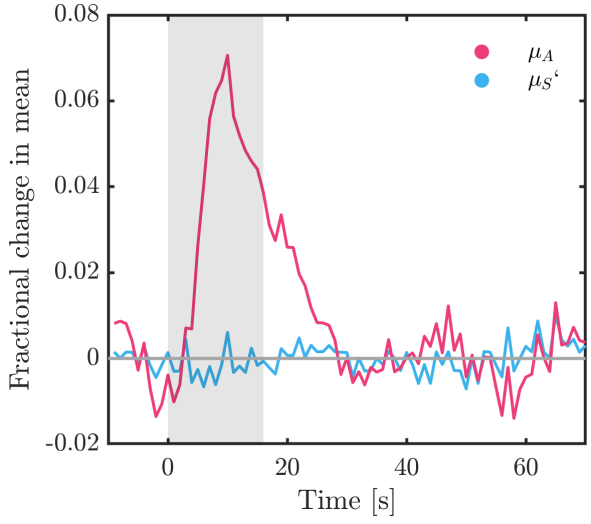

Figure 7.14: An example SFDI response to a standard 16 seconds stimulus, averaged over 7 repeats.

the MRI fibre.

The values are only intended as a rough estimate, it was for example assumed during the correction for exposure time that the measured camera intensity was proportional to light levels, though this is not necessarily the case. The results do however highlight the challenge of performing optical imaging within the MR bore; there is significant light loss associated both with illuminating the sample from a remote source, and with recording output light which is transmitted back through the fibres. For OIS, the setup can be simplified by illuminating directly via a long light guide from the switching galvanometer. With SFDI, there will be an added loss of transmission associated with the projector and the input fibre, requiring high transmission rates.

7.2 Visual stimulus script

```
1
2 % addpath(genpath('C:\toolbox\Psychtoolbox'))
3
4 % addpath(genpath('/groups/software/psychtoolbox'));
5
6 % Clear the workspace and the screen
7 sca; close all; clearvars;
8
9 % Testing:
10 Screen('Preference', 'SkipSyncTests', 1);
11
12 % --- Stimulus parameters ---
13 frequency = 12; % Frequency of 'on' flickering, in Hz
14 seconds_baseline = 60; % 61 for diffusion
15 seconds_stimulus = 16;
16 seconds_interval = 24;
17 repeats = 15;%15 % Number of (stimulus + interval)
     repeats
18 rcycles = 6; % Number of white/black circle pairs
19 tcycles = 18; % Number of white/black angular segment
     pairs (integer)
20
21 % --- Setup toolbox ---
22 PsychDefaultSetup(2);
23 screens = Screen('Screens'); % Get screen numbers for all
      attached screens
24 screenNumber = max(screens); % Select the maximum,
     external screen
25 % Define black and white (white will be 1 and black 0).
     This is because
26 % in general luminace values are defined between 0 and 1
     with 255 steps in
27 % between. All values in Psychtoolbox are defined between
      0 and 1
28 white = WhiteIndex(screenNumber);
29 black = BlackIndex(screenNumber);
30 grey = white / 2;
31 pale_grey = grey+0.1;
32 % Open an on screen window using PsychImaging and color
```

```
    it grey.
[window, windowRect] = PsychImaging('OpenWindow',
    screenNumber, grey);
% Measure the vertical refresh rate of the monitor
ifi = Screen('GetFlipInterval', window);
% Retreive the maximum priority number and set max
    priority
topPriorityLevel = MaxPriority(window);
Priority(topPriorityLevel);

% --- Generate pattern ---
xRadius = windowRect(3) / 2; % Radial distance from
    screen center to edges
yRadius = windowRect(4) / 2;
screenYpix = windowRect(4); % Screen resolution in Y
screenXpix = windowRect(3);
% Make checkerboard pattern

xylim = 2 * pi * rcycles;
[x, y] = meshgrid(-xylim: 2 * xylim / (screenYpix - 1):
    xylim,...
     -xylim: 2 * xylim / (screenYpix - 1): xylim);
at = atan2(y, x);
checks_w = ((1 + sign(sin(at * tcycles) + eps)...
     .* sign(sin(sqrt(x.^2 + y.^2)))) / 2) * (white -
    black) + black;
checks_b(:,:) = ((1 + -sign(sin(at * tcycles) + eps)...
     .* sign(sin(sqrt(x.^2 + y.^2)))) / 2) * (white -
    black) + black;
circle = x.^2 + y.^2 <= xylim^2;
checks_w = circle .* checks_w + grey * ~circle;
checks_b = circle .* checks_b + grey * ~circle;
checks_g = checks_b; checks_g(:,:) = grey;

% Make this into a PTB texture
radialCheckerboardTexture1  = Screen('MakeTexture',
    window, checks_w);
radialCheckerboardTexture2  = Screen('MakeTexture',
    window, checks_b);
radialGreyTexture = Screen('MakeTexture', window,
    checks_g);
```

```
64
65 % Create fixation cross
66 % Set up alpha-blending for smooth (anti-aliased) lines
67 Screen('BlendFunction', window, 'GL_SRC_ALPHA', '
       GL_ONE_MINUS_SRC_ALPHA');
68 Screen('TextFont', window, 'Ariel'); Screen('TextSize',
       window, 36);
69 [xCenter, yCenter] = RectCenter(windowRect); % Centre
       coordinate of window
70 fixCrossDimPix = 40;
71 xCoords = [-fixCrossDimPix fixCrossDimPix 0 0];
72 yCoords = [0 0 -fixCrossDimPix fixCrossDimPix];
73 allCoords = [xCoords; yCoords];
74 lineWidthPix = 4;
75
76 numSecs = 1/frequency;
77 numFrames = round(numSecs / ifi);
78 duration_frames = seconds_stimulus*(frequency/2);
79 numWaitFrames = round(seconds_interval / ifi);
80 numBaselineFrames = round(seconds_baseline / ifi);
81
82 waitframes = 1;
83
84 % Flip outside of the loop to get a time stamp
85 Priority(topPriorityLevel);
86 vbl = Screen('Flip', window);
87
88 keys = zeros(1,256);
89
90 % --- Wait for trigger ---
91 keyPressed = '0';
92 while ~strcmp(keyPressed,'5%')
93     [~,key] = KbWait;
94     keyPress = KbName(key);
95     if strcmp(keyPress,'5%')
96         keyPressed = keyPress;
97         [~,~,keyCode] = KbCheck;
98         trigger = find(keyCode); keyCode = 0;
99     end
100 end
101 Screen('DrawLines', window, allCoords,...
```

```
    lineWidthPix, white, [xCenter yCenter], 2);


% --- Run stimulus ---
esc = 0; f = 0; r = 0; done = 0;
for frame = 1:numBaselineFrames
    Screen('DrawTexture', window, radialGreyTexture); % Draw
    Screen('DrawLines', window, allCoords,...
    lineWidthPix, white, [xCenter yCenter], 2);

    vbl = Screen('Flip', window, vbl + (waitframes-0.5)*ifi); % Flip
end
while ~(esc == 1)
    while ~(esc == 1) && ~(done == 1)
        for frame = 1:numFrames
        Screen('DrawTexture', window, radialCheckerboardTexture1); % Draw
        Screen('DrawLines', window, allCoords,...
    lineWidthPix, white, [xCenter yCenter], 2);

        vbl = Screen('Flip', window, vbl + (waitframes-0.5)*ifi); % Flip
        end
%
%         [ keypress, ~, keyCode ] = KbCheck; % check for keypress
%         if keypress == 1 && KbName(keyCode) == 'q'
%             esc = 1; Screen('CloseAll');
%         end

        for frame = 1:numFrames
        Screen('DrawTexture', window, radialCheckerboardTexture2);% Draw
        Screen('DrawLines', window, allCoords,...
    lineWidthPix, white, [xCenter yCenter], 2);

        vbl = Screen('Flip', window, vbl + (waitframes-0.5)*ifi); % Flip
        end
```

```
136
137         f = f+1;
138         if f >= duration_frames
139             done = 1;
140         end
141     end
142     done = 0; f = 0;
143
144     for frame = 1:numWaitFrames
145     Screen('DrawTexture', window, radialGreyTexture); %
    Draw
146     Screen('DrawLines', window, allCoords,...
147     lineWidthPix, white, [xCenter yCenter], 2);
148
149     vbl = Screen('Flip', window, vbl + (waitframes-0.5)*
    ifi); % Flip
150     end
151 %
152 %     [ keypress, ~, keyCode ] = KbCheck; % check for
    keypress
153 %     if keypress == 1 && KbName(keyCode) == 'q'
154 %         esc = 1; Screen('CloseAll');
155 %     end
156
157     r = r+1;
158     if r >= repeats
159         esc = 1;
160     end
161 end
162
163 Priority(0); % Clear the screen.
164 ListenChar(0); sca;
```

York NeuroImaging Centre
THE UNIVERSITY of York
The Biocentre, York Science Park, Heslington, York, YO10 5NY
Tel.(01904) 435329, Fax (01904) 435356

General Consent Form

R_____
Registered by:_____
For Office Use Only
Version: 2 - 2014-01-31

Thank you for applying to be a participant in a study at the York NeuroImaging Centre (YNiC). You must complete each of the following sections in full. This form must be returned at least 24 hours prior to the experiment in order to receive a participant ID. Once completed, please return to reception at YNiC.

Please note we do not accept completed forms via email. If your weight is over 21 stones (133Kg) please contact YNiC before completing this form. If you do not want to answer any question(s) on this form you are free to withdraw without any prejudice.

Title	Forename	Other initial(s)	Surname	DOB	Sex

Email Address	Contact Telephone No.

Home Address	General Practitioner's UK Practice Address

Do you wish to become a member of the YNiC volunteer pool? Y / N
(If you choose to become a member you may be asked to participate in further studies, though you will be under no obligation to do so).

Do you have normal vision *(without glasses or contact lenses)*? Y / N

Please indicate your handedness: Right Left Ambidextrous

What is your native language? _____

Clinical Diagnostic Policy

- The York Neuroimaging Centre is not a clinical diagnostic facility and as such does not routinely inspect all scans for anomalies. However a small number of scans are sent for clinical evaluation. This does not indicate the presence or absence of an anomaly.
- We will send the result of any clinical evaluation to your GP for their records. Your GP may decide that further action is or is not required.
- We will advise you that we have sent the clinical evaluation of your scan to your GP.
- If your scan has been sent for clinical evaluation your research data will not be released for processing until you have indicated you are happy for us to release it by completing our data-release form.

I understand that the York Neuroimaging Centre is not offering a diagnostic service and that no clinical advice will be offered.
I fully consent to the personal details collected on this form being stored securely at YNiC in both digital and hard copy formats.
I confirm that I have read and understood the YNiC Clinical Diagnostic Policy and fully consent to it being applied to any and all scans acquired on me at YNiC.
I confirm that I consent to my scans and any results obtained being stored and used for research purposes as approved by the York NeuroImaging Centre.
I confirm that I consent to my anonymised data being used for the creation of scientific publications.

Signature: _____ **Date:** _____

York Neuroimaging Centre THE UNIVERSITY of York

"Diffusion Weighted functional brain imaging: investigating cellular swelling as a potential direct measure of neuronal activity"

Participants should complete items 1 to 10 themselves.

	Please circle either YES or NO
1. I have read the information sheet entitled 'Diffusion Weighted functional brain imaging: investigating cellular swelling as a potential direct measure of neuronal activity'.	YES / NO
2. I have had the chance to discuss the study and to ask questions.	YES / NO
3. I have had satisfactory answers to all of my questions.	YES / NO
4. Who has explained the study to you? Prof/Dr/Mr/Mrs/Ms……	
5. I understand that I am free to withdraw from the study: • At any time. • Without having to give a reason. • Without prejudice to my academic standing at the University of York.	YES / NO
6. I understand that as part of this study I will be shown several repeated visual stimuli in the form of a flickering image projected onto a screen within the scanner environment. I have been given the opportunity to see this outside the magnet and am comfortable to proceed.	YES / NO
7. I know that the research information that I will provide will be kept strictly confidential. I understand that the information collected about me will be used to support other research in the future, and may be shared with collaborators and/or used in research/teaching. Fully anonymised data may also be made publicly accessible and used in publications. In all these cases, no personally identifiable information will be revealed without my written agreement.	YES / NO
8. If I have any questions or concerns about the research, I know I can contact either Frida H. Torkelsen (fht502@york.ac.uk), Dr Aneurin J. Kennerley (01904 324230, Aneurin.kennerley@york.ac.uk) or Prof. Alex Wade (Alex.wade@york.ac.uk) at the University of York.	YES / NO
9. Do you agree to take part in the study?	YES / NO

10. **PARTICIPANT**

Signature of Participant…….. Date……..……

Name (BLOCK LETTERS) ……..…..

11. **INVESTIGATOR**

I have explained the study to the above participant and he/she has indicted his/her willingness to take part.

Signature of Investigator..…….…….…….. Date……..…..……

Name (BLOCK LETTERS) ……..…..

THE UNIVERSITY of York

York Neuroimaging Centre

"Diffusion Weighted functional brain imaging: investigating cellular swelling as a potential direct measure of neuronal activity"

Participant Information Sheet

You are being invited to take part in a research study. It is important for you to understand why the research is being done and what it will involve. Please read the following carefully and ask any questions if you wish.

What is the purpose of the study?

Current neuroimaging techniques which rely on measuring changes in blood oxygenation, flow and volume are limited in resolution by the large volume of vessels involved and a slow response to activation. An alternative method which relies on measuring biophysical changes in the active brain cells appears to overcome these limitations, but has yet to gain traction in the neuroimaging community. This study employs both methods with the aim to explore their performance and to aid in the validation of the new method by improving our understanding of the underlying biophysical origins of the measured signal.

Why have I been chosen?

Because you are a healthy volunteer with no known vision problems.

Do I have to take part?

No. It is up to you to decide whether or not to take part. If you do, you will be given this information sheet to keep and will be asked to sign a consent form. You are still free to withdraw any time and without giving a reason.

What will happen to me if I take part?

You will first be asked to fill out a participant form to allow you to register as a participant with York Neuroimaging Centre (YNiC). We will also run through the MRI exclusion criteria with you at this stage to ensure you are eligible.

On the day of the scan, you will be met by the researcher and taken to York Neuroimaging Centre (YNiC). You will have the opportunity to change clothes at this stage, and to remove any metal items etc. You will then be positioned inside the MRI scanner.

The scan will last no longer than 60 minutes. During the scan, a flickering image will be projected onto a screen visible to you inside of the scanner. This will take the form of a checkerboard and will be switched on and off for various durations of time.The whole procedure will take less than 2 hours and take place at a suitable time between 9-7pm Monday to Friday. The exact time of your scan will be confirmed at least one week before.

After the scan session you will be free to retrieve your personal items and leave.

Benefits of taking part in the research

This project is part of ongoing efforts by researchers at York University to explore the physical basis of functional MRI signals with an aim to aid development of increasingly accurate methods for measuring neuronal activity. You will be contributing to the evaluation of a method which has the potential to replace current functional neuroimaging strategies and provide superior spatial and temporal resolution, to the great benefit of the field of neuroimaging.

Is there a chance that the brain scan will detect something wrong with my brain?

Yes, neuroimaging research can detect brain anomalies (abnormal structural features). Such anomalies are uncommon (~3% of volunteers scanned). Most frequently anomalies are benign and will not affect

York NeuroImaging Centre
THE UNIVERSITY of York

Safety Questionnaire and Consent for Participants

Version: 3 - 2019-01-29

Modality – Siemens MRI

Participant ID: R	Surname:	Forename:	Date of Birth:	Height:	Weight:	Phone No:
Address		GP Address				
Verified		Verified				

If your, or your GPs, address are different to those shown above please cross out the old address and write the new one next to it. Please do not assume we will accept you for a research scan on the basis that you have been scanned elsewhere (regardless of whether it was for research or clinical reasons). Please remove all eye make up prior to attending for your scan.

It is essential that all questions on this sheet are answered truthfully. This information is essential in order to ensure your safety and will be kept completely confidential. If you do not want to answer any question(s) on this form you are free to withdraw from this scanning session without any prejudice.

Please answer the following questions accurately by ticking the appropriate box. If you answer YES to any of the safety questions please call YNIC on 01904 435329	**Participants Answers**		**YNIC STAFF USE ONLY**
Safety	**Yes**	**No**	**Approval for individuals with contraindications**
Do you have a cardiac (heart) pacemaker or pacing wires?			NEVER SCAN
Have you ever had any operations on your heart, head or spine? *If yes please give details*			
Do you have or have ever had a spinal or other neuro stimulator			
Have you had any surgery which involved the use of medical implants? E.g. Hip or knee replacements, breast or penile implants or any procedure using metal stents e.g. coronary arteries. *If yes please give details*			
Do you have a programmable hydrocephalus shunt?			NEVER SCAN
Do you have a cochlear (ear) implant?			NEVER SCAN
Do you have a fixed dental brace?			
Have you any surgery in the last 3 months?			
Have you,at any time, had an injury to your eye involving metal fragments?			
If YES Did you see a doctor or get medical advice?			
If YES, did the doctor tell you that everything had been removed?			
Do you have any shrapnel in your body?			
Are you currently wearing any jewellery? – e.g. piercings, watches, bracelets, necklaces, hair clips, rings			
Do you have any tattoos?			WARN ABOUT HEATING
Do you have any medicinal patches? Including nicotine,hormone			
Are you a close relative of any of the investigators, i.e. Spouse, sibling, parent, grandparent, child or grandchild?			
Do you have epilepsy? Have you ever had a fit or seizure?			

Please answer the following questions accurately by ticking the appropriate box. If you answer YES to any of the safety questions please call YNIC on 01904 435329	**Participants Answers**	
Safety	**Yes**	**No**
Do you have an Intra-Uterine Contraceptive Device? *if yes please give details (certain types are not safe at 3T)*		
Are you, or could you be pregnant?		
Consent		
I have fully understood and completed the safety section of this form.		
I understand the nature of the procedures to be carried out		
I have been able to ask questions regarding the procedures		
I have had the emergency evacuation procedures explained to me		
I give my full consent to MRI scans being performed on me		
I give my consent to my anonymised images from my scan being used for display		
I am aware that I may end the scan or procedure at any time by informing a member of staff		

Signatures

Only sign if you are in **no doubt** about the participant's suitability for MRI

Project ID: -		**Date**
Participant		
Guardian (if under 18 years old)		
Approved operator A		
Approved operator B		

Complete the section below only after completion of final metal screening:

I confirm that I have checked that there is no metal about my person immediately before entering the scanner.	**Participant signature:** _____

7.3.4 MRI safety form